



THESIS / THÈSE

DOCTOR OF SCIENCES

A geometric approach to modular and weak values

Cormann, Mirko

Award date:
2017

Awarding institution:
University of Namur

[Link to publication](#)

General rights

Copyright and moral rights for the publications made accessible in the public portal are retained by the authors and/or other copyright owners and it is a condition of accessing publications that users recognise and abide by the legal requirements associated with these rights.

- Users may download and print one copy of any publication from the public portal for the purpose of private study or research.
- You may not further distribute the material or use it for any profit-making activity or commercial gain
- You may freely distribute the URL identifying the publication in the public portal ?

Take down policy

If you believe that this document breaches copyright please contact us providing details, and we will remove access to the work immediately and investigate your claim.



UNIVERSITY OF NAMUR
FACULTY OF SCIENCES
Namur, Belgium

A geometric approach to modular and weak values

Author: MIRKO CORMANN

*A thesis submitted in fulfillment of the requirements for the degree of
Doctor of Science.*

Members of the jury:

Prof. PHILIPPE LAMBIN (President)

Prof. JOHN MARTIN

Prof. ALEXANDRE MATZKIN

Prof. BERTRAND HESPEL (Co-supervisor)

Dr. YVES CAUDANO (Supervisor)

June 2017

Abstract

Weak and modular values are unbounded complex numbers that usually describe observations in weak measurements of pre- and postselected ensembles. In practice, only their real or/and imaginary part have been measured directly so far, or related to observations. Our work brings a wholly new perspective to the research of weak and modular values by studying their polar form.

An interferometric measurement of the visibility and the phase in a quantum eraser experiment allows us to probe directly the polar form of weak and modular values: the interferometric visibility is related to the modulus; the phase provides the argument. Our proof-of-concept experiment relies on nonlocal correlations of two qubits (entangled photons), which act as the meter and probed systems, respectively. This system has a fundamental quantum nature; yet it remains relatively simple.

The Majorana representation of N -level quantum systems in terms of symmetric states of $N - 1$ qubits provides us with a description on the Bloch sphere. With this geometric approach, weak and modular values of N -level systems can be factored in $N - 1$ contributions. Their modulus is determined by the product of $N - 1$ ratios involving projection probabilities between qubits, while their argument is deduced from a sum of $N - 1$ solid angles on the Bloch sphere.

These theoretical results allow us to study the geometric origin of the quantum phase discontinuity around singularities of weak and modular values in two- and three-level systems. This geometric approach opens also the way to describe weak measurements of high-level quantum systems by the manipulation of multi-qubit states. Furthermore, the three-box paradox (a so-called quantum paradox) is analyzed from the point of view of a bipartite quantum system. In the Majorana representation of this paradox, an observer comes to opposite conclusions about the entanglement state of the particles that were successfully pre- and postselected.

Acknowledgments

I would like to thank Prof. B. Hespel and the department of physics of the University of Namur for giving me the opportunity to realize my thesis.

I am grateful to my adviser Dr. Y. Caudano for his careful reading of my work and his insightful remarks during the last six years. I would also like to thank the other members of my thesis committee, Prof. P. Lambin, Prof. J. Martin, Prof. A. Matzkin and Prof. B. Hespel for their brilliant comments and suggestions.

I would like to thank all former and current members of the laboratory for their enriching guidance, encouragement and support in all these years. I would also like to express my sincere thanks to all persons who contributed, directly or indirectly, to this great challenge.

I am grateful to my friends and my family who for six years had to wonder what I do all day.

I would like to express my special gratitude to my girlfriend Annabelle for her moral support throughout the duration of my thesis. We've done it!

Thanks, Merci, Danke!

Contents

Abstract	i
Acknowledgments	ii
Contents	iii
List of figures	vi
List of tables	viii
1 Introduction	1
2 Quantum measurements	6
2.1 Projective measurements	7
2.2 Standard measurements	7
2.2.1 Ideal measurements	7
2.2.2 Non-ideal measurements	9
2.3 Pre- and postselected measurements	11
2.3.1 Ideal pre- and postselected measurements	11
2.3.2 Non-ideal pre- and postselected measurements	13
2.4 Properties of the weak value	18
2.5 A generalization of weak values	19
2.6 Applications of weak and modular values	21
2.7 Summary and Motivation	22
3 Interferometric measurements of weak and modular values	24
3.1 Theoretical Approach	26
3.1.1 General probe state	26
3.1.2 Signal-to-noise ratio	31
3.1.3 Qubit probe state	33
3.2 Experiment	34
3.2.1 Materials	34
3.2.2 Methods	36
3.3 Results and discussion	42

3.3.1	Calibration of the quartz plate	42
3.3.2	Meter state preparation	44
3.3.3	Real weak values: analysis of the purity and the measurement strength	49
3.3.4	Complex weak values: analysis of the quantum phase	54
3.4	Summary	57
4	Geometric representation of weak and modular values of discrete quantum systems	59
4.1	Bloch vector representation of modular and weak values	60
4.2	Geometrical representation of modular and weak values of two-level quantum systems	61
4.2.1	Weak value of projectors	61
4.2.2	Modular value	64
4.3	Three-level quantum systems	69
4.3.1	Weak values of projectors in qutrit systems	72
4.3.2	Modular values in qutrit systems	74
4.3.3	Generalization to arbitrary N -level quantum systems	76
4.4	Summary	79
5	Applications of the geometric representation involving discrete quantum systems	80
5.1	Response of the meter detection system around phase discontinuities	81
5.2	Singularities in weak values of three-level quantum systems	86
5.3	Weak measurement of the modular value by probed bipartite qubit systems	91
5.4	Summary	97
6	A well-known quantum paradox in a new form	99
6.1	The three-box paradox	100
6.2	The two-particle version of this three-box paradox	102
6.3	Summary	107
7	Conclusion and Perspectives	108
	Bibliography	112
	Appendices	123

A	Gaussian meter in von Neumann measurement protocol	124
B	Derivation of the meter average	129
	B.1 Relation to the real and the imaginary parts of the modular value . . .	129
	B.2 Relation to the modulus and the argument of the modular value	130
	B.3 Relation to the probability ratio x_s	131
C	Phase-matching of the nonlinear down-conversion process	132
D	Relative phase induced by a z-cut quartz plate	135
E	Quantum tomography table	138
F	Quantum tomography density matrix	139
G	Modulus of complex weak value	142
H	Weak and modular values of qubit observables expressed using Bloch vectors	143
	H.1 Projection probability and modulus expression	143
	H.2 Qubit projection Operator	144
	H.3 Qubit unitary operator	145
I	Algebraic structure of qutrits	147
J	Majorana representation for an arbitrary state	149
K	Orthogonal-state decomposition	150
L	Orthogonal-state decomposition of the three-box states	151

List of Figures

1.1	The experimental device for measurement of the weak value proposed in the seminal paper [1] from 1988 by Aharonov, Albert and Vaidman . . .	2
2.1	An ideal standard measurement	9
2.2	A non-ideal standard measurement	11
3.1	Controlled quantum evolution with corresponding meter states	27
3.2	Set-up of the controlled evolution protocol	35
3.3	Entangled photon source	37
3.4	Coincidence count protocol	40
3.5	Quartz plate calibration	43
3.6	Experimental density matrix of the biphoton state $\hat{\rho}_{exp}^{(1)}$	48
3.7	Experimental outcome of the visibility and the criterion x_s used to select the appropriate weak value solution	50
3.8	Weak value acquisition for different measurement strengths	52
3.9	Modulus of complex weak values	55
3.10	Argument of complex weak values	57
4.1	Solid angle representation on the Bloch sphere	63
4.2	Spherical quadrangle representation on the Bloch sphere	68
5.1	Measurement results of the argument $\arg \sigma_{x,w}$ for two preparations and the corresponding reconstructed postselected polarization states in the form of Bloch vectors \vec{f}	82
5.2	Evolution of the spherical quadrangle Ω_{irsf} due to the reconstructed, postselected vector \vec{f} with fixed phase ϕ_1	84
5.3	Evolution of the spherical quadrangle Ω_{irsf} due to the reconstructed, postselected vector \vec{f} with fixed phase ϕ_4	85
5.4	Evolution of the angles $\alpha_{1,2}$ and $\beta_{1,2}$ characterizing the initial qubit states $ \phi_i^{(1,2)}\rangle$ with respect to the parameter θ	88
5.5	Modulus of the weak value $\Pi_{r,w}^{(3)}$ and solid angle defining its argument $\arg \Pi_{r,w}^{(3)}$	90
5.6	Majorana qubits resulting from the modular value $\lambda_{r,m}^{\alpha,\beta}$	94

List of Figures

5.7	Orthogonal qubits resulting from the geometric approach to the modular value $\lambda_{r,m}^{\alpha,\beta}$	95
5.8	Controlled quantum weak measurement protocol of a symmetric bipartite qubit state	97
6.1	Representation in the Bloch sphere of the relevant states appearing in the three-box experiment.	104
C.1	Phase-matching condition generating the nonlinear down-conversion process inside a type-I BBO	133
D.1	Phase and position change induced by a z-cut quartz plate	136
F.1	Density matrix of the experimental biphoton state $\hat{\rho}_{exp}^{(2)}$	139
F.2	Density matrix of the experimental biphoton state $\hat{\rho}_{exp}^{(3)}$	140
F.3	Density matrix of the experimental biphoton state $\hat{\rho}_{exp}^{(4)}$	141
G.1	Modulus of complex weak values	142

List of Tables

3.1	Coincidence counts and total counts to reconstruct the experimental produced two-photon state $\hat{\rho}_{exp}^{(1)}$	46
3.2	Experimental meter parameters determined by the quantum state tomography method for the first four experimental set-ups (real weak value).	49
3.3	Experimental meter parameters determined by nonlinear regressions for the first four experimental set-ups (real weak value).	51
3.4	Experimental meter parameters determined by nonlinear regressions for the last four experimental set-ups (complex weak value).	54
6.1	Weak values of the box projectors in the three-box paradox determined from the weak values of the associated qubit projectors deduced from the Majorana representation.	105
E.1	Coincidence counts and total counts to reconstruct the experimental produced two-photon state $\hat{\rho}_{exp}$: complete table	138

1

Introduction

Quantum mechanics is currently the most successful theory to describe the nature of the microscopic world. Instead of predicting deterministically the states of microscopic systems, quantum theory refers rather to probabilistic predictions. The measurement process in quantum mechanics is as old as quantum theory itself. A quantum measurement of a microscopic, isolated system is realized by its interaction with a classical, macroscopic measuring apparatus. When this interaction is sufficiently strong, then the measuring apparatus features an unambiguous readout determining entirely the state of the quantum system. The gained knowledge about the original state of the microscopic system completely disturbs the latter: the original, unknown state is completely erased and no subsequent measurement can provide any information about it. During the last several decades, there has been considerable advancement in the study of the measurement process. In particular, measurement techniques with weak interactions between quantum systems and measuring apparatuses have been studied with increasing interest. As the disturbance of the observed quantum systems is reduced, the gained knowledge about the original states decreases, too. The information gained from a single interaction is less reliable, and the measuring apparatus features an ambiguous readout. Thus, the quantum system is left in an indetermined state.

In the seminal paper [1] from 1988 by Aharonov, Albert and Vaidman, the authors demonstrate that the mean deflection of an arbitrary measuring apparatus provides a reliable readout about the quantum system if the weak interaction is accomplished many times over identical prepared quantum systems. The process to select only quantum systems with the same initial state is known as preselection. In their paper, Aharonov and his collaborators observe a beam of spin-1/2 particles through a Stern-Gerlach device which weakly measures the spin orientation as shown in figure 1.1. In this way,

the mean deflection of the particles' beam indicates the average spin orientation \bar{S}_z of the preselected particles. Then, the authors ask what the apparatus would record if only a part of the original ensemble of spin particles will be taken into account? This sub-ensemble is formed by a final, strong measurement process, which is defined as postselection. The revolutionary observation is that the measuring apparatus indicates now a deflection related to an average value with unusual properties. This marks the discovery of the weak value. In the case of their spin-1/2 experiment, the mean deflection of the particles' beam provides a spin average value of 100! While the usual average value of a spin-1/2 observable is bounded by its eigenvalues, here ± 1 , it seems strange that a measuring apparatus assigns the mean value of 100 to the spin observable \hat{S}_z for pre- and postselected quantum systems. Besides this unbounded character, the authors demonstrate also that weak values can even be complex. In fact, the mean deflection of the particles' beam reveals only the real part of the weak value of the spin observable \hat{S}_z . Its imaginary part can be recovered by measuring the mean deflection in momentum space.

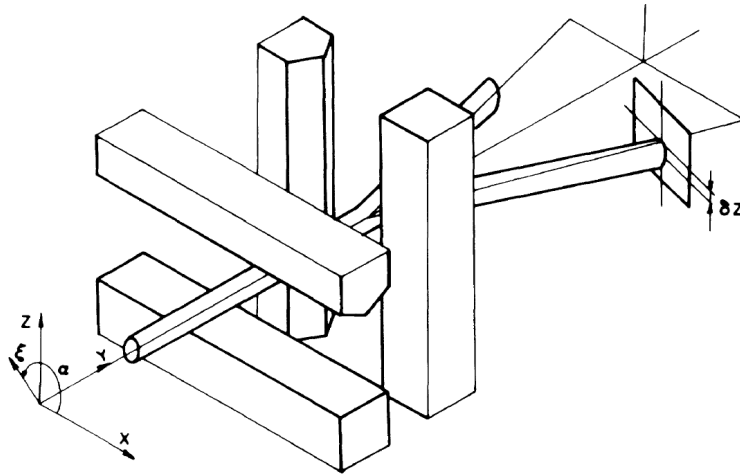


Figure 1.1: The experimental device for measurement of the weak value proposed in the seminal paper [1] from 1988 by Aharonov, Albert and Vaidman. The beam of particles with the spin oriented in the ξ -direction passes through a first Stern-Gerlach device applying an inhomogeneous weak magnetic field in the z -direction. Then, the beam is split by a second Stern-Gerlach device applying an inhomogeneous strong magnetic field in the x -direction. The beam of spin-1/2 particles with an eigenvalue of $+1$ is collected on the screen and the deflection of the spot in the z -direction determines the real part of the weak value of the spin operator \hat{S}_z .

Since weak values are unusual measurement outcomes, their introduction brought a new perspective into the standard debate of quantum mechanics. In a further paper [2] from 2010 by Kedem and Vaidman, the authors characterize the interaction of pre- and postselected quantum systems with discrete measuring apparatuses. They demonstrate the existence of an additional unbounded, complex value: the modular value. This value extends the family of pre- and postselected weak values. In general, modular values are not often reported as such in literature because they are directly related to weak values in a first order approximation. The proper physical interpretation of weak and modular values remains highly debated and this discussion continues until today. For example, on the one hand, weak values were used to develop a time-symmetrized approach to standard quantum theory, the two-state vector formalism [3], where they appear as purely quantum objects. On the other hand, a purely classical view of the occurrence of unbounded, real weak values was proposed [4] (which is criticizable though [5–7]). The authors even suggest that complex weak values have a classical explanation as well because, in practice, only the real or the imaginary part of weak values have been measured directly so far. A more detailed discussion can be found in [8].

Independently of the physical interpretation of weak and modular values, the concept of pre- and postselected weak measurements has proven useful in various experimental fields of physics and chemistry. In the field of high precision metrology, the unbounded character of weak values is used to amplify small effects [9–13]. For example, this weak measurement technique is implemented to demonstrate experimentally the spin Hall effect of light. A sensitivity to displacements of 1 Ångström must be reached to realize this measurement. Novel procedures using the complex nature of weak and modular values are performed to determine unknown quantum states [14–16]. This technique even allows the reconstruction of average trajectories of single photons in the double-slit experiment [17]. Interestingly, weak values of the momentum operator are directly related to components of the energy-momentum tensor in the Bohm approach to quantum mechanics [18, 19]. Thus, it is not surprising that these weakly measured trajectories correspond to the two-slit trajectories calculated in the Bohm approach. Moreover, pre- and postselected weak measurements are applied in the field of quantum paradoxes [20, 21]. A quantum paradox is a phenomenon that classical physics cannot explain. In particular, the paradox in the three-box experiment results from the certitude to find a single particle in two separated boxes [22, 23]. This three-box paradox has been experimentally studied with great interest by weak measurements. In

these experiments, weak values of -1 appear as measurement results. Unfortunately, the meaning of these outcomes in terms of probability amplitudes is not clear, yet.

Most weak measurement studies target the simplest non-trivial Hilbert space, of dimension two. Three-level or higher-dimensional discrete quantum systems have rarely been studied using the weak measurement formalism [24–26]. Recent applications of weak measurement theory in the context quantum computation research attest the interest of investigating weak values of high-level systems [27,28]. Weak values of qutrit observables show their usefulness in the experimental demonstration of the Kochen-Specker test of noncontextuality [29] and can be applied to the quantum Cheshire cat experiment [30]. In the past, it was pointed out that the argument of weak values of qubit states has a topological origin, similar to the Pancharatnam geometric phase [31]. This purely geometric approach to the description of the quantum phase is useful to understand rapid displacements of interference fringes in quantum eraser experiments [32,33]. Furthermore, it explains prior observations involving discontinuous phase jumps, such as the π -phase jump in cross-phase modulation [34], as well as discontinuities around phase singularities [35]. A first approach to express the argument of weak values of three- and higher-level quantum systems by geometric quantities was indirectly demonstrated in references [36,37].

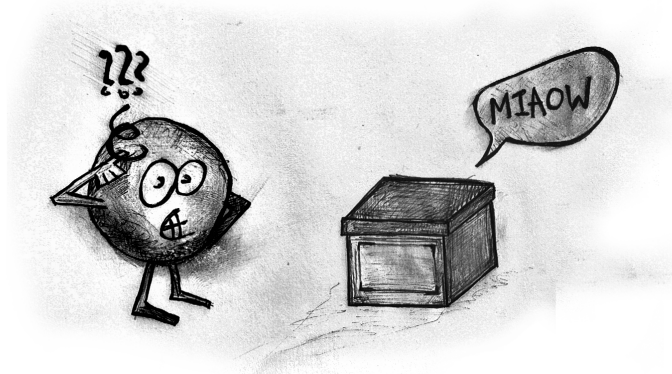
This thesis is a first step to a pure geometric description of weak and modular values of discrete quantum systems. Theoretically, I demonstrated a direct connection of the complex weak and modular values with the Pancharatnam-Berry phase. The application of this geometric representation on several examples given in the literature opens the way to deeper investigations into the physical interpretation of weak and modular values. These theoretical results led to a publication [38] in 2017. On the basis of this geometric description (chapter 4), I studied the origin of discontinuous phase jumps of weak values (chapter 5). In the same publication, I also recasted the three-box paradox in terms of pairs of spin- $\frac{1}{2}$ particles (chapter 6). Experimentally, I realized a procedure to determine completely these geometric components of the complex weak and modular values by using polarization-entangled photons. This procedure permitted me to discuss the physics of weak and modular values in real interferometric experiments. These experimental results led to a publication [39] in 2016, which are detailed in chapter 3.

This work is organized as following. Chapter 2 will introduce the standard weak measurement technique applied on pre- and postselected ensembles. This theoretical background will be helpful to understand how quantum measurements reveal the real and the imaginary parts of the complex unbounded weak and modular values by simply varying the measurement strength. This chapter will conclude with a discussion of the unusual properties of these values and their large field of applications in physics. In chapter 3, an alternative interferometric measurement technique will be devised to measure the polar components of the complex weak and modular values instead of the usually determined real and imaginary parts. Using polarization-entangled photons, it will experimentally be shown that this procedure works for arbitrary measurement strengths and for nearly orthogonal initial and final states. Then, in chapter 4, the focus will be put on weak and modular values of discrete quantum systems. In a purely theoretical approach, it will be shown that the polar components of these values can be described by geometrical quantities, as spherical polygons, on the Bloch sphere. In chapter 5, this approach will be used to explain discontinuous effects around singularities of weak values of discrete quantum systems. Moreover, it will allow to apply the interferometric measurement technique developed in chapter 3 on symmetric two-qubit systems. This geometric representation of weak values will be helpful once again to revisit a well-known paradox previously studied by weak measurements: the quantum three-box paradox [22]. In chapter 6, it will be shown that when the equivalent three-level system is recast as a pair of spin- $\frac{1}{2}$ particles in a symmetric spin state, this experiment involves contradictory conclusions about the entanglement state of the pre- and postselected particle pairs. Finally, chapter 7 will close this thesis by a conclusion and some perspectives discussing potential applications and experiments of this geometric description of weak and modular values.

2

Quantum measurements

In this chapter, we will recall the basic concepts of measurements in quantum mechanics starting with the projection postulate. This postulate will be helpful to understand how a measuring apparatus is able to measure a physical quantity \mathcal{A} of a quantum system. Therefore, we will consider a simple interaction Hamiltonian coupling the measuring apparatus with the probed quantum system. By varying the coupling strength, we will present in the following sections the notions of ideal and non-ideal standard measurements. Moreover, the concept of pre- and postselected quantum systems will be added to this measurement process, resulting in the appearance of the unbounded complex weak and modular values. Then, we will discuss the properties of these values and their large field of applications in physics. This first chapter will conclude with the motivation of the research presented in this thesis.



2.1 Projective measurements

In quantum mechanics, each physical quantity \mathcal{A} of a quantum system is described by a Hermitian operator \hat{A} . Let the operator \hat{A} have discrete, non degenerate eigenvalues a_k with a spectral decomposition defined as:

$$\hat{A} = \sum_k a_k \hat{\Pi}_k, \quad (2.1)$$

where $\hat{\Pi}_k$ is the projector onto the eigenstate $|a_k\rangle$ with the corresponding eigenvalue a_k . The initial state of the probed quantum system is described by the density operator $\hat{\rho}_i$. Then, the projection postulate induces that the measurement of \mathcal{A} yields the value a_k with the probability:

$$P_k = \text{Tr} \left[\hat{\Pi}_k \hat{\rho}_i \right]. \quad (2.2)$$

Due to this measurement, the system state becomes:

$$\hat{\rho}_k = \frac{\hat{\Pi}_k \hat{\rho}_i \hat{\Pi}_k}{\text{Tr} \left[\hat{\Pi}_k \hat{\rho}_i \right]}. \quad (2.3)$$

No subsequent measurement can provide any information on the original state of the system, since the states of the system before and after the measurement are independent. In this case, the measurement is complete. An important generalization of the projective measurements is described by the positive-operator valued measure approach (POVM) [40]. Such a measurement is generally incomplete, i.e. it does not specify a single state that is independent of the state before the measurement.

2.2 Standard measurements

2.2.1 Ideal measurements

In a standard measurement, the quantum system is coupled to the measuring apparatus, called meter or pointer, via a unitary interaction. The readout of the meter provides information about the system. The mathematician von Neumann introduced a simple model which describes how this process produces projective measurements, which defines an ideal measurement [41]. In this scheme, the quantum measurement of the physical quantity \mathcal{A} is performed by coupling the system with the meter via the

interaction Hamiltonian during the time interval $[t_i, t_f]$:

$$\hat{H}_{int} = g(t) \hat{A} \otimes \hat{P}, \quad (2.4)$$

where \hat{P} is the momentum operator corresponding to the meter variable P and $g(t)$ the instantaneous coupling rate depending on t , with $g(t) = 0$ when t is outside of the interval $[t_i, t_f]$. We suppose that the initial states at $t < t_i$ of the system and the meter are independent and both in a pure state. They are represented by the tensor product of the state vectors $|\psi_i\rangle \otimes |\psi_m\rangle \equiv |\psi_i\rangle|\psi_m\rangle$, where the indices i and m stand for the initial states of the system and the meter, respectively. After the interaction $t > t_f$, when the coupling rate $g(t)$ is zero again, the complete wave-function of the coupled systems is:

$$\begin{aligned} |\psi\rangle &= \exp\left(-\frac{i}{\hbar} \int_{t_i}^{t_f} \hat{H}_{int} dt\right) |\psi_i\rangle|\psi_m\rangle \\ &= \exp\left(-\frac{i}{\hbar} g \hat{A} \otimes \hat{P}\right) |\psi_i\rangle|\psi_m\rangle, \end{aligned} \quad (2.5)$$

with the coupling strength $g = \int_{t_i}^{t_f} g(t) dt$. Finally, a measurement of the conjugate meter variable X delivers information about the probed quantum system. Let the operator \hat{A} have discrete and non degenerate eigenvalues a_k with the corresponding eigenvectors $|a_k\rangle$. In this eigenvector basis, the wave-function of the system can be decomposed as following $|\psi_i\rangle = \sum_k c_k |a_k\rangle$, with the complex amplitude $c_k = \langle a_k | \psi_i \rangle$. Equation (2.5) becomes:

$$\begin{aligned} |\psi(x)\rangle &= \langle x | \exp\left(-\frac{i}{\hbar} g \hat{A} \otimes \hat{P}\right) \left(\sum_k c_k |a_k\rangle\right) |\psi_m\rangle \\ &= \sum_k c_k \sum_{n=0}^{\infty} \frac{1}{n!} \left(-\frac{i}{\hbar} g\right)^n \hat{A}^n |a_k\rangle \int_{-\infty}^{+\infty} \langle x | p \rangle \langle p | \hat{P}^n | \psi_m \rangle dp \\ &= \sum_k c_k \left(\frac{1}{\sqrt{2\pi\hbar}} \int_{-\infty}^{+\infty} \exp\left(\frac{i}{\hbar} [x - ga_k] p\right) \psi_m(p) dp\right) |a_k\rangle \\ &= \sum_k c_k \psi_m(x - ga_k) |a_k\rangle, \end{aligned} \quad (2.6)$$

where $|\psi(x)\rangle = \langle x | \psi \rangle$, $\psi_m(x) = \langle x | \psi_m \rangle$ and we used the relation $\langle x | p \rangle = \frac{1}{\sqrt{2\pi\hbar}} \exp\left(\frac{i}{\hbar} xp\right)$ as well as $\langle p | \hat{P}^n | \psi_m \rangle = p^n \psi_m(p)$. The meter wave-packets $\psi_m(x - ga_k)$ are entangled with the eigenvectors $|a_k\rangle$ of the quantity \mathcal{A} . If the overlap between the wave-packets goes to zero, the system is strongly coupled to the meter. This is realized, when the deflections $g(a_k - a_{k+1})$ are much larger than the uncertainty in the position Δx of

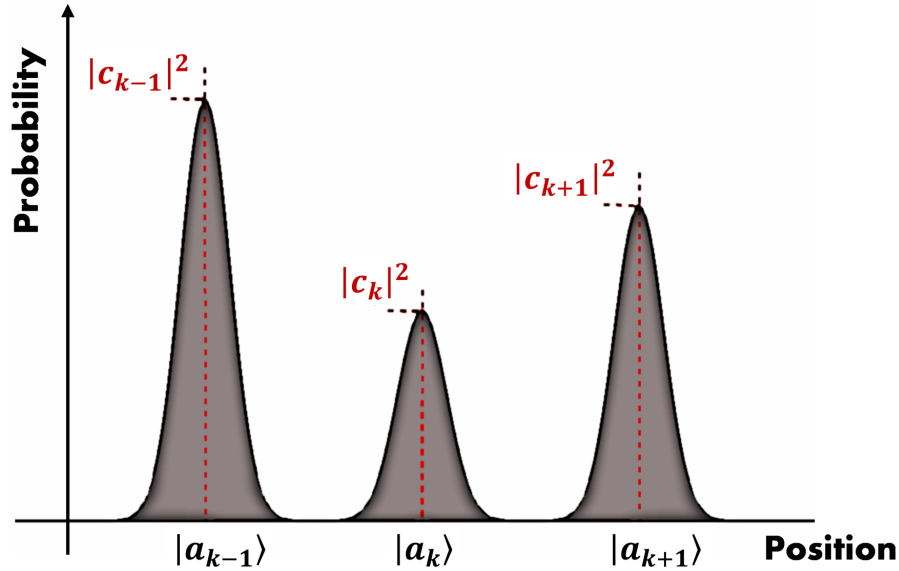


Figure 2.1: An ideal standard measurement. The deflection is large enough so that after the interaction all meter wave-packets are spatially separated from each other and centered around the meter position representing the system eigenvalue. Furthermore, the measurement of the area of each meter wave-packet indicates the probability that the initial system state is found along the corresponding eigenvector.

the initial meter wave-function. In this case, the projective measurement of x results in a projective or ideal measurement of \mathcal{A} , as shown in figure 2.1. By performing this ideal measurement on a sufficiently large ensemble of systems prepared in the same initial state, the meter outcomes give an estimation of the probabilities $P(k|i)$, i.e. the probabilities that the measurement of the initial system results in the values a_k , respectively. These probabilities are determined by the complex amplitudes $c_k = \langle a_k | \psi_i \rangle$ in equation (2.6), where $|c_k|^2$ represents $P(k|i)$. An estimation of the expectation value \bar{A} is deduced from the probabilities $P(k|i)$ through the relation:

$$\bar{A} = \sum_k a_k P(k|i) . \quad (2.7)$$

2.2.2 Non-ideal measurements

When the coupling between the system and the meter decreases, i.e. when the overlap between the wave-packets of equation (2.6) increases, the measurement of the meter does no longer project the quantum system onto an identified eigenvector state of the

observable \hat{A} . The system is left in an ambiguous superposition of eigenvectors $|a_k\rangle$. In the limit of weak coupling strength, the deflection between the eigenstates is so small, that the readout of the measurement of a single system provides no significant information about the observable \hat{A} . As shown in figure 2.2, the measurement of the probabilities $P(k|i)$ is no longer possible with the process described in the last section. However, for small couplings g , we can still determine the average of \hat{A} over the initial system by acquiring the meter shift¹:

$$\bar{x} - \bar{x}_i = g\bar{A}, \quad (2.8)$$

where \bar{x} and \bar{x}_i are the mean position value of the meter after and before the interaction with the system. Aharonov, Albert, and Vaidman (AAV) derived equation (2.8) by assuming a spatial Gaussian distribution of the meter position [1]. They showed also that it is valid for any distribution weakly coupled to the system. Alternatively, the average of \hat{A} can be determined by measuring all the underlying projection operators $\hat{\Pi}_k$ rather than \hat{A} itself. This is due to the linearity of equation (2.1) with respect to the projection operators, which are independent of each other. Thus, each of the $\hat{\Pi}_k$ measurement set-ups provides the probability $P(k|i)$, which is used to estimate the average \bar{A} by relation (2.7).

To estimate the minimum size N_0 of the ensemble necessary for non-ideal measurements, we evaluate the signal-to-noise ratio (SNR). Consider an ensemble of N system-meter pairs. For Gaussian meters, the von Neumann scheme yields an expectation value of $N(\bar{x} - \bar{x}_0)$ and a standard deviation $\sqrt{N\Delta x}$, with the variance Δx . The SNR is the ratio of the magnitude of the expected meter shift to the standard deviation [42]:

$$SNR = \frac{|\bar{x} - \bar{x}_0|}{\sqrt{\Delta x}} \sqrt{N}. \quad (2.9)$$

By definition, the minimum size N_0 of the ensemble is reached for a signal-to-noise ratio which is equal to one, i.e. $N_0 = \frac{\Delta x}{(\bar{x} - \bar{x}_0)^2}$. This shows that the minimum size can take high values for large variance Δx of the meter.

¹The following measurement technique can also be used to estimate the average of \hat{A} in the case of ideal measurements.

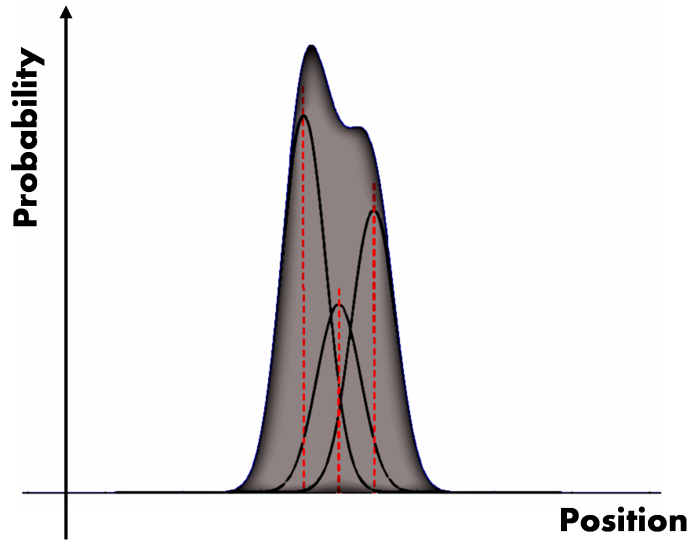


Figure 2.2: A non-ideal standard measurement. The deflection is too small to separate spatially the different outcomes. Although each meter distribution corresponds to an eigenvector state of $|a_k\rangle$, the spatial overlap makes it impossible to distinguish between the $|a_k\rangle$.

2.3 Pre- and postselected measurements

2.3.1 Ideal pre- and postselected measurements

In ideal and non-ideal measurements, the physical quantity \mathcal{A} is studied by considering the initial state $|\psi_i\rangle$ at time t_i . Extending this concept, Aharonov, Bergmann and Lebowitz (ABL) [43] introduced in 1964 an additional final measurement at time t_f with the idea of obtaining a more complete description of the system property \mathcal{A} . In their scheme, an ensemble of independent quantum systems is prepared in the same initial state $|\psi_i\rangle$, which defines the preselection. Then each system interacts strongly with the meter during the measurement of the physical quantity \mathcal{A} . Finally, a projective measurement of the state $|\psi_f\rangle$ is performed, a procedure known as postselection. Such a sub-ensemble of systems with identical initial and final states is called a pre- and postselected ensemble. Interestingly, the statistical distribution of the outcomes depends on both the initial and final states resulting in a complete different distribution than for the whole non-postselected system.

Mathematically, the joint probability to measure the eigenvalue a_k of the observable \hat{A} and to observe in a second measurement the state $|\psi_f\rangle$ is:

$$P(k, f|i) = \text{Tr} \left[\hat{\Pi}_f \hat{\Pi}_k \hat{\rho}_i \hat{\Pi}_k \right], \quad (2.10)$$

with the initial density operator $\hat{\rho}_i$, which is in the pure case $\hat{\rho}_i = |\psi_i\rangle\langle\psi_i|$. Using Bayes theorem, ABL derived the conditional probability that an intermediate projective measurement would produce the value a_k for a given initial and final state:

$$P(k|i, f) = \frac{P(k, f|i)}{\sum_l P(l, f|i)} = \frac{\text{Tr} \left[\hat{\Pi}_f \hat{\Pi}_k \hat{\rho}_i \hat{\Pi}_k \right]}{\sum_l \text{Tr} \left[\hat{\Pi}_f \hat{\Pi}_l \hat{\rho}_i \hat{\Pi}_l \right]} \equiv P_{ABL}, \quad (2.11)$$

with a normalized probability distribution $P(k|i, f)$, $\sum_f P(k|i, f) = 1$. This equation is called the ABL formula². In this expression, the numerator represents the probability of observing the particle successively in the k^{th} state assuming it was in the initial state, then in the final state assuming it was in the k^{th} state: $P(k|i)P(f|k)$. On the other hand, the denominator represents the sum of the probability of each alternative pathway from the initial to the final state: $\sum_l P(l|i)P(f|l)$ where l represents the possible pathways. A generalization of the ABL formula for arbitrary postselected POVM can be found in reference [42]. When the projector $\hat{\Pi}_f$ is replaced by the identity operator, strong pre- and postselected measurements are equivalent to strong standard measurements. In the case of pure states, the ABL formula is invariant under the exchange of the initial and final states. This symmetry may suggest a quantum mechanical formalism, which is symmetric under time-reversal for pre- and postselected ensembles [3, 43–45]. We shall discuss this possible interpretation of quantum mechanics and the corresponding two-state vector formalism later. Another surprising result of the ABL formula is its contextuality. For systems with a Hilbert space with dimensions $d \geq 3$, the probabilities given by the ABL formula depend not only on the outcome associated to the final measurement but also on how the intermediate property \mathcal{A} was measured. Or, in other words, these probabilities directly rely on how the projectors $\hat{\Pi}_k$ of the observable \hat{A} are applied in between the pre- and postselection process. Depending on the specifics of the measurement set-up, the projector decomposition in the denominator

²The usual form of the ABL formula is given in the state-vector representation by:

$$P_{ABL} = \frac{|\langle\psi_f|a_k\rangle|^2 |\langle a_k|\psi_i\rangle|^2}{\sum_l |\langle\psi_f|a_l\rangle|^2 |\langle a_l|\psi_i\rangle|^2},$$

with the initial state $\hat{\rho}_i = |\psi_i\rangle\langle\psi_i|$ and the final state $\hat{\Pi}_f = |\psi_f\rangle\langle\psi_f|$.

of the ABL formula (2.11) changes (and the conditional probability, too). The most popular example of contextuality in strong pre- and postselected measurements is the three-box problem [20].

2.3.2 Non-ideal pre- and postselected measurements

Because the system is left in an ambiguous superposition of eigenvectors $|a_k\rangle$ for weak coupling strengths, a subsequent final measurement of the system at time t_f may cause interferences and provoke a non-classical behavior of the whole system. Similarly to non-ideal measurements without postselection, we estimate the expectation value of the observable \hat{A} by the shift of the meter position. Moreover, we use a weak coupling strength g with approximations that hold up to the first order in g . This corresponds to the linear-response regime³. By considering the von Neumann measurement scheme, the unnormalized meter wave-function after the postselection of $|\psi_f\rangle$ becomes:

$$\begin{aligned}
 \psi(x) &= \langle\psi_f|\langle x| \exp\left(-\frac{i}{\hbar}g\hat{A}\otimes\hat{P}\right)|\psi_i\rangle|\psi_m\rangle \\
 &\approx \langle\psi_f|\langle x|\left(1-\frac{i}{\hbar}g\hat{A}\otimes\hat{P}\right)|\psi_i\rangle|\psi_m\rangle \\
 &= \langle\psi_f|\psi_i\rangle\left(\int_{-\infty}^{+\infty}\langle x|p\rangle\langle p|\psi_m\rangle dp - \frac{i}{\hbar}g\frac{\langle\psi_f|\hat{A}|\psi_i\rangle}{\langle\psi_f|\psi_i\rangle}\int_{-\infty}^{+\infty}\langle x|p\rangle\langle p|\hat{P}|\psi_m\rangle dp\right) \\
 &= \langle\psi_f|\psi_i\rangle\int_{-\infty}^{+\infty}\frac{1}{\sqrt{2\pi\hbar}}\left(1-\frac{i}{\hbar}g\frac{\langle\psi_f|\hat{A}|\psi_i\rangle}{\langle\psi_f|\psi_i\rangle}p\right)\exp\left(\frac{i}{\hbar}xp\right)\psi_m(p) dp \\
 &\approx \langle\psi_f|\psi_i\rangle\int_{-\infty}^{+\infty}\frac{1}{\sqrt{2\pi\hbar}}\exp\left(-\frac{i}{\hbar}g\frac{\langle\psi_f|\hat{A}|\psi_i\rangle}{\langle\psi_f|\psi_i\rangle}p\right)\exp\left(\frac{i}{\hbar}xp\right)\psi_m(p) dp \\
 &= \langle\psi_f|\psi_i\rangle\int_{-\infty}^{+\infty}\frac{1}{\sqrt{2\pi\hbar}}\exp\left(\frac{i}{\hbar}[x-gA_w]p\right)\psi_m(p) dp \\
 &= \langle\psi_f|\psi_i\rangle\int_{-\infty}^{+\infty}\frac{1}{\sqrt{2\pi\hbar}}\exp\left(\frac{i}{\hbar}[x-g\Re A_w]p\right)\psi_m(p) dp \\
 &= \langle\psi_f|\psi_i\rangle\psi_m(x-g\Re A_w), \tag{2.12}
 \end{aligned}$$

where the appearing quantity,

$$A_w = \frac{\langle\psi_f|\hat{A}|\psi_i\rangle}{\langle\psi_f|\psi_i\rangle}, \tag{2.13}$$

³The coupling strength g is small with respect to the variance of the initial pointer position Δx . A more precise description of the conditions for the linear regime is given later.

is by definition the weak value of the observable \hat{A} for given initial and final states $|\psi_i\rangle, |\psi_f\rangle$. We supposed that the imaginary part of the weak value A_w is zero. The conditions justifying the validity of both approximations made in the last development were shown in reference⁴ [46]:

$$g \left| \frac{\langle \psi_f | \hat{A}^n | \psi_i \rangle}{\langle \psi_f | \psi_i \rangle} \right|^{1/(n-1)} \Delta p \ll 1 \quad \text{for all } n \geq 2$$

$$g \left| \langle \hat{A} \rangle_{if}^w \right| \Delta p \ll 1, \quad (2.14)$$

where the first condition justifies the approximation made for the second line in (2.12) and the second condition the last approximation. Equation (2.12) presents a deflection that depends on the real part of the weak value A_w . By considering a Gaussian meter, Aharonov, Albert, and Vaidman (AAV) deduced the following relation between the meter shift and the real part of the weak value [1]:

$$\bar{x}_{if} - \bar{x}_i = g \Re A_w, \quad (2.15)$$

where \bar{x}_{if} is the average position of the meter after the postselection and \bar{x}_i the initial average position of the meter. The same developments can be carried out in momentum space. This time, the momentum shift is in direct relation to the imaginary part of the weak value:

$$\bar{p}_{if} - \bar{p}_i = \frac{2g\Delta p}{\hbar} \Im A_w, \quad (2.16)$$

where Δp is the variance in the momentum of the initial meter. Together, these equations provide the real and the imaginary parts of the weak value, pointing out its complex character. Hence, not only the measurement of the position x , but also of the momentum p contains information about the pre- and postselected system. The results obtained for real Gaussian-meter functions have to be completed for arbitrary meter wave-functions. In reference [47], Jozsa showed that there is an additional term, proportional to the imaginary part of the weak value, on the right side of (2.15). Equation (2.16) remains valid in the general case.

Since for weak measurements in the absence of postselection, the meter shift is proportional to the average of the observable \hat{A} (see equation (2.8)), a direct physical interpretation of the weak value assumes that it represents the average of \hat{A} in the pre- and postselected ensemble. However, this weak value, with its real and imaginary

⁴In the cited reference, they derived both conditions for the case where the mean values of the position and the momentum without postselection are zero.

parts, has an unusual behavior, which differs strongly from the expectation value of \hat{A} in standard measurements. A surprising property is that the weak value diverges when the overlap between the initial and the final states, i.e. the denominator of (2.13), goes to zero. Thus, for sufficiently large weak values, the linear-response approximation used in (2.12) is not applicable anymore. Even if the first condition of (2.14) holds and the coupling strength g is weak, the bound required by the second condition is violated. A development to all orders in \hat{A}^n is inevitable. A precise study of higher order contributions is shown in [42]. In the linear-response regime for pre- and postselected measurements, the meter mean deflections can be strongly amplified. However, this amplification is obtained for low probabilities to postselect the probed system. The ratio of signal-to-noise, the SNR , is of the same order than the SNR in standard measurements, if the meter is optimal⁵. Consequently, weak measurements with and without postselection need ensembles of comparable size. For the weak interaction regime with the variance of Δx and with the probability to postselect the initial state of $P(f|i)$, the minimum size N_0 of the pre- and postselected ensemble is:

$$N_0 = \frac{\Delta x}{P(f|i) g^2 |A_w|^2}. \quad (2.17)$$

In the case of strongly amplified deflections, the weak value $|A_w|$ is large, but the postselection probability $P(f|i)$ is low in such a manner that the denominator in (2.17) doesn't change considerably. A more precise description of optimal and non-optimal meters as well as their impact on the minimum size of the ensemble is given in reference [42].

The weak value of the projector $\hat{\Pi}_k$, known as the weak probability $P_{k,w}$, is the non-classical conditional probability that the weak measurement of \hat{A} yields the value a_k for a given pre- and postselected ensemble. In other words, the weak value $P_{k,w}$ is the counterpart for weak measurements of the conditional probability defined by the ABL formula (2.11). To demonstrate this point of view, we consider once more the von Neumann measurement model with the interaction Hamiltonian $\hat{H}_{int} = g(t) \hat{\Pi}_k \otimes \hat{P}$, where $g(t) = g \delta(t - t_0)$ is the interaction strength and $\hat{\Pi}_k$ the eigenprojector of \hat{A} . In this way, we determine the property \mathcal{A} of the preselected system by applying successively

⁵In reference [42], an optimal meter with the wave-function $|\psi\rangle$ is defined by the equality $|\langle \psi | [\hat{R}, \hat{F}] | \psi \rangle| = 2\Delta F \Delta R$, where \hat{R} and \hat{F} are arbitrary conjugate meter operators. A Gaussian meter with the conjugate operators \hat{X} and \hat{P} verifies this equality.

the projectors $\hat{\Pi}_k$ by the evolution operator:

$$\begin{aligned}\hat{U}(t) &= \exp \left[-\frac{i}{\hbar} \int_{-\infty}^{+\infty} g(t) \hat{\Pi}_k \hat{P} dt \right] \\ &= \hat{\Pi}_{1-k} \otimes \hat{I} + \hat{\Pi}_k \otimes \exp \left[-i \frac{g}{\hbar} \hat{P} \right],\end{aligned}\quad (2.18)$$

where the projector $\hat{\Pi}_{1-k} = \hat{I} - \hat{\Pi}_k$. The initial meter system $|\psi_m\rangle$ is described by a real Gaussian function with an expectation value of zero and a variance of σ^2 :

$$\langle x | \psi_m \rangle = \frac{1}{\sqrt{\sigma\sqrt{2\pi}}} \exp \left[-\frac{x^2}{4\sigma^2} \right]. \quad (2.19)$$

By considering an initial probe $\hat{\rho}_i$ which is finally postselected by $\hat{\Pi}_f$, the probability to find the probe at the position x after the interaction is:

$$\begin{aligned}P_{if}(x) &= \text{Tr} \left[\hat{\Pi}_f \hat{\Pi}_{1-k} \hat{\rho}_i \hat{\Pi}_{1-k} \right] |\psi_m(x)|^2 \\ &+ \text{Tr} \left[\hat{\Pi}_f \hat{\Pi}_k \hat{\rho}_i \hat{\Pi}_k \right] |\psi_m(x-g)|^2 \\ &+ 2 \Re e \left\{ \text{Tr} \left[\hat{\Pi}_f \hat{\Pi}_{1-k} \hat{\rho}_i \hat{\Pi}_k \right] \right\} \psi_m(x-g) \psi_m(x),\end{aligned}\quad (2.20)$$

where the Fourier transform led to:

$$\langle x | \exp \left[-\frac{i}{\hbar} g \hat{P} \right] | \psi_m \rangle = \frac{1}{\sqrt{2\pi\hbar}} \int_{-\infty}^{+\infty} \exp \left(\frac{i}{\hbar} [x-g] p \right) \psi_m(p) dp = \psi_m(x-g). \quad (2.21)$$

Because the wave-function is a real Gaussian, the imaginary part of the interference contribution in (2.20) is zero. Then, the probability distribution $P_{if}(x)$ is used to establish a relation for the meter mean displacement with respect to the pre- and postselected probe:

$$\bar{x}_{if} = C_1(g) \frac{\text{Tr} \left[\hat{\Pi}_f \hat{\Pi}_k \hat{\rho}_i \hat{\Pi}_k \right]}{\text{Tr} \left[\hat{\Pi}_f \hat{\Pi}_k \hat{\rho}_i \hat{\Pi}_k \right] + \text{Tr} \left[\hat{\Pi}_f \hat{\Pi}_{1-k} \hat{\rho}_i \hat{\Pi}_{1-k} \right]} + C_2(g) \Re e \frac{\text{Tr} \left[\hat{\Pi}_f \hat{\Pi}_k \hat{\rho}_i \right]}{\text{Tr} \left[\hat{\Pi}_f \hat{\rho}_i \right]}, \quad (2.22)$$

where the first term corresponds to the ABL formula and the second to the weak value $P_{k,w}$ expressed in the density operator representation [48]. The coefficients $C_1(g)$ and $C_2(g)$ depend directly on the interaction strength g , but also on conditional probabilities determined by the applied probe states. Their complete expressions are detailed in Appendix A. When the interaction is strong with $\frac{g}{2\sqrt{2}\sigma} \gg 1$, then the coefficients in (2.22) become $C_1(g) \approx g$ and $C_2(g) \approx 0$, resulting in a meter displacement proportional to the ABL conditional probability: $\bar{x}_{if} \approx g P_{ABL}$. In contrast, when the interaction strength is small with $\frac{g}{2\sqrt{2}\sigma} \ll 1$, then the linear-response regime is reached and this time the coefficients are $C_1(g) \approx 0$ and $C_2(g) \approx g$. Thus, the meter system reveals the

weak value $P_{k,w}$. The mean spatial displacement delivers the real part of $P_{k,w}$, while the displacement in momentum space provides its imaginary part: $\bar{x}_{if} \approx g \Re P_{k,w}$ and $\bar{p}_{if} \approx \frac{g\hbar}{2\sigma^2} \Im P_{k,w}$. However, this displacement in the momentum space is zero when the strength becomes strong: $\bar{p}_{if} \approx 0$. All calculation details can be found in Appendix A.

The measurement of weak values is not limited to the von Neumann measurement scheme involving the continuous variables X and P . In many works [17, 49–51], the weak value A_w appears for pre- and postselected systems, which are weakly coupled to discrete meters. For example, the coupling of a pre- and postselected system with the meter qubit state $|\phi_m\rangle = \frac{1}{\sqrt{2}}(|0\rangle + |1\rangle)$ via the interaction:

$$\hat{H}_{int} = g(t) \hat{A} \otimes \hat{\sigma}_z, \quad (2.23)$$

with the Pauli operator:

$$\hat{\sigma}_z = \begin{pmatrix} 1 & 0 \\ 0 & -1 \end{pmatrix}, \quad (2.24)$$

induces the following final meter state:

$$\begin{aligned} |\phi_f\rangle &= \langle\psi_f|\psi_i\rangle \frac{1}{\sqrt{2}} \left(\frac{\langle\psi_f|e^{-ig\hat{A}}|\psi_i\rangle}{\langle\psi_f|\psi_i\rangle} |0\rangle + \frac{\langle\psi_f|e^{ig\hat{A}}|\psi_i\rangle}{\langle\psi_f|\psi_i\rangle} |1\rangle \right) \\ &\approx \langle\psi_f|\psi_i\rangle \frac{1}{\sqrt{2}} (e^{-igA_w} |0\rangle + e^{igA_w} |1\rangle), \end{aligned} \quad (2.25)$$

where we used the approximations $\frac{\langle\psi_f|e^{\pm ig\hat{A}}|\psi_i\rangle}{\langle\psi_f|\psi_i\rangle} \approx 1 \pm igA_w \approx e^{\pm igA_w}$ due to the small coupling constant g . Similar to the spatial shift in the von Neumann protocol, the effect of the weak coupling to the meter qubit yields an evolution of its orientation on the Bloch sphere by a value proportional to A_w .

Protocols with varying interaction strengths are also studied in the field of quantum measurements. Particularly, the contribution of weak values in the meter readout is of interest. A complete study of quantum measurements of pre- and postselected systems for arbitrary interaction strengths and measuring apparatuses can be found in reference [42]. Applications of these protocols are found in quantum computing, such as in quantum error correction [52] and quantum feedback control [53], or in weak value measurements of qubit states [54–60] or of photon arrival times [61]. Additionally, several theoretical methods were developed to reconstruct weak values by few strong measurements acquiring the Margenau-Hill [62, 63] or the Dirac distribution [56, 64].

2.4 Properties of the weak value

As mentioned above, the weak value has non-classical properties, in the sense that it is not bounded by the range of the eigenvalues of \hat{A} or is complex. However, it is possible to obtain an expression for the weak value similar to the classical equation (2.7), due to the linearity of A_w :

$$A_w = \sum_k a_k P_{k,w} , \quad (2.26)$$

where $P_{k,w}$ is the weak value of the projector $\hat{\Pi}_k$. The correspondence between expressions (2.7) and (2.26) suggests a probabilistic interpretation of the weak value of the projector $\hat{\Pi}_k$. This linearity in the weak value formalism can also be used to show that the weak probabilities are normalized, $\sum_k P_{k,w} = 1$. Because the weak values $P_{k,w}$ in relation (2.26) are independent of each other, the weak value of an observable \hat{A} is not a contextual quantity, i.e. do not depend on the measurement context, contrary to strong pre- and postselected measurements. Moreover, the weak values $P_{k,w}$ can be interpreted as non-classical conditional probabilities of the measurement of \mathcal{A} given that the initial state is $|\psi_i\rangle$ and that the final measurement results in $|\psi_f\rangle$ [65]. This image is more clear, when we rewrite the weak value in the form of Bayes' theorem:

$$P_{k,w} = \frac{\text{Tr} \left[\hat{\Pi}_f \hat{\Pi}_k \hat{\rho}_i \right]}{\text{Tr} \left[\hat{\Pi}_f \hat{\rho}_i \right]} = \frac{\tilde{P}(k, f|i)}{P(f|i)} = \tilde{P}(k|i, f) , \quad (2.27)$$

where the quasiprobability distribution $\tilde{P}(k, f|i) = \text{Tr} \left[\hat{\Pi}_f \hat{\Pi}_k \hat{\rho}_i \right]$ is known as the Kirkwood or Dirac distribution [62, 66, 67]. This distribution can be interpreted as the joint probability that the observation of a system results in the particular eigenstates $|a_k\rangle$ and $|\psi_f\rangle$. The product of both projectors can be seen as the quantum mechanical equivalent of the logical *AND* [56]. Since, in general, this product is not Hermitian, the conditional quasiprobability distribution $\tilde{P}(k|i, f)$ is non-classical, i.e. negative or complex. To remind us of this connection between the weak value of projectors and the conditional quasiprobability distribution, the weak value $P_{k,w}$ will also be called the weak probability in this work. Expressing the Dirac distribution by its state-vector representation, i.e. by $\langle \psi_f | a_k \rangle \langle a_k | \psi_i \rangle \langle \psi_i | \psi_f \rangle$, the appearing quantity is also known as the three-vertex Bargmann invariant [68]. This quantity is invariant under gauge transformation and reparametrization. Later in this thesis, we will use the connection between the weak probabilities and the Bargmann invariant to derive the geometric

representation of weak and modular values.

In the same way, relation (2.27) points out a direct relation between weak values and the Dirac distribution. A simple multiplication of the weak value by the ordinary postselection probability $P(f|i)$ yields the non-classical joint distribution. Contrary to weak probabilities, the Dirac distribution is bounded and only contains values with modulus smaller or equal to one. Another interesting property is, that for arbitrary states, pure or mixed, the Dirac distribution contains the same information as the density operator $\hat{\rho}_i$ [15, 16]. Moreover, the weak value A_w can be brought in a relation with the result obtained in a standard measurement by the sum rule:

$$\bar{A} = \sum_f A_w P(f|i) = \sum_f \text{Tr} \left[\hat{\Pi}_f \hat{A} \hat{\rho}_i \right] = \text{Tr} \left[\hat{A} \hat{\rho}_i \right], \quad (2.28)$$

with $\sum_f \hat{\Pi}_f = \hat{I}$. The first equality in (2.28) shows that the result of a standard measurement \bar{A} is the sum over all sub-ensembles resulting from postselection of the corresponding weak value A_w weighed by the postselection probability $P(f|i)$. The second equality shows that the sum over all sub-ensembles of the corresponding Dirac distribution $\text{Tr} \left[\hat{\Pi}_f \hat{A} \hat{\rho}_i \right]$ induces the average of a standard measurement.

The meaning attributed to the weak value can even be more consistent. The weak value is interpreted as the mean value of the observable \hat{A} , when it is measured weakly between pre- and postselected states. In the two-state vector formalism [3, 44, 45], this point of view is used to justify a time-symmetric formulation of quantum mechanics. For sufficiently weak couplings, the two-state vector defined in the past by the preselection and in the future by the postselection is not significantly disturbed. Neither the forward-evolving quantum state, nor the backward-evolving quantum state is changed significantly. As a result, the outcome of the measurement of \hat{A} is affected by both states and is equal to its weak value.

2.5 A generalization of weak values

In weak measurement theory, there are two different physical methods which transform the von Neumann measurement scheme into a weak measurement. The first is to reduce the strength of the coupling g during the interaction between the meter and the system.

Till now, we considered this method for the continuous meter variables X and P of a Gaussian probability distribution, and for discrete variables like a qubit meter. The second method is to keep the coupling as strong as in ideal measurements, but to select the initial meter state in such a way that the probability of measuring the observable is low and that the probed system is left unperturbed most of time. Many examples of this scheme can be found in the literature [42, 55, 57, 58, 61, 69]. In particular, the work of Kedem and Vaidman is of interest [2]. They pointed out that the action of projectors in the coupling (2.23) applied on meter qubits leads in the weak measurement case to a readout, which reveals a new type of pre- and postselected value, which they called the modular value of the observable \hat{A} :

$$A_m = \frac{\langle \psi_f | e^{-ig\hat{A}} | \psi_i \rangle}{\langle \psi_f | \psi_i \rangle}. \quad (2.29)$$

The modular value is not often reported as such in literature because it is directly related to the weak value in the usual weak approximation limit for small coupling strengths, through a first order polynomial development in g :

$$A_m = 1 - ig A_w + o(g^2). \quad (2.30)$$

This first order approximation was used in several cases in the weak value literature: the photon trajectory measurements in Young's interference experiment [17] or the quantum Cheshire Cat experiment with neutrons [49, 51] are only two examples. In reality, the experimental outcome was the modular value, which generalizes the weak value in a non-perturbative way. Nevertheless, the modular value can be equivalent to the weak value in some cases, as we will see later in this thesis. A general expression for the modular value using the weak value of an arbitrary observable for any coupling strength is given in [70]. However, a clear physical meaning of modular values is still missing. In a first attempt, reference [71] shows that the modular value can be interpreted as an average of the dynamic phase factor $e^{-ig a_k}$ over all eigenvalues of \hat{A} with the complex conditional probability:

$$A_m = \sum_k e^{-ig a_k} P_{k,w}, \quad (2.31)$$

where $P_{k,w}$ is the weak value of the projector $\hat{\Pi}_k$. The latter is the analogue to the weak value relation (2.26).

2.6 Applications of weak and modular values

The first proposal to measure weak values was for spin- $\frac{1}{2}$ particles in a Stern-Gerlach apparatus by Aharonov, Albert, and Vaidman [1] as described in the previous chapter. Applying the von Neumann scheme, they showed theoretically the appearance of the weak value of the spin-operator $\hat{\sigma}_z$. The experimental realization was presented in reference [72], for an optical set-up analogous to the Stern-Gerlach apparatus. The measurement of weak shifts of the transverse momentum of photons yielded the real part of weak values of their polarization states. Similar descriptions and experiments are showed in references [46, 73]. Currently, the experimental systems measuring weak and modular values involve particularly spin- $\frac{1}{2}$ particles, photon polarization, which-path states in Sagnac [10, 11, 74] and Mach-Zehnder [20, 21, 69] interferometers, or transverse translation degrees of freedom of particles [14, 15, 17].

Furthermore, we can find many applications of weak values in various fields of physics. For example, weak pre- and postselected measurements can produce large shifts in the mean position of the meter, which are directly related to large weak values. The role is to amplify tiny displacement induced during the interaction, rather than a measurement of the weak value of an observable. Since the experimental sensitivity can increase beyond the detector resolution, this measurement protocol promise large applications in metrology. In reference [9], the amplification effect was used to detect for the first time the wave-packet shift of 1 angstrom due to the spin Hall effect of light. Weak amplifying effects are also employed to detect small differences in the index of refraction [72, 75], mirror angular deflections [10, 76] or small frequency differences [74]. Furthermore, this amplification can be used to produce superluminal and slow light propagation [35, 65, 77, 78].

Another, more fundamental, field of applications of weak values is the quantum retrodiction in paradoxes with pre- and postselection, such as the three-box problem [20], Hardy's paradox [21] or the quantum Cheshire Cat [30]. In all these paradoxes, the observer tries to deduce from pre- and postselected systems the value of a physical quantity in the middle of its time evolution. It seems that weak measurements are suited to determine this value, since the resulting context-independent weak value is related to the intermediate evolution, hopefully without perturbing the evolution.

Moreover, weak pre- and postselected measurements are applied to obtain information on the quantum state of particles. In references [17], weak and modular values are used to obtain average trajectories of single photons in a double-slit interferometer. In reference [14], the transverse spatial wave function of a single photon was directly measured with weak pre- and postselected measurements. This quantum state reconstruction is also used to determine mixed polarization states of photons [15] and can be extended for arbitrary quantum states [16].

Apart from all these applications, most studies are restricted to the simplest non-trivial Hilbert space, i.e. the two-dimensional one. Three- or high-dimensional discrete quantum systems have rarely been studied using the weak measurement formalism [24–26]. However, recent applications of weak measurement theory in the context quantum computation research attest the interest of investigating weak values of high-level systems [27, 28]. Weak values of qutrits show their usefulness in the experimental demonstration of the Kochen-Specker test of noncontextuality [29] and can be applied to the quantum Cheshire cat experiment [30].

2.7 Summary and Motivation

According to the standard approach of weak measurements, weak and modular values arise from observations where the measurement apparatus interacts weakly with the pre- and postselected system. Thus, each individual weak measurement reveals an outcome with high uncertainty. However, by repeating many times this weak measurement on identical pre- and postselected quantum systems, the apparatus gives rise to the weak or to the modular value as reliable measuring readout. Weak measurements are based principally on small values of the coupling strength during the interaction or on low probabilities to apply the observable on the probe system.

Over the last few years, several quantum measurement protocols with varying measurement strengths have been studied in the field of the weak value theory. The approach is always the same: for arbitrary measurement strengths, weak and modular values are determined by an indirect reconstruction process that is based on observations realized in several measurement configurations. In contrast to the standard weak measurement approach, weak and modular values are identified by using more than two apparatus

mean outcome (e.g. the meter shifts in the position and in the momentum to determine directly the real and the imaginary parts of the weak value). This thesis is an attempt to demonstrate a measurement procedure that determines weak and modular values by exploiting the visibility and the phase readouts in an interferometric measurement. Because this procedure does not require the weak measurement approximations (the linear-response regime) it should be applicable for arbitrary large weak and modular values. Currently, the breakdown of these approximations made the acquisition of extreme large values difficult or even impossible. Thus, this interferometric procedure can be a good alternative to the existing weak measurement technique.

The physical meaning of weak values is strongly discussed in the literature; even a purely classical view of the occurrence of these values was proposed. However, weak values are generally interpreted as a shift in the measuring apparatus readout due to the weak coupling. In contrast, modular values have rarely been reported as such in literature because they are generalizations of weak values. Mathematically, these values are the averages of non-classical conditional probability distributions. Prior to this thesis work, a physical interpretation of modular values, in terms of a meter shift, was completely missing. As it will be demonstrated in this thesis, an interpretation of these modular values will be provided by the interferometric visibility.

In a similar way, deeper investigations and researches are needed to identify the classical or the non-classical origin of weak and modular values. To demonstrate their quantum nature, this thesis attempts to emphasize a connection between these complex, unbounded values and a geometric phase known as Pancharatnam-Berry phase. In the past, non-classical effects, such as the Aharonov-Bohm effect [79], were already explained using this geometric phase. Moreover, this quantum origin of weak values can be helpful for the interpretation of the strange weak measurement outcomes in different quantum paradoxes, such as the three-box paradox. A clear physical meaning of weak values could clarify the origin of negative quasiprobabilities equal to -1 , that appear in the three-box paradox.

3

Interferometric measurements of weak and modular values

In this chapter, we will devise an interferometric procedure to measure the polar components, i.e. the modulus and the argument, of complex weak and modular values instead of the usually determined real or imaginary parts. Our procedure relies essentially on a joint phase and visibility measurement in a quantum interferometer where the meter system acts as a quantum eraser. It proceeds by optimizing the interference phase to measure simultaneously the modulus and the argument of the modular value in a single step. Using polarization-entangled photons, we will experimentally show that our procedure works in conditions where the usual weak measurement procedure fails completely: for arbitrary measurement strengths (including strong measurements) and for orthogonal and nearly orthogonal initial and final probe states.

This chapter, containing the first results of my research, is divided in three different parts. In the first one (3.1 Theoretical Approach, p.26), the interferometric measurement procedure will be theoretically described for an arbitrary, pure quantum system that interacts with a qubit meter, i.e. a two-level quantum system acting as measurement apparatus. All involved qubit states are represented by three-dimensional vectors on a unitary sphere, called the Bloch sphere. This representation will lead to a better understanding of the chosen configurations for the qubit measurement apparatus. As it will be demonstrated, this measurement scheme reveals the polar components of the modular value and improves the signal-to-noise ratio compared to the standard protocol. In a final step, this theoretical protocol will be applied on two-qubit states to proof an experimental realization of this protocol by polarization-entangled photons.

The second part of this chapter (3.2 Experiment, p.34) will be relatively technical. In the first section (3.2.1 Materials, p.34), the experimental set-up manipulating the polarization-entangled photons will be presented without going into the details (a summary of the set-up can be also found in figure 3.2, p.35). Important aspects about experimental realization and statistical analysis will be explained in more details in the second section (3.2.2 Methods, p.36).

In the third part (3.3 Results and discussion, p.42), all experimental results leading to the measurement of the complex weak value will be shown and analyzed. The first two sections (3.3.1 Calibration of the quartz plate, p.42, and 3.3.2 Meter state preparation, p.44) will focus the attention on the calibration of the detection system as well as on the experimental meter state preparation. Then, the third section (3.3.3 Real weak values: analysis of the purity and the measurement strength, p.49) will show the experimental results for the case of weak values that are real numbers. In particular, the role of the meter system in the measurement protocol will be analyzed in more details. Finally, the last section (3.3.4 Complex weak values: analysis of the quantum phase, p.54) will illustrate the results of the acquisition of complex weak values. We will put a special focus on the discontinuous behavior of the weak values argument.

Finally, all theoretical and experimental results are summarized in the last part of this chapter (3.4 Summary, p.57). The advantages and the limitations of the developed interferometric protocol compared to the standard weak measurement scheme will be discussed.



3.1 Theoretical Approach

In the last chapter, we demonstrated how the weak interaction of an arbitrary pre- and postselected quantum system with a measuring apparatus, the meter, reveals weak and modular values. As a result of these measurement procedures, the meter average value is directly related to the real and to the imaginary part of weak and modular values. In the next section, we will consider a new measurement technique based on a controlled quantum evolution. In contrast to the standard weak measurement technique, this procedure relies essentially on a joint phase and visibility measurement. The two interferometric outcomes are related to the modulus and to the argument of weak and modular values.

3.1.1 General probe state

As shown in figure 3.1.a, the measurement procedure implements a controlled quantum evolution, in which an arbitrary quantum system $|\psi_i\rangle$, the probe, interacts with a qubit meter via the quantum gate:

$$\hat{U}_{GATE} = \hat{I} \otimes \hat{\Pi}_r + e^{i\delta} \hat{U}_A \otimes \hat{\Pi}_{-r}, \quad (3.1)$$

where $\hat{\Pi}_{\pm r}$ are orthogonal projectors acting on the meter and δ is a phase factor first supposed to be null. Without loss of generality, we describe the initial meter state by the density operator $\hat{\rho}_m = \frac{1}{2} \left(\hat{I} + P_m \vec{m} \cdot \vec{\sigma} \right)$ with the Pauli operators $\vec{\sigma} = (\hat{\sigma}_x, \hat{\sigma}_y, \hat{\sigma}_z)^1$. This representation introduces the purity of the meter quantum state P_m and a normalized vector \vec{m} . The parameter P_m ranges from 1 for pure states to 0 for a maximally mixed state. The vector \vec{m} indicates a point on the surface of a unitary sphere, called the Bloch sphere, which entirely characterizes the initial meter qubit $|m\rangle$. Similarly, we consider the Bloch vectors $\pm \vec{r}$ associated to the meter projectors controlling the gate interaction, with $\hat{\Pi}_{\pm r} = \frac{1}{2} \left(\hat{I} \pm \vec{r} \cdot \vec{\sigma} \right)$. The probe transformation $\hat{U}_A = e^{-ig\hat{A}}$ is expressed in terms of a time independent Hermitian operator \hat{A} and an arbitrary coupling strength g , defined by the integral $g = \hbar^{-1} \int g(t) dt$. A simple transformation

¹The Pauli matrices are a set of three 2×2 complex matrices which are Hermitian and unitary:

$$\hat{\sigma}_x = \begin{pmatrix} 0 & 1 \\ 1 & 0 \end{pmatrix}, \quad \hat{\sigma}_y = \begin{pmatrix} 0 & -i \\ i & 0 \end{pmatrix}, \quad \hat{\sigma}_z = \begin{pmatrix} 1 & 0 \\ 0 & -1 \end{pmatrix}. \quad (3.2)$$

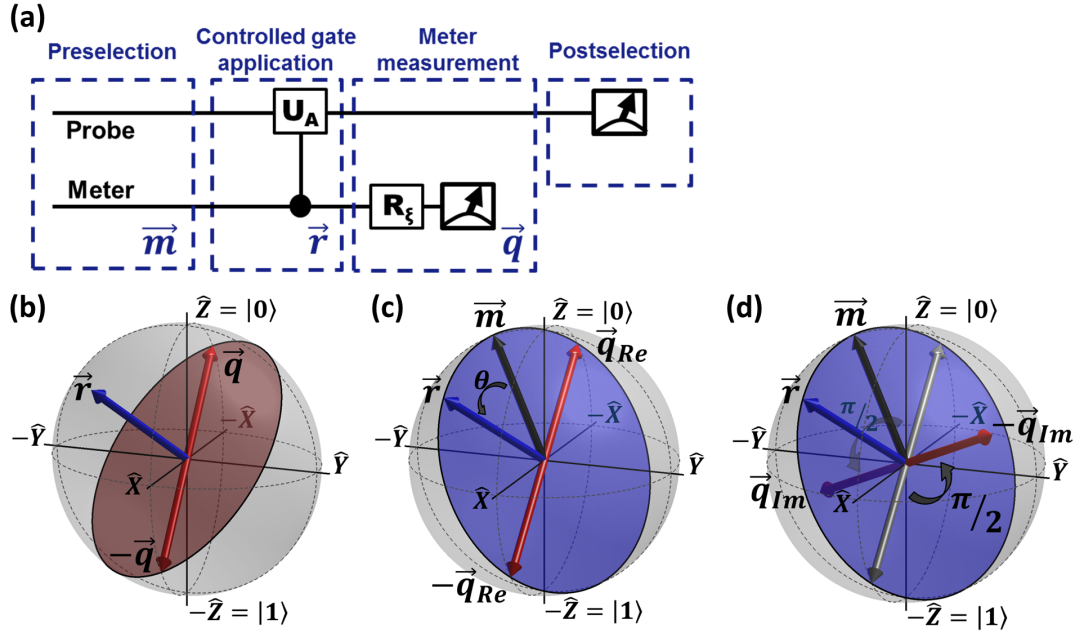


Figure 3.1: Quantum controlled evolution: (a) protocol, (b-d) representation in the Bloch sphere of the relevant meter states. (b) The red plane is perpendicular to the control state \vec{r} . It contains all final meter states \vec{q} and $-\vec{q}$ implementing the quantum eraser condition. (c-d) The blue plane contains the initial meter state \vec{m} and the control state \vec{r} . The final meter states (c) \vec{q}_{Re} in the blue plane and (d) \vec{q}_{Im} perpendicular to the blue plane measure the real and imaginary parts of the modular value, respectively.

of the interaction Hamiltonian $\hat{H}_{int} = g(t) \hat{A} \otimes \hat{\Pi}_{-r}$ reveals the connection between the von Neumann coupling (see relation (2.4)) and our gate application \hat{U}_{GATE} :

$$\begin{aligned}
 \hat{U} &= e^{-\frac{i}{\hbar} \int \hat{H}_{int}(t) dt} \\
 &= e^{-ig \hat{A} \otimes \hat{\Pi}_{-r}} \\
 &= \hat{I} \otimes \hat{I} + \left(\sum_{k=1}^{\infty} \frac{(-ig)^k}{k!} \hat{A}^k \right) \otimes \hat{\Pi}_{-r} \\
 &= \hat{I} \otimes \hat{\Pi}_r + e^{-ig \hat{A}} \otimes \hat{\Pi}_{-r} .
 \end{aligned} \tag{3.3}$$

After this nonlocal quantum gate, the probe and the meter are entangled: the information about whether the transformation \hat{U}_A was applied on the probe is encoded in the meter state. According to the final meter readout, this information can be preserved or erased, completely or partially. By measuring the meter observable $\hat{\sigma}_q = \hat{\Pi}_q - \hat{\Pi}_{-q}$, a third Bloch vector \vec{q} is introduced. Finally, a projective measurement of the probe

system postselects the state vector $|\psi_f\rangle$. The average $\bar{\sigma}_q^m$ of the meter observable for a given pre- and postselected ensemble of the system is then:

$$\bar{\sigma}_q^m = 2P_m \frac{(\vec{m} \cdot \vec{q}) \Re A_m + [(\vec{r} \times \vec{m}) \cdot \vec{q}] \Im A_m}{(1 + P_m \vec{r} \cdot \vec{m}) + (1 - P_m \vec{r} \cdot \vec{m}) |A_m|^2}. \quad (3.4)$$

The complex modular value:

$$A_m = \frac{\langle \psi_f | e^{-ig\hat{A}} | \psi_i \rangle}{\langle \psi_f | \psi_i \rangle}, \quad (3.5)$$

appears in terms of its real and imaginary parts (see numerator) and its modulus (see denominator). A detailed derivation of the average $\bar{\sigma}_q^m$ can be found in Appendix B.1. In this expression, the direction of \vec{q} was chosen orthogonal to \vec{r} to select maximally interfering pathways through the meter measurement. Then, the nonlocal gate action appears as a superposition of having applied both \hat{U}_A and \hat{I} , and all information about the gate action is lost. This configuration of \vec{q} and \vec{r} fulfills the quantum eraser condition. In our procedure, the interaction strength is not determined by the coupling g . Instead, it reflects the probability of the application of \hat{U}_A by the quantum gate, which is controlled by the measurement strength $\theta = \arccos(\vec{m} \cdot \vec{r})$, with $\theta \in [0, \pi]$. When the vectors \vec{m} and \vec{r} are parallel the nonlocal quantum gate applies always the identity operator \hat{I} and never the unitary transformation \hat{U}_A . This configuration corresponds to zero measurement strength. Thus, the initial system state $|\psi_i\rangle$ leaves the quantum gate without transformation and the meter average $\bar{\sigma}_q^m$ in (3.4) is zero. Oppositely, when the vectors \vec{m} , \vec{r} are anti-parallel, the quantum gate applies always the operator \hat{U}_A on the state $|\psi_i\rangle$. This configuration corresponds to maximal measurement strength. As a result, the meter average $\bar{\sigma}_q^m$ becomes zero again. For all intermediate strengths, the operators \hat{I} and \hat{U}_A are coherently applied: the information if the observable \hat{U}_A is applied or not (encoded on the meter qubit) is uncertain and the uncertainty reaches its maximum for perpendicular vectors \vec{m} and \vec{r} .

For a given vector \vec{r} controlling the quantum gate action, the quantum eraser condition $\vec{r} \cdot \vec{q} = 0$ constrains \vec{q} to the red plane in figure 3.1.b. We choose particular final vectors \vec{q} of the meter system in relationship to the initial vector \vec{m} (characterizing the meter initial state), in order to determine the real and imaginary parts of the modular value from the average meter observable $\bar{\sigma}_q^m$. We pick the real part of A_m when the three vectors \vec{m} , \vec{r} , \vec{q} are coplanar (\vec{q}_{Re} in blue plane in figure 3.1.c), so that $(\vec{r} \times \vec{m}) \cdot \vec{q} = 0$ in equation (3.4). We isolate the imaginary part with orthogonal initial and final states of the meter (\vec{q}_{Im} orthogonal to blue plane in figure 3.1.d), so that $\vec{m} \cdot \vec{q} = 0$ in

equation (3.4). For small measurement strengths $\theta \approx 0$ when the purity P_m is close to one, we obtain the modular value according to the standard approximations of weak measurements (the linear-response regime):

$$\Re A_m \approx \frac{1}{\theta} \bar{\sigma}_{q_{Re}}^m \quad \Im A_m \approx \frac{1}{\theta} \bar{\sigma}_{q_{Im}}^m, \quad (3.6)$$

where the weak measurement approximation effectively removes the nonlinear dependence of equation (3.4) on the modulus of the modular value (see denominator).

For an arbitrary measurement strength, we seek instead to measure the modular value in its polar form to assess directly its modulus $|A_m|$ and argument $\varphi = \arg A_m$. We introduce an additional unitary transformation \hat{R}_ξ in the meter path:

$$\hat{R}_\xi = \hat{\Pi}_r + e^{-i\xi} \hat{\Pi}_{-r}. \quad (3.7)$$

It creates a relative phase shift ξ between the orthogonal states $|r\rangle$ and $|-r\rangle$ that is effectively equivalent to a rotation of the modular value in the complex plane. When the phase shift compensates precisely the argument of the modular value (i. e. when $\xi = \varphi$), this rotation aligns the modular value with the real axis. Choosing the meter configuration \vec{q}_{Re} that picks the real part of the modular value provides now its full modulus, while its argument is equal to the introduced phase shift. In practice, our procedure implements a quantum interferometer exploiting entanglement to measure the two quantities concurrently. Indeed, the expression for the joint probability outcome P_{joint} of the meter and the probe measurements is proportional to:

$$P_{joint} \propto 1 + V \cos(\varphi - \xi), \quad (3.8)$$

typical of an interference phenomenon, where V represents the visibility and $\varphi - \xi$ the phase. Experimentally, the visibility is determined by measuring the maximum and the minimum of the joint probability, denoted by P_{max} and P_{min} , respectively:

$$V = \frac{P_{max} - P_{min}}{P_{max} + P_{min}}. \quad (3.9)$$

When the phase introduced by \hat{R}_ξ equals the argument of the modular value, the maximum of the joint probability is obtained for the meter vector \vec{q}_{Re} , while its minimum is obtained for the orthogonal state $-\vec{q}_{Re}$. The two situations correspond to constructive and destructive interference in the joint measurement, respectively. The visibility depends on the coupling strength and on the modulus of the modular value:

$$V = \frac{2 P_m \tan\left(\frac{\theta}{2}\right)}{C_{\theta+\pi} + C_\theta \tan^2\left(\frac{\theta}{2}\right) |A_m|^2} |A_m|, \quad (3.10)$$

with coefficients C_ϵ defined by:

$$C_\epsilon = \frac{1 + P_m}{2} + \frac{1 - P_m}{2} \cot^2 \frac{\epsilon}{2}. \quad (3.11)$$

A detailed derivation of the interferometric visibility V can be found in Appendix B.2. In particular, the weak measurement approximation gives $|A_m| \approx V/\theta$, similarly to equation (3.6). In this expression of the modular value, the visibility plays the same role than the pointer shift in weak values. This shows a strong connection between modular values and weak interferometric experiments. The quadratic equation (3.10) unfortunately provides two different solutions for the modulus $|A_m|$:

$$|A_m|_{\pm} = \frac{1 \pm \sqrt{1 - C_\theta C_{\theta+\pi} P_m^{-2} V^2}}{C_\theta \tan\left(\frac{\theta}{2}\right) P_m^{-1} V}, \quad (3.12)$$

which requires the introduction of a criterion selecting the correct solution for $|A_m|$. By considering a visibility V close to zero, only $|A_m|_-$ allows to determine small modular values. On the contrary, it is $|A_m|_+$ that provides large modular values. Both solutions $|A_m|_{\pm}$ are equivalent for the visibility $V = (C_\theta C_{\theta+\pi})^{-\frac{1}{2}} P_m$. By substituting this value in equation (3.10), we deduce an equality, which defines the searched criterion:

$$\tan^2\left(\frac{\theta}{2}\right) \frac{C_\theta}{C_{\theta+\pi}} |A_m|^2 = 1. \quad (3.13)$$

In the following, the left-hand side of relation (3.13) is denoted by x_s . The values of $x_s \in [0, +\infty]$ are determined by the initial meter state as well as by the pre- and postselected probe operator \hat{A} . The solution $|A_m|_-$ corresponds to the modulus $|A_m|$, if the value of x_s is equal or smaller than one ($x_s \leq 1$), and $|A_m|_+ = |A_m|$, if x_s is larger than one ($x_s > 1$):

$$|A_m| = \frac{1 - (-1)^{H_{x_s-1}} \sqrt{1 - C_\theta C_{\theta+\pi} P_m^{-2} V^2}}{C_\theta \tan\left(\frac{\theta}{2}\right) P_m^{-1} V}, \quad (3.14)$$

where H_{x_s-1} is the Heaviside step function:

$$H_{x_s-1} = \begin{cases} 0, & \text{if } x_s \leq 1 \\ 1, & \text{if } x_s > 1. \end{cases} \quad (3.15)$$

At first sight, the definition (3.14) of $|A_m|$ appears circular because x_s itself depends on $|A_m|$. However, it is very relevant experimentally. The value of x_s is a classical probability ratio deduced from an additional measurement with a different meter configuration. The involved probabilities are classical in the sense that they correspond to non-interfering pathways (no quantum superpositions are created by the gate). This

time, the final meter vector, noted as \vec{q}_C , is chosen parallel to \vec{r} revealing completely the probe state after the quantum gate interaction. The probability ratio $P_{joint}^{-q_C} / P_{joint}^{+q_C}$ determines the value of x_s (more details can be found in Appendix B.3). This additional measurement is a necessary step in our reconstruction method. However, weak measurement strengths θ yield small values of x_s (even for large modular values). As a result, the solution $|A_m|_-$ is valid for a large range of $|A_m|$.

Alternatively, the solution (3.14) can be written as following:

$$|A_m| = \tan^{-1} \left(\frac{\theta}{2} \right) \sqrt{\frac{C_{\theta+\pi}}{C_\theta}} \tan \left((-1)^{H_{x_s-1}} \frac{\arcsin(\sqrt{C_\theta C_{\theta+\pi}} P_m^{-1} V) - \pi H_{x_s-1}}{2} \right). \quad (3.16)$$

This notation is particularly useful in the case of the intermediate measurement strength $\theta = \pi/2$:

$$\arctan \sqrt{(\Re A_m)^2 + (\Im A_m)^2} = \begin{cases} \frac{1}{2} \arcsin(P_m^{-1} V), & \text{if } x_s \leq 1 \\ \frac{1}{2} [\pi - \arcsin(P_m^{-1} V)], & \text{if } x_s > 1, \end{cases} \quad (3.17)$$

where the values lie in the bounded interval $[0, \pi/2]$. Interestingly, the interferometric phase outcome ξ (specific to our interferometric measurement procedure) is similarly related to the real and the imaginary parts of the modular value A_m :

$$\arctan \left(\frac{\Im A_m}{\Re A_m} \right) = \xi. \quad (3.18)$$

In this way, the two meter readouts lead directly (for the interferometric phase ξ) or indirectly (for the visibility V) to bounded quantities depending on the real and the imaginary parts of the modular value A_m .

3.1.2 Signal-to-noise ratio

As for experiments with Gaussian meters, we evaluate now the signal-to-noise ratio for the above protocol, which uses two-level quantum systems as meters. In order to evaluate the signal-to-noise ratio for the visibility V , we chose the measurement configuration that nullifies the interferometric phase, i.e. $\xi = \varphi$. Figure 3.2 illustrates the experimental set-up of the measurement protocol applied to the case of polarization states of photons. Although this figure shows a particular case of the studied probe system, the illustrated set-up helps us to better understand the derivation of the signal-to-noise ratio that is applicable to arbitrary quantum systems.

For given pre- and postselected probe states, we consider a final meter outcome which follows a binomial distribution: the meter qubit is measured either by detector D_1 or by detector D_2 . The postselected probes are counted by the detector D_3 . All coincidences counts arriving simultaneously on D_1 and D_3 contribute to N_{13}^{max} , and on detectors D_2 and D_3 to N_{23}^{min} . The expectation value of N_{23}^{min} is therefore $E[N_{23}^{min}] = P(2|3)N$ and its variance $\Delta N_{23}^{min} = P(2|3)[1 - P(2|3)]N$, where $N = N_{13}^{max} + N_{23}^{min}$ is the total number of pre- and postselected detector events and $P(2|3)$ is the conditional probability to trigger the meter detector D_2 for a given probe detection by D_3 . Consequently, the expectation value of the measured visibility is:

$$\begin{aligned}
 E_V &= E \left[\frac{N_{13}^{max} - N_{23}^{min}}{N_{13}^{max} + N_{23}^{min}} \right] \\
 &= 1 - \frac{2}{N} E[N_{23}^{min}] \\
 &= 1 - 2P(2|3) \\
 &= V,
 \end{aligned} \tag{3.19}$$

where the last equality follows directly from the definition of the conditional probability: $P(2|3) = \frac{P_{min}}{P_{max} + P_{min}}$, with P_{max} and P_{min} the maximum and the minimum of the joint probability of the measurement protocol. The corresponding variance is:

$$\begin{aligned}
 \Delta_V &= \Delta \left(\frac{N_{13}^{max} - N_{23}^{min}}{N_{13}^{max} + N_{23}^{min}} \right) \\
 &= \frac{4}{N^2} \Delta(N_{23}^{min}) \\
 &= \frac{4P(2|3)[1 - P(2|3)]}{N} \\
 &= \frac{1 - V^2}{N},
 \end{aligned} \tag{3.20}$$

where we used the relationship $P(2|3) = \frac{1-V}{2}$. This leads to the standard deviation:

$$\sigma_V = \sqrt{\frac{1 - V^2}{N}}. \tag{3.21}$$

Finally, the signal-to-noise ratio of the presented measurement scheme is:

$$SNR = \frac{V}{\sqrt{1 - V^2}} \sqrt{N}. \tag{3.22}$$

The standard protocol determines the real (or the imaginary) part of the modular value by measuring the meter observable $\hat{\sigma}_{q_{Re}}$ (or $\hat{\sigma}_{q_{Im}}$). In this case, the visibility V in the signal-to-noise relation (3.22) is replaced by the absolute value of the meter average $\bar{\sigma}_{q_{Re}}^m$ (or $\bar{\sigma}_{q_{Im}}^m$). In the weak measurement limit, the latter is related to the modular

value by the approximation $\bar{\sigma}_{qRe}^m \approx \theta \Re A_m$ (or $\bar{\sigma}_{qIm}^m \approx \theta \Im A_m$). This expression is similar to the one obtained for our scheme in the weak measurement limit, relating the visibility to the modulus of the modular value: $V \approx \theta |A_m|$. Because the modulus of a complex number is always larger or equal than its real and imaginary parts ($|A_m| \geq \Re A_m$ and $|A_m| \geq \Im A_m$), our scheme improves the signal-to-noise ratio of the weak measurement compared to the standard protocol.

3.1.3 Qubit probe state

Now we consider for the arbitrary probe a qubit system and for the transformation $\hat{U}_A = e^{-i\frac{\delta}{2}\hat{\sigma}_n}$ a qubit rotation operator involving the Pauli observable $\hat{\sigma}_n = \vec{n} \cdot \vec{\sigma}$ (\vec{n} a unit vector). Furthermore, we connect the modular with the weak value to gain insight into the physics of weak values. We set therefore a strong coupling strength $g = \pi$. Then, $\hat{U}_A = -i\hat{\sigma}_n$ and the quantum gate acting on the two qubits becomes:

$$\hat{U}_{GATE} = \hat{I} \otimes \hat{\Pi}_r + \hat{\sigma}_n \otimes \hat{\Pi}_{-r}, \quad (3.23)$$

where the phase factor δ in (3.1) was set to $\frac{\pi}{2}$. This shows the equivalence of modular and weak values of $\hat{\sigma}_n$ (see also [2]). We can thus apply our scheme to determine an arbitrary weak value of the Pauli operator in its polar representation. Experimentally, we will implement a conceptual CNOT gate $\hat{U}_{GATE} = \hat{I} \otimes \hat{\Pi}_{|0\rangle} + \hat{\sigma}_x \otimes \hat{\Pi}_{|1\rangle}$. The initial meter state $\hat{\rho}_m = \frac{1}{2} \left(\hat{I} + P_m \vec{m} \cdot \vec{\sigma} \right)$, with $\vec{m} = (\sin \theta, 0, \cos \theta)$, controls the application of the unitary observable $\hat{\sigma}_x$ on the target probe state preselected in the $|\psi_i\rangle = |0\rangle$ state. The entangled bipartite qubit state describing the probe and the meter after their interaction by the quantum gate is then:

$$\hat{\rho} = \begin{pmatrix} \frac{1+P_m \cos \theta}{2} & 0 & 0 & \frac{P_m \sin \theta}{2} \\ 0 & 0 & 0 & 0 \\ 0 & 0 & 0 & 0 \\ \frac{P_m \sin \theta}{2} & 0 & 0 & \frac{1-P_m \cos \theta}{2} \end{pmatrix}, \quad (3.24)$$

where the density matrix is expressed in the standard basis $\{|0\rangle|0\rangle, |0\rangle|1\rangle, |1\rangle|0\rangle, |1\rangle|1\rangle\}$. The meter projective measurement is performed in the $\hat{\sigma}_x$ basis (\vec{q}). It erases the information about the application of $\hat{\sigma}_x$ on the target since it was controlled by the meter basis vectors $|0\rangle$ and $|1\rangle$ of $\hat{\sigma}_z$ (\vec{r}). It is followed by the probe measurement of the final postselected state $|\psi_f\rangle = \cos \alpha |0\rangle + e^{i\phi} \sin \alpha |1\rangle$. Finally, we obtain the weak value $\sigma_{x,w}$ as a function of the chosen initial meter state (\vec{m}), which defines the measurement

strength θ and the purity P_m , and the postselected probe state $|\psi_f\rangle$ with the parameters α and ϕ .

3.2 Experiment

3.2.1 Materials

In practice, the entangled qubit state after the CNOT-gate, as given by relation (3.24), is simulated by polarization-entangled photon pairs produced by type-I spontaneous parametric down-conversion (SPDC) in two orthogonal nonlinear BBO-crystals in the “sandwich configuration” [80, 81] (see figure 3.2). One photon is assimilated to the meter and the other to the probe. A polarizing beam-splitter (PBS), a rotatable half-wave plate (HWP) and a tiltable wave plate, here a third birefringent BBO-crystal², are placed in front of the entangled photon source to control the produced two-qubit state. The polarizing beam-splitter (PBS) fixes a pure polarization state. The half-wave plate (HWP) adjusts the linear polarization and the tiltable wave plate adjusts the relative phase. Via the nonlinear SPDC-process, the pump laser (blue diode DL-7146-101S from SANYO Electric Co.) centered at 408.7 nm generates two polarization-entangled photons at 817.4 nm. They are emitted into a cone of half-opening angle of 2.23°. This angle is determined by the BBO crystal cut. The laser diode is controlled by temperature (Thorlabs TED 200C) and current (Thorlabs LDC202C) controllers. It produces a continuous laser output power of 60 mW. We adjust the phase ξ by turning a birefringent, 1 mm thin, z-cut quartz plate mounted on a motorized rotation stage. The polarization basis are selected by half- and quarter-wave plates (QWP) followed by a polarizing beam-splitter (RCHP-15.0-CA-670-1064 from CVI Melles Griot). In front of the detection system, adjustable irises and colored low-pass filters (FGL780 from Thor-

²Additionally, the BBO-plate is used to precompensate the temporal separation between the horizontal and vertical polarization induced by the first birefringent and dispersive BBO-crystal in the entangled photon source. This temporal mismatch is due to different speeds of propagation (i.e. the group velocity) of the ordinary and extraordinary waves. When this separation exceeds the coherence length of the pump beam, which is the inverse of its bandwidth, then the entanglement of the down-converted photons is not preserved. Therefore, the BBO-plate has the same thickness as each of the other BBO-crystals in the entangled photon source and is oriented perpendicular to the first one. As a result, the pump polarizations overlap again at the interface between the two BBO-crystals in the source. More details about this temporal walkoff can be found on the website: <http://people.whitman.edu/~beckmk/QM/>.

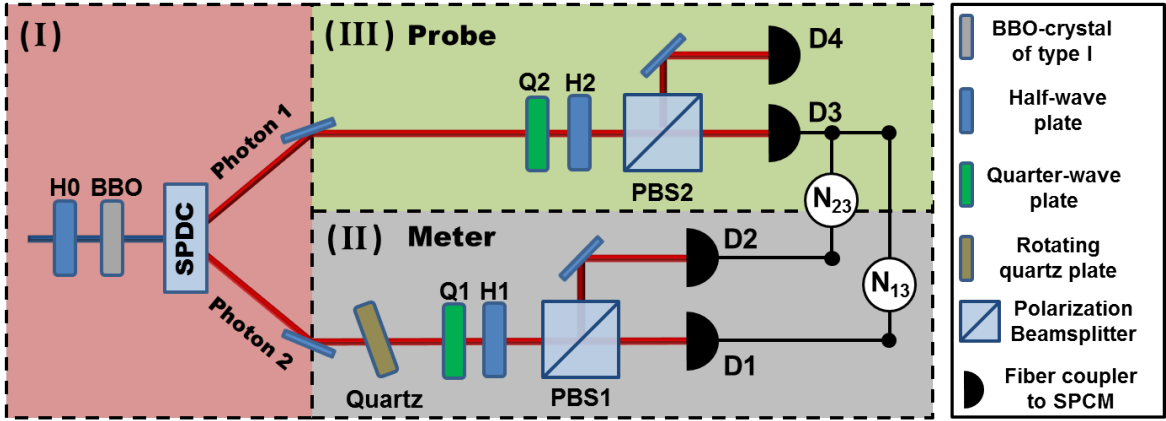


Figure 3.2: The set-up comprises three areas: the state preparation with the two qubits generation (I), the meter measurement by detectors D_1 and D_2 (II) and the final probe post-selection by D_3 (III). The coincidence counts N_{13} and N_{23} are acquired by four single photon counting modules (SPCM) placed in the meter and probe paths.

labs) with a maximum transmission of 90% are placed to reduce background counts. In reference [80], they use interference filters with a full width at half maximum (FWHM) of 5 nm centered at the down-converted wavelength to select only photons with the same (or nearly) wavelength. These interference filters ensure lower background counts and improve the detection of polarization-entangled photons with higher purities. In the following, the photons are coupled into multimode fibers (SPCM-QC9 from Perkin-Elmer) by using 10.99-mm-focal-length lenses (F220FC-B from Thorlabs) with a numerical aperture³ (NA) of 0.25. To ensure a maximum detection of photon counts, the numerical aperture of the multimode fibers is 0.27. The collected photons are detected by four single-photon-counting modules (SPCM-AQ4C from Perkin-Elmer). Each module is a silicon avalanche photodiode based on a p-n junction working in Geiger mode. For a wavelength at 817.4 nm, their quantum efficiency is $\sim 50\%$. The total rate of coincidence counts per second, here 4000 s^{-1} , is recorded by using a homemade coincidence counter build around a FPGA (Field-Programmable Gate Array - SE3BOARD from Xilinx) coincidence counter.

³The numerical aperture is a dimensionless number that characterizes the range of angles over which the lens can emit or accept light.

3.2.2 Methods

Entangled Photons Source. The production of the polarization-entangled two-photon state relies on the Spontaneous Parametric Down-Conversion process (SPDC) in a nonlinear crystal, which splits spontaneously a pump photon into two daughter photons. The conservation of energy and momentum during the whole process induces entanglements in these two continuous degrees of freedom. The source of polarization-entangled photon pairs was realized by two identical, adjacent, 0.5 mm thin, nonlinear β -barium borate (BBO) crystals [80]. Their principal planes are defined by the momentum \vec{k} of the incident photons and the crystal optic axis, here the extraordinary axis n_e (see figure 3.3.a). Each crystal is cut for type-I phase matching with $\varphi = 90^\circ$ and $\theta = 29.2^\circ$. For this cut, phase matching occurs only for photons polarized in the principal plane of the BBO crystal and generates a pair of photons, the signal and the idler, perpendicularly polarized to this plane and aligned with its ordinary axis n_o . The down-conversion process emits for the pump wavelength of 408.7 nm two daughter photons at 817.4 nm into a cone of half-opening angle of 2.23° (see figure 3.3.b and Appendix C). The conversion efficiency of this process is very low. Experimentally, we observe count rates of 10^8 photons per second for each crystal. This corresponds to a conversion efficiency of maximum 10^{-9} , i.e. only one pair is generated by the nonlinear SPDC-process per every 10^9 incoming photons.

The nonlinear crystals are oriented with their principal planes perpendicular, where the first (second) crystal defines the horizontal (vertical) plane. Therefore, the down-conversion process occurs only for a horizontally polarized pump beam in the first crystal. The resulting light cone is vertically polarized. In contrast, for a vertically polarized pump, the down-conversion process occurs only in the second crystal and produces a horizontally polarized light cone. Because the source is constituted of relatively thin crystals, both light cones are spatially superposed. In the case of an arbitrary polarized pump beam, this leads to a coherent production of horizontally and vertically polarized pairs of photons as long as the emitted spatial and temporal modes are indistinguishable and deliver no information about their origin. This temporal indistinguishability is ensured by a coherence time of the incoming pump photons which is of the same order of magnitude as the time to traverse both nonlinear crystals.

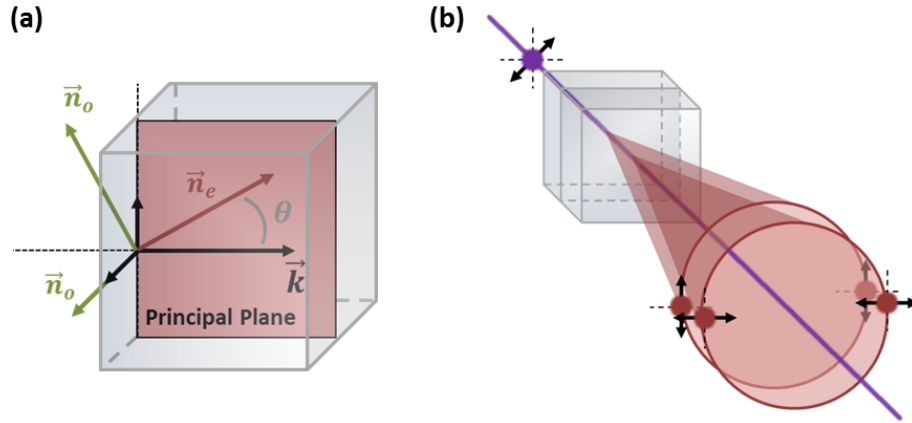


Figure 3.3: (a) Schematic illustration of the principal plane in the nonlinear type-I BBO crystal with $\theta = 29.2^\circ$. (b) The polarization-entangled photon source. By the nonlinear process SPDC, diagonally polarized photons are converted in the first and in the second nonlinear BBO crystal. Since the emitted photons (frequency degenerated) are spatially and temporally indistinguishable, this conversion is a coherent process and creates polarization-entangled photons.

Measurement Protocol. For each weak and modular value determination, the protocol performs in a first step the measurement of the interferometric phase and visibility, and in a second step the measurement of the probability ratio x_s , determining the correct value for the weak values modulus. This first, interferometric measurement requires the acquisition of diagonally and anti-diagonally polarized photons by the meter detectors D_1 and D_2 , respectively. A motorized stage introduces a phase change ξ by turning the quartz plate in the meter path to obtain the interference visibility V from the coincidence counts. When the coincidence counts N_{13} for detectors D_1 and D_3 are maximal (constructive interference), the coincidence counts N_{23} for detectors D_2 and D_3 are minimal (destructive interference). Then, the introduced phase change annihilates the argument of the recorded weak value, while the visibility can be estimated by:

$$V = \frac{N_{13}^{max} - N_{23}^{min}}{N_{13}^{max} + N_{23}^{min}}. \quad (3.25)$$

In practice, the motorized stage is piloted by a homemade program turning the 1 mm thin quartz plate from its initial position of 26° to its final position of 38° by steps of 0.5° . For each position, the coincidence counts N_{13} between the detectors D_1 and D_3 are recorded 9 times. Each one of these acquisitions lasts 3 s. The software analyzes

the data and determines the quartz orientation for which the coincidence counts N_{13} are maximal. To this end, a nonlinear regression is applied on the data points by fitting the regression model:

$$f(x) = c_1 + c_2 \cos [c_3 (x - c_4)] , \quad (3.26)$$

where the independent variable x represents the quartz position ϵ and the dependent variable $f(x)$ the coincidence counts N_{13} . The best fit parameters are estimated using the weighted least-square method. The estimation of the parameter c_4 is of particular interest since it indicates the quartz position inducing maximal coincidence counts. After determining the relation between this position ϵ and the phase change ξ , the parameter c_4 leads directly to an estimation of the weak values argument. As shown in Appendix D, between the initial and final quartz positions of 26° and 38° , the induced phase change ξ follows linearly the rotation angle ϵ indicated by the motorized stage. A preliminary calibration determining the parameters of this proportional relation must be realized. Once the value of the parameter c_4 is identified, the motorized stage is set at this position and proceed with the acquisition of N_{13}^{max} and N_{13}^{min} . Both coincidence measurements are recorded n times, each during 5 s. Because the value of n changes from one measurement series to another, its value is not specified yet.

Once the interferometric visibility and phase are recorded, the meter measurement configuration is adapted to count horizontally and vertically polarized photons on detectors D_1 and D_2 , respectively. As described above, this configuration removes completely the interferometric character of our measurement protocol: the meter readout reveals completely the information about whether the transformation $\hat{\sigma}_x$ was applied. The coincidence counts N_{13}^C of detectors D_1 and D_3 determine the number of postselected photons that traversed the CNOT-gate without transformation. Oppositely, the coincidence counts N_{23}^C of D_2 and D_3 determine the number of postselected photons that evolved under the action of the gate. The coincidence counts N_{13}^C and N_{23}^C deliver finally an estimation for the value $x_s = N_{23}^C/N_{13}^C$, where both are acquired m times, each repetition during 5 s. The value of m is specified later.

Additionally, our measurement procedure requires a complete characterization of the initial meter state, i.e. of the meter purity P_m and of the measurement strength θ . Both parameters remain constant for each measurement series. Thus, they must only be determined once, at the beginning.

Coincidence Measurements. In the case of a photon detection, the single photon counting module generates and sends a TTL pulse to the FPGA (Field-Programmable Gate Array). This pulse is 4.5 V high and 25 ns width. The dead time of each counting module⁴ Δt_{dead} is 50 ns. A homemade program used by the FPGA allows to record the number of detected photons N_i for each counting module as well as the number of coincidences N_{ij} between the probe and meter detectors during the total measurement time T . Each detector has a dark count rate⁵ of 350 to 390 counts per second. The FPGA records a coincidence count from two incoming TTL pulses by applying the detection protocol shown in figure 3.4. We consider two TTL signals, the first arriving through channel 1 and the second through channel 3. Every 8 ns with a clock rate of 125 MHz, the FPGA samples each single channel. In the case of an incoming pulse, the FPGA produces its own internal signal, where the width Δt is adjustable by the user by a multiple of 8 ns. For our measurements, we chose a width of $\Delta t = 2 \times 8$ ns, which induces lower rates of accidental coincidences⁶. Then, the signals of channel 1 and 3 pass through the AND-gate. If a partial or complete overlap between two signals is detected, the gate attributes a logical 1, and otherwise a logical 0. Each sequence of ones finally generates a coincidence count between the detectors D_1 and D_3 .

In theory, a coincidence recorded by the probe and meter detectors is induced by a pair of correlated photons, which are generated at the same time by the nonlinear SPDC process. However, there is a small chance that two uncorrelated photons are counted as a coincidence, the accidental coincidence. When the signal channels are far from saturation, with $N_i \Delta t_{dead} \ll T$, the total number of accidental coincidences is approximated by [82]:

$$N_{ij}^{acc} = 2\Delta t \frac{N_i N_j}{T}. \quad (3.27)$$

Knowing the accidental counts is necessary for analyzing the data. They are calculated from the singles counts N_i for each measurement and are subtracted from the recorded coincidence counts.

⁴The dead time is the time after each detection during which the counting module is not able to record another photon.

⁵The dark count rate is the average rate of registered counts without any incident light.

⁶In reference [80], time windows of 7 ns are used to capture coincidences achieving lower accidental coincidence rates.

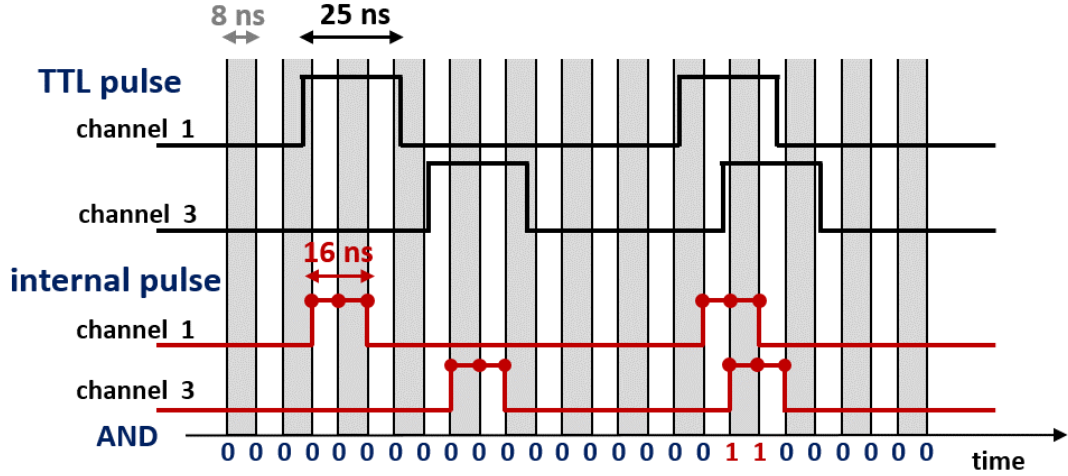


Figure 3.4: Coincidence count protocol. The FPGA samples every 8 ns the incoming signal which has a width of 25 ns. The generated, internal pulses with a width of now 16 ns pass then through the logical AND-gate, which allows to determine the coincidence counts.

Statistical Analysis. In the experimental procedure, the measurement outcomes are determined by two different types of acquisitions. Each of them requires a specific evaluation to calculate the confidence interval of the experimental data. In the first section, we consider direct acquisitions such as for the visibility V or for the solution criterion x_s . Then, in the second section, the statistical analysis for the weak values argument are precised.

In statistical theory, a sample X_1, X_2, \dots, X_n is a randomly selected subset from a statistical population, which estimates one or more properties of the whole population. Each X_i has its own estimated value. The distribution of these estimations is called the sampling distribution. Under the hypothesis that this distribution comes from a normally distributed population $\mathcal{N}(\mu, \sigma)$, the searched value of the experimental data corresponds to the sample mean $\mu = \frac{1}{n} \sum_i^n X_i$ and has a standard error of $\frac{\sigma}{\sqrt{n}}$, where σ is standard deviation and n the sample size, i.e. the number of different acquisitions for the same measurement set-up. Consequently, each data point must be tested whether its corresponding sample came from a normally distributed population or not. Knowing that our sample size is limited by $n = 100$, we chose the Shapiro-Wilk test with the null-hypothesis that the population is normally distributed [83, 84]. The

test determines the p-value, which is the probability, assuming that the null-hypothesis is true, to obtain a sample result at least as extreme as the one that was actually observed. The test compares the obtained p-value to a predetermined significance level, the α -level, generally chosen at $\alpha = 0.05$. When the p-value is less than the chosen α -level, the null hypothesis is rejected: there is evidence that the data are not from a normally distributed population. On the contrary, when the p-value is greater than the chosen α -level, the null hypothesis cannot be rejected. In this case, on the basis of the definition of the confidence interval, the resulting error bars are given by $\left[\mu - t_{n-1}^{\alpha} \frac{\sigma}{\sqrt{n}}, \mu + t_{n-1}^{\alpha} \frac{\sigma}{\sqrt{n}} \right]$, where t_{n-1}^{α} can be found in the Student's t -distribution tables. The value of t_{n-1}^{α} depends on the confidence level C with $\alpha = \frac{1-C}{2}$ and on the degrees of freedom $n - 1$ (n is the sample size). The error bar of each data point will be represented for a confidence level greater than 0.99. In such a way, the true value for the whole population is found with more than 99% probability in the fixed confidence interval.

The weak values argument is determined by fitting the nonlinear regression model (3.26) on a weighted data-set with known standard deviation. By using the Levenberg-Marquardt nonlinear (weighted) least-square algorithm [85] in the form of a MATLAB application⁷, we estimate numerically the value of the coefficient c_4 , the estimand, resulting as the best fit parameter from this algorithm. This estimator for the given data-set is denoted as \hat{c}_4 . Additionally, the covariance matrix for the estimated parameters is provided and used to determine the confidence interval for the estimand \hat{c}_4 . By assuming an asymptotic normal distribution for the parameter estimates, this covariance matrix contains on its diagonal the variance of \hat{c}_4 , denoted as $\sigma^2(\hat{c}_4)$ [86]. The corresponding confidence interval of the estimand \hat{c}_4 is given by $[\hat{c}_4 - t_{n-4}^{\alpha} \sigma(\hat{c}_4), \hat{c}_4 + t_{n-4}^{\alpha} \sigma(\hat{c}_4)]$, with $n = 24$ the number of data points⁸. We will chose a confidence interval with a confidence level of 99.7%, which is calculated by a second MATLAB application⁹. Finally, the linear relation between the quartz position ϵ and the phase change ξ achieved during the calibration allows to express the confidence interval for the weak values argument in terms of the phase change.

⁷We use the nonlinear regression Matlab function *nlinfit*. For more information, see the website www.mathworks.com.

⁸Because the motorized quartz stage moves from 26° to 38° and takes measurements every 0.5° , the number of data points is $n = 24$. The number of different measurements for a given quartz position, here, 9 acquisitions each during 3 s, simply determines the standard deviation for each data point.

⁹We use the Matlab function *nlparci* to calculate the confidence interval of the parameters deduced from the nonlinear regression.

3.3 Results and discussion

3.3.1 Calibration of the quartz plate

The z-cut quartz plate is calibrated by preparing a maximally polarization-entangled state. By adjusting the optical elements placed in front of the entangled photon source, the following Bell-state is experimentally created:

$$|\phi^+\rangle = \frac{1}{\sqrt{2}} (|0\rangle_p |0\rangle_m + |1\rangle_p |1\rangle_m) , \quad (3.28)$$

where p indicates the probe and m the meter¹⁰. The prepared state of the photon pair is then recorded in the diagonally and anti-diagonally polarized measurement basis. For this configuration, the variation in the visibility introduced by the phase change ξ of the quartz crystal is maximized, increasing the sensitivity of the calibration. Theoretically, it is not difficult to show that:

$$P(1|3) = \frac{N_{13}}{N_{13} + N_{23}} = \frac{1}{2} (1 + \cos [a_1 \epsilon + a_2]) , \quad (3.30)$$

where we substituted the phase change ξ by the linear relation $\xi = a_1 \epsilon + a_2$ that depends on the quartz plate position ϵ (see Appendix D). The values of N_{13} are the number of coincidences recorded by the detectors D_1 and D_3 measuring both diagonally polarized photons, while N_{23} is the number of coincidences recorded by D_3 and D_2 , with detector D_2 counting anti-diagonally polarized photons. Both coefficients, a_1 and a_2 , are determined by applying a nonlinear regression on a weighted data-set by fitting the regression model:

$$f(x) = \frac{1}{2} (1 + a_3 \cos [a_1 x + a_2]) , \quad (3.31)$$

where the independent variable x represents the quartz position ϵ and the dependent variable $f(x)$ the conditional probability $P(1|3)$. The coefficient a_3 appears in the regression model to take into account the purity of the polarization-entangled state. For the acquisition of the weighted data-set, we turn the quartz plate from the initial

¹⁰In reality, both photons are in a quantum state involving a spatial degree of freedom:

$$|\psi\rangle = \frac{1}{\sqrt{2}} (|0\rangle|0\rangle + |1\rangle|1\rangle) \otimes \frac{1}{\sqrt{2}} (|P\rangle|M\rangle + |M\rangle|P\rangle) , \quad (3.29)$$

with the probe path P and the meter path M . Since this spatial degree of freedom does not interfere in our measurement protocol, we can adopt the simpler notation in (3.28). However, there are many examples in the literature, as the experiments in the Hong-Ou-Mandel interferometer [87], where this simplification is not allowed.

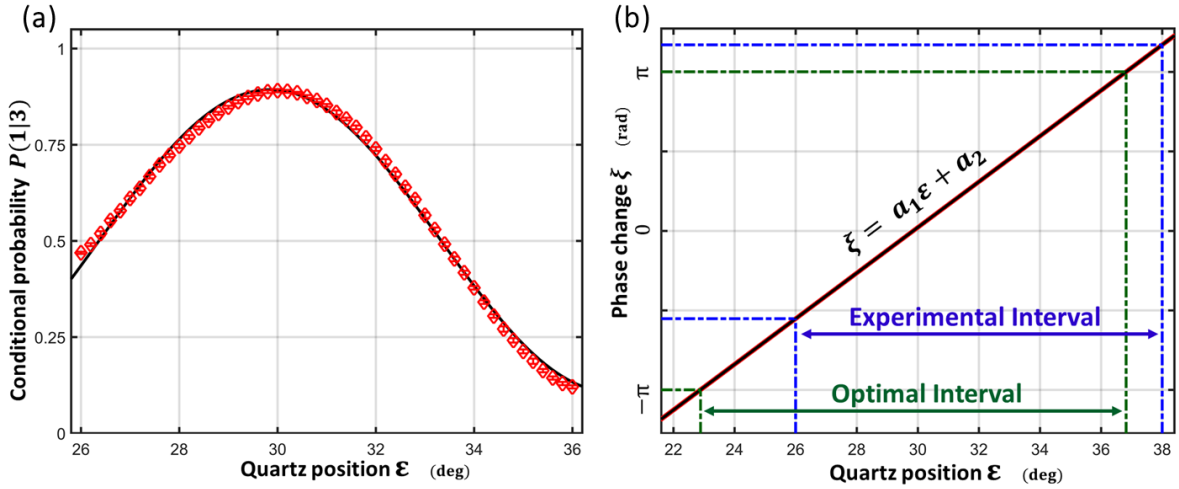


Figure 3.5: Quartz plate calibration. (a) Data fitting by applying a non-linear regression on the recorded conditional probabilities $P(1|3)$ (see equation (3.30)). (b) Resulting linear relationship between the quartz position ϵ and the phase change ξ with the corresponding prediction interval based on the data fitting.

position of 26° to 36° by steps of 0.2° . At each position, the coincidence counts N_{13} and N_{23} are recorded 24 times, each repetition during 5 s. Figure 3.5.a shows the mean with the associated standard deviation for each quartz position (red diamonds) and the curve resulting from the data fitting (black line) with the best fit parameters:

$$\begin{aligned} a_1 &= 0.4531 \pm 0.0064, \\ a_2 &= -13.53 \mp 0.20, \\ a_3 &= 0.788 \pm 0.015. \end{aligned} \quad (3.32)$$

Based on these (fit) parameters, figure 3.5.b reveals the linear relation between the quartz position ϵ and the introduced phase change ξ (black line). The narrow prediction interval¹¹, i.e. the confidence interval on new observations (red surface), with a

¹¹On the basis of this data fitting, a new, independent measurement of the quartz position ϵ after the calibration process predicts the following value for the estimate of the phase change: $\hat{\xi} = 0.4531 \epsilon - 13.53$. The error bars of the estimate $\hat{\xi}$ includes both the error from the fitted model and the error associated with this new position measurement. Thus, we refer to a prediction interval rather than the confidence interval. This interval is given by [88]:

$$\hat{\xi} \pm t_{n-p}^\alpha \sqrt{\frac{MSE}{n-p} \sqrt{1 + \frac{1}{n} + \frac{(\epsilon - \bar{\epsilon}_c)^2}{\sum_{i=1}^n (\epsilon_{c,i} - \bar{\epsilon}_c)^2}}}, \quad (3.33)$$

where the size of the data-set n , the quartz positions $\epsilon_{c,i}$ and the mean square error MSE are determined by the data used for the calibration. We set the parameter $p = 3$, since there are three different coefficients in the non-linear regression model.

confidence level of 99%, points out the high accuracy of this calibration. Experimentally, the quartz positions are limited to the interval of 26° to 38° . This interval does not, unfortunately, cover a whole phase change of 2π , as it is the case for the optimal interval. This limitation causes problems during the acquisition of the weak values argument. When the maximum of the coincidence counts N_{13} lies outside of this range of quartz positions, then the accuracy of the calibration is no longer ensured. In practice, we introduce, in this case, an additional phase change of π by a half-wave plate in the meter path, shifting the maximum of N_{13} in the experimentally accessible interval of the quartz positions.

3.3.2 Meter state preparation

The proposed measurement protocol involves the identification of two parameters characterizing the meter system: the measurement strength θ and the purity P_m . These requirements are not specific to our scheme. In all weak value measurement protocols, the acquisition of the measurement strength θ is a necessary and inevitable process. The additional measurement of the purity P_m is only required because we considered the most general case of an initial incoherent state of the qubit meter. Most of the literature assumes the meter to be in a known pure state to avoid this supplementary step. To determine the initial meter state in our protocol, it is only necessary to perform the quantum tomography on single meter states. In practice, in our experimental implementation, we simulated the CNOT gate by using spontaneous parametric down-conversion, instead of using a true CNOT gate with two separate entries that could be characterized independently. Because the input meter photons could not be measured directly, we determined the measurement strength and the purity by performing our analysis on the resulting two-photon states.

By a half-wave and a birefringent plate, here by a third BBO crystal, the incident pump photons are prepared in a specific polarization state. This pump photons generate inside the entangled photon source a two-photon polarization state modeled as following:

$$\hat{\rho}_{exp} = \gamma \begin{pmatrix} \cos^2 \beta & 0 & 0 & e^{i\alpha} \cos \beta \sin \beta \\ 0 & 0 & 0 & 0 \\ 0 & 0 & 0 & 0 \\ e^{-i\alpha} \cos \beta \sin \beta & 0 & 0 & \sin^2 \beta \end{pmatrix} + (1 - \gamma) \begin{pmatrix} \cos^2 \beta & 0 & 0 & 0 \\ 0 & 0 & 0 & 0 \\ 0 & 0 & 0 & 0 \\ 0 & 0 & 0 & \sin^2 \beta \end{pmatrix}, \quad (3.34)$$

where the purity is by definition $\gamma = \text{Tr} [\hat{\rho}_{exp}^2]$. In fact, the density operator $\hat{\rho}_{exp}$ describes two kinds of polarization states. Firstly, there are polarization-entangled photons obtained with a probability of γ (the non-classical part), and secondly, a distribution of horizontally and vertically polarized photons produced with a probability of $1 - \gamma$ (the classical part). The entanglement between the down-converted photons results directly from their indistinguishability at the quantum source. When the emitted pairs reveal their quantum origin (one of the two orthogonal BBO crystals) through their spatial or temporal modes, the coherence during the production of horizontally and vertically polarized photons disappears completely. To evaluate the reconstruction process of weak and modular values in our measurement procedure, we prepare incoherent meter states with purities smaller than one. Experimentally, this requires the preparation and detection of classical, unentangled polarization states of photons. We can amplify the detection of these photons by using longpass colored glass filters rather than interference bandpass filters with small full width at half maximum (FWHM) at 5 – 10 nm. The bandpass filters are usually used to reduce background and select only the degenerate photons coming from the overlapping light cones [80]. The relative amount of horizontally and vertically polarized pairs of photons is determined by the parameter $\beta \in [0, \frac{\pi}{2}]$. This parameter is adjusted by the half-wave plate controlling the polarization of the incident pump photons. The relative quantum phase α appearing in the non-classical part of the density operator $\hat{\rho}_{exp}$ is set to zero by turning the BBO plate mounted after the half-wave plate. This rotation induces a dephasing between the horizontal and vertical polarization of the pump photons that cancels the relative phase α . By considering the measurement strength θ and the purity P_m introduced by our weak value measurement protocol (see the density matrix (3.24)), it is straightforward to show that $P_m = \gamma \sqrt{1 + \frac{1-\gamma^2}{\gamma^2} \cos^2(2\beta)}$ and $\theta = \arctan(\gamma \tan[2\beta])$. Both meter parameters depend on the experimental values γ and β , which can be determined by the quantum tomography technique. For an equal amount of horizontally and vertically polarized photons with $\beta = \frac{\pi}{4}$, the purity parameters γ and P_m are equal and the measurement strength θ becomes 2β .

Quantum tomography technique. Quantum state tomography is the process that completely characterizes the unknown state of an identical ensemble of quantum systems. This reconstruction of the quantum state is achieved by a sequence of identical measurements within a series of different measurement bases. To identify the prepared

	Coincidence Counts				N_H	Detector Counts		
	N_{HR}	N_{HL}	N_{VR}	N_{VL}		N_R	N_V	N_L
$ H\rangle R\rangle$	155 549	154 920	144 492	154 547	5 846 923	10 105 894	6 830 831	10 100 326

Table 3.1: Coincidence counts and total counts of each detector resulting from the prepared biphoton state. The counts are recorded, during 150 s, for the horizontal and right-handed measurement basis.

two-photon state, we use the tomography technique developed by Paul Kwiat's quantum information group¹² [82]. In a first approach assuming error-free and exact measurements, their reconstruction technique, applicable to multiple-qubit states, is based on the identification of the Stokes parameters. These parameters, characterizing entirely the multiple-qubit state, are obtained by a series of projective measurements. The research group used this theoretical approach to provide a state tomography tool working for real two-photon systems. Because any acquisition of the photons polarization contains statistical and systematic errors, their tomography technique of an unknown polarization state relies on an algorithm using the maximum likelihood method. This algorithm delivers the state which is the most likely to have produced the measuring results. The corresponding MATLAB or Python code is freely accessible on the research group's website.

The complete characterization of the biphoton state requires a series of 36 measurements each recording the coincidence counts between the detectors. In fact, the reconstruction of the polarization state of only one photon (with 3 degrees of freedom) requires the average measurements of the three Pauli operators $\hat{\sigma}_x$, $\hat{\sigma}_y$ and $\hat{\sigma}_z$. These averages are obtained by acquiring the probabilities that the unknown state is projected onto the eigenvector states of the Pauli operators: the horizontal, vertical, diagonal and anti-diagonal states $|H\rangle$, $|V\rangle$, $|D\rangle$, $|A\rangle$ for linear polarization, and the right- and left-handed states $|R\rangle$, $|L\rangle$ for circular polarization. To reconstruct the polarization state of two photons, we simply determine the joint probabilities of all 36 combinations between these eigenvector states. For example, we consider the projection of the prepared biphoton state onto the horizontal state $|H\rangle$ for the meter and the right-handed state $|R\rangle$ for the probe. Therefore, during 150 s, the detector D_1 records all horizontally polarized photons and the detector D_3 all right-handed photons. Simultaneously, the detector

¹²More information of the research group's website: <http://research.physics.illinois.edu/QI/Photonics>.

D_2 counts the photons with vertical polarization and D_4 the left-handed photons. The acquisition system provides the coincidence counts, as well as the total counts of each detector for the correction of the accidental coincidences (see table 3.1 for horizontal and right-handed states and Appendix E for the complete table).

When the acquisition of the remaining measurement configurations is completed, then the whole table is analyzed by the quantum tomography algorithm. Although the application features options to correct several errors in the preparation and measurement process, as an unstable laser source, faulty beamsplitters or variations in the detector efficiency, we only use the correction of accidental coincidences. Because the experimental set-up remains equivalent for the weak value collection, this non-application of the error corrections has no impact on further measurement outcomes. The error analysis of the reconstructed density matrix is unfortunately a non-trivial process. Errors in the counting statistics propagates through the algorithm calculations. The theoretical calculation of the error propagation, which is analyzed in details in reference [89], overestimates the error on the density matrix [82]. To derive a reliable estimation of this error, the measurements and the application of the tomography algorithm must be repeated many times. For different reasons, which will become clearer later, we do not evaluate this error.

Experimental analysis. For the whole experimental demonstration of the controlled quantum evolution protocol, eight measurement series with different initial meter configurations are considered in the following sections. The first four preparations are analysed by the described quantum tomography technique, and the last four by non-linear regressions on the acquired data points (this method will be clarified later). In the next section, we show only the density matrix of the experimental two-photon state $\hat{\rho}_{exp}^{(1)}$ resulting from the first preparation. The density matrices of the other three experimental preparations are specified in Appendix F. The resulting density matrix of the first two-photon state preparation is:

$$\hat{\rho}_{exp}^{(1)} = \begin{pmatrix} 0.486 & 0.000 - 0.007i & 0.018 - 0.010i & 0.394 + 0.008i \\ 0.000 + 0.007i & 0.016 & 0.011 - 0.002i & -0.023 + 0.011i \\ 0.018 + 0.010i & 0.011 + 0.002i & 0.016 & -0.004 + 0.003i \\ 0.394 - 0.008i & -0.023 - 0.011i & -0.004 - 0.003i & 0.482 \end{pmatrix}. \quad (3.35)$$

Schematically, this density matrix is represented in the form of its real and its imaginary part in figure 3.6. The reconstructed density matrix reveals that only the elements

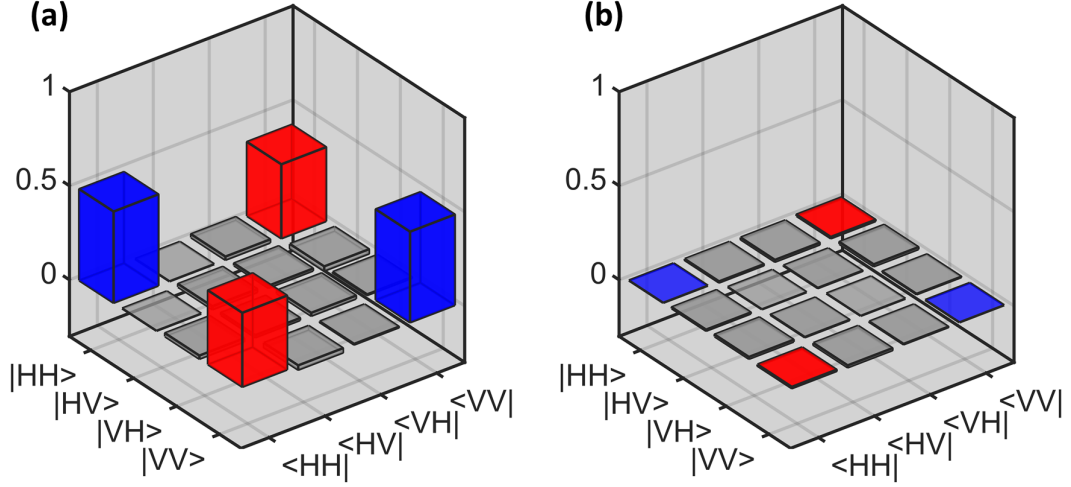


Figure 3.6: Density matrix of the first preparation, deduced by the quantum tomography technique. (a) Only the corners of the real matrix elements contribute to the observed polarization correlations between both photons. The appearing non-classical correlations results directly from the off-diagonal elements (red balks). (b) All imaginary elements are close to zero and have no impact on the correlations.

located on the matrix corners are not close to zero. This result is in full agreement with the experimental production method of the polarization-entangled quantum state, which produces density matrices given by the model (3.34). For further analysis, we neglect all elements that are close to zero. Moreover, we deduce from this tomography the quantum purity γ_1 and the amount of horizontally and vertically polarized photons β_1 :

$$\gamma_1 = \frac{\rho_{14}^{(1)} (\rho_{11}^{(1)} + \rho_{44}^{(1)})}{\sqrt{\rho_{11}^{(1)} \rho_{44}^{(1)}}} = 0.788, \quad (3.36)$$

$$\beta_1 = \frac{1}{2} \arccos \left(\frac{\rho_{11}^{(1)} - \rho_{44}^{(1)}}{\rho_{11}^{(1)} + \rho_{44}^{(1)}} \right) = 0.249 \pi \approx \frac{\pi}{4}. \quad (3.37)$$

In a similar way, we determine the meter purity P_{1m} and the measurement strength θ_1 introduced by the density matrix (3.24):

$$P_{1m} = 2\sqrt{(\rho_{14}^{(1)})^2 + (\rho_{11}^{(1)} - \rho_{44}^{(1)})^2} = 0.788, \quad (3.38)$$

$$\theta_1 = \arctan \left(\frac{2\rho_{14}^{(1)}}{\rho_{11}^{(1)} - \rho_{44}^{(1)}} \right) = 0.499 \pi \approx \frac{\pi}{2}. \quad (3.39)$$

	set-up 1	set-up 2	set-up 3	set-up 4
γ	0.788	0.762	0.810	0.905
β	0.249π	0.167π	0.055π	0.014π
P_m	0.788	0.822	0.965	0.985
θ	0.499π	0.297π	0.092π	0.025π

Table 3.2: Summary of the preparation parameters appearing in the density matrixes (3.24) and (3.34) for the four experimental set-ups.

Because the amount of horizontally and vertically polarized photons is equal, the values of the meter parameters P_{1m} and θ_1 are approximately γ_1 and $2\beta_1$. Experimentally, we prepared three additional polarization-entangled quantum states, which were analyzed by the state tomography technique. The density matrices as well as the schematic representations can be found in Appendix F. Table (3.2) summarizes the values of the couples of parameters γ , β and P_m , θ used in the next section. Only the state prepared by set-up 4 features a meter purity P_{4m} and a measurement strength θ_4 for which the standard weak measurement approximations (the linear-response regime) are applicable most of the time. All other preparations are incompatible with these approximations.

3.3.3 Real weak values: analysis of the purity and the measurement strength

In this section, we consider a probe postselection along the linear polarization state $|\psi_f\rangle = \cos \alpha |H\rangle + \sin \alpha |V\rangle$. This choice produces only real weak values of the observable $\hat{\sigma}_x$ as the initial state is $|\psi_i\rangle = |H\rangle$: $\sigma_{x,w}(\alpha) = \tan \alpha$, with $\alpha \in [0, 2\pi]$. Its argument is either 0 or π . It determines the sign of the weak value. In this case, the quartz plate in the meter path is not necessary. By default, the coincidence counts N_{12} (N_{13}) are maximized for a positive (for a negative) sign of $\sigma_{x,w}$ and minimized for negative (for a positive) values. Hence, in this section, we focus our attention on the role of the meter purity and of the measurement strength in the weak value acquisition process. Only in the next section, we shall consider the effects of the quantum phase adjustment, when we will measure complex values for $\sigma_{x,w}$.

Figure 3.7.a presents the visibility V as a function of the final probe polarization fixed by the postselected angle α , which varies from -90° to 90° by steps of 2° . The results are

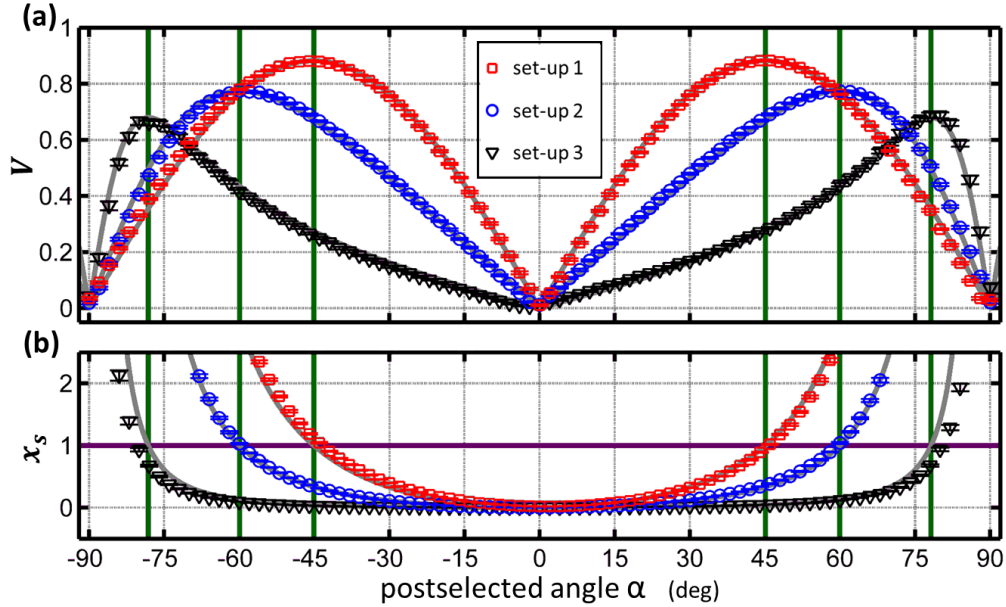


Figure 3.7: (a) Visibility as a function of the postselected polarization $|\psi_f\rangle = \cos \alpha |H\rangle + \sin \alpha |V\rangle$ with preselected $|H\rangle$ polarization for the first three meter preparations. (b) Criterion x_s used to select the appropriate weak value solution. Values larger (smaller) than unity (violet, solid horizontal line) admit the positive (negative) solution $|\sigma_{x,w}|_{\pm}$, respectively. Final meter states are $|D\rangle$ and $|A\rangle$ for measurements (a) and $|H\rangle$ and $|V\rangle$ for (b). Gray, solid lines represent theoretical curves.

shown for the first three polarization preparations, which are all unconciliable with the weak measurement approximations. The visibility is measured by selecting diagonally and anti-diagonally polarized meter photons, which are recorded by detectors D_1 and D_2 , respectively. For the reasons described above, we do not implement the quartz plate in the meter path. However, the weak values argument is determined during the acquisition of the visibility as it appears in the form of a positive or negative value:

$$V = \frac{N_{13} - N_{23}}{N_{13} + N_{23}}. \quad (3.40)$$

In the case of a weak value argument of π , the coincidence counts N_{23} are greater than N_{13} . A relative phase of $-\pi$ is introduced by switching the role of the detectors. Then, detector D_1 records the anti-diagonally polarized photons and D_2 the diagonal photons. Thus, we acquire the argument of the weak value and the visibility concurrently. Each data point in figure 3.7.a results from 49 different acquisitions of 5 s duration each. The corresponding error bars present a confidence interval of 99%. The gray, solid lines represent the theoretical curves fixed by the values of the meter purity P_m and of the

	set-up 1	set-up 2	set-up 3
$P_m^{(old)}$	0.788	0.822	0.965
$P_m^{(new)}$	0.882 ± 0.002	0.836 ± 0.002	0.956 ± 0.001

Table 3.3: Summary of the new values of purity P_m used for the reconstruction of the weak value $\sigma_{x,w}$ for the first three experimental set-ups.

measurement strength θ . Unfortunately, the theoretical curves do not fit the experimental data if we use the value of the purity P_m determined previously by quantum state tomography. Because the reconstruction of the weak value is extremely sensitive on the values of the meter purity, it is inevitable to determine this purity by another method than quantum tomography. Therefore, we use the values of the measurement strength θ determined by tomography but apply a nonlinear regression on the data points to estimate the purity P_m by the best fit parameter. The latter step may be skipped if the meter is supposed in a pure initial state, as usually done in the literature. The new purity estimates given for a confidence interval of 95% are shown in table 3.3.

The values of the postselected angle for which the Heaviside step function H_{x_s-1} in equation (3.14) switches from 0 to 1, denoted by α_s , are identified by recording horizontally and vertically polarized photons in the meter path. The resulting coincidence counts ratio N_{23}/N_{13} reveals the values of x_s as a function of the postselected angle α . Each data point is obtained by 30 different 5 s measurements and, for a confidence interval of 99%. In figure 3.7.b, the gray, theoretical curves and the acquired data points for x_s agree strongly. Except for strengths approaching the range of weak measurements, as the strength θ_3 , a disagreement between experiment and theory is observed for values of x_s that are close or larger than one. Due to increasing experimental noise in this weak measurement range, a difference of $2 - 4^\circ$ between the theoretical and experimental values of the angle α_s is observed. The theoretical values of α_s are indicated in both figures by vertical, green lines. These pass necessarily through the maximal value of the visibility $V_{max} = (C_\theta C_{\theta+\pi})^{-\frac{1}{2}} P_m$ for the corresponding preparation. The position of this maximum α_s is determined by the meter parameters:

$$\alpha_s = \pm \arctan \left(\sqrt{\frac{C_{\theta+\pi}}{C_\theta}} \tan^{-1} \frac{\theta}{2} \right). \quad (3.41)$$

The range of parameter α , where the solution $|\sigma_{x,w}|_-$ is valid, increases with the weak-

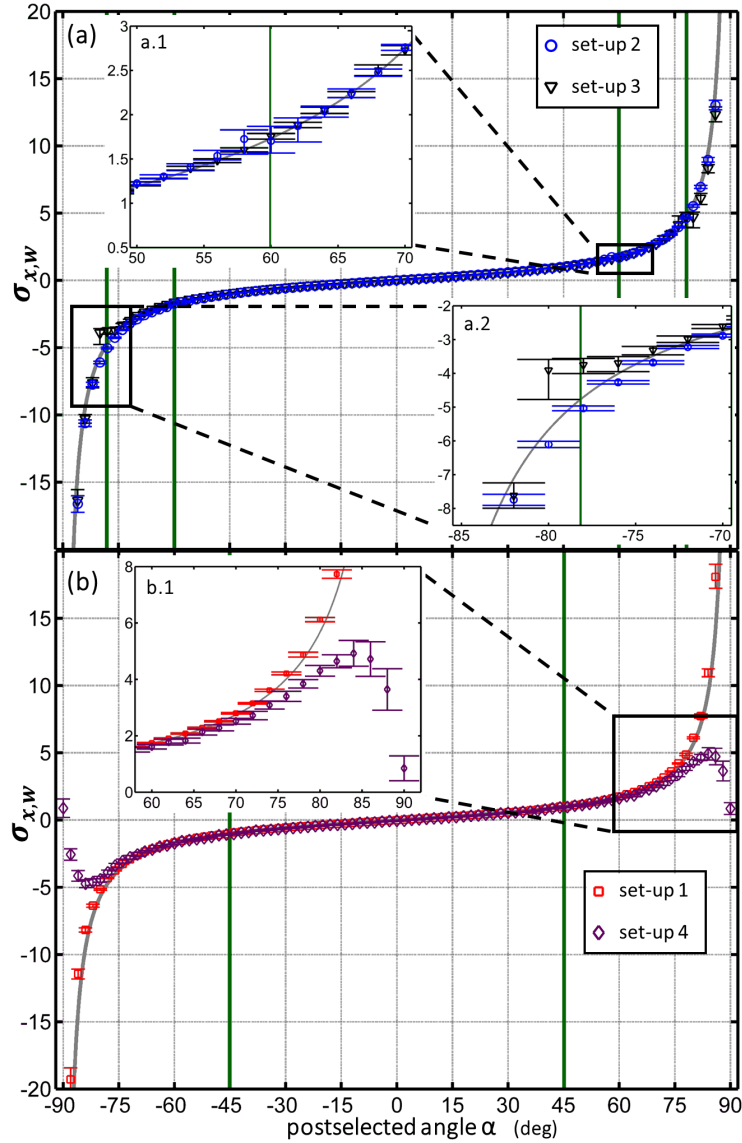


Figure 3.8: Weak values determined from phase and visibility measurement for the three strengths θ_1 (red squares), θ_2 (blue circles), and θ_3 (black triangles), and from the standard weak measurement technique (violet diamonds) using the strength θ_4 and the purity P_{4m} .

ness of the measurement strength. However, this range is limited by the meter purity P_m , which fixes its bounds at the values $\alpha_s^{\theta \rightarrow 0} = \pm \arctan\left(\sqrt{\frac{1+P_m}{1-P_m}}\right)$.

The full weak values reconstruction is shown in figure 3.8. For this purpose, we multiplied the weak values modulus resulting from the visibility data (figure 3.7) by the positive or negative sign determined during the visibility acquisition. The confidence

intervals are obtained by applying formula (3.14) on both extremes of the visibility error bars. They are asymmetric due to the non-linearity of (3.14) and contains the researched value with a probability of 99%. The gray, solid line represents the theoretical curve of the weak value $\sigma_{x,w}(\alpha) = \tan \alpha$, which remains the same for all preparations. To compare our method to the standard weak measurement technique, we use a fourth preparation. It has a meter purity of $P_{4m} = 0.982 \pm 0.001$ and a measurement strength of $\theta_4 = 0.025\pi$. It verifies the weak measurement conditions for a large range of the weak value $\sigma_{x,w}$. With these parameters, the weak measurement approximation breaks down around the values $\alpha_s \approx \pm 84.1^\circ$. The acquisition of the real part of the weak value $\Re \sigma_{x,w}$ is performed in the same measurement basis as the visibility, but without the phase adaption. The additional measurement in the right- and left-handed polarization basis is not performed since its imaginary part is zero for the chosen pre- and postselected ensemble. Each data point results from 49 different measurements, each repetition during 5 s and for a confidence interval of 99%.

The weak values using a strong, θ_2 , and a weaker, θ_3 , strength are compared in figure 3.8.a. Both preparations provide excellent agreement with the theoretical curve, except at the solution switch, where the accuracy of the set-up using weaker measurement strengths decreases (see insets a.1 and a.2). In figure 3.8.b, we compare our method to the standard weak measurement technique. For a small modulus of the weak value $\sigma_{x,w}$, both techniques provide results close to theoretical predictions. However, for large moduli, the weak measurement approximation completely breaks down (zoom b.1) for a wide range of postselected states approaching orthogonality to the preselected state. Weak measurement results are useless there and only our method works. The latter exhibits nevertheless some weaknesses in the reliability of the reconstructed values when the measurement strength and the meter purity are misestimated. Potential problems can be observed around the angle α_s , i.e. around the range of parameter α , where the Heaviside step function H_{x_s-1} switches from 0 to 1. For underestimated purities, for example, the obtained values of $|\sigma_{x,w}|$ become complex due to the square root in (3.14). A kind of plateau is formed. On the contrary, for overestimated purities, the resulting values of the solutions $|\sigma_{x,w}|_-$ and $|\sigma_{x,w}|_+$ do not continuously blend into each other. A gap appears between them. Because, in all three cases, the obtained estimations agree with theory, our implemented methods (the quantum state tomography technique for the measurement strength and the nonlinear fit for the purity) achieve correct values for the meter parameters.

3.3.4 Complex weak values: analysis of the quantum phase

In this section, we generalize our measurement protocol for complex weak values. We prepare four different quantum states with four different relative phases ϕ . Experimentally, a second z-cut quartz plate is introduced in the probe path followed by a half-wave plate and a polarizing beam-splitter. The relative phase in the postselected state $|\psi_f\rangle = \cos\alpha|H\rangle + e^{-i\phi}\sin\alpha|V\rangle$ is modified by tilting this quartz plate. In the following, we consider the four preparations given in table 3.4. This time, both parameters describing the initial meter state are deduced from a nonlinear regression applied on the weighted data points of the visibility. The resulting best fit parameters estimate P_m and θ with a confidence interval of 99.7%. All four preparations are close to the measurement strength $\theta = \pi/2$, which induces several simplifications in the calculation of the modulus $|\sigma_{x,w}|$. Hence, equation (3.16) can be approximated by (3.17):

$$\arctan |\sigma_{x,w}(\alpha, \phi)| \approx \begin{cases} \frac{1}{2} \arcsin(P_m^{-1}V), & \text{if } x_s \leq 1 \\ \frac{1}{2} [\pi - \arcsin(P_m^{-1}V)], & \text{if } x_s > 1, \end{cases} \quad (3.42)$$

In our case, the theoretical values of the bounded function become $\arctan |\sigma_{x,w}(\alpha, \phi)| = |\alpha|$. As previously, the visibility as well as the probability ratio x_s are recorded for an angle α varying from -90° to 90° by steps of 2° . Each acquisition includes 25 different measurements, each repetition during 5 s. The resulting data is then used to estimate the modulus $|\sigma_{x,w}|$ (figure 3.9.a-.b) and $\arctan |\sigma_{x,w}(\alpha, \phi)|$ (figure 3.9.c-.d) for a confidence level of 99.5%. All preparations provide excellent agreement with the theoretical, gray curve, except at the solution switch at $\alpha_s \approx \pm 45.9^\circ$ (green lines). Due to the finite values resulting from the function $\arctan(x)$, these potential disagreements are no longer masked by large scales generally chosen to represent large weak values. For set-up 1, we identify a small plateau of the estimations at $\alpha_s = 45.9^\circ$, and a small gap between them at $\alpha_s = -45.9^\circ$ (see figure 3.9.c). These effects result from experimental impurities due to the quartz plates and from small errors in the estimates

	set-up 1	set-up 2	set-up 3	set-up 4
P_m	0.777 ± 0.005	0.795 ± 0.007	0.804 ± 0.007	0.802 ± 0.006
θ	$0.488\pi \pm 0.004\pi$	$0.491\pi \pm 0.006\pi$	$0.483\pi \pm 0.006\pi$	$0.486\pi \pm 0.005\pi$
ϕ	0	$\pi/2$	$\pi/7$	$5\pi/9$

Table 3.4: Summary of the values of the purity P_m and of the measurement strength θ used for the reconstruction of the complex weak value $\sigma_{x,w}$.

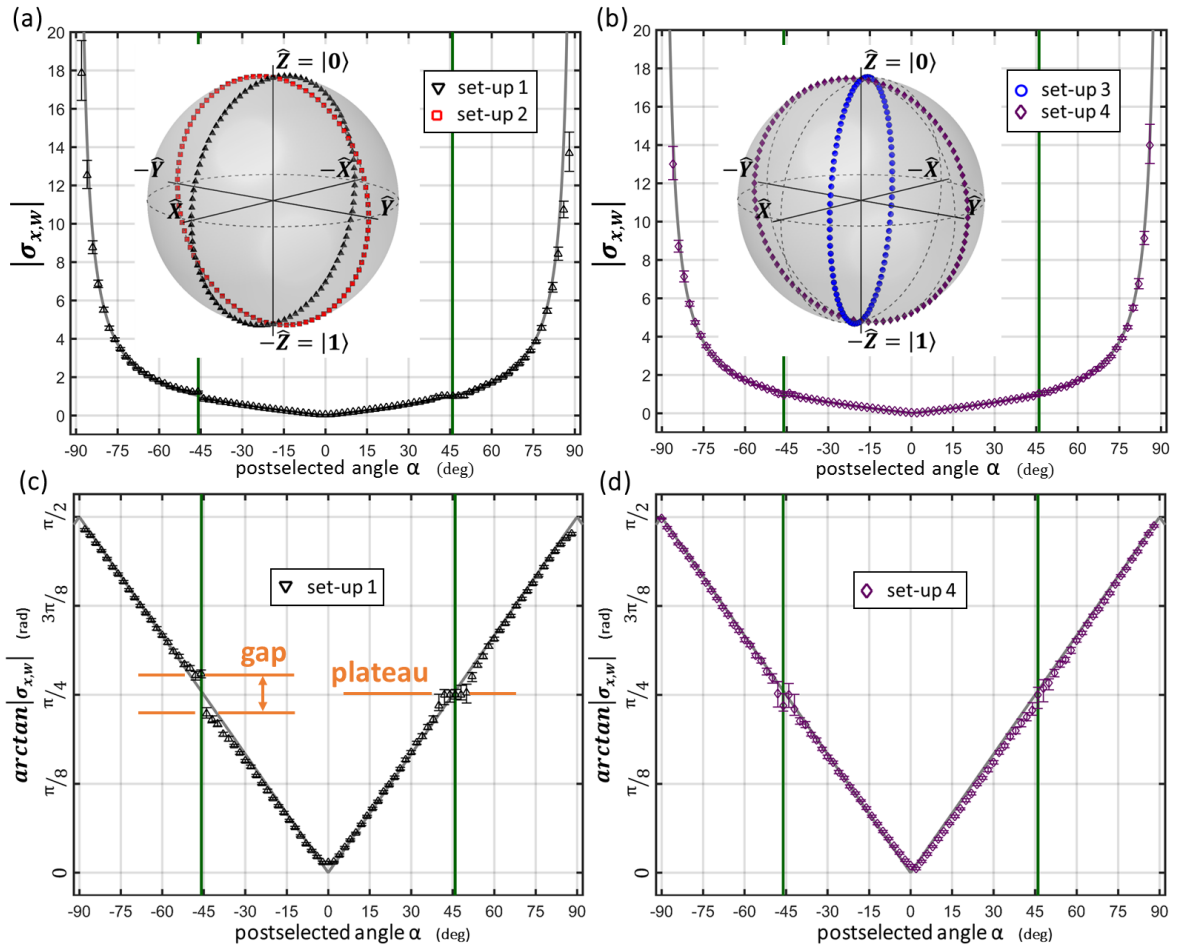


Figure 3.9: Modulus of complex weak values. (a-b) The unbounded modulus $|\sigma_{x,w}(\alpha, \phi)|$ determined from the visibility and the phase measurements for the relative phases $\phi_1 = 0$ and $\phi_4 = 5\pi/9$. All chosen postselected states with different relative phases are represented on the Bloch spheres. (c-d) The corresponding bounded values of $\arctan|\sigma_{x,w}(\alpha, \phi)|$ are represented. Potential disagreements between theory and experiment are no longer masked by large scales. A better evaluation of the estimates is possible.

of the meter parameters¹³. A variation of this parameters during the acquisition cannot be excluded. In practice, the collection of all data requires more than four days for each preparation. Unfortunately, during this period, the laser source was turned off several times. It is therefore possible that some parameters of the laser beam, such as its spatial and temporal profile, were slightly modified. These effects have direct consequences on the values of meter parameters. In figure 3.9.c, the small gap around $\alpha_s = -45.9^\circ$

¹³In the main text only the figures showing $\arctan|\sigma_{x,w}(\alpha, \phi)|$ for set-up 1 and 3 are illustrated and analysed. Similar results arise for set-up 2 and 3. The missing figures are found in Appendix G.

corresponds to a slightly overestimated meter purity. In contrast, the plateau with constant values around $\alpha_s = 45.9^\circ$ is induced by a small underestimation of this purity. However, these reconstruction disagreements are so small that they have no significance for values spaced by 4° from the green vertical lines. Similar conclusions can be reached for the other two preparations shown in Appendix G.

Figure 3.10 summarizes the experimental results of the weak values argument measurement. Each data point represents the estimate of $\arg \sigma_{x,w}$ for a confidence interval of 99.7%. Whenever the weak value changes its sign, here at $\alpha = \{-90^\circ, 0^\circ, 90^\circ\}$, its argument jumps discontinuously by a value of π . Experimentally, rapid variations of the data points are observed for all acquisitions. Due to experimental errors, these data points rounds slightly up the theoretical, gray curves. The large confidence intervals of the data around these phase jumps are a direct consequence of disappearing interference. In fact, the postselection of horizontally and vertically polarized photons destroy completely the interfering pathways. For both polarizations, a variation of the interferometric phase ξ (introduced by the quartz plate in the meter path) has no longer an effect on the coincidence counts. The determination of the phase corresponding to the maximum of coincidence counts is theoretically impossible. As a result, estimates with high incertitude are deduced from the measurements. The impact of the meter acquisition system on the readout of the argument $\arg \sigma_{x,w}$ is evaluated in figure 3.10.a. In fact, for the first preparation with a relative phase of $\phi = 0$, no quartz plate is introduced in the probe path, so that the difference between the theoretical and experimental values of the argument results from the meter detection system, and, in particular, from small misalignments of the meter quartz plate. This meter influence on the argument readout causes two different evolutions of the weak values argument. On the one hand, for set-ups 1 and 3, the phase-jumps induce, each time, a subtraction of π , so that the data-set looks like the step function. On the other hand, for set-ups 2 and 4, the experimental outcomes form a signature like a square wave. To evaluate these different behaviors, we still have to wait for the geometric description of weak and modular values, which will be elaborated in the next chapter. Using this description, we will study the weak and modular values argument by spherical quadrangles on the Bloch sphere.

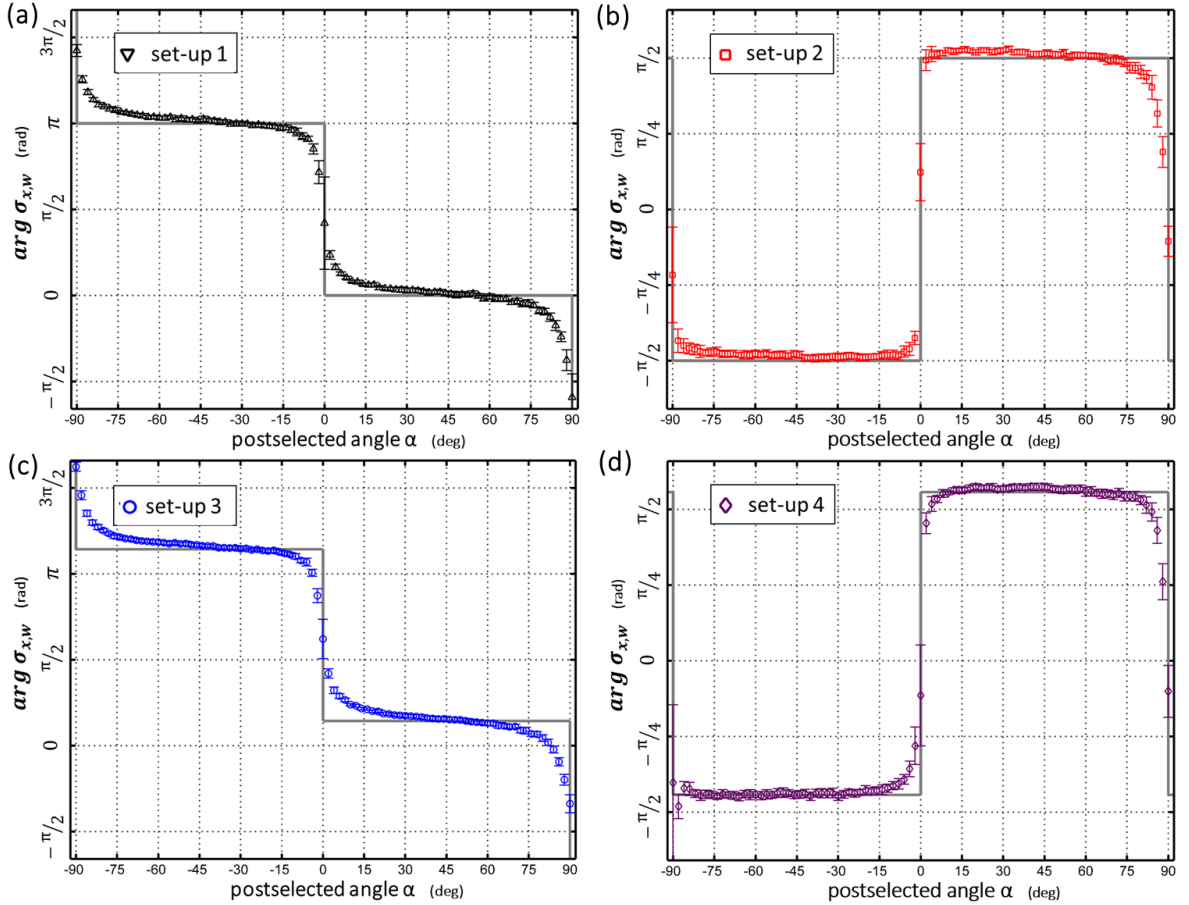


Figure 3.10: Argument of complex weak values. The values of $\arg \sigma_{x,w}$ determined from a nonlinear regression during the visibility measurement for the relative phases (a) $\phi_1 = 0$, (b) $\phi_2 = \pi/2$, (c) $\phi_3 = \pi/7$ and (d) $\phi_4 = 5\pi/9$. For all set-ups, the argument outcomes jump discontinuously by π around the values $\alpha = \{-90^\circ, 0^\circ, 90^\circ\}$. Experimentally, we observed two types of acquisitions: for set-ups 1 and 3, the argument decreases each time by a value of π (like a step function), and for set-ups 2 and 4, the argument changes alternately by the values $-\pi$ and $+\pi$ (like a square function).

3.4 Summary

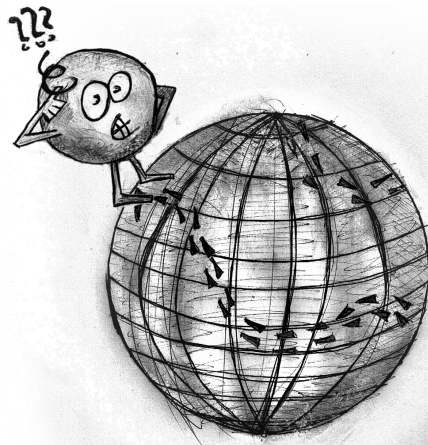
In this chapter, we presented a quantum eraser procedure exploiting a qubit meter to measure directly the modulus and the argument of complex modular and weak values for arbitrary measurement strengths. The derived relations between the meter and probe were particularly useful in the case of the intermediate measurement strength $\theta = \pi/2$. Our measurement procedure provided us with deeper insight into the physics of weak and modular values, beyond the association of their real and imaginary part

to meter shifts. In fact, the interferometric visibility revealing the modulus of modular values plays the same role than the pointer shift in standard weak measurements. The connection between modular and weak values allowed us to investigate directly weak values of qubit systems in their polar representation by performing a one-step visibility and phase measurement. Our measurement protocol improved the signal-to-noise ratio (SNR) with respect to the standard weak measurement technique. Experimentally, this interferometric protocol was demonstrated using polarization-entangled photon pairs produced by type-I spontaneous parametric down-conversion. By performing firstly the calibration of the meter detection system, the visibility and phase measuring results determined finally the complex weak value $\sigma_{x,w}$. Thereby, we put a special focus on the unbounded and complex characteristics of weak values. In practice, the developed measuring protocol does not suffer from the limitations of the standard weak measurement technique for large weak values. It is thus applicable for both weak and strong measurement conditions. This opens the way to exploiting with greater accuracy the measure of weak values, particularly for nearly orthogonal pre- and postselected states. Moreover, we studied experimentally the discontinuous behavior of the quantum phase around the sign flips of weak values. The experimental data is in full agreement with theory, but it features small deviations from theory. These disagreements result from experimental errors which influence directly the argument readouts. Further analysis related to these readouts will be presented after the introduction of the geometric description of weak and modular values in the next chapter.

4

Geometric representation of weak and modular values of discrete quantum systems

In this chapter, we will explore the polar representation of weak and modular values in discrete quantum systems of arbitrary dimensions. We will first express the modulus and the argument of weak and modular values of qubit observables in terms of vectors on the Bloch sphere to provide a purely geometric description of these values. For higher-dimensional N -level systems, we will use the Majorana representation to describe their states by symmetric states of $N - 1$ qubits. Then, we will proceed with demonstrating that an arbitrary weak or modular value of three-dimensional discrete quantum systems can be deduced from geometric quantities defined on the Bloch sphere. In particular, we will find that both the modulus and the argument can be factored in two contributions, each connected to our results on qubit observables. Finally, we will generalize our results to higher-dimensional systems.



4.1 Bloch vector representation of modular and weak values

In quantum information, qubit states are generally studied by the application of the Pauli observable $\hat{\sigma}_r = \vec{r} \cdot \vec{\sigma}$, with $\vec{\sigma} = (\hat{\sigma}_x, \hat{\sigma}_y, \hat{\sigma}_z)$ and the unit vector $\vec{r} \in \mathbb{R}^3$. Thus, it is not surprising that the weak value of this operator possess a representation in terms of pre- and postselected vectors \vec{i}, \vec{f} on the Bloch sphere [42]:

$$\sigma_{r,w} = \frac{\langle \psi_f | \hat{\sigma}_r | \psi_i \rangle}{\langle \psi_f | \psi_i \rangle} = \frac{\vec{f} \cdot \vec{r} + \vec{r} \cdot \vec{i} + j \left[\vec{f} \cdot (\vec{r} \times \vec{i}) \right]}{1 + \vec{f} \cdot \vec{i}}, \quad (4.1)$$

where j is the imaginary unit. This expression gives the real and the imaginary parts of the weak value in a natural matter. However, in the previous chapter, we described (theoretically and experimentally) an interferometric procedure that measures the polar components of complex weak and modular values instead of the usually determined real or imaginary parts. In order to complete this Bloch vector representation of weak and modular values, we will in the following derive expressions in terms of Bloch vectors for their polar components. These expressions will provide us with deeper insight into the physics of weak and modular values, beyond the association of their real and imaginary part to meter shifts. In particular, we will see that the argument depends on an enclosed area on the Bloch sphere surface accumulated during the evolution from the initial pre- to the final postselected state. Thus, this argument has a topological origin, similar to the Pancharatnam geometric phase [31]. This purely geometric approach to the description of the quantum phase is useful to understand rapid displacements of interference fringes in quantum eraser experiments [32, 33]. Furthermore, it explains prior observations involving discontinuous phase jumps, such as the π -phase jump in cross-phase modulation [34], as well as discontinuities around phase singularities [35].

Most weak measurement studies target the simplest non-trivial Hilbert space, of dimension two. Three-level or higher-dimensional discrete quantum systems have rarely been studied using the weak measurement formalism [24–26]. A geometric representation of weak and modular values of their observables is lacking. A first approach to express the argument of the weak value of three-level quantum systems by real vectors was indirectly demonstrated in reference [36]. In fact, the authors derived a vector relation of a quantity known as the Bargmann invariant, which is related to the argument of weak

values of projection operators. Because the algebraic structure describing three-level quantum states is much more complex than the structure of two-level systems, this relation for the geometric phase involves 8-dimensional vectors as well as unusual symmetric and antisymmetric two-vector products. Tamate et al. [37] pointed out that the geometric phase of this Bargmann invariant of three- and higher-level quantum systems can simply be represented by spherical triangles on the Bloch sphere. In order to show this, they represented the states of the N -level system in terms of symmetric states of $N - 1$ qubits, an interesting representation, known as the Majorana representation, which was introduced by Majorana in 1932 [90]. Both works [36, 37] are pioneering research results for the geometric representation of weak and modular values of two- and high-level quantum systems as we will see in the next sections. Recent applications of weak measurement theory in the context quantum computation research attest the interest of investigating weak values of high-level systems [27, 28]. Weak values of qutrit observables show their usefulness in the experimental demonstration of the Kochen-Specker test of noncontextuality [29] and can be applied to the quantum Cheshire cat experiment [30]. For these reasons, we will study the geometry of weak and modular values of three- and N -level systems in addition of the more simple two-level qubit systems.

4.2 Geometrical representation of modular and weak values of two-level quantum systems

4.2.1 Weak value of projectors

We start our developments by considering the two-level projection operator $\hat{\Pi}_r$ on the qubit state $|\phi_r\rangle$. This state is identified by the unit vector $\vec{r} \in \mathbb{R}^3$ on the Bloch sphere. We consider an initial, preselected state $|\phi_i\rangle$ and a final, postselected state $|\phi_f\rangle$, defined by the unit vectors \vec{i} and \vec{f} , respectively. The weak value $\Pi_{r,w}$ of the projector equals

then (the complete demonstration is found in Appendix H.2):

$$\begin{aligned}\Pi_{r,w} &= \frac{\langle\phi_f|\phi_r\rangle\langle\phi_r|\phi_i\rangle}{\langle\phi_f|\phi_i\rangle} \\ &= \frac{1}{2} \frac{1 + \vec{r} \cdot \vec{f} + \vec{r} \cdot \vec{i} + \vec{f} \cdot \vec{i} + j \left[\vec{f} \cdot (\vec{r} \times \vec{i}) \right]}{(1 + \vec{i} \cdot \vec{f})},\end{aligned}\quad (4.2)$$

where j is the imaginary unit. In the following, the complex weak value $\Pi_{r,w}$ is represented in its polar form, i.e. by its modulus and its argument. The resulting modulus $|\Pi_{r,w}|$ is given by:

$$|\Pi_{r,w}| = \sqrt{\frac{1}{2} \frac{(1 + \vec{f} \cdot \vec{r})(1 + \vec{r} \cdot \vec{i})}{(1 + \vec{f} \cdot \vec{i})}},\quad (4.3)$$

which is directly related to projection probabilities between the three qubit states. This is an obvious consequence of the definition of the weak value of a projector, which involves three bra-ket inner products. The modulus expression is quickly deduced from the correspondance linking the bra-ket inner product and the scalar product between Bloch vectors:

$$|\langle\phi_u|\phi_v\rangle| = \sqrt{\frac{1}{2}(1 + \vec{u} \cdot \vec{v})},\quad (4.4)$$

as shown in Appendix H.1. The argument of the weak value $\Pi_{r,w}$ is given by:

$$\begin{aligned}\arg \Pi_{r,w} &\stackrel{(a)}{=} \arctan \frac{\Im \langle\phi_f|\hat{\Pi}_r|\phi_i\rangle\langle\phi_f|\phi_i\rangle}{\Re \langle\phi_f|\hat{\Pi}_r|\phi_i\rangle\langle\phi_f|\phi_i\rangle} \\ &\stackrel{(b)}{=} \arctan \frac{\vec{f} \cdot (\vec{r} \times \vec{i})}{1 + \vec{f} \cdot \vec{r} + \vec{r} \cdot \vec{i} + \vec{f} \cdot \vec{i}} \\ &\stackrel{(c)}{=} -\frac{\Omega_{irf}}{2}.\end{aligned}\quad (4.5)$$

Equality (a) results directly from the definition of the weak value $\Pi_{r,w}$, (b) from equation (4.2) and (c) is deduced from [91]. Ω_{irf} is the oriented solid angle subtended at the center of the Bloch sphere by the geodesic triangle defined by the three vertices \vec{i} , \vec{r} and \vec{f} , as shown in figure 4.1.a. The geodesic orientation is determined by the sequence of states $|\phi_i\rangle \rightarrow |\phi_r\rangle \rightarrow |\phi_f\rangle \rightarrow |\phi_i\rangle$. The argument of $\Pi_{r,w}$ is the same as the quantum phase of the projections $\langle\phi_i|\phi_f\rangle\langle\phi_f|\phi_r\rangle\langle\phi_r|\phi_i\rangle$, which is known as the three-vertex Bargmann invariant [68]. Introduced by Bargmann for studying the difference between unitary and anti-unitary transformation, the quantity $\left(\prod_{k=1}^{N-1}\langle\phi_k|\phi_{k+1}\rangle\right)\langle\phi_N|\phi_1\rangle$ is invariant under gauge transformation and reparameterization. Mukunda and Simon showed by their kinematic approach [92] that the argument of the Bargmann invariant is related

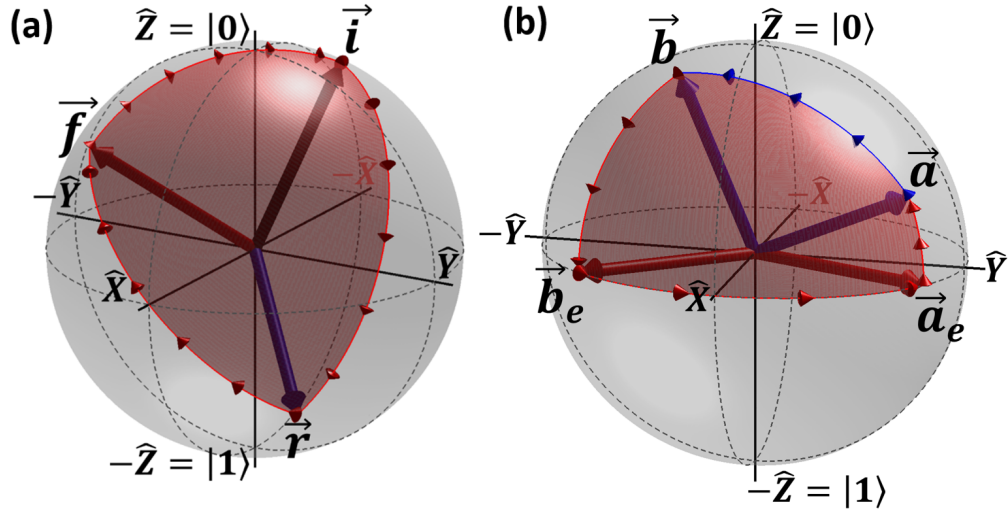


Figure 4.1: Solid angle representation on the Bloch sphere. (a) The red solid angle Ω_{irf} of the clockwise sequence of states $|\phi_i\rangle \rightarrow |\phi_r\rangle \rightarrow |\phi_f\rangle \rightarrow |\phi_i\rangle$ (with negative sign) is directly proportional to the argument of the weak value $\Pi_{r,w}$. (b) The solid angle $\Omega_{abb_e a_e}$ of the four vertices \vec{a} , \vec{b} , \vec{b}_e and \vec{a}_e represented in the Bloch sphere (the red surface). The states $|a_e\rangle$ and $|b_e\rangle$ lying on the equator are horizontal lifts of the associated states $|a\rangle$ and $|b\rangle$, respectively. The solid angle of the counterclockwise sequence of states $|a\rangle \rightarrow |b\rangle \rightarrow |b_e\rangle \rightarrow |a_e\rangle \rightarrow |a\rangle$ is related to the Pancharatnam connection $\arg \langle b|a\rangle$.

to the geometric phase $\gamma(C_0)$ [31,93] acquired on a closed loop C_0 on the Bloch sphere. The weak value of projectors is thus invariant under gauge transformations.

The geometric phase attracted a special interest in quantum mechanics following the publication of Berry in 1984 [93]. Berry studied quantum systems undergoing a cyclic, unitary evolution under the action of a time-dependent Hamiltonian. This evolution was supposed to be adiabatic, i.e. the physical system remains in its instantaneous eigenstate during the whole temporal evolution. At that time, it was assumed that after a complete cycle the quantum state acquires a dynamical phase with no physical meaning: this phase can always be eliminated by applying a gauge transformation on the quantum state, $|\psi\rangle \rightarrow e^{j\beta}|\psi\rangle$. However, Berry pointed out the accumulation of an additional phase, known as the geometric phase or the Pancharatnam–Berry phase, which remains under gauge transformations. Its origin is topological, i.e. it depends on the path that the quantum state traced out in the parameter space of the time-dependent Hamiltonian. Berry’s formulation is often associated to spin-1/2 systems evolving under the action of a slowly varying magnetic field. Applications can be also

found in the case of other two-level systems, such as the polarization of light. The first experimental test of Berry's geometric phase was done using polarized, classical light in 1986 [94]. In fact, similar observations with polarized light were first described by Pancharatnam in 1956 [31]. He discovered that the interference of two polarized light beams gives rise to a geometric phase. The latter is determined by the evolution in the space of polarization states. Interestingly, Pancharatnam's approach showed that Berry's assumption of cyclic, adiabatic and unitary evolutions are unnecessary conditions to acquire a geometric phase. This fact was clarified by several authors after Berry's discovery [95, 96]. Some years later Simon and Mukunda developed a general theory of the geometric phase in quantum mechanics, the kinematic approach [92]. They discovered that the gauge and reparametrization invariant geometric phase can be naturally associated with any smooth open curve of unit vectors in Hilbert space. The roles of geodesics and the Bargmann invariants emerge naturally in their kinematic approach.

4.2.2 Modular value

Now, we evaluate modular values in terms of vectors on the Bloch sphere. We consider an arbitrary unitary operator of a two-level system and relate it to the Pauli matrices by:

$$\hat{U}_{\sigma_r}^{\alpha,\beta} = e^{j\frac{\beta}{2}} e^{-j\frac{\alpha}{2}\hat{\sigma}_r}, \quad (4.6)$$

where α, β are real parameters and where by definition $\hat{\sigma}_r = \vec{r} \cdot \vec{\sigma} = r_x \hat{\sigma}_x + r_y \hat{\sigma}_y + r_z \hat{\sigma}_z$. Physically, the normalized vector \vec{r} on the Bloch sphere is equivalent to the direction of a spin measurement. The first component of the unitary operator applies a global $\frac{1}{2}\beta$ -phase shift. The second component rotates all vectors on the Bloch sphere by an angle α around the \vec{r} -axis (in the Hilbert state space representation of the qubit, the rotation angle is $\frac{1}{2}\alpha$). Its modular value $\sigma_{r,m}^{\alpha,\beta}$ is thus equal to (the complete demonstration is found in Appendix H.3):

$$\begin{aligned} \sigma_{r,m}^{\alpha,\beta} &= e^{j\frac{\beta}{2}} \frac{\langle \phi_f | e^{-j\frac{\alpha}{2}\hat{\sigma}_r} | \phi_i \rangle}{\langle \phi_f | \phi_i \rangle} \\ &= e^{j\frac{\beta}{2}} \frac{\cos \frac{\alpha}{2} (1 + \vec{f} \cdot \vec{i}) + \sin \frac{\alpha}{2} \left[\vec{f} \cdot (\vec{r} \times \vec{i}) - j (\vec{r} \cdot \vec{i} + \vec{f} \cdot \vec{r}) \right]}{1 + \vec{f} \cdot \vec{i}}. \end{aligned} \quad (4.7)$$

We define the state $|\phi_S\rangle = e^{-j\frac{\alpha}{2}\hat{\sigma}_r}|\phi_i\rangle$, which results from applying the rotation operator to the initial, preselected state. After rotating the initial vector \vec{i} around the \vec{r} -axis by the angle α , we obtain the vector \vec{s} characterizing $|\phi_S\rangle$ on the Bloch sphere. It is given by Rodrigue's rotation formula:

$$\vec{s} = \cos \alpha \vec{i} + \vec{r} \cdot \vec{i} (1 - \cos \alpha) \vec{r} + \sin \alpha \vec{r} \times \vec{i}. \quad (4.8)$$

We deduce immediately the modulus of the modular value $|\sigma_{r,m}^{\alpha,\beta}| = |\langle\phi_f|\phi_S\rangle\langle\phi_f|\phi_i\rangle^{-1}|$ from the correspondance (4.4) linking the inner product in Hilbert space to the scalar product between Bloch vectors:

$$|\sigma_{r,m}^{\alpha,\beta}| = \sqrt{\frac{1 + \vec{f} \cdot \vec{s}}{1 + \vec{f} \cdot \vec{i}}}. \quad (4.9)$$

During its rotation around the \vec{r} -axis, the trajectory of the initial vector \vec{i} follows a non-geodesic open arc on the Bloch sphere [97], contrary to the projector case (which involved solely geodesic arcs). Consequently, the rotated state $|\phi_S\rangle$ is no longer in phase with the initial state $|\phi_i\rangle$, i.e. $\arg\langle\phi_S|\phi_i\rangle \neq 0$. The argument of the modular value is therefore evaluated by the following reasoning. We express the resulting state as $|\phi_S\rangle = e^{j\varphi_{i \rightarrow s}}|\phi_s\rangle$, where the phase $\varphi_{i \rightarrow s}$ is due to the non-geodesic movement of $|\phi_i\rangle$ to the output state $|\phi_S\rangle$. The state $|\phi_s\rangle$ corresponds to the state $|\phi_S\rangle$ written in its canonical form, i.e. without the global phase factor $\varphi_{i \rightarrow s}$ that it may have acquired under the unitary transformation. This total phase $\varphi_{i \rightarrow s}$ is determined by projecting $|\phi_S\rangle$ onto one of the orthogonal eigenvectors $|\phi_r\rangle$ and $|\phi_{-r}\rangle$ of the unitary operator $e^{-j\frac{\alpha}{2}\hat{\sigma}_r}$:

$$e^{-j\frac{\alpha}{2}\hat{\sigma}_r} = e^{-j\frac{\alpha}{2}}|\phi_r\rangle\langle\phi_r| + e^{j\frac{\alpha}{2}}|\phi_{-r}\rangle\langle\phi_{-r}|. \quad (4.10)$$

The projection of $|\phi_S\rangle$ onto the eigenvector $|\phi_r\rangle$ yields the following two equalities:

$$\langle\phi_r|\phi_S\rangle = e^{j\varphi_{i \rightarrow s}}\langle\phi_r|\phi_s\rangle = e^{-j\frac{\alpha}{2}}\langle\phi_r|\phi_i\rangle. \quad (4.11)$$

The moduli $|\langle\phi_r|\phi_i\rangle| = |\langle\phi_r|\phi_s\rangle|$ are equal as shown by taking the modulus of (4.11). This is a result of the unitary character of the operator $e^{-j\frac{\alpha}{2}\hat{\sigma}_r}$. This can also be seen on the Bloch sphere: as \vec{s} results from the rotation of \vec{i} around \vec{r} , the projection of \vec{i} and \vec{s} on \vec{r} remain constant for any α . Consequently, the accumulated total phase $\varphi_{i \rightarrow s}$ of the open loop $|\phi_i\rangle \rightarrow |\phi_S\rangle$ is given by:

$$\varphi_{i \rightarrow s} = -\frac{\alpha}{2} + \arg\langle\phi_r|\phi_i\rangle - \arg\langle\phi_r|\phi_s\rangle. \quad (4.12)$$

The quantity $\arg\langle b|a\rangle$ relating two arbitrary states $|a\rangle$ and $|b\rangle$ is known as Pancharatnam connection. In practice, $\arg\langle b|a\rangle$ is determined by calculating the spherical quad-

range $\Omega_{abb_e a_e}$ on the Bloch sphere (see figure 4.1.b), where the supplemental vertices \vec{a}_e and \vec{b}_e are vectors lying on the equator [97]. To understand how they are determined, we must express their position in the spherical coordinate system. By convention, η corresponds to the azimuth angle and θ to the polar angle. In this representation, a pure state $|a\rangle$ expressed by:

$$|a\rangle = |\eta, \theta\rangle = \cos \frac{\theta}{2} e^{-j\frac{\eta}{2}} |0\rangle + \sin \frac{\theta}{2} e^{j\frac{\eta}{2}} |1\rangle, \quad (4.13)$$

is defined on the Bloch sphere by the vector \vec{a} :

$$\vec{a}(\theta, \eta) = \begin{pmatrix} \cos \eta \sin \theta \\ \sin \eta \sin \theta \\ \cos \theta \end{pmatrix}. \quad (4.14)$$

Thus, the Pancharatnam connection is given by:

$$\arg\langle b|a\rangle = -\arctan \left(\tan \left(\frac{\eta_a - \eta_b}{2} \right) \frac{\cos \left(\frac{\theta_a + \theta_b}{2} \right)}{\cos \left(\frac{\theta_a - \theta_b}{2} \right)} \right). \quad (4.15)$$

The connection is in phase, i.e. $\arg\langle b|a\rangle = 0$, for transports with the same azimuth angles η and for transformations happening around the equator of the Bloch sphere¹, i.e. for the polar angle $\theta = \pi/2$. These two kinds of transports are known as horizontal lifts along the geodesic connecting the states $|a\rangle$ and $|b\rangle$ on the Bloch sphere. The states $|a_e\rangle = |\eta_a, \frac{\pi}{2}\rangle$ and $|b_e\rangle = |\eta_b, \frac{\pi}{2}\rangle$ are fixed with the same azimuth angle as $|a\rangle$ and $|b\rangle$, respectively, and with a polar angle $\theta = \pi/2$. The closed loop $|a\rangle \rightarrow |b\rangle \rightarrow |b_e\rangle \rightarrow |a_e\rangle \rightarrow |a\rangle$ along the geodesic arcs determines the spherical quadrangle $\Omega_{abb_e a_e}$, which is equivalent to $\arg\langle b|a\rangle$:

$$\begin{aligned} \arg\langle b|a\rangle &= \arg\langle a|a_e\rangle + \arg\langle a_e|b_e\rangle + \arg\langle b_e|b\rangle + \arg\langle b|a\rangle \\ &= \arg(\langle a|a_e\rangle\langle a_e|b_e\rangle\langle b_e|b\rangle\langle b|a\rangle) \\ &= -\frac{\Omega_{abb_e a_e}}{2}. \end{aligned} \quad (4.16)$$

Note that the sign present in front of the solid angle for a given sequence of states is positive when the sequence is followed anti-clockwise and is negative when the sequence is followed clockwise. The sign of the solid angle changes when the sequence of projections is inversed, $\Omega_{a \rightarrow b} = -\Omega_{b \rightarrow a}$. It is possible to express a solid angle linking three

¹The Pancharatnam connection $\arg\langle b|a\rangle$ is zero for states with a polar angle of $\theta = \pi/2$ because of a particular global phase chosen in the definition of the qubit state (4.13). Since the final relation (4.20) is invariant under gauge transformations, this choice of the global phase has no impact on the result.

vertices as a sum of three spherical quadrangles [97]:

$$\Omega_{abc} = \Omega_{abb_e a_e} + \Omega_{bcc_e b_e} + \Omega_{caa_e c_e} , \quad (4.17)$$

where each spherical quadrangle contains two vertices of the initial solid angle. We use the decomposition property of equation (4.17) to rewrite the expression giving $\varphi_{i \rightarrow s}$ according to:

$$\varphi_{i \rightarrow s} = -\frac{\alpha}{2} - \frac{\Omega_{irs} + \Omega_{iss_e i_e}}{2} , \quad (4.18)$$

where we made use of relation (4.16) to express the connexions appearing in (4.12). Following the indices may be tedious but, essentially, equations (4.12) and (4.16) show together that the expression of the phase $\varphi_{i \rightarrow s}$ includes a sum of two spherical quadrangles; then we used relation (4.17) to express the sum of these two spherical quadrangles as a function of the third spherical quadrangle and of the spherical triangle appearing in equation (4.17). Expression (4.18) points out that the non-geodesic phase $\varphi_{i \rightarrow s}$ is the sum of the geometric phase of the closed loop $|\phi_i\rangle \rightarrow |\phi_r\rangle \rightarrow |\phi_s\rangle \rightarrow |\phi_i\rangle$ (first term) and the phase of the Pancharatnam connection $|\phi_i\rangle \rightarrow |\phi_s\rangle$ (second term). Using the last results, the argument of the weak value of the unitary operator $e^{-j\frac{\alpha}{2}\hat{\sigma}_r}$ is:

$$\begin{aligned} \arg \frac{\langle \phi_f | e^{-j\frac{\alpha}{2}\hat{\sigma}_r} | \phi_i \rangle}{\langle \phi_f | \phi_i \rangle} &\stackrel{(a)}{=} \arg \left(e^{j\varphi_{i \rightarrow s}} \frac{\langle \phi_f | \phi_s \rangle}{\langle \phi_f | \phi_i \rangle} \right) \\ &\stackrel{(b)}{=} \arg \left(\frac{|\langle \phi_f | \phi_s \rangle|}{|\langle \phi_f | \phi_i \rangle|} e^{j\varphi_{i \rightarrow s}} e^{-j\frac{\Omega_{sffe s_e}}{2}} e^{-j\frac{\Omega_{fii_e f_e}}{2}} \right) \\ &\stackrel{(c)}{=} \varphi_{i \rightarrow s} - \frac{\Omega_{sffe s_e} + \Omega_{fii_e f_e}}{2} \\ &\stackrel{(d)}{=} \varphi_{i \rightarrow s} - \frac{\Omega_{isf} - \Omega_{iss_e i_e}}{2} \\ &\stackrel{(e)}{=} -\frac{\alpha}{2} - \frac{\Omega_{irs}}{2} - \frac{\Omega_{iss_e i_e}}{2} - \frac{\Omega_{isf}}{2} + \frac{\Omega_{iss_e i_e}}{2} \\ &\stackrel{(f)}{=} -\frac{\alpha}{2} - \frac{\Omega_{irs}}{2} - \frac{\Omega_{isf}}{2} \\ &\stackrel{(g)}{=} -\frac{\alpha}{2} - \frac{\Omega_{irsf}}{2} . \end{aligned} \quad (4.19)$$

Equality (a) results from the definition of the states $|S\rangle$ and $|s\rangle$. (b) expresses the Pancharatnam connexions in terms of solid angles using equation (4.16). (c) takes the argument of the previous expression. (d) exploits the decomposition property of relation (4.17). (e) follows from the expression of $\varphi_{i \rightarrow s}$ in (4.18). (f) is due to canceling terms. (g) combines the two spherical triangles in one spherical quadrangle (as the paths $i \rightarrow s$ and $s \rightarrow i$ present in the triangles cancel each other). Finally, the expression of the

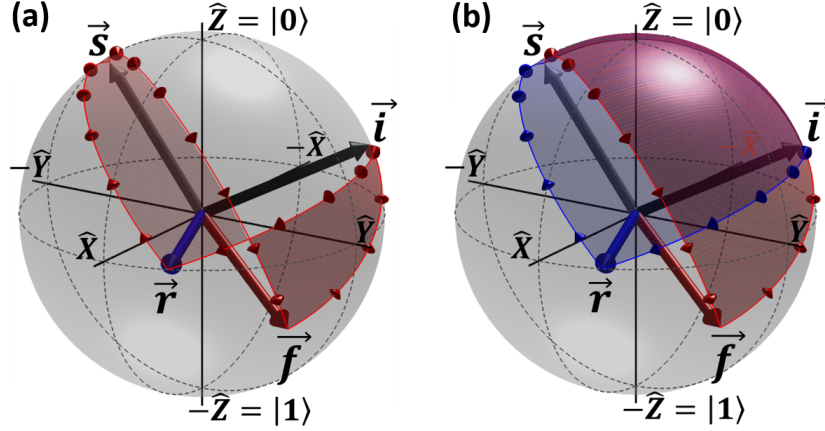


Figure 4.2: Spherical quadrangle representation on the Bloch sphere. (a) The geometric component of the argument of the modular value $\sigma_{r,w}$ is related to the spherical quadrangle Ω_{irsf} , which can be written in form of two solid angles (b) depending on the clockwise sequence $|\phi_i\rangle \rightarrow |\phi_r\rangle \rightarrow |\phi_s\rangle \rightarrow |\phi_i\rangle$ due the application of $\hat{\sigma}_r$ and on the anti-clockwise sequence $|\phi_i\rangle \rightarrow |\phi_s\rangle \rightarrow |\phi_f\rangle \rightarrow |\phi_i\rangle$ due the postselection of $|\phi_f\rangle$.

accumulated phase in terms of a solid angle is:

$$\arg \sigma_{r,m}^{\alpha,\beta} = \arg \left(e^{j\frac{\beta}{2}} \frac{\langle \phi_f | e^{-j\frac{\alpha}{2} \hat{\sigma}_r} | \phi_i \rangle}{\langle \phi_f | \phi_i \rangle} \right) = \frac{\beta - \alpha}{2} - \frac{\Omega_{irsf}}{2}. \quad (4.20)$$

The argument contains a dynamical contribution that depends on the parameters α and β , and a geometric phase $-\frac{1}{2}\Omega_{irsf}$ that depends solely on vectors defined on the Bloch sphere. The dynamical contribution can vanish by choosing β equal to α . The geometric phase Ω_{irsf} depends on the oriented spherical quadrangle delimited by the four vectors \vec{i} , \vec{r} , \vec{s} and \vec{f} on the Bloch sphere, as depicted on figure 4.2.a. The orientation is defined by the corresponding sequence of states $|\phi_i\rangle \rightarrow |\phi_r\rangle \rightarrow |\phi_s\rangle \rightarrow |\phi_f\rangle \rightarrow |\phi_i\rangle$. As illustrated on figure 4.2.b, the oriented spherical quadrangle $i \rightarrow r \rightarrow s \rightarrow f \rightarrow i$ can be written using the two oriented spherical triangles $i \rightarrow r \rightarrow s \rightarrow i$ (blue curve) and $i \rightarrow s \rightarrow f \rightarrow i$ (red curve), as the paths $i \rightarrow s$ and $s \rightarrow i$ present in these triangles cancel each other. The solid angles that they subtend at the center of the Bloch sphere are thus related by:

$$\Omega_{irsf} = \Omega_{irs} + \Omega_{isf}, \quad (4.21)$$

The sequence of states associated to the solid angle Ω_{irs} arises from the application of the operator $e^{-j\frac{\alpha}{2}\hat{\sigma}_r}$, while the solid angle Ω_{isf} is associated to the postselection of $|\phi_f\rangle$. Thanks to this decomposition, the argument of the modular value can be evaluated using expression (4.5), found for the argument of the projector weak value.

This property will prove to be useful for higher-level quantum systems. The solid angle Ω_{irsf} is given in closed form by (H.12) so that it is not necessary to know the individual vector \vec{s} to determine the geometrical phase. In relation (H.12) the solid angle is simply expressed by the Bloch vectors \vec{i} , \vec{f} and the parameter α .

To close this discussion of two-level systems, we note that the modulus and the argument of the weak value of an arbitrary spin observable $\hat{\sigma}_r$ can be obtained from the modular value by setting $\alpha = \beta = \pi$ because then $A_w = A_m$. In this case, the Bloch vector \vec{s} becomes $\vec{s} = 2 \left(\vec{r} \cdot \vec{i} \right) \vec{r} - \vec{i}$ and the expression of the accumulated phase is $\arg \sigma_{r,w} = -\frac{\Omega_{irsf}}{2}$.

4.3 Three-level quantum systems

In the previous section, we derived geometric expressions for weak and modular values of qubit observables. This was made possible thanks to the unique one-to-one correspondance linking the qubit states in two-dimensional Hilbert space and the vectors on the unit sphere in three-dimensional physical space. Unfortunately, such a correspondance does not exist for higher-level systems: their states cannot be identified bijectively with the vectors on a unit sphere in a higher-dimensional real vectorial space. However, following an approach developed by Majorana [90], it is possible to represent states of a N -level system by $N - 1$ vectors on the Bloch sphere. With this essential insight, we will now be able to find geometric expressions for weak and modular values of observables of three-level quantum systems, which can be easily generalized to arbitrary N -level systems.

According to the Majorana approach, amongst the pure quantum states of a system of $N - 1$ qubits, it is possible to distinguish a class of states which are symmetric with respect to all possible permutations of the $N - 1$ qubit subsystems. This class of symmetric pure quantum states can be identified with the set of all states of a single system described in a N -dimensional Hilbert space [98, 99]. An arbitrary symmetric state of this set $|\Psi\rangle$ can be written as:

$$|\Psi\rangle = K \sum_P \hat{P} [|\phi^{(1)}\rangle|\phi^{(2)}\rangle\dots|\phi^{(N-1)}\rangle] , \quad (4.22)$$

where

$$|\phi^{(k)}\rangle = \cos \frac{\beta_k}{2} e^{-j\frac{\alpha_k}{2}} |0\rangle + \sin \frac{\beta_k}{2} e^{j\frac{\alpha_k}{2}} |1\rangle, \quad k = 1, 2, \dots, N-1, \quad (4.23)$$

denotes the k^{th} qubit state, $\sum_P \hat{P}$ corresponds to the set of all $(N-1)!$ permutations of the qubits and K is the normalization factor. The state $|\Psi\rangle$ is determined by an unordered set of $N-1$ points on the Bloch sphere, called the Majorana points. The N -dimensional Hilbert space is spanned by a set of symmetric basis state vectors $\{|\Psi_k^{(b)}\rangle, k = 0, 1, 2, \dots, N-1\}$, where each state vector is defined by one of the N Dicke states [100]:

$$|\Psi_k^{(b)}\rangle = \frac{1}{\sqrt{C_k^{N-1}}} \sum_P \hat{P} [\underbrace{|0\rangle|0\rangle \dots |0\rangle}_k \underbrace{|1\rangle|1\rangle \dots |1\rangle}_{N-1-k}], \quad (4.24)$$

with the binomial coefficient $C_k^{N-1} = \frac{(N-1)!}{k!(N-1-k)!}$. A pure symmetric state $|\Psi\rangle$ can always be written as a superposition of these symmetric basis states (4.24):

$$|\Psi\rangle = \sum_{k=0}^{N-1} c_k |\Psi_k^{(b)}\rangle. \quad (4.25)$$

We assume that the coefficients c_k define a normalized state in its canonical form, for which the global phase is set to 0. From these coefficients c_k , it is possible to obtain the parameters α_k and β_k determining the Majorana qubits $|\phi^{(k)}\rangle$ of an arbitrary pure symmetric state $|\Psi\rangle$. To do this, Devi et al. [100] considered a unitary operator inducing collective, identical rotations:

$$\hat{\mathcal{R}}_k = \hat{R}(\alpha_k, \beta_k) \otimes \hat{R}(\alpha_k, \beta_k) \otimes \dots \otimes \hat{R}(\alpha_k, \beta_k), \quad (4.26)$$

where each operator $\hat{R}(\alpha_k, \beta_k)$ aligns the state $|\phi^{(k)}\rangle$ on $|0\rangle$:

$$\hat{R}(\alpha_k, \beta_k) |\phi^{(k)}\rangle = |0\rangle. \quad (4.27)$$

The application of $\hat{\mathcal{R}}_k$ on the N -dimensional state vector $|\Psi\rangle$ implies that each term in the superposition (4.22) of the rotated state has at least one $|0\rangle$. Therefore, the projection of the rotated state onto the orthogonal state $|1\rangle^{\otimes N-1}$ is zero:

$$\langle 1| \langle 1| \dots \langle 1| \hat{\mathcal{R}}_k |\Psi\rangle = 0 \quad (4.28)$$

In total, there exist $(N-1)$ collective rotations $\hat{\mathcal{R}}_k$ satisfying equation (4.28). To find out all of these $(N-1)$ rotations, equation (4.28) is written as the following:

$$\langle 1| \langle 1| \dots \langle 1| \hat{\mathcal{R}} \left[\sum_{k=0}^{N-1} c_k \frac{1}{\sqrt{C_k^{N-1}}} \sum_P \hat{P} [\underbrace{|0\rangle|0\rangle \dots |0\rangle}_k \underbrace{|1\rangle|1\rangle \dots |1\rangle}_{N-1-k}] \right] = 0. \quad (4.29)$$

Then, the collective, rotation operators $\hat{R}(\alpha, \beta)$ defined by:

$$\hat{R}(\alpha, \beta) = \begin{pmatrix} e^{j\frac{\alpha}{2}} \cos \frac{\beta}{2} & e^{-j\frac{\alpha}{2}} \sin \frac{\beta}{2} \\ -e^{j\frac{\alpha}{2}} \sin \frac{\beta}{2} & e^{-j\frac{\alpha}{2}} \cos \frac{\beta}{2} \end{pmatrix}, \quad (4.30)$$

are used, and equation (4.29) becomes:

$$\begin{aligned} \sum_{k=0}^{N-1} c_k \sqrt{C_k^{N-1}} \left[\cos \frac{\beta}{2} \right]^{N-1-k} \left[-\sin \frac{\beta}{2} \right]^k e^{j(k-\frac{N-1}{2})\alpha} &= 0, \\ \mathcal{A} \sum_{k=0}^{N-1} (-1)^k \sqrt{C_k^{N-1}} c_k z^k &= 0, \end{aligned} \quad (4.31)$$

where $z = \tan \frac{\beta}{2} e^{j\alpha}$ and $\mathcal{A} = \left[\cos \frac{\beta}{2} \right]^{N-1} e^{-j(\frac{N-1}{2})\alpha}$. To obtain finally the parameter α_k and β_k of the qubits $|\phi^{(k)}\rangle$ in terms of the complex coefficients c_k , we must identify the $N-1$ roots $z = \tan \frac{\beta_k}{2} e^{j\alpha_k}$, with $k = 1, 2, \dots, N-1$, of the Majorana polynomial² $P(z)$:

$$P(z) = \sum_{k=0}^{N-1} (-1)^k \sqrt{C_k^{N-1}} c_k z^k. \quad (4.32)$$

Tamate et al. [37] demonstrated that a set of three symmetric states $|\Psi_1\rangle$, $|\Psi_2\rangle$ and $|\Psi_3\rangle$ of an ensemble of $N-1$ qubits can always be transformed by an appropriate unitary transformation to the following specific set of symmetric states:

$$\begin{aligned} |\Psi_1''\rangle &= K \sum_P \hat{P} \left[|\phi_1^{(1)}\rangle \dots |\phi_1^{(N-1)}\rangle \right], \\ |\Psi_2''\rangle &= \underbrace{|\phi_2\rangle \dots |\phi_2\rangle}_{N-1}, \quad |\Psi_3''\rangle = \underbrace{|\phi_3\rangle \dots |\phi_3\rangle}_{N-1}. \end{aligned} \quad (4.33)$$

After this unitary transformation, the states $|\Psi_2\rangle$ and $|\Psi_3\rangle$ are factored in products of $N-1$ identical qubit states. Only $|\Psi_1\rangle$ remains in an entangled state of $N-1$ qubits. Thus, $|\Psi_1\rangle$ is represented by $N-1$, generally distinct, points $\vec{p}_1^{(k)}$ on the Bloch sphere, while the states $|\Psi_2\rangle$ and $|\Psi_3\rangle$ are described by single degenerate points, \vec{p}_2 and \vec{p}_3 , respectively. Consequently, the argument of the corresponding three-vertex Bargmann invariant $\langle \Psi_1 | \Psi_2 \rangle \langle \Psi_2 | \Psi_3 \rangle \langle \Psi_3 | \Psi_1 \rangle$ is expressed by a sum of $N-1$ geometric phases [37]:

$$\gamma(\Psi_1, \Psi_2, \Psi_3) = \sum_{k=1}^{N-1} \gamma(\phi_1^{(k)}, \phi_2, \phi_3), \quad (4.34)$$

where each term of this sum is equal to the solid angle $-\frac{1}{2}\Omega_{123}^{(k)}$ defined by the corresponding three vectors $\vec{p}_1^{(k)}$, \vec{p}_2 and \vec{p}_3 through relation (4.5).

²It is possible that all $N-1$ Majorana qubits $|\phi^{(k)}\rangle$ are not determined when the Majorana polynomial $P(z)$ is of degree $r < N-1$. For more details, see reference [100].

4.3.1 Weak values of projectors in qutrit systems

With this knowledge, we proceed now with the evaluation of the weak value $\Pi_{r,w}^{(3)}$ of the projector on an arbitrary state $|\psi_r\rangle$ of a three-level quantum system. Similarly to the two-level case, the weak value $\Pi_{r,w}^{(3)}$ of a three-level quantum system involves a set of three qutrit states $|\psi_i\rangle$, $|\psi_r\rangle$ and $|\psi_f\rangle$. Their Majorana representation in terms of symmetric two-qubit states are given by $|\Psi_i\rangle$, $|\Psi_r\rangle$ and $|\Psi_f\rangle$, respectively. Through a unitary transformation U , we transform these states to the set:

$$\begin{aligned} |\Psi_i''\rangle &= K_i \left[|\phi_i^{(1)}\rangle|\phi_i^{(2)}\rangle + |\phi_i^{(2)}\rangle|\phi_i^{(1)}\rangle \right], \\ |\Psi_f''\rangle &= |\phi_f\rangle|\phi_f\rangle, \quad |\Psi_r''\rangle = |\phi_r\rangle|\phi_r\rangle. \end{aligned} \quad (4.35)$$

where the normalization factor $K_i = (2 + 2|\langle\phi_i^{(2)}|\phi_i^{(1)}\rangle|^2)^{-\frac{1}{2}}$. The form taken by the unitary transform and the exact expression of the different qubit states will be determined quantitatively later. Indeed, their formulation is not needed to obtain the researched expression as a function of vectors on the Bloch sphere. We can now evaluate the weak value, which is invariant under the unitary transformation:

$$\Pi_{r,w}^{(3)} = \frac{\langle\Psi_f''|\Psi_r''\rangle\langle\Psi_r''|\Psi_i''\rangle}{\langle\Psi_f''|\Psi_i''\rangle} = \frac{\langle\phi_f|\phi_r\rangle^2\langle\phi_r|\phi_i^{(1)}\rangle\langle\phi_r|\phi_i^{(2)}\rangle}{\langle\phi_f|\phi_i^{(1)}\rangle\langle\phi_f|\phi_i^{(2)}\rangle}, \quad (4.36)$$

In the Majorana representation, the weak value of a qutrit projector is thus given by the product of two weak values of a qubit projector, but for different initial states $|\phi_i^{(1)}\rangle$ and $|\phi_i^{(2)}\rangle$. Using the expressions obtained for the modulus (4.3) and the argument (4.5) of weak values of qubit projectors, we obtain immediately the modulus the weak value of the qutrit projector:

$$|\Pi_{r,w}^{(3)}| = \sqrt{\frac{1}{2} \frac{(1 + \vec{f} \cdot \vec{r}) (1 + \vec{r} \cdot \vec{i}_2)}{(1 + \vec{f} \cdot \vec{i}_2)}} \sqrt{\frac{1}{2} \frac{(1 + \vec{f} \cdot \vec{r}) (1 + \vec{r} \cdot \vec{i}_1)}{(1 + \vec{f} \cdot \vec{i}_1)}}, \quad (4.37)$$

as well as its argument:

$$\arg \Pi_{r,w}^{(3)} = -\frac{\Omega_{i_2 r f}}{2} - \frac{\Omega_{i_1 r f}}{2}, \quad (4.38)$$

where the four relevant qubit states were described with their vectors on the Bloch sphere in an obvious notation. Interestingly, the three-level weak value is determined by two independent sequences of the Bloch vectors \vec{i}_1 and \vec{i}_2 . The modulus $\Pi_{r,w}^{(3)}$ is given by the product of two square roots. Each ratio inside a square root represents the projection probability that the initial vectors \vec{i}_k aligns with the final Bloch vector \vec{f} by passing through the intermediate vector \vec{r} , divided by the projection probability

that the initial vectors \vec{i}_k aligns directly with the final Bloch vector \vec{f} . The argument is proportional to the sum of two solid angles $\Omega_{i_1 r f}$ and $\Omega_{i_2 r f}$ delimited by the geodesic triangles on the Bloch sphere with the three vertices $\vec{i}_1, \vec{r}, \vec{f}$ and $\vec{i}_2, \vec{r}, \vec{f}$, respectively.

We now construct the unitary transformation U in order to determine the qubit states. The normalized state $|\psi_r\rangle$ is written as a function of four real parameters θ, ϵ, χ_1 and χ_2 so that $|\psi_r\rangle = (e^{j\chi_1} \cos \epsilon \sin \theta, e^{j\chi_2} \sin \epsilon \sin \theta, \cos \theta)^T$. We define the unitary operator $\hat{U}^{(1)} \in U(3)$ which maps $|\psi_r\rangle$ to the state $|\psi'_r\rangle = (0, 0, 1)^T$:

$$\hat{U}^{(1)} = \begin{pmatrix} -e^{-j\chi_1} \sin \epsilon & e^{-j\chi_2} \cos \epsilon & 0 \\ -e^{-j\chi_1} \cos \epsilon \cos \theta & -e^{-j\chi_2} \sin \epsilon \cos \theta & \sin \theta \\ e^{-j\chi_1} \cos \epsilon \sin \theta & e^{-j\chi_2} \sin \epsilon \sin \theta & \cos \theta \end{pmatrix}. \quad (4.39)$$

It also induces the transformations $|\psi_i\rangle \rightarrow |\psi'_i\rangle$ and $|\psi_f\rangle \rightarrow |\psi'_f\rangle$. As we shall see later, the resulting state $|\psi'_r\rangle$ is associated to the factored state $|\Psi'_r\rangle = |0\rangle|0\rangle$ in the Majorana representation. This state presents two overlapping Majorana points on the Bloch sphere's north pole. We consider now a second unitary operator $\hat{U}^{(2)} \in U(3)$ which leaves $|\psi'_r\rangle$ invariant, but transforms the postselected state $|\psi'_f\rangle$ into a separable two-qubit state in the Majorana representation. In particular, we rewrite $|\psi'_f\rangle$ using a general expression³ with the four real parameters η, δ, ξ_1 and ξ_2 so that $|\psi'_f\rangle = (e^{j\xi_1} \cos \delta \sin \eta, e^{j\xi_2} \sin \delta \sin \eta, \cos \eta)^T$. This unitary transformation is given by:

$$\hat{U}^{(2)} = \begin{pmatrix} e^{-j\xi_1} \cos \alpha & e^{-j\xi_2} \sin \alpha & 0 \\ e^{-j\xi_1} \sin \alpha & -e^{-j\xi_2} \cos \alpha & 0 \\ 0 & 0 & 1 \end{pmatrix}, \quad (4.40)$$

with $\alpha = \delta + \arccos(\tan \frac{\eta}{2})$. After this unitary transformation, the postselected state becomes $|\psi''_f\rangle = (1 - \cos \eta, \sqrt{2 \cos \eta (1 - \cos \eta)}, \cos \eta)^T$. As will be explained later, its Majorana representation is given by the factored state $|\Psi''_f\rangle = |\phi_f\rangle|\phi_f\rangle$, where $|\phi_f\rangle = \sqrt{\cos \eta}|0\rangle + \sqrt{1 - \cos \eta}|1\rangle$. Due to the sequential application of the transformations $\hat{U}^{(1)}$ and $\hat{U}^{(2)}$, the initial three-level state $|\psi_i\rangle$ evolves to the normalized state $|\psi''_i\rangle = c_0|0\rangle + c_1|1\rangle + c_2|2\rangle$. Its Majorana representation can be obtained by solving the Majorana polynomial [99, 100]:

$$\frac{c_0}{\sqrt{2}} - c_1 z + \frac{c_2}{\sqrt{2}} z^2 = 0. \quad (4.41)$$

³The unitary operator $\hat{U}^{(1)}$ generally adds a phase factor to all three components of the state vector. However, as the weak value is gauge invariant, we can remove arbitrarily the phase factor from the third component without loss of generality. Note that this operation does not preserve the phase of the inner product between two states. Therefore the unitary operator must be applied to all states involved in the weak value expression, and all global phases should be removed accordingly.

The two roots z_k of this polynomial are related to the polar and azimuthal angle on the Bloch sphere by:

$$z_k = e^{j\phi_k} \tan \frac{\theta_k}{2}. \quad (4.42)$$

Separable states occur when the discriminant of the polynomial is nul, so that the roots are identical. The Majorana representation associates the following states together:

$$\begin{aligned} |0\rangle &\rightarrow |\Psi_0^{(b)}\rangle = |1\rangle|1\rangle, \\ |2\rangle &\rightarrow |\Psi_2^{(b)}\rangle = |0\rangle|0\rangle, \\ |1\rangle &\rightarrow |\Psi_1^{(b)}\rangle = 2^{-\frac{1}{2}}(|0\rangle|1\rangle + |1\rangle|0\rangle), \end{aligned} \quad (4.43)$$

where the (b) suffix denotes that these are basis states. In the end, we find thus that the projector state was mapped to the Bloch sphere vector $\vec{r} = (0, 0, 1)$, the postselected, final state was mapped to the vector:

$$\vec{f} = (\sqrt{4 \cos \eta (1 - \cos \eta)}, 0, 2 \cos \eta - 1). \quad (4.44)$$

The initial state is given by $|\Psi_i''\rangle = K_i \left[|\phi_i^{(1)}\rangle |\phi_i^{(2)}\rangle + |\phi_i^{(2)}\rangle |\phi_i^{(1)}\rangle \right]$ where the two qubits states are deduced from the roots (4.42) of the Majorana polynomial and where the normalization factor can also be evaluated to $K_i = 1/\sqrt{3 + \vec{i}_1 \cdot \vec{i}_2}$.

4.3.2 Modular values in qutrit systems

The same kind of relations can also be established for the modular value of an arbitrary three-level evolution operator:

$$\hat{U}_{\lambda_r}^{\alpha, \beta} = e^{j\beta} e^{-ja\hat{\lambda}_r}, \quad (4.45)$$

where $\hat{\lambda}_r = \vec{r}_{(8)} \cdot \vec{\hat{\lambda}}$ with $\vec{r}_{(8)} \in \mathbb{R}^8$ a normalized vector pointing in a 8-dimensional space. The k^{th} element ($k = 1, 2, \dots, 8$) of the vector $\vec{\hat{\lambda}}$ corresponds to the Gell-Mann operator $\hat{\lambda}_k$. A summary containing the essential properties of the Gell-Mann operators is presented in Appendix I or in reference [101]. For our purposes, it suffices to know that the hermitian operator $\hat{\lambda}_r$ is traceless, that the trace of $\hat{\lambda}_r^2$ equals 2, and that, when it verifies the condition $\det(\hat{\lambda}_r) = 0$, its eigenvalues are $-1, 0$ and $+1$. The parameter β induces a phase shift while the parameter α was defined so that it corresponds to the rotation angle when $\hat{\lambda}_r$ is a spin-1 operator.

We consider the set of three qutrits states $|\psi_i\rangle, |\psi_r\rangle$ and $|\psi_f\rangle$, where $|\psi_i\rangle$ is the initial,

preselected state, $|\psi_f\rangle$ is the final, postselected state and $|\psi_r\rangle$ is an eigenvector state of the operator $\hat{\lambda}_r$, associated with an eigenvalue λ_r . Any eigenvector can be selected but we could arbitrarily select the largest eigenvalue to remain in line with the spirit of the developments we followed for the qubit case. The modular value $\lambda_{r,m}^{\alpha,\beta}$ of the Gell-Mann operator defined through the previous unitary operator becomes:

$$\lambda_{r,m}^{\alpha,\beta} = e^{j\beta} \frac{\langle \psi_f | e^{-j\alpha \hat{\lambda}_r} | \psi_i \rangle}{\langle \psi_f | \psi_i \rangle}. \quad (4.46)$$

Following the procedure developed for two-level systems, we define the state $|\psi_S\rangle = e^{-j\alpha \hat{\lambda}_r} |\psi_i\rangle$, which result from applying the α -evolution operator to the initial, preselected state. As for the qutrit projector case, there exists a couple of unitary operators $\hat{U}^{(1)}, \hat{U}^{(2)} \in U(3)$ transforming the eigenvector state $|\psi_r\rangle$ and the postselected state $|\psi_f\rangle$ to $|\Psi_r''\rangle = |0\rangle|0\rangle$ and $|\Psi_f''\rangle = |\phi_f\rangle|\phi_f\rangle$, respectively. Additionally, the initial state $|\psi_i\rangle$ is mapped to the state $|\Psi_i''\rangle = K_i \left[|\phi_i^{(1)}\rangle|\phi_i^{(2)}\rangle + |\phi_i^{(2)}\rangle|\phi_i^{(1)}\rangle \right]$ while the state $|\psi_S\rangle$ is associated to the state $|\Psi_s''\rangle = K_s \left[|\phi_s^{(1)}\rangle|\phi_s^{(2)}\rangle + |\phi_s^{(2)}\rangle|\phi_s^{(1)}\rangle \right]$. Therefore, the modular value is expressed by:

$$\lambda_{r,m}^{\alpha,\beta} = e^{j\beta} \frac{K_s \langle \Psi_f'' | \Psi_s'' \rangle}{K_i \langle \Psi_f'' | \Psi_i'' \rangle} = e^{j\beta} \frac{K_s \langle \phi_f | \phi_s^{(1)} \rangle \langle \phi_f | \phi_s^{(2)} \rangle}{K_i \langle \phi_f | \phi_i^{(1)} \rangle \langle \phi_f | \phi_i^{(2)} \rangle}, \quad (4.47)$$

which contains the contributions of two modular values of qubits. This factorisation is very similar to the one obtained in the qutrit projector case. Consequently, the modulus of the modular value $\lambda_{r,m}^{\alpha,\beta}$ is given as a function of vectors on the Bloch sphere according to the expression:

$$|\lambda_{r,m}^{\alpha,\beta}| = \frac{K_s}{K_i} \sqrt{\frac{(1 + \vec{f} \cdot \vec{s}_2)}{(1 + \vec{f} \cdot \vec{i}_2)}} \sqrt{\frac{(1 + \vec{f} \cdot \vec{s}_1)}{(1 + \vec{f} \cdot \vec{i}_1)}}, \quad (4.48)$$

where $K_n = 1/\sqrt{3 + \vec{n}_2 \cdot \vec{n}_1}$ (with $n = i, s$), while its argument is found to be:

$$\arg \lambda_{r,m}^{\alpha,\beta} = \beta - \alpha \lambda_r - \frac{\Omega_{i_2 r s_2 f}}{2} - \frac{\Omega_{i_1 r s_1 f}}{2}, \quad (4.49)$$

where the solid angles were defined similarly to the qubit case. The vectors \vec{s}_1 and \vec{s}_2 and \vec{i}_1 and \vec{i}_2 can be found by solving the Majorana polynomial for the states $|\psi_s''\rangle$ and $|\psi_i''\rangle$, respectively. The procedure leading to (4.49) is specified in the next section for modular values of N -level systems.

Because the algebraic structure of the Gell-Mann $\hat{\lambda}$ -operators is significantly different from the structure of the Pauli $\hat{\sigma}$ -operators, the weak value of the $\hat{\lambda}_r$ observable cannot

be evaluated from its modular value simply by setting particular values for α and β , contrary to what was possible in the qubit case. It is however possible to express the modular value as a function of weak values of $\hat{\lambda}_r$ and $\hat{\lambda}_r^2$ in a closed form. For example, in the simple case of a spin-1 observable (which verifies $\det(\hat{\lambda}_r) = 0$), setting the phase shift β to zero, the relationship between weak modular values of $\hat{\lambda}_r$ is deduced readily from the exact value of the exponential operator: $e^{-j\alpha\hat{\lambda}_r} = 1 - j \sin \alpha \hat{\lambda}_r + (\cos \alpha - 1) \hat{\lambda}_r^2$ [102], which can be obtained using the Cayleigh-Hamilton theorem.

4.3.3 Generalization to arbitrary N -level quantum systems

As for the three-level quantum system, any set of three N -level quantum states can be transformed to the specific set (4.35) :

$$\begin{aligned} |\Psi''_i\rangle &= K_i \sum_P \hat{P} \left[|\phi_i^{(1)}\rangle \dots |\phi_i^{(N-1)}\rangle \right], \\ |\Psi''_f\rangle &= \underbrace{|\phi_f\rangle \dots |\phi_f\rangle}_{N-1}, \quad |\Psi''_r\rangle = \underbrace{|\phi_r\rangle \dots |\phi_r\rangle}_{N-1}, \end{aligned} \quad (4.50)$$

by applying the appropriate unitary transformations $\hat{U}^{(1)}, \hat{U}^{(2)} \in U(N)$. Consequently, weak values of a N -level pre- and postselected projector are always deduced by the product of $N - 1$ square roots of a probability ratio for the modulus and the sum of $N - 1$ spherical triangles for the argument by introducing $N - 1$ initial two-level states:

$$|\Pi_{r,w}^{(N)}| = |\Pi_{1,w}| \cdot |\Pi_{2,w}| \cdot \dots \cdot |\Pi_{N-1,w}|, \quad (4.51)$$

$$\arg \Pi_{r,w}^{(N)} = \arg \Pi_{1,w} + \arg \Pi_{2,w} + \dots + \arg \Pi_{N-1,w}. \quad (4.52)$$

For modular values, this generalization remains valid if they are defined by traceless Hermitian operators $\hat{\Lambda}_r$. The associated unitary operator is $\hat{U}_{\Lambda_r}^{\alpha,\beta} = e^{j\beta} e^{-j\alpha \frac{N-1}{2} \hat{\Lambda}_r}$. The Majorana representation of the state $|\psi_s\rangle = \hat{U}_{\Lambda_r}^{\alpha,\beta} |\psi_i\rangle$ introduces the additional set of $N - 1$ Bloch vectors \vec{s}_k (with $k = 1, \dots, N - 1$), so that

$$|\Lambda_{r,m}^{\alpha,\beta}| = \frac{K_s}{K_i} \sqrt{\prod_{k=1}^{N-1} \frac{(1 + \vec{f} \cdot \vec{s}_k)}{(1 + \vec{f} \cdot \vec{i}_k)}}, \quad (4.53)$$

$$\arg \Lambda_{r,m}^{\alpha,\beta} = \beta - \alpha \frac{N-1}{2} \Lambda_r - \sum_{k=1}^{N-1} \frac{\Omega_{i_k r s_k f}}{2}, \quad (4.54)$$

where the parameter α is defined to respect convention on angular momentum for spin operators and where $|\psi_r\rangle$ is an arbitrary eigenvector of $\hat{\Lambda}_r$ with eigenvalue Λ_r .

In order to demonstrate relation (4.54), we express the traceless Hermitian operator $\hat{\Lambda}_r$ acting on the N -level system in the basis of its eigenvectors $\hat{\Lambda}_r = \sum_{r'=1}^N \Lambda_{r'} |\psi_{r'}\rangle \langle \psi_{r'}|$. The associated unitary operator is:

$$\hat{U}_{\Lambda_r}^{\alpha,\beta} = e^{j\beta} e^{-j\alpha \frac{N-1}{2} \hat{\Lambda}_r} = e^{j\beta} \sum_{r'=1}^N e^{-j\alpha \frac{N-1}{2} \Lambda_{r'}} |\psi_{r'}\rangle \langle \psi_{r'}|. \quad (4.55)$$

We define the initial state $|\psi_i\rangle$ and write it in the basis of the eigenvectors of $\hat{\Lambda}_r$, so that $|\psi_i\rangle = \sum_{r'=1}^N \langle \psi_{r'} | \psi_i \rangle |\psi_{r'}\rangle$. We also define the state $|\psi_S\rangle$ that result from applying the unitary operator to the initial state:

$$|\psi_S\rangle = \hat{U}_{\Lambda_r}^{\alpha,\beta} |\psi_i\rangle = e^{j\varphi_s} |\psi_s\rangle, \quad (4.56)$$

where $|\psi_s\rangle$ corresponds to the state $|\psi_S\rangle$ written in its canonical form, i. e. without the global phase factor φ_s that it may have acquired under the unitary transformation. To evaluate the phase φ_s , we project the state $|\psi_S\rangle$ on an arbitrary eigenvector $|\psi_r\rangle$ of the unitary operator:

$$\langle \psi_r | \psi_S \rangle = e^{j\varphi_s} \langle \psi_r | \psi_s \rangle = e^{j\beta} e^{-j\alpha \frac{N-1}{2} \Lambda_r} \langle \psi_r | \psi_i \rangle, \quad (4.57)$$

where the first equality results from (4.56) and the second from (4.55) and the definition of $|\psi_S\rangle$. Equation (4.57) shows that the projections $|\langle \psi_r | \psi_S \rangle|$ and $|\langle \psi_r | \psi_i \rangle|$ are identical, which is due to the unitary character of the operator $\hat{U}_{\Lambda_r}^{\alpha,\beta}$. By equating the arguments of both sides of equality (4.57), we find the value of the phase φ_s :

$$\varphi_s = \beta - \alpha \frac{N-1}{2} \Lambda_r + \arg \langle \psi_r | \psi_i \rangle - \arg \langle \psi_r | \psi_S \rangle. \quad (4.58)$$

The modular value is given by $\Lambda_{r,m}^{\alpha,\beta} = \langle \psi_f | \psi_S \rangle \langle \psi_f | \psi_i \rangle^{-1}$. Therefore its argument is given by:

$$\arg \Lambda_{r,m}^{\alpha,\beta} = \varphi_s + \arg \langle \psi_f | \psi_S \rangle - \arg \langle \psi_f | \psi_i \rangle. \quad (4.59)$$

Now, we apply the unitary transformation that maps the initial state $|\psi_i\rangle$ and the

eigenvector state $|\psi_r\rangle$ to factored states in the Majorana representation:

$$\begin{aligned} |\Psi''_i\rangle &= K_i \sum_P \hat{P} [|\phi_{i_1}\rangle|\phi_{i_2}\rangle\cdots|\phi_{i_{N-1}}\rangle] , \\ |\Psi''_s\rangle &= K_s \sum_P \hat{P} [|\phi_{s_1}\rangle|\phi_{s_2}\rangle\cdots|\phi_{s_{N-1}}\rangle] , \\ |\Psi''_r\rangle &= \underbrace{|\phi_r\rangle\cdots|\phi_r\rangle}_{N-1} , \quad |\Psi''_f\rangle = \underbrace{|\phi_f\rangle\cdots|\phi_f\rangle}_{N-1} . \end{aligned} \quad (4.60)$$

This transformation leaves invariant the argument of the modular value, so that, ignoring for now the global phase $\beta - \alpha \frac{N-1}{2} \Lambda_r$, the geometrical component becomes:

$$\varphi_g = \arg\langle\Psi''_f|\Psi''_s\rangle - \arg\langle\Psi''_f|\Psi''_i\rangle + \arg\langle\Psi''_r|\psi''_i\rangle - \arg\langle\Psi''_r|\Psi''_s\rangle . \quad (4.61)$$

We can rewrite this phase into two components $\varphi_g = \varphi_{g_1} + \varphi_{g_2}$ defined by:

$$\varphi_{g_1} = \arg\langle\Psi''_f|\Psi''_s\rangle + \arg\langle\Psi''_i|\Psi''_f\rangle , \quad (4.62)$$

$$\varphi_{g_2} = \arg\langle\Psi''_r|\Psi''_i\rangle + \arg\langle\Psi''_s|\Psi''_r\rangle , \quad (4.63)$$

where we used the property $\arg\langle\Psi_a|\Psi_b\rangle = -\arg\langle\Psi_b|\Psi_a\rangle$. In terms of the qubits defining the Majorana representation, these phase components become:

$$\varphi'_{g_1} = \sum_{k=1}^{N-1} (\arg\langle\phi_f|\phi_{s_k}\rangle + \arg\langle\phi_{s_k}|\phi_{i_k}\rangle + \arg\langle\phi_{i_k}|\phi_f\rangle) , \quad (4.64)$$

$$\varphi'_{g_2} = \sum_{k=1}^{N-1} (\arg\langle\phi_r|\phi_{i_k}\rangle + \arg\langle\phi_{i_k}|\phi_{s_k}\rangle + \arg\langle\phi_{s_k}|\phi_r\rangle) , \quad (4.65)$$

where the middle terms that were added to both equations compensate each other so that $\varphi_g = \varphi'_{g_1} + \varphi'_{g_2}$. Each triplet of arguments summed in (4.64) corresponds to the argument of the weak value $\langle\phi_f|\hat{\Pi}_{s_k}|\phi_{i_k}\rangle\langle\phi_f|\phi_{i_k}\rangle^{-1}$ of a qubit projector on the state $|\phi_{s_k}\rangle$. Correspondingly, each triplet of arguments summed in (4.65) is equal to the argument of the weak value $\langle\phi_{s_k}|\hat{\Pi}_r|\phi_{i_k}\rangle\langle\phi_{s_k}|\phi_{i_k}\rangle^{-1}$ of a qubit projector on the state $|\phi_r\rangle$. Using our results (4.5) on qubits, we find thus that:

$$\arg\Lambda_{r,m}^{\alpha,\beta} = \beta - \alpha \frac{N-1}{2} \Lambda_r - \frac{1}{2} \sum_{k=1}^{N-1} (\Omega_{i_k s_k f} + \Omega_{i_k r s_k}) , \quad (4.66)$$

where the geometrical component can be recast as $\Omega_{i_k r s_k f} = \Omega_{i_k s_k f} + \Omega_{i_k r s_k}$ according to (4.5). When the operator $\Lambda_{r,m}^{\alpha,\beta}$ is a spin operator, the associated unitary operator $\hat{U}_{\Lambda_r}^{\alpha,\beta}$ is rotation operator that corresponds to a rotation of an angle α in physical space and to a rotation of an angle $\frac{N-1}{2}\alpha$ in the Hilbert space of the N -level system. Thus, it rotates the initial vectors \vec{i}_k around the axis \vec{r} by an angle α until they reach the

vectors \vec{s}_k . In that case, the solid angle $\Omega_{i_k r s_k f}$ is given in closed form by (H.12) so that it is not necessary to know the individual vectors \vec{s}_k to determine the geometrical phase. When $\hat{U}_{\Lambda_r}^{\alpha, \beta}$ is not a spatial rotation operator, the expression of \vec{s}_k as a function of \vec{i}_k , \vec{r} and α is a priori not known, so that the phase of the modular value should be evaluated through (4.66), using the general formula (4.5) to calculate each solid angle.

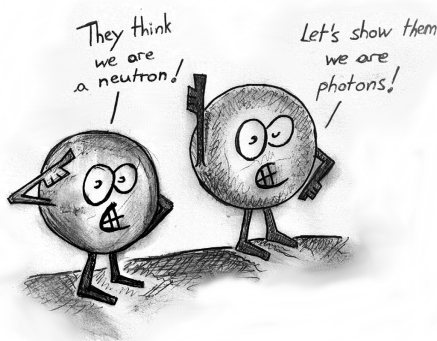
4.4 Summary

In this chapter, we expressed the polar form of weak and modular values of operators of two-, three- and higher-level systems that describe preselected and postselected experiments, such as weak measurements involving discrete quantum systems. We used the Majorana representation of N -level systems, which assigns a correspondence between states of N -level systems and symmetric states of $N - 1$ qubits. This new approach led to a geometric description of weak and modular values in terms of vectors on the Bloch sphere. We found that weak values of projectors and modular values can be factored in $N - 1$ contributions by considering the underlying qubit contributions associated with the Majorana representation. Their modulus is determined by a product of $N - 1$ square roots involving ratios of projection probabilities between qubit states. The latter are expressed as a function of scalar products between Bloch vectors. Their argument is given by a sum of $N - 1$ half solid angles related to $N - 1$ spherical polygons defined by qubit states on the Bloch sphere. The arguments of weak and modular values correspond thus to a quantum geometric phase (the Pancharatnam–Berry phase). Their values are expressed as a function of scalar and cross products between Bloch vectors.

5

Applications of the geometric representation involving discrete quantum systems

As an application of the new geometric description, we will examine phase discontinuities around singularities of weak values, which occur for orthogonal pre- and post-selected states. In a first application (5.1 Response of the meter detection system around phase discontinuities, p.81), we will study the behavior of the weak values argument of two-level quantum systems in terms of spherical quadrangles on the Bloch sphere. For this reason, we will use the experimental data of the argument that results from the interferometric measurements in chapter 3. Then, we will proceed with demonstrating that these phase discontinuities of the weak value have also a topological origin for three-dimensional discrete quantum systems (5.2 Singularities in weak values of three-level quantum systems, p.86). Finally, we will discuss the feasibility to determine the polar components of modular values of a three-level quantum system by applying the controlled weak measurement scheme on entangled bipartite qubit states (5.3 Weak measurement of the modular value by probed bipartite qubit systems, p.91).



5.1 Response of the meter detection system around phase discontinuities

In chapter 3, we described theoretically a quantum eraser procedure exploiting a qubit meter to measure directly the modulus and the argument of weak values. This interferometric procedure was demonstrated using polarization-entangled photon pairs produced by type-I spontaneous parametric down-conversion. These pairs of photons are purely quantum objects, i.e. a classical description of these particles by Maxwell's equations is not possible. We studied experimentally the discontinuous behavior of the quantum phase around sign flips of the weak value $\sigma_{x,w}$. Whenever $\sigma_{x,w}$ changes its sign, we experimentally observed discontinuous jumps of the argument by a value of π . Similar discontinuities in quantum phase of weak values are already observed in [34,35] for two-level quantum systems.

In the following section, we will describe the observed behavior of the weak values argument $\arg \sigma_{x,w}$ in terms of spherical quadrangles on the Bloch sphere. This description will help us to better understand the origin of these discontinuities: the coexistence of opposing spherical quadrangles.

The experimental results of chapter 3 are summarized in figures 5.1.a-b for two different preparations of the weak value $\sigma_{x,w}$ (set-up 1 and 4). Due to experimental errors associated to the meter measurement system, the outcomes round slightly up the theoretical predications (gray lines). The weak values argument jumps discontinuously¹ by $\pm \pi$ at the values $\alpha = \{-90^\circ, 0^\circ, 90^\circ\}$. Experimentally, we observed two types of evolution of the argument $\arg \sigma_{x,w}$ around these discontinuous jumps. For set-up 1, the argument decreases each time by a value of π and looks therefore like a step function with respect to α . On the other hand, for set-up 4, the argument changes alternately by the values $-\pi$ and $+\pi$ like a square function. In order to evaluate these two behaviors of the experimental data, we reconstruct the final, postselected polarization states on the basis of the argument readouts. In practice, this reconstruction of quantum states by weak values is a common method in the field of weak measurements [14–17].

For the preselected, linear polarization state $|\phi_i\rangle = |H\rangle$ and the postselected, ellip-

¹The positive and the negative sign associated to the jump of π has no importance, since the corresponding values for the argument cause equivalent weak values: $\sigma_{x,w} = |\sigma_{x,w}| \exp [j(\phi \pm \pi)]$.

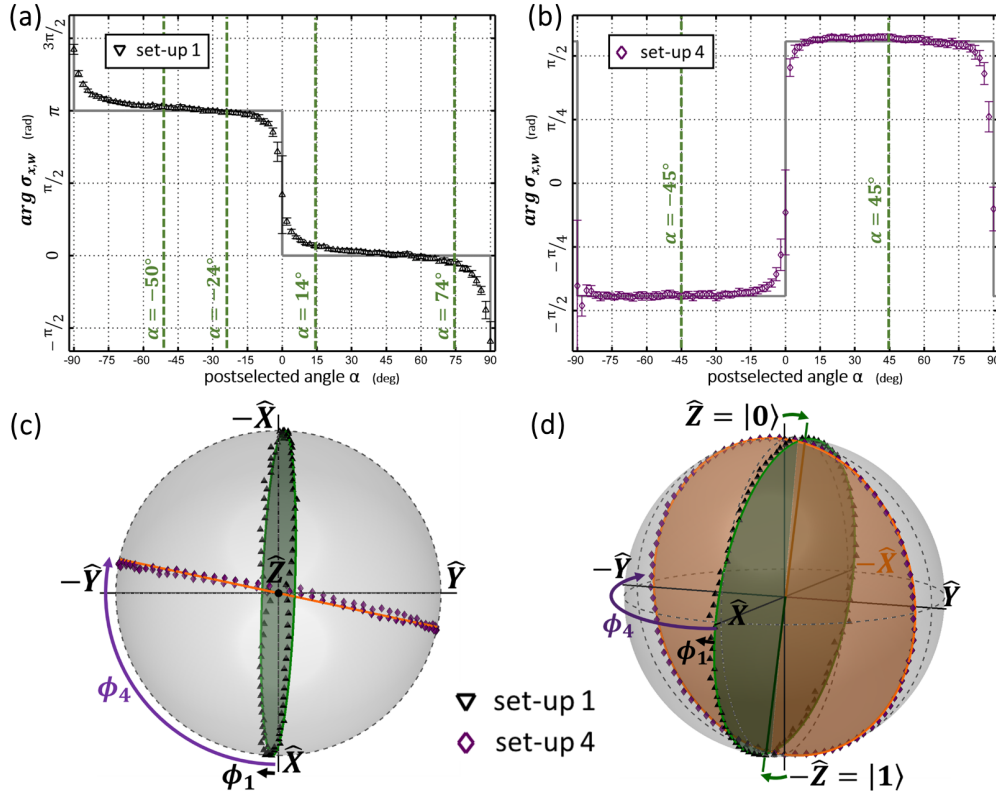


Figure 5.1: (a-b) Measurement results of the argument $\arg \sigma_{x,w}$ for two preparations (set-up 1 and 4). Discontinuous jumps of the argument are observed at $\alpha = \{-90^\circ, 0^\circ, 90^\circ\}$. The green, dashed lines indicate particular values of this argument which will be represented by spherical quadrangles in figures 5.2-3. (c-d) Reconstruction of the postselected polarization states in the form of Bloch vectors \vec{f} (black and violet markers). For set-up 4, the argument readouts reproduces correctly the prepared final states (situated on the orange line forming an angle $\phi_4 = 5\pi/9$ from the bird's-eye view), while the measurement outcomes for set-up 1 feature small disagreements with the final preparation process.

tical state $|\phi_f\rangle = \cos\alpha|H\rangle + e^{-j\phi} \sin\alpha|V\rangle$ the weak value of the Pauli operator $\hat{\sigma}_x$ is theoretically given by $\sigma_{x,w}(\alpha, \phi) = \tan\alpha e^{j\phi}$. During the postselection process of $|\phi_f\rangle$, the parameter α varies from -90° to 90° by a step of 2° . Thus, the argument $\arg \sigma_{x,w}$ determines the relative phase ϕ that appears in the postselected polarization state $|\phi_f\rangle$. Figures 5.1.c-d illustrate the reconstructed states represented by vectors \vec{f} on the Bloch sphere (black and violet markers). According to the preparation process of the postselected states, these Bloch vectors have to be situated on a line that forms an angle ϕ with the \vec{e}_x -axis when looking from the bird's-eye view (c). For set-up 1

and 4 these angles have to be $\phi_1 = 0$ and $\phi_4 = 5\pi/9$, respectively. The orientation ϕ also determines the azimuthal angle of the Bloch vectors which are either $-\phi \pm \pi$ for $\alpha \in [-90^\circ, 0^\circ[$ or $-\phi$ for $\alpha \in [0^\circ, 90^\circ]$. Set-up 4 features all these characteristics: the postselected vectors (violet diamonds) have an azimuthal angle of either $-\phi_4$ or $-\phi_4 + \pi$ and they are situated on the orange line. Oppositely, the postselected vectors of set-up 1 (black triangles) reveal an unexpected repartition. Their azimuthal angle features a dependence in function of the parameter α with values close to the prepared relative phase ϕ_1 . Thus, at the bird's-eye view, these vectors are distributed like a screw around the \vec{e}_z -axis. At the side view, they are approximately situated on the border of the green circular plane which forms a small angle with the \vec{e}_z -axis (d).

On the basis of the reconstructed, postselected vectors \vec{f} , we apply now the geometric description of the last chapter on the argument $\arg \sigma_{x,w}$. The latter is directly related to the spherical quadrangle Ω_{irsf} by the expression: $\arg \sigma_{x,w} = -\Omega_{irsf}/2 + 2\pi n$ where $n = 0, \pm 1, \pm 2 \dots$. Thus, we can always add (or subtract) a multiple of 4π to Ω_{irsf} . We start our analysis with set-up 1. To do this, we describe the quadrangle Ω_{irsf} , that is formed by the four vertices \vec{i} , \vec{r} , \vec{s} and \vec{f} on the Bloch sphere, for particular values of α (see green, dashed lines in figure 5.1.a). We chose the convention that $\Omega_{irsf} \in [-2\pi, +2\pi]$. For all quadrangles Ω_{irsf} , the preselected vector \vec{i} points to the north pole, \vec{r} aligns with the \vec{e}_x -axis and the resulting vector \vec{s} points to the south pole. As illustrated in figure 5.2, at $\alpha = -50^\circ$, the spherical quadrangle Ω_{irsf} occupies a large area of the whole eastern hemisphere by traversing the anti-clockwise sequence $\vec{i} \rightarrow \vec{r} \rightarrow \vec{s} \rightarrow \vec{f} \rightarrow \vec{i}$. Thus, the value of Ω_{irsf} is close, but smaller, than 2π . Its sign is positive. Then, at $\alpha = -24^\circ$, the spherical quadrangle completely changes its properties: it nearly fills out the western hemisphere by rotating clockwise. This attributes a negative sign to Ω_{irsf} . As shown in figure 5.1.a, the argument does not change discontinuously in the range between -50° and -24° . In fact, we have to add 2π to the values of $-\Omega_{irsf}/2$. For spherical quadrangles that are positive and smaller than 2π (as it is the case for $\alpha = -50^\circ$), the values of the argument $\arg \sigma_{x,w}$ become finally larger than π . For values greater than $\alpha = -24^\circ$, the spherical quadrangle becomes quickly small and close to zero. These rapid variations describe the discontinuous phase jump of the weak value around $\alpha = 0^\circ$ (similar behaviors of Ω_{irsf} are identified at -90° and 90°). An explanation of this behavior in terms of spherical quadrangles will be given in the next section for set-up 4. Finally, in the range between 14° and 74° , Ω_{irsf} changes continuously a second time its sign and becomes positive again.

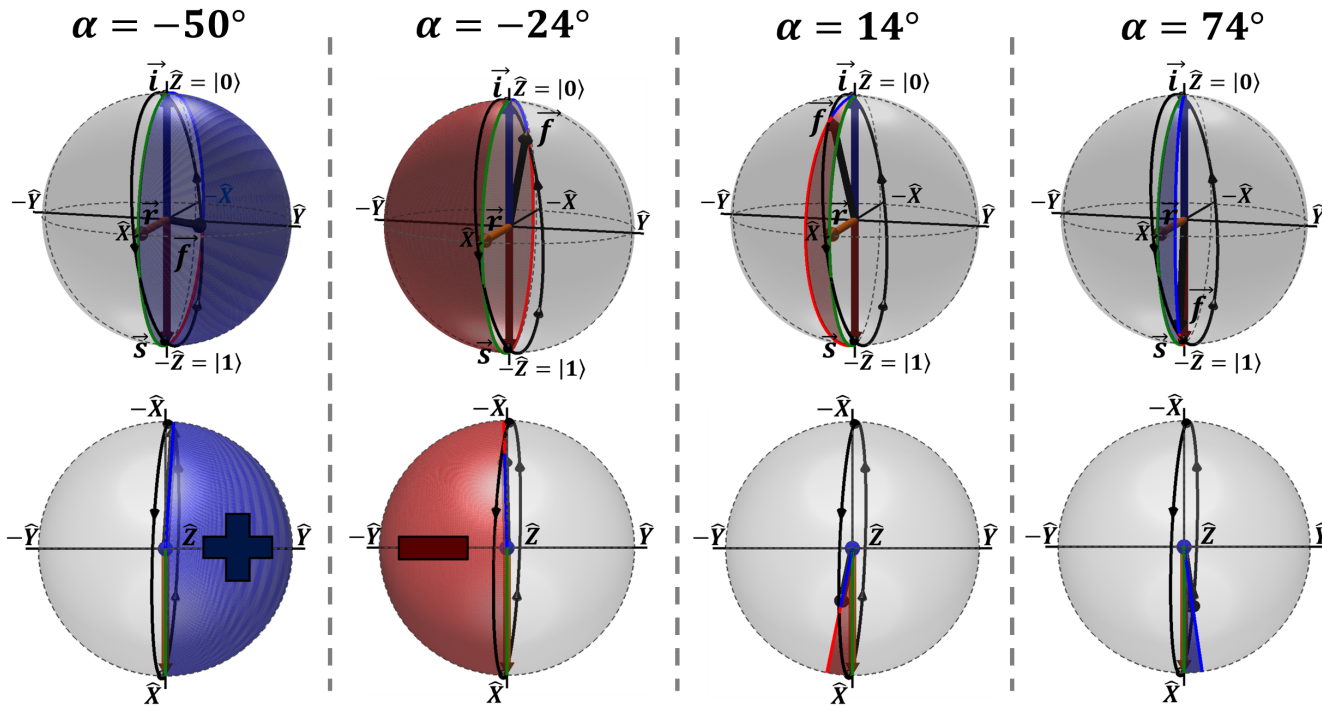


Figure 5.2: The spherical quadrangle Ω_{irsf} in function of the reconstructed, postselected vector \vec{f} of set-up 1 (closed, black arc). The preselected vector \vec{i} (blue) points to the north pole, \vec{r} (orange) aligns with the \vec{e}_x -axis and the resulting vector \vec{s} (brown) points to the south pole. The evolution of the preselected vector \vec{i} to \vec{s} is indicated by a green arc that passes through \vec{r} . To demonstrate the behavior of the weak values argument $\arg \sigma_{x,w}$, the quadrangle Ω_{irsf} is represented for particular values of the parameter α . At $\alpha = -50^\circ$, Ω_{irsf} occupies a large area of the whole eastern hemisphere by traversing the anti-clockwise sequence $\vec{i} \rightarrow \vec{r} \rightarrow \vec{s} \rightarrow \vec{f} \rightarrow \vec{i}$ (blue surface on the Bloch sphere). The value of Ω_{irsf} is close, but smaller, than 2π and its sign is positive. At $\alpha = -24^\circ$, the quadrangle fills out the western hemisphere by rotating clockwise (red surface on the Bloch sphere). This attributes a negative sign to Ω_{irsf} . In the range between 14° and 74° , Ω_{irsf} changes continuously a second time its sign and becomes positive again

To close this discussion for set-up 1, we note that for the convention $\Omega_{irsf} \in [0, 4\pi]$ the spherical quadrangle increases continuously in the range between the values -50° and -24° , while it features a discontinuous change between 14° and 74° from 4π to 0 . In a similar manner, the addition of 2π to $-\Omega_{irsf}/2$ yields a continuous variation of the argument $\arg \sigma_{x,w}$.

In set-up 4, the discontinuous behavior of the argument can also be studied by spherical quadrangles. To do this, we describe Ω_{irsf} for particular values of α (see green, dashed lines in figure 5.1.b). The preselected vector \vec{i} points to the north pole, \vec{r} aligns with the \vec{e}_x -axis and the resulting vector \vec{s} points to the south pole. For the reconstructed, final Bloch vectors, Ω_{irsf} changes discontinuously its value and its sign at

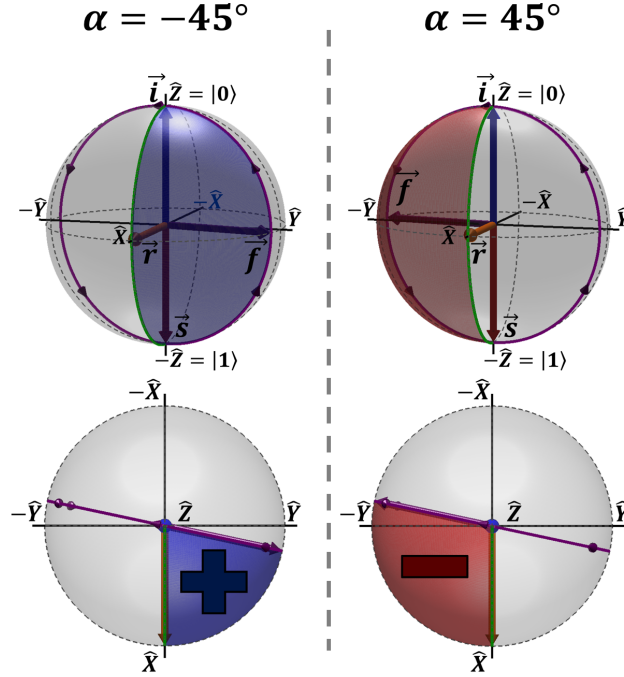


Figure 5.3: The spherical quadrangle Ω_{irsf} in function of the reconstructed, postselected vector \vec{f} of set-up 4 (closed, violet arc). The preselected vector \vec{i} (blue) points to the north pole, \vec{r} (orange) aligns with the \vec{e}_x -axis and the resulting vector \vec{s} (brown) points to the south pole. The evolution of the preselected vector \vec{i} to \vec{s} is indicated by a green arc that passes through \vec{r} . To demonstrate the discontinuous behavior of the weak values argument $\arg \sigma_{x,w}$, the quadrangle Ω_{irsf} is represented for particular values of the parameter α . For $\alpha \in]-90^\circ, 0^\circ[$ the quadrangle Ω_{irsf} turns anti-clockwise with positive sign, and for $\alpha \in]0^\circ, 90^\circ[$ it turns clockwise with negative sign.

$\alpha = \{-90^\circ, 0^\circ, 90^\circ\}$. At the values $\pm 90^\circ$, the postselected vector \vec{f} is anti-parallel to the preselected vector \vec{i} (i.e the initial and final polarization states are orthogonal). Thus, the modulus of the weak value diverges and the corresponding spherical quadrangle is not defined: for the postselected vector \vec{f} , there exist at least two geodesic trajectories to reach the initial vector \vec{i} . Similarly, at the value 0° , the postselected vector \vec{f} aligns with the preselected vector \vec{i} and Ω_{irsf} is indetermined. As shown in figure 5.3, for $\alpha \in]-90^\circ, 0^\circ[$ the quadrangle Ω_{irsf} turns anti-clockwise with positive sign (blue surface on the Bloch sphere), and for $\alpha \in]0^\circ, 90^\circ[$ it turns clockwise with negative sign (red surface on the Bloch sphere). The two situations coexist at $\alpha = 0^\circ$, so that the argument is undefined. This induces a discontinuity of Ω_{irsf} , which abruptly increases by 2π .

Finally, the observed behavior of the weak values argument $\arg \sigma_{x,w}$ is perfectly described by the evolution of spherical quadrangles on the Bloch sphere. Whenever the weak value changes its sign, the quadrangle passes through an indetermination and its value jumps discontinuously by 2π . In the last chapter, a direct connection between these spherical quadrangles and the Pancharatnam–Berry phase was demonstrated. Although some effects of classical, polarized light could also be understood by a geometric phase, this phase has in the case of photons (which are purely quantum objects) a non-controversial meaning with no classical counterpart. Since the observation of the weak value $\sigma_{x,w}$ relies on the manipulation of single photons, the purely classical interpretation of weak values [4] must be rejected.

5.2 Singularities in weak values of three-level quantum systems

In this section, we will examine the discontinuous behavior around singularities of weak values of three-level projectors. They occur when the preselected and postselected states are orthogonal to each other, as the denominator of the weak value diverges then. We will show that these discontinuities rely on discontinuous evolutions of spherical triangles similar to the two-level case. For this purpose, we will fix for a given projector a pre- and postselected ensemble of qutrit states that defines an unbounded, real weak value. Then, the application of the geometric representation will allow us to study this

weak value by two independent contributions on the Bloch sphere.

We fix three-level projector to $|\psi_r\rangle = (0, 0, 1)^T$ and pick the particular final state $|\psi_f\rangle = \frac{1}{2}(\sqrt{2}, 1, 1)^T$. An arbitrary initial state can then be written in the form of:

$$|\psi_i\rangle = (e^{i\chi_2} \sin \epsilon \sin \theta, e^{i\chi_1} \cos \epsilon \sin \theta, \cos \theta)^T. \quad (5.1)$$

The projector weak value is given by:

$$\Pi_{r,w}^{(3)} = [1 + \tan \theta (\sqrt{2} \sin \epsilon e^{j\chi_2} + \cos \epsilon e^{j\chi_1})]^{-1}. \quad (5.2)$$

The set of three states $|\psi_i\rangle$, $|\psi_r\rangle$ and $|\psi_f\rangle$ is transformed to the specific set (4.35) by applying the unitary operator:

$$\hat{U}^{(2)} = \begin{pmatrix} 0 & 1 & 0 \\ 1 & 0 & 0 \\ 0 & 0 & 1 \end{pmatrix}. \quad (5.3)$$

This operator corresponds to the $\hat{U}^{(2)}$ operator defined in (4.40) with its parameters set to $\alpha = \frac{\pi}{2}$ and $\xi_1 = \xi_2 = 0$. In this way, the final state $|\Psi_f''\rangle$ becomes $|x_+\rangle|x_+\rangle$ in the Majorana representation, with $|x_+\rangle = \frac{1}{\sqrt{2}}(|0\rangle + |1\rangle)$, while the projector state $|\Psi_r''\rangle = |0\rangle|0\rangle$. With these states, the projector is represented by the vector \vec{e}_z on the Bloch sphere, while the final state is represented by the vector \vec{e}_x . The initial state evolves to:

$$|\psi_i''\rangle = (e^{i\chi_1} \cos \epsilon \sin \theta, e^{i\chi_2} \sin \epsilon \sin \theta, \cos \theta)^T. \quad (5.4)$$

To find the Majorana representation $|\Psi_i''\rangle$ of the initial state, we need to solve its Majorana polynomial. The solutions are cumbersome for an arbitrary initial state (see Appendix J). To gain physical insight, we adopt here a simplified set of parameters to describe the initial state: $\epsilon = \arcsin(\tan \frac{\pi}{6})$ and $\chi_1 = 2\chi_2 = \frac{4}{3}\pi$. With these parameters, the initial state becomes:

$$|\psi_i''\rangle = (e^{-j\frac{2}{3}\pi} \sqrt{\frac{1}{3}} \sin \theta, e^{j\frac{2}{3}\pi} \sqrt{\frac{2}{3}} \sin \theta, \cos \theta)^T, \quad (5.5)$$

and the weak value is a real number that depends only on the parameter θ so that $\Pi_{r,w}^{(3)} = \left(1 - \sqrt{\frac{2}{3}} \tan \theta\right)^{-1}$. The roots of the corresponding second-degree Majorana polynomial are:

$$z_{1,2} = \tan\left(\frac{\beta_{1,2}}{2}\right) e^{j\alpha_{1,2}} = e^{-j\frac{1}{3}\pi} \frac{-\tan \theta \pm \sqrt{(\tan \theta - 2\sqrt{6}) \tan \theta}}{\sqrt{6}}. \quad (5.6)$$

The two qubits states are thus given by $|\phi_i^{(1,2)}\rangle = e^{-j\frac{\alpha_{1,2}}{2}} \cos \frac{\beta_{1,2}}{2} |0\rangle + e^{j\frac{\alpha_{1,2}}{2}} \sin \frac{\beta_{1,2}}{2} |1\rangle$,

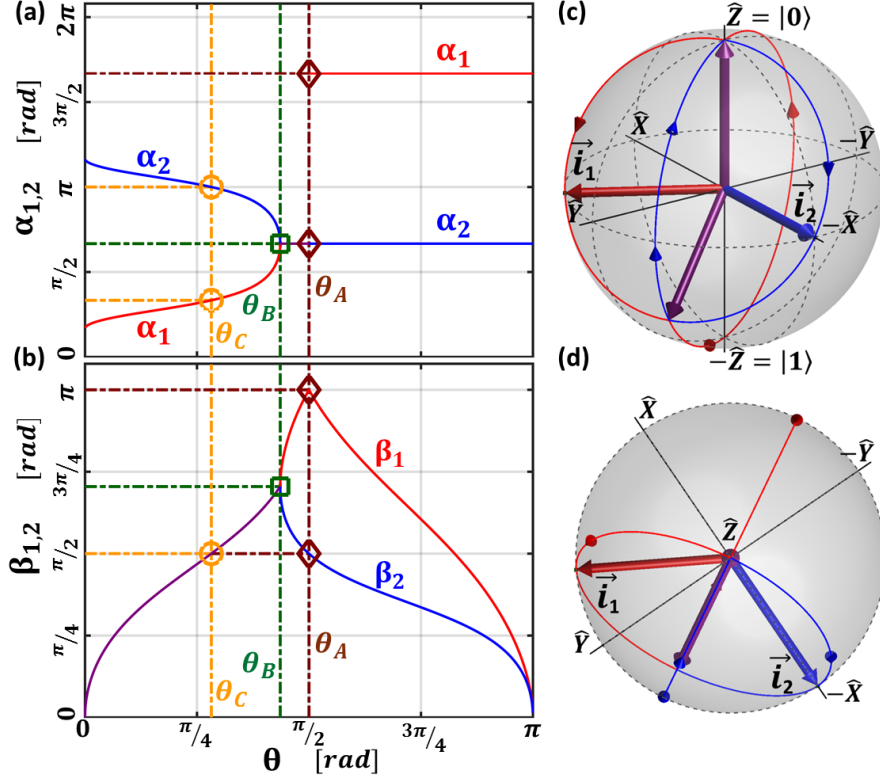


Figure 5.4: (a-b) Evolution of the angles $\alpha_{1,2}$ and $\beta_{1,2}$ characterizing the initial qubit states $|\phi_i^{(1,2)}\rangle$ with respect to θ for $\epsilon \approx 0.19(6)\pi$, $\chi_1 = \frac{4\pi}{3}$ and $\chi_2 = \frac{2\pi}{3}$. The bifurcation is represented by the green square: (a) for $\theta_B < \theta < \theta_A$, the values of the azimuth angles α_1 (red) and α_2 (blue) are degenerate (violet), (b) while for $\theta < \theta_B$, the polar angles β_1 (red) and β_2 (blue) are degenerate (violet). (c-d) Representation of the corresponding trajectories of the vectors $\vec{i}_{1,2}$ on the Bloch sphere in front (c) and bird's-eye views (d). The orientation of the illustrated red and blue Bloch vector corresponds to the particular value $\theta = \theta_C$, for which the weak value diverges.

with the corresponding Bloch vectors $\vec{i}_{1,2} = (\cos \alpha_{1,2} \sin \beta_{1,2}, \sin \alpha_{1,2} \sin \beta_{1,2}, \cos \beta_{1,2})$, where α_1, α_2 are the azimuth angles and β_1, β_2 the polar angles. In figure 5.4.a-b, we observe a bifurcation in the values of $\alpha_{1,2}$ and $\beta_{1,2}$, when expressed as a function of θ (green squares). This bifurcation occurs when the discriminant of the Majorana polynomial equals zero, for $\tan \theta_B = 2\sqrt{6}$ so that $\theta_B \approx 0.43(6)\pi$. At this particular value, the initial state $|\psi_i''\rangle$ is a product state of two identical qubits. For all parameters $\theta < \theta_B$, the polar angles β_1 and β_2 are degenerate (violet). In contrast, the values of the azimuth angles α_1 (red) and α_2 (blue) are initially different, but then symmetrically

reach the joint value $\chi_1/2$ (violet). This behavior result from the square root of the discriminant in (5.6) being a pure imaginary number for $\theta < \theta_B$: the two roots pick up opposite phase with respect to the global phase factor while their modulus is identical. For $\theta_B < \theta < \theta_A$, only the angles β_1 (red) and β_2 (blue) evolve. The Bloch vectors \vec{i}_1 and \vec{i}_2 move away from each other on the same longitude, as shown on figure 5.4.c-d. In this case, the discriminant square root is a positive real number and the phase of the solutions does not change as both solutions remain positive in this parameter range. This behavior abruptly changes at $\theta = \pi/2$ (brown diamonds), defined by θ_A , where the Bloch vector \vec{i}_1 aligns with the $-\vec{e}_z$ direction. For $\theta_A < \theta < \pi$, the solution for this vector \vec{i}_1 becomes negative increasing the value of the azimuth angle α_1 by π . In this parameter range, the polar angle β_1 evolves from $\pi/2$ to 0, i.e. to the same value as the second polar angle β_2 . Reaching at $\theta = \pi$, both Bloch vectors \vec{i}_1 and \vec{i}_2 align again with the \vec{e}_z direction (which corresponds to the initial situation) indicating a complete evolution cycle with respect to the parameter θ .

The weak value $\Pi_{r,w}^{(3)}$ diverges for $\theta_C \approx 0.28(2)\pi$ (yellow circles). The argument of the weak value is a discontinuous function of θ as it experiences a π -phase jump at θ_C . The divergence of the weak value occurs when the initial state becomes orthogonal to the final state. In the Majorana representation, at least one of the Bloch vectors describing the initial state has to be anti-parallel to the postselection vector $\vec{f} = \vec{e}_x$. Figure 5.4 reveals that the blue, second Bloch vector \vec{i}_2 aligns with the $-\vec{e}_x$ direction (azimuth angle $\alpha_2 = \pi$ and polar angle $\beta_2 = \pi/2$). Hence, the modulus of the weak value $\Pi_{2,w}$ diverges (see figure 5.5.a) and the corresponding solid angle Ω_{i_2rf} is not defined. For the preselected vector \vec{i}_2 , there exist at least two geodesic trajectories to reach the Bloch vector \vec{f} . This induces multiple values for the corresponding solid angle. The origin of the π -phase jump around this indeterminacy becomes clearer by analyzing the solid angles around the critical angle θ_C on figure 5.5.b. When $\theta < \theta_C$, the sequence $|\phi_i^{(2)}\rangle \rightarrow |\phi_r\rangle \rightarrow |\phi_f\rangle \rightarrow |\phi_i^{(2)}\rangle$ defines a small solid angle in the XY_-X_- hemisphere. The sequence travels clockwise so that the angle is negative. When $\theta > \theta_C$, this sequence runs anti-clockwise and corresponds to a positive solid angle that covers a large part of the XY_-X_- hemisphere. The two situations coexist at $\theta = \theta_C$, so that the argument is undefined. This induces a discontinuity of Ω_{i_2rf} , which abruptly increases by 2π across θ_C . The solid angle Ω_{i_1rf} associated with the sequence $|\phi_i^{(1)}\rangle \rightarrow |\phi_r\rangle \rightarrow |\phi_f\rangle \rightarrow |\phi_i^{(1)}\rangle$ runs anti-clockwise over the parameter range $0 < \theta < \theta_A$ with $\theta_A = \pi/2$. Its value is continuous across the weak value divergence. For $\theta < \theta_C$, the values of the two solid

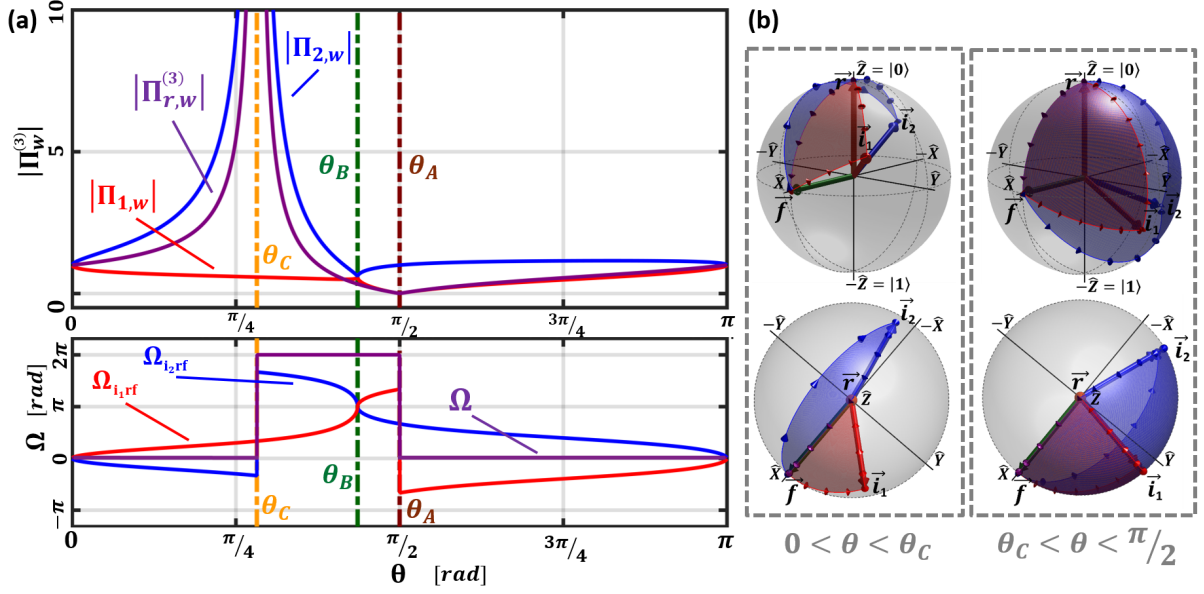


Figure 5.5: (a) Modulus of the weak value $\Pi_{r,w}^{(3)}$ and solid angle defining its argument $\arg \Pi_{r,w}^{(3)} = -\frac{1}{2}\Omega$, as a function of the parameter θ (violet lines). The weak value of the qutrit projector is related to the weak values of a qubit projector for two different initial states: $|\Pi_{r,w}^{(3)}| = |\Pi_{1,w}^{(3)}| \cdot |\Pi_{2,w}^{(3)}|$ and $\arg \Pi_{r,w}^{(3)} = \arg \Pi_{1,w}^{(3)} + \arg \Pi_{2,w}^{(3)}$. The two initial Bloch vector \vec{i}_1 and \vec{i}_2 define independent trajectories on the Bloch sphere as a function of θ (red and blue lines, respectively). (b) Representation of the solid angles $\Omega_{i_1,rf}$ and $\Omega_{i_2,rf}$ (red and blue surface respectively) corresponding to two particular situations, with $0 < \theta < \theta_C$ and $\theta_C < \theta < \pi/2$.

angles are symmetric with respect to 0, while for $\theta_C < \theta < \theta_A$, they are symmetric with respect to π . Therefore their sum is 0 below θ_C and 2π between θ_C and θ_A . When $\theta > \theta_A$, the initial anti-clockwise sequence delimiting $\Omega_{i_1,rf}$ becomes clockwise and corresponds to a negative solid angle. Both situations coexist at $\theta = \theta_A$, so that the argument is not defined. This induces a discontinuity of $\Omega_{i_1,rf}$, which abruptly decreases by 2π across θ_A . In fact, the preselected vector \vec{i}_1 aligns with the $-\vec{e}_z$ -direction (see figure 5.4) and is antiparallel to the projector vector \vec{r} . Because the values of both solid angles $\Omega_{i_1,rf}$ and $\Omega_{i_2,rf}$ are now symmetric with respect to 0, their sum is again 0 above θ_A .

The origin of these discontinuities of the weak values argument is found in the geometric phase: one of its contributing spherical triangle on the Bloch sphere jumps by a value of 2π . This behavior is pointed out each time when the weak values argument is

not defined, i.e. when the weak value changes its sign. These results agree with the observations made in the case of a two-level quantum system. Since the exploited representation is valid for arbitrary N -level systems, similar geometrical effects could be expected for high-level quantum systems.

5.3 Weak measurement of the modular value by probed bipartite qubit systems

In this last section of the chapter, we will study the feasibility to determine the polar components of modular values of a three-level quantum system by applying the quantum controlled weak measurement scheme on entangled bipartite qubit states. To do this, we will recall the controlled measurement protocol (introduced in the first part of chapter 3) for three-level systems. Then, all involved qutrit states will be expressed as symmetric two-qubit states. This will permit to study the geometric contributions of the modular value as well as to recast the protocol for two-qubit states. A similar reformulation of a qutrit measurement experiment will be also applied in the case of the three-box paradox studied in the next chapter.

As demonstrated in chapter 3, the modular value of a qutrit system can be evaluated experimentally using the controlled quantum evolution protocol. This measurement technique requires a controlled evolution, in which the probe qutrit $|\psi_i\rangle$ interacts with a qubit meter via a nonlocal quantum gate. This gate induces the application of the unitary transformation $\hat{U}_{\lambda_r}^{\alpha,\beta}$ on the probe as a function of the initial meter state:

$$\hat{U}_{GATE} = \hat{I} \otimes \hat{\Pi}_z + \hat{U}_{\lambda_r}^{\alpha,\beta} \otimes \hat{\Pi}_{-z} . \quad (5.7)$$

In this expression $\hat{\Pi}_z$ and $\hat{\Pi}_{-z}$ are orthogonal projectors acting on the qubit meter, while \hat{I} and $\hat{U}_{\lambda_r}^{\alpha,\beta}$ are operators acting on the qutrit probe. After this interaction, the information about whether $\hat{U}_{\lambda_r}^{\alpha,\beta}$ was applied or not is completely erased by measuring the meter state in the basis $\{|x_+\rangle, |x_-\rangle\}$ (this corresponds to a quantum eraser configuration). Finally, the probe system is postselected by a projective measurement. The argument and the modulus of the modular value $\lambda_{r,m}^{\alpha,\beta}$ is then determined by introducing a local phase transformation in the meter path and by measuring the interferometric visibility V . In the weak measurement regime with initial meter states close to the ground

state $|0\rangle$, we obtain the following relation: $V \simeq \theta |\lambda_{r,m}^{\alpha,\beta}|$ where θ is the measurement strength.

Now, we study the impact of a parameter $\eta \in [0, \pi]$ in the unitary operator $\hat{U}_{\lambda_r}^{\alpha,\beta}$ on fixed pre- and postselected three-level states, and, in particular, on the resulting Bloch vectors used in the geometric description. To gain physical insight, we construct a pre- and postselected ensemble for which the modular value $\lambda_{r,m}^{\alpha,\beta}$ does not depend on the value of the parameter η . Its value is constant and equal to one. We set the initial, preselected state at $|\psi_i\rangle = (0, e^{i\frac{\pi}{4}} \frac{\sqrt{3}}{2}, \frac{1}{2})^T$ and the final, postselected state at $|\psi_f\rangle = (0, 0, 1)^T$. The parameter η determines the orientation of the normalized, 8-dimensional vector

$$\vec{r}_{(8)} = \left(\frac{\sin 2\eta}{2\sqrt{2}}, \frac{\sin 2\eta}{2\sqrt{2}}, \frac{\cos 2\eta}{2}, 0, 0, 0, 0, \frac{\sqrt{3}}{2} \right) \quad (5.8)$$

and defines the traceless, Hermitian operator $\hat{\lambda}_r$:

$$\hat{\lambda}_r = \begin{pmatrix} \cos^2 \eta & e^{-i\frac{\pi}{4}} \sin 2\eta & 0 \\ e^{i\frac{\pi}{4}} \sin 2\eta & \sin^2 \eta & 0 \\ 0 & 0 & -1 \end{pmatrix}, \quad (5.9)$$

where $\hat{\lambda}_r = \vec{r}_{(8)} \cdot \vec{\lambda}$. Since $\det \hat{\lambda}_r = 0$, it is possible to deduce from $\hat{\lambda}_r$ the eigenvector state $|\psi_r\rangle = (\cos \eta, e^{i\frac{\pi}{4}} \sin \eta, 0)^T$ with the eigenvalue $+1$. The successive application of both transformations

$$\hat{U}^{(1)} = \begin{pmatrix} -\sin \eta & e^{-i\frac{\pi}{4}} \cos \eta & 0 \\ 0 & 0 & 1 \\ \cos \eta & e^{-i\frac{\pi}{4}} \sin \eta & 0 \end{pmatrix}, \quad (5.10)$$

and

$$\hat{U}^{(2)} = \begin{pmatrix} 0 & 1 & 0 \\ 1 & 0 & 0 \\ 0 & 0 & 1 \end{pmatrix} \quad (5.11)$$

leads to the specific set (4.35) with the Majorana points lying on the Bloch sphere north pole for $|\Psi_r''\rangle = |0\rangle|0\rangle$ and on the south pole for the postselected state $|\Psi_f''\rangle = |1\rangle|1\rangle$. The Majorana polynomial $P(z)$ of the transformed initial state

$$|\psi_i''\rangle = \left(\frac{1}{2}, \frac{\sqrt{3}}{2} \cos \eta, \frac{\sqrt{3}}{2} \sin \eta \right)^T \quad (5.12)$$

is given by:

$$P(z) = z^2 - \sqrt{6} \cos \eta z + \sqrt{3} \sin \eta. \quad (5.13)$$

There does not exist a close connection between the modular value $\lambda_{r,m}^{\alpha,\beta}$ and the weak value $\lambda_{r,w}^{\alpha,\beta}$. In fact, it can be shown that for the traceless observable $\hat{\lambda}_r$ the unitary operator $\exp(-i\alpha\hat{\lambda}_r)$ satisfies the following relation [102]:

$$\exp(-i\alpha\hat{\lambda}_r) = \hat{I} - i \sin \alpha \hat{\lambda}_r - (1 - \cos \alpha) \hat{\lambda}_r^2, \quad (5.14)$$

where $\hat{\lambda}_r^2 = \frac{2}{3}\hat{I} + \frac{1}{\sqrt{3}}(\vec{r}_{(8)} * \vec{r}_{(8)}) \cdot \vec{\lambda}$. The star product relationship for $\vec{r}_{(8)}$ is given by: $(\vec{r}_{(8)} * \vec{r}_{(8)}) \cdot \vec{\lambda} = \sqrt{3}\vec{r}_{(8)} \cdot \vec{\lambda} - 2\lambda_8$ (for more details see Appendix I). In contrast to the Pauli operator $\hat{\sigma}_r$, a strong coupling strength implies the application of $\hat{\lambda}_r$, but also of the identity operator \hat{I} and of the Hermitian operator $\hat{\lambda}_r^2$ defined in terms of the star product $\vec{r}_{(8)} * \vec{r}_{(8)}$. By considering $\alpha = \pi$ and $\beta = \pi$, the unitary three-level transformation $\hat{U}_{\lambda_r}^{\alpha,\beta}$ becomes:

$$\hat{U}_{\lambda_r}^{\alpha,\beta} = 2\hat{\lambda}_r - \text{diag}\{1, 1, -3\}. \quad (5.15)$$

The subsequent application of the transformations $\hat{U}_{\lambda_r}^{\alpha,\beta}$, $\hat{U}^{(1)}$ and $\hat{U}^{(2)}$ on $|\psi_i\rangle$ results in the state,

$$|\psi_s''\rangle = \left(\frac{1}{2}, -\frac{\sqrt{3}}{2} \cos \eta, \frac{\sqrt{3}}{2} \sin \eta \right)^T, \quad (5.16)$$

where a negative sign for the second coordinate appears with respect to the state $|\psi_i''\rangle$. The resolution of the Majorana polynomial $P(z)$ of the state $|\psi_s''\rangle$ is therefore similar to the case of $|\psi_i''\rangle$ and implies two Majorana qubits $|\phi_s^{(1,2)}\rangle$, which are the mirror images of $|\phi_i^{(1,2)}\rangle$ on the Bloch sphere as shown in figure 5.6.a.

The pairwise evolution of the corresponding Bloch vectors \vec{i}_1 and \vec{s}_1 (red, green) as well as \vec{i}_2 and \vec{s}_2 (blue, yellow) under the parameter η is illustrated in figure 5.6.a. Although all Bloch vectors evolve under the parameter η , the modular value $\lambda_{r,m}^{\alpha,\beta}$ is a real, constant value equal to one. In fact, both couples of vectors evolve symmetrically with respect to the plane ZY . The projections of a vector lying on this plane onto the vectors \vec{i}_1 and \vec{s}_1 (or on \vec{i}_2 and \vec{s}_2) are always equal. Since the final vector \vec{f} points at the south pole of the Bloch sphere (i.e. in the $-\vec{e}_z$ -direction), the modulus of $\lambda_{r,m}^{\alpha,\beta}$ is always one. Moreover, figure 5.6.b shows the behavior of the spherical quadrangles $\Omega_{i_1 r s_1 f}$ (red curve), $\Omega_{i_2 r s_2 f}$ (blue curve) and their sum (violet horizontal line) as a function of η . Because both spherical quadrangles feature a symmetric behavior with respect to 0 but with opposite signs, their sum remains constant at zero. As illustrated, we identify a change in the Bloch vectors behavior at the particular value $\eta_B = \arctan \frac{1}{\sqrt{2}} \approx 0.19(6)\pi$ (green line): the azimuth angles of both vectors \vec{i}_1 and \vec{s}_1 (\vec{i}_2 and \vec{s}_2) evolve symmetrically to the

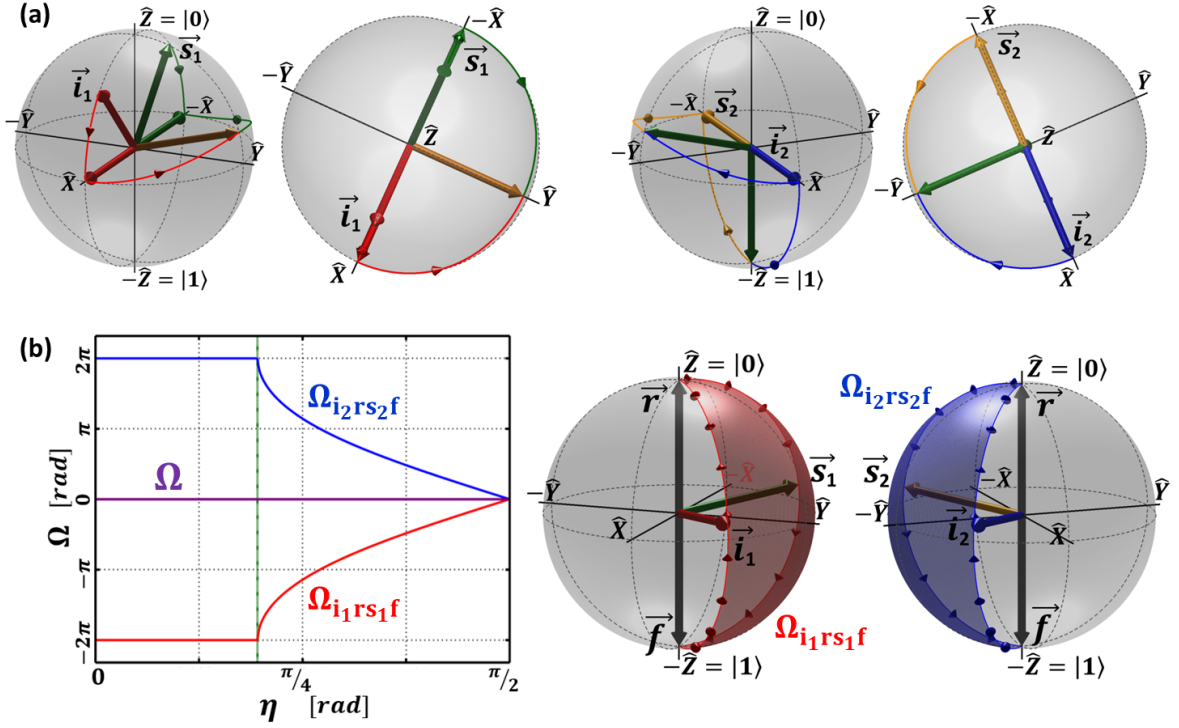


Figure 5.6: (a) Symmetric evolution of the initial Bloch vectors \vec{i}_1 (red) and \vec{i}_2 (blue) with respect to the resulting vectors \vec{s}_1 (green) and \vec{s}_2 (yellow) under the parameter η (front and bird's eye view). All illustrated Bloch vectors aligned with the $\pm \vec{e}_x$ -direction for $\eta_B \approx 0.19(6)\pi$. (b) The values of the solid angles $\Omega_{i_1 r s_1 f}$ (red), $\Omega_{i_2 r s_2 f}$ (blue) and their sum (violet) as a function of η as well as their representation on the Bloch sphere for a fixed η .

same value, here $\frac{\pi}{2}$ ($-\frac{\pi}{2}$). Because the Bloch vectors \vec{r} and \vec{f} finally lie on the same geodesic arc, the resulting solid angle $\Omega_{i_1 r s_1 f}$ ($\Omega_{i_2 r s_2 f}$) is zero.

The controlled evolution protocol acting on qutrit states can be reproduced by the interaction of three qubit states, where the first represents the meter and the other two the probed qutrit (see figure 5.8). Therefore, the notation of the initial probe as a symmetric product state is less practical. We use the general result demonstrated in Appendix K: a symmetric state $|\Psi\rangle = K(|\phi^{(1)}\rangle|\phi^{(2)}\rangle + |\phi^{(2)}\rangle|\phi^{(1)}\rangle)$ can always be written as a superposition of two orthogonal states $|\Psi\rangle = c_+|++\rangle - c_-|--\rangle$, where

the real parameters c_{\pm} and the state vectors $|\pm\rangle$ are given by:

$$\begin{aligned} c_{\pm} &= K (1 \pm |\langle\phi^{(2)}|\phi^{(1)}\rangle|) , \\ |\pm\rangle &= \frac{1}{\sqrt{2}} \left(\sqrt{1 \pm |\langle\phi^{(2)}|\phi^{(1)}\rangle|} |\epsilon_0\rangle \pm e^{-i\phi_{12}} \sqrt{1 \mp |\langle\phi^{(2)}|\phi^{(1)}\rangle|} |\epsilon_1\rangle \right) , \end{aligned} \quad (5.17)$$

with $\phi_{12} = \arg\langle\phi^{(1)}|\phi^{(2)}\rangle$. The orthogonal states $|\pm\rangle$ are expressed in the particular basis:

$$\begin{aligned} |\epsilon_0\rangle &= |\phi^{(1)}\rangle , \\ |\epsilon_1\rangle &= (1 - |\langle\phi^{(2)}|\phi^{(1)}\rangle|^2)^{-\frac{1}{2}} (|\phi^{(2)}\rangle - \langle\phi^{(1)}|\phi^{(2)}\rangle |\phi^{(1)}\rangle) . \end{aligned} \quad (5.18)$$

In the following, the orthogonal qubit states $|\pm\rangle$ are represented by the antiparallel vectors \vec{i}_{\pm} on the Bloch sphere. As shown in figure 5.7.a, both vectors are included in the plane ZX . Consequently, all state vectors $|\pm\rangle$ can be written as a simple superposition with real amplitudes of the ground states $|0\rangle$ and $|1\rangle$. In practice, this decomposition considerably simplifies the preparation process of the initial entangled two-qubit state $|\Psi_i''\rangle$. At the particular value $\eta_B \approx 0.19(6)\pi$, the Bloch vector \vec{i}_+ (\vec{i}_-) aligns with the \vec{e}_x -direction ($-\vec{e}_x$ -direction) and the real parameter c_+ becomes one (c_- is zero) as illustrated in figure 5.7.b. The preselected state $|\Psi_i''\rangle$ is then identified by the factorized two-qubit

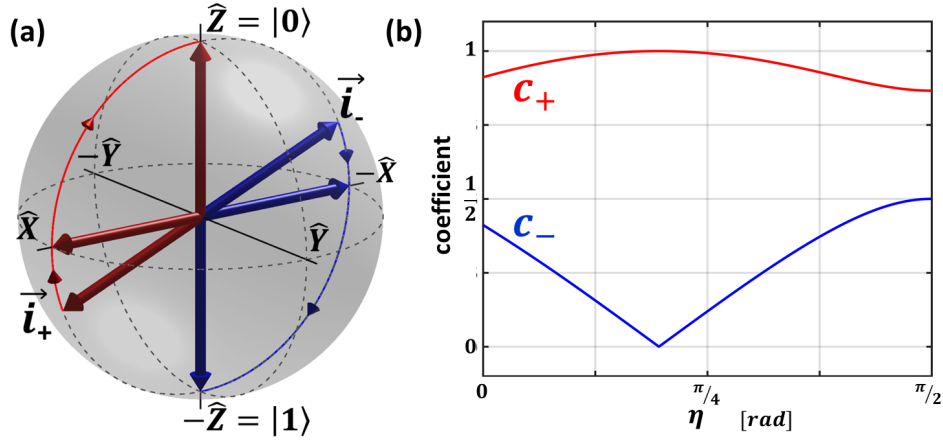


Figure 5.7: Alternative representation of the preselected symmetric state $|\Psi_i''\rangle$. (a) Evolution of the orthogonal vector states $|+\rangle$, $|-\rangle$ expressed by the antiparallel Bloch vectors \vec{i}_+ , \vec{i}_- with respect to the parameter η . (b) Representation of the coefficients c_+ , c_- determining the degree of entanglement of the preselected state as a function of η .

state $|x_+\rangle|x_+\rangle$ where $|x_+\rangle = 2^{-\frac{1}{2}}(|0\rangle + |1\rangle)$. This result agrees with the observations made in figure 5.6.a: the vectors \vec{i}_1 and \vec{i}_2 point both along the \vec{e}_x -direction. The coefficient c_- is used to determine the degree of entanglement $\epsilon = c_-/c_+$ [103]. In our case, this value evolves between $\left[0, \frac{1}{\sqrt{3}}\right]$ with the minimum at $\eta = \eta_B$ and the maximum at $\eta = \frac{\pi}{2}$. The degree of entanglement $\epsilon = 1$ corresponding to maximal entangled states is not reached.

Furthermore, the three-level unitary operator $\hat{U}_{\lambda_r}^{\alpha,\beta}$ conceptually applied on $|\psi_i\rangle$ must be replaced by the transformation:

$$\hat{U}_{3\times 3} = \hat{U}^{(2)}\hat{U}^{(1)}\hat{U}_{\lambda_r}^{\alpha,\beta} \left(\hat{U}^{(2)}\hat{U}^{(1)}\right)^\dagger, \quad (5.19)$$

acting on the initial state $|\psi_i''\rangle$. Because we consider now a quantum gate controlling the evolution of two incoming qubit systems, the three-level transformation $\hat{U}_{3\times 3}$ must be replaced by an operator $\hat{U}_{4\times 4}$ acting on the four dimensional Hilbert space defined by the two qubits. The equivalent form of the operator, which results directly from the Majorana representation, is given by:

$$\begin{pmatrix} a_{11} & a_{12} & a_{13} \\ a_{21} & a_{22} & a_{23} \\ a_{31} & a_{32} & a_{33} \end{pmatrix} \begin{pmatrix} c_0 \\ c_1 \\ c_2 \end{pmatrix} \rightarrow \begin{pmatrix} a_{33} & a_{32}/\sqrt{2} & a_{32}/\sqrt{2} & a_{31} \\ a_{23}/\sqrt{2} & (a_{22}-1)/2 & (a_{22}+1)/2 & a_{21}/\sqrt{2} \\ a_{23}/\sqrt{2} & (a_{22}+1)/2 & (a_{22}-1)/2 & a_{21}/\sqrt{2} \\ a_{13} & a_{12}/\sqrt{2} & a_{12}/\sqrt{2} & a_{11} \end{pmatrix} \begin{pmatrix} c_2 \\ c_1/\sqrt{2} \\ c_1/\sqrt{2} \\ c_0 \end{pmatrix} \quad (5.20)$$

Using the above described replacement on $\hat{U}_{3\times 3}$ defined in (5.19), we deduce the following transformation $\hat{U}_{4\times 4} \in SU(4)$ acting on the incoming two-qubit state² $|\Psi_i''\rangle$:

$$\hat{U}_{4\times 4} = \begin{pmatrix} 1 & 0 & 0 & 0 \\ 0 & -1 & 0 & 0 \\ 0 & 0 & -1 & 0 \\ 0 & 0 & 0 & 1 \end{pmatrix} = \hat{\sigma}_z \otimes \hat{\sigma}_z, \quad (5.21)$$

where the dependence on the parameter η disappears completely. The unitary transformations $\hat{U}_{4\times 4}$ is simply expressed as a product of two identical, local transformations and verifies: $|\Psi_s''\rangle = \hat{U}_{4\times 4}|\Psi_i''\rangle$. Finally, the controlled quantum evolution in (5.7) applied on a two-qubit probe can be summarized by the implementation of the unitary observable $\hat{\sigma}_z \otimes \hat{\sigma}_z$ (see figure 5.8). This observable is generally used to point out non-classical correlations between entangled qubit systems. Because the postselected two-qubit state $|1\rangle \otimes |1\rangle$ is an eigenvector state with the eigenvalue of $+1$ of the weakly

²Notice that the application of the *SWAP*-gate leaves invariant the symmetric two-qubit state $|\Psi_i''\rangle$. Even if this gate appertains to the class of nonlocal gates, it does not influence the entanglement [104].

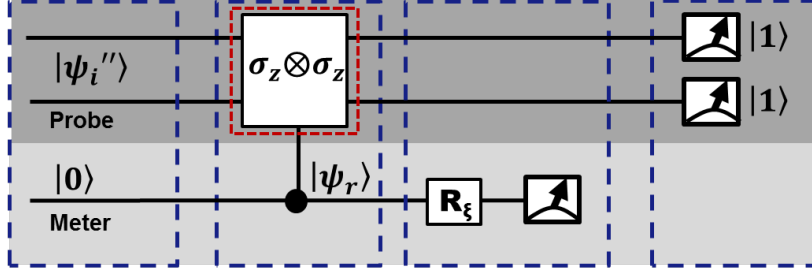


Figure 5.8: Controlled weak measurement protocol (see chapter 3) applied on the entangled two-qubit state $|\Psi_i''\rangle$. After the state preparation, both systems (the qubit meter and the two-qubit probe) interact via the nonlocal quantum gate. The latter applies with low probabilities the observable $\hat{\sigma}_z \otimes \hat{\sigma}_z$ on the two-qubit probe. Then, a local phase transformation to determine the quantum phase as well as the visibility is applied on the meter. Finally, the probe qubits are postselected along the state $|1\rangle \otimes |1\rangle$.

observed unitary operator $\hat{U}_{4 \times 4}$, the modular value is constant and equal to one for an arbitrary, preselected two-qubit state $|\Psi_i''\rangle$.

5.4 Summary

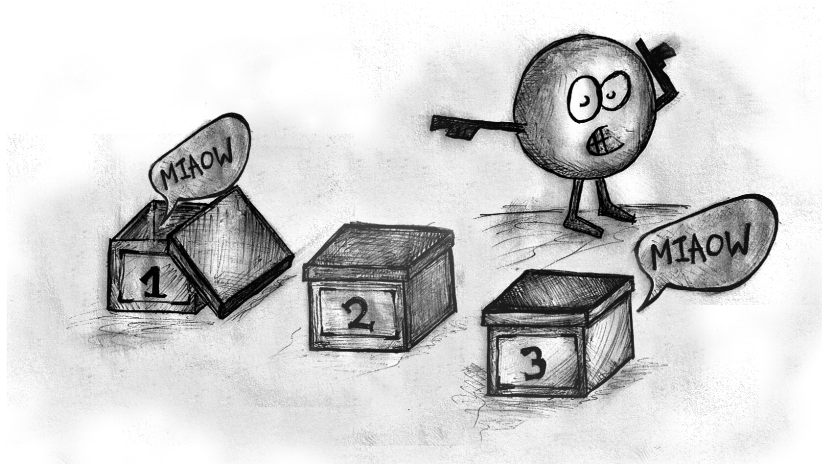
Exploiting the geometric representation described in chapter 4, we studied the discontinuities of the weak values argument of a two-level Pauli operator as well as a three-level projector, which occur around singularities of the weak value for orthogonal pre- and postselected states. We found its origin in the geometric phase, as one of its contributing solid-angle jumps by 2π across the singularity, which translates in a π -phase jump in the weak value (equivalent to a sign flip). In the case of photon measurement experiments (and in all other experiments using pure quantum objects), the appearance of the geometric phase assigns a non-classical meaning to the weak and modular values. Since the observation of the weak value $\sigma_{x,w}$ bases on the manipulation of non-classical photons, the purely classical interpretation of weak values [4] must be rejected. Moreover, this purely theoretical framework permitted to study the impact of a pre- and postselected three-level transformation on the controlled evolution protocol. To do this, we considered the preparation of entangled two-qubit states and the nonlocal application

of the unitary observable $\hat{\sigma}_z \otimes \hat{\sigma}_z$. Because we selected a final two-qubit state that is an eigenvector state of the weakly observed unitary operator, the modular value is constant and equal to one. Thus, the weakly pre- and postselected operator features a usual character. In the next chapter, we will describe the three-box paradox, where the same kind of unitary operator is weakly studied, but this time, for a final postselected state that induces unusual behaviors for the weak value.

6

A well-known quantum paradox in a new form

In this chapter, the three-box paradox will be recast in a new form, which involves quantum entanglement. To do this, the three-level quantum states involved in the paradox will be transformed by the Majorana representation to symmetric states of two qubits. Thus, we will present a two-particle version of this three-box paradox, where the particles will be pre- and postselected in classical separable states but will necessarily be found in entangled intermediate states when opening one amongst two of the three boxes. In this representation of the paradox, an observer will come to opposite conclusions about the entanglement state of the particles. In the past, some authors investigated this paradoxical behavior with weak measurements and weak values. Similarly, these weak values will be studied by the geometric approach, which will emphasize the non-classical origin of the three-box paradox.



6.1 The three-box paradox

The original three-box experiment involves a spinless particle and three separate quantum boxes described respectively by the mutually orthogonal vector states $|1\rangle$, $|2\rangle$ and $|3\rangle$ [22, 23]. The particle is preselected in the state:

$$|\psi_i\rangle = \frac{1}{\sqrt{3}} (|1\rangle + |2\rangle + |3\rangle) , \quad (6.1)$$

and postselected in the state:

$$|\psi_f\rangle = \frac{1}{\sqrt{3}} (|1\rangle - |2\rangle + |3\rangle) . \quad (6.2)$$

Only the ensemble of preselected particles with a successful postselection are taken into account during the experiment. The probability to find a preselected particle in the postselected state is $1/9$. In between this pre- and postselection, either the first box or the third box is observed using the projector $\hat{P}_k = |k\rangle\langle k|$, with $k = 1, 3$. If during an observation of \hat{P}_1 the particle is not found in the box, then its state is projected on the orthogonal subspace to box k by the projector $\hat{I} - \hat{P}_1$. Thus, when the preselected particle is not found in the first box, the projector $\hat{I} - \hat{P}_1$ projects the state of the particle on $\frac{1}{\sqrt{2}} (|2\rangle + |3\rangle)$, which is orthogonal to the postselected state $|\psi_f\rangle$. A similar reasoning is obtained for the third box: when the preselected particle is not found in this box, then the resulting quantum state is $\frac{1}{\sqrt{2}} (|1\rangle + |2\rangle)$, which is also orthogonal to $|\psi_f\rangle$. Consequently, a particle that was not observed in the opened box (when looking at box 1 or 3) is never postselected. Hence, references [22, 23] conclude that, for a successful postselection, the preselected particle is certain to be found in box 1, when searched for in this box (and not in boxes 2 or 3), and the particle is certain to be found in box 3, when searched for in this box (and not in 1 or 2) instead. Here, the quantum paradox, i.e. the phenomenon that classical physics cannot explain [23], results from the certitude to find a single particle in the box it is searched for (as the experiment deals essentially with observations of box 1 and 3). However, both observations exist separately and cannot be considered together. In fact, the conditional probabilities to observe the particle in between the pre- and postselection measurements are deduced from the ABL-rule first discussed by Aharonov, Bergman and Leibowitz in 1964. Applied to the three-box experiment, the conditional probabilities to find the spinless particle in the

three separate quantum boxes are given by:

$$P(1|i, f) = \frac{|\langle \psi_f | \hat{P}_1 | \psi_i \rangle|^2}{|\langle \psi_f | \hat{P}_1 | \psi_i \rangle|^2 + |\langle \psi_f | (\hat{I} - \hat{P}_1) | \psi_i \rangle|^2} = 1, \quad (6.3)$$

$$P(2|i, f) = \frac{|\langle \psi_f | \hat{P}_2 | \psi_i \rangle|^2}{|\langle \psi_f | \hat{P}_2 | \psi_i \rangle|^2 + |\langle \psi_f | (\hat{I} - \hat{P}_2) | \psi_i \rangle|^2} = \frac{1}{5}, \quad (6.4)$$

$$P(3|i, f) = \frac{|\langle \psi_f | \hat{P}_3 | \psi_i \rangle|^2}{|\langle \psi_f | \hat{P}_3 | \psi_i \rangle|^2 + |\langle \psi_f | (\hat{I} - \hat{P}_3) | \psi_i \rangle|^2} = 1. \quad (6.5)$$

In these expressions, the numerator represents the probability of observing the particle successively in the k^{th} state assuming it was in the initial state, then in the final state assuming it was in the k^{th} state: $P(k|i)P(f|k)$. On the other hand, the denominator represents the sum of the probability of each alternative pathway from the initial to the final state: $\sum_m P(m|i)P(f|m)$ where m represents the possible pathways (here, the projectors \hat{P}_k and $\hat{I} - \hat{P}_k$). The conditional probability to find the particle in one of the three boxes should obviously be one, which is in contrast to the sum of each individual conditional probability: $P(1|i, f) + P(2|i, f) + P(3|i, f) = 11/5$. The ABL-rule is contextual for systems with a Hilbert space $d \geq 3$. The conditional probabilities depend not only on the outcome associated to the final measurement but also on how the intermediate observable is measured. For example, when all boxes are simultaneously opened, the conditional probabilities to find the single particle in one of the three separate quantum boxes are given by:

$$P(1|i, f) = P(2|i, f) = P(3|i, f) = \frac{1}{3}. \quad (6.6)$$

This time, no contradiction is observed, since the sum rule holds, i.e. $P(1|i, f) + P(2|i, f) + P(3|i, f) = 1$. The paradoxical nature of the three-box experiment is strongly debated in the literature [20, 22, 23, 105]. Interestingly, some authors investigated this paradoxical behavior with weak measurements of the box projectors, considering their weak values as non-contextual quasiprobabilities [20]. These weak measurements reveal the non-contextual weak probabilities as they can be performed concurrently. Thus, the weak probabilities $P_{k,w}$, with $k = 1, 2, 3$, to find the particle in the separate quantum boxes can be considered simultaneously for any kind of observation. Moreover, the sum rule holds for the resulting weak probabilities, with $P_{123,w} = P_{1,w} + P_{2,w} + P_{3,w}$. Experimentally, these results are demonstrated in references [20, 105]. Now, we apply

the theorem proved in [22] on the box projectors: if the ABL-rule for a projector is equal to one then the weak value of this projector is one, too. Thus,

$$P_{1,w} = 1, \quad (6.7)$$

$$P_{3,w} = 1, \quad (6.8)$$

$$P_{123,w} = 1. \quad (6.9)$$

Similarly, the calculation of each of these weak probabilities for the given pre- and postselected states $|\psi_i\rangle, |\psi_f\rangle$ yields the same values. Since the sum rule holds for weak values, it is straightforward to show that the weak probability $P_{2,w}$ to find the particle in box 2 is the negative value -1 , which lies outside the range of eigenvalues of the projector \hat{P}_2 . Other authors have criticized several aspects of this interpretation, which can be found in references [106–109].

6.2 The two-particle version of this three-box paradox

In this section, we exploit the Majorana representation to extend the three-box paradox [22] to a larger class of quantum phenomena: quantum entanglement. Conceptually, the three-box experiment involves particles that were successfully pre- and postselected in the three-level quantum states $|\psi_i\rangle = \frac{1}{\sqrt{3}}(1, 1, 1)^T$ and $|\psi_f\rangle = \frac{1}{\sqrt{3}}(1, -1, 1)^T$. All other particles are ignored. We define the boxes by the basis states $|\psi_1\rangle = (1, 0, 0)^T$, $|\psi_2\rangle = (0, 1, 0)^T$ and $|\psi_3\rangle = (0, 0, 1)^T$. We now reformulate this paradox in terms of a bipartite quantum system, using the Majorana representation of all states involved in the experiment. The successive application of the unitary transformations:

$$\hat{U}^{(1)} = \frac{1}{\sqrt{6}} \begin{pmatrix} -\sqrt{3} & \sqrt{3} & 0 \\ -1 & -1 & 2 \\ \sqrt{2} & \sqrt{2} & \sqrt{2} \end{pmatrix}, \quad \hat{U}^{(2)} = \begin{pmatrix} \frac{-1-\sqrt{3}}{2\sqrt{2}} & \frac{1-\sqrt{3}}{2\sqrt{2}} & 0 \\ \frac{1-\sqrt{3}}{2\sqrt{2}} & \frac{1+\sqrt{3}}{2\sqrt{2}} & 0 \\ 0 & 0 & 1 \end{pmatrix} \quad (6.10)$$

leads to the factorisable pre- and postselected states $|\Psi_i''\rangle = |0\rangle|0\rangle$ and $|\Psi_f''\rangle = |\phi_f\rangle|\phi_f\rangle$ with the appropriate Bloch vectors $\vec{i} = (0, 0, 1)$ and $\vec{f} = \frac{1}{3}(2\sqrt{2}, 0, -1)$. The resolution of the Majorana polynomial of the three box states transformed under the unitary

transformations (6.10) provides the following three pairs of Bloch vectors:

$$\begin{aligned}
 |\Psi_1''\rangle &\rightarrow \vec{n}_{1,2} = \frac{1}{\sqrt{3}} \left(-\sqrt{2}x, \pm \sqrt[4]{3}\sqrt{6}x, -x \right), \\
 |\Psi_2''\rangle &\rightarrow \vec{r}_{1,2} = \pm \frac{1}{\sqrt{3}} \left(\sqrt{2}, 0, 1 \right), \\
 |\Psi_3''\rangle &\rightarrow \vec{m}_{1,2} = \frac{1}{\sqrt{3}} \left(\pm 2 \sqrt{x(1 \pm \sqrt[4]{3}\sqrt{x})}, 0, x \mp 2\sqrt[4]{3}\sqrt{x} \right),
 \end{aligned} \tag{6.11}$$

where $x = 2 - \sqrt{3}$. The appropriate normalization factors for the symmetrized states are $K_r^{-1} = \sqrt{2}$ and $K_m^{-1} = K_n^{-1} = 2\sqrt{3} - 2$. We represent these six vectors on the Bloch sphere in figure 6.1.a, revealing an elegant symmetry. The vectors \vec{r}_1 and \vec{r}_2 are anti-parallel and lie at the intersection between the blue and red planes defined by the other pairs of Bloch vectors $\vec{m}_{1,2}$ and $\vec{n}_{1,2}$, respectively. These planes are orthogonal to each other and each plane acts as a mirror plane for the vectors defining the other plane (i. e. the plane containing vectors \vec{n}_1 and \vec{n}_2 defines a reflection symmetry between the vectors \vec{m}_1 and \vec{m}_2 and the converse symmetry holds as well when exchanging the roles of the pairs). Let us also note that the $\sim 74^\circ$ angle between \vec{r}_1 and the two vectors $\vec{m}_{1,2}$ is equal to the angle between \vec{r}_2 and the two vectors $\vec{n}_{1,2}$ (the $\vec{m}_{1,2}$ and $\vec{n}_{1,2}$ pairs are related through a 90° rotation-reflection symmetry with respect to the $\vec{r}_{1,2}$ axis). Finally, the vectors \vec{i} and \vec{f} associated with the pre- and postselected states are placed symmetrically around the \vec{r}_1 vector in the blue plane defined by the $\vec{m}_{1,2}$ pair, so that they are mirror images of each other with respect to the red symmetry plane. Consequently, the structure formed on the Bloch sphere by all vectors involved in the three-box experiment corresponds to the symmetry group C_{2v} .

This symmetry allows us to introduce the local rotation operation $\hat{U}_r = -\hat{\sigma}_r \otimes \hat{\sigma}_r$ under which the three-box experiment is left invariant (the operator $\hat{\sigma}_r = \vec{r}_1 \cdot \vec{\sigma}$ effectively exchanges the vectors \vec{m}_1 with \vec{m}_2 , \vec{n}_1 with \vec{n}_2 , and \vec{i} with \vec{f} , while leaving $\vec{r}_{1,2}$ invariant; note that states may pick up a phase in the process). In particular, $\hat{\sigma}_r|0\rangle = |\phi_f\rangle$. Therefore, the weak values of the box projectors are necessarily real, while their argument of either 0 or π determines their sign. Indeed, the weak value on the k^{th} box consist of the products of two projector weak values $\Pi_{k,w}^{(3)} = \Pi_{k_1,w}^{(2)} \Pi_{k_2,w}^{(2)}$. For the projectors on box two and three, all vectors are in the same (blue) plane. As result, the solid angles determining the argument of the weak values can take only the values 0 or 2π , as shown figure 6.1.b-c, so that they determine the sign of the weak values. To show that the first projector takes

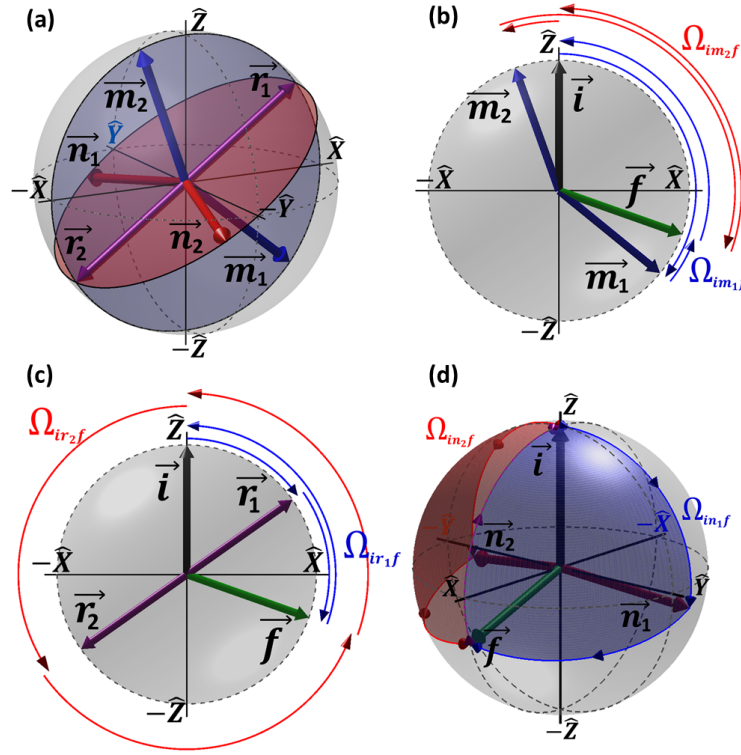


Figure 6.1: Representation in the Bloch sphere of the relevant states appearing in the three-box experiment. (a) The three couples of vectors $\vec{m}_{1,2}$, $\vec{r}_{1,2}$ and $\vec{n}_{1,2}$ form a structure which corresponds to the symmetry group $C_{2\nu}$. (b-d) By introducing the pre- and postselected vectors \vec{i} and \vec{f} , each solid angle is determined by following the geodesic trajectories.

a real value, we apply the unitary transformation $\hat{\sigma}_r$ associated with the symmetry: $\Pi_{n_1,w}^{(2)} = \langle \phi_f | \hat{\sigma}_r^\dagger \hat{\sigma}_r | \phi_{n_1} \rangle \langle \phi_{n_1} | \hat{\sigma}_r^\dagger \hat{\sigma}_r | \phi_i \rangle \langle \phi_f | \hat{\sigma}_r^\dagger \hat{\sigma}_r | \phi_i \rangle^{-1} = \langle \phi_i | \phi_{n_2} \rangle \langle \phi_{n_2} | \phi_f \rangle \langle \phi_i | \phi_f \rangle^{-1} = \Pi_{n_2,w}^{(2)*}$, so that the two weak values are complex conjugates of each other. The corresponding solid angles are shown on figure 6.1.d. By applying the general relations (4.51) and (4.52), it is straightforward to show, that the values determined by the geometric approach are in agreement with the standard results of the quantum three-box paradox (see Table 6.1). Here, we see that the negative sign of the weak value of the second box projector $\hat{P}_{2,w}$ arises from the quantum geometric phase of π , which emphasizes its non-classical origin.

We now consider the physical interpretation of the box projectors in the two-qubit space. Due to the rotational invariance of the problem, the orthogonal box states are

Box 1	$ \Pi_{n_1,w} = 1$	$\Omega_{in_1f} = -2 \arctan \sqrt{3 + 2\sqrt{3}}$
$\hat{P}_{1,w} = 1$	$ \Pi_{n_2,w} = 1$	$\Omega_{in_2f} = +2 \arctan \sqrt{3 + 2\sqrt{3}}$
Box 2	$ \Pi_{r_1,w} = \sqrt{2 + \sqrt{3}}$	$\Omega_{ir_1f} = 0$
$\hat{P}_{2,w} = -1$	$ \Pi_{r_2,w} = \sqrt{2 - \sqrt{3}}$	$\Omega_{ir_2f} = 2\pi$
Box 3	$ \Pi_{m_1,w} = 1$	$\Omega_{im_1f} = 0$
$\hat{P}_{3,w} = 1$	$ \Pi_{m_2,w} = 1$	$\Omega_{im_2f} = 0$

Table 6.1: Weak values of the box projectors in the three-box paradox determined from the weak values of the associated qubit projectors deduced from the Majorana representation.

orthogonal eigenstates of the rotation operator \hat{U}_r . Because the qubit states associated with the vectors $\vec{r}_{1,2}$ are orthogonal, they define a basis of the qubit Hilbert space, noted $\{|\phi_r\rangle, |\phi_{-r}\rangle\}$ where the actual states are $|\phi_{\pm r}\rangle = \sqrt{\frac{1}{6}(3 \pm \sqrt{3})}|0\rangle \pm \sqrt{\frac{1}{6}(3 \mp \sqrt{3})}|1\rangle$. Using this basis to express the box states in the Majorana representation, we find that the relevant four orthogonal eigenstates of the operator are:

$$|\Psi''_1\rangle = \frac{|\phi_r\rangle|\phi_r\rangle + \sqrt{3}|\phi_{-r}\rangle|\phi_{-r}\rangle}{2}, \quad (6.12)$$

$$|\Psi''_2\rangle = \frac{|\phi_r\rangle|\phi_{-r}\rangle + |\phi_{-r}\rangle|\phi_r\rangle}{\sqrt{2}}, \quad (6.13)$$

$$|\Psi''_3\rangle = \frac{\sqrt{3}|\phi_r\rangle|\phi_r\rangle - |\phi_{-r}\rangle|\phi_{-r}\rangle}{2}, \quad (6.14)$$

$$|\tilde{\Psi}''_4\rangle = \frac{|\phi_r\rangle|\phi_{-r}\rangle - |\phi_{-r}\rangle|\phi_r\rangle}{\sqrt{2}}, \quad (6.15)$$

where $|\Psi''_2\rangle$ and $|\tilde{\Psi}''_4\rangle$ are associated with the eigenvalue $+1$ and where $|\Psi''_1\rangle$ and $|\Psi''_3\rangle$ are associated with the eigenvalue -1 . The state $|\Psi''_2\rangle$ above defines box 2 because it matches obviously the symmetrized form obtained from the Majorana representation in terms of the states associated with the vectors $\vec{r}_{1,2}$. It corresponds to a maximally entangled Bell state. The eigenvector $|\tilde{\Psi}''_4\rangle$ shares its eigenvalue with $|\Psi''_2\rangle$ but cannot represent a state of the three-level system because it corresponds to the anti-symmetric subspace of the two-qubit space. Therefore, the states representing the box-1 and box-3 projectors are necessarily orthogonal vectors in the subspace spanned by the two-qubit states $|\phi_r\rangle|\phi_r\rangle$ and $|\phi_{-r}\rangle|\phi_{-r}\rangle$, which share the same eigenvalue -1 of \hat{U}_r . The calculations leading to the exact form (6.12) and (6.14) of states $|\Psi''_1\rangle$ and $|\Psi''_3\rangle$ are explained in Appendix L. The states are non-maximally entangled, with a von

Neumann entropy of 0.81 (the von Neumann entropy is 0 for pure states and 1 for maximally entangled 2-qubit states). The degree of entanglement of these states can also be ascertain geometrically on the Bloch sphere [100, 110–112], by looking at the angle between the two vectors representing the symmetric state (antipodal Majorana points correspond to maximally entangled states while superposed Majorana points correspond to separable states). Let us note as well that the closest separable state is given by the angle bisector between the two Majorana points [111]. These corresponds to the state $|\phi_{-r}\rangle|\phi_{-r}\rangle$ for box-1 state $|\Psi_1''\rangle$ and to the orthogonal state $|\phi_r\rangle|\phi_r\rangle$ for box-3 state $|\Psi_3''\rangle$.

Now we can reformulate the three-box paradox in terms of the two-particle system. We consider all –and only– the particles that were successfully pre- and postselected in the separable states $|\Psi_i''\rangle = |0\rangle|0\rangle$ and $|\Psi_f''\rangle = |\phi_f\rangle|\phi_f\rangle$, respectively. We define the boxes by projective measurements on the states $|\Psi_1''\rangle$, $|\Psi_2''\rangle$, $|\Psi_3''\rangle$, and $|\tilde{\Psi}_4''\rangle$. Note that we can safely ignore the fourth box defined by the projector on the antisymmetric state $|\tilde{\Psi}_4''\rangle$ because it is orthogonal to both the initial and final symmetric states. This experiment corresponds to a Bell-type measurement, related to the unitary observable $\hat{U}_r = -\hat{\sigma}_r \otimes \hat{\sigma}_r$. This observable is generally used to point out non-classical correlations between bipartite qubit systems. Exactly as in the standard formulation of the paradox, if we were to open box one or box three, we would find the particle there with certainty. In this case however, we would deduce that the particles are necessarily entangled, although both their initial and final states are classical separable states. In the standard formulation of the paradox, the particles start and end in a superposed quantum state and the measurement is represented by three classical boxes. After transposing the paradox in the two-qubit Majorana representation, our particles start and end in a classical state but our boxes become quantum and entangle the particles in the process. The occurrence of entanglement in the bipartite system is an unavoidable feature of the Majorana representation of the paradox. In particular, it cannot be removed through a unitary transformation because one of the basis state of the three-level system is necessarily entangled in the symmetric two-qubit representation and any attempt to disentangle the qubit states associated with the box projectors would entangle the qubit states describing the initial and final states.

6.3 Summary

The geometric representation introduced in chapter 4 allowed us to recast the three-box paradox in a new form, which involves quantum entanglement. We analyzed the weak values of the box projectors in terms of vectors on the Bloch sphere. We found that the origin of the negative sign occurring in one of the weak values – which has been sometimes interpreted as a -1 quasiprobability in the literature – is directly related to a geometric quantum phase defined on the Bloch sphere. In the two-particle version of the three-box paradox, the particles are pre- and postselected in classical separable states but are necessarily found in entangled intermediate states when opening one amongst two of the three boxes. In this representation of the paradox, the boxes are quantum, represented by projectors on eigenvectors of a Bell-type measurement observable, while the initial and final states are classical. A paradoxical formulation of this observation would pose the question of the classical vs quantum evolution of the particle pairs in the pre- and postselected ensemble.

7

Conclusion and Perspectives

In this thesis, a full geometric description of weak and modular values of discrete quantum systems is achieved using the polar representation of these values. For this purpose, the unusual properties of weak and modular values are experimentally studied by devising a controlled evolution protocol. Then, theoretical investigations demonstrate that these properties of weak and modular values can all be explained by the behavior of geometric quantities described on the Bloch sphere.

The first part of this thesis provides an interferometric procedure determining experimentally the modulus and the argument of weak and modular values for arbitrary measurement strengths. The relations between these polar components and the meter readouts allow the investigation of weak and modular values by performing a one-step visibility and phase measurement. In the standard approach to weak measurements, it is the meter shift in position and in momentum that yield the real and the imaginary part of weak values. Thus, the interferometric visibility revealing the modulus of weak and modular values plays the same role than the pointer shifts in standard weak measurements. This provides us with deeper insight into the physics of weak and modular values, beyond the association of their real and imaginary part to meter shifts. Experimentally, this interferometric protocol is demonstrated using polarization-entangled photon pairs produced by type-I spontaneous parametric down-conversion. The acquisition does not suffer the limitations of the standard weak measurement technique for large weak and modular values, while the presented procedure is applicable for both weak- and strong measurement conditions. This opens the way to determine these values with greater accuracy, particularly for nearly orthogonal pre- and postselected states. The weak point of this reconstruction procedure is its sensitive dependence on the experimental meter parameters. In the range of slight variations of the interferomet-

ric visibility, a misestimation of these parameters causes errors in the determination of the modulus. A better evaluation of the meter parameters is however possible by representing the modulus of weak and modular values by the bounded arc tangent function: potential disagreements are no longer masked by large scales due to an unbounded modulus. To finalize the study of this quantum measurement procedure, the behavior of the argument acquisitions around discontinuous phase jumps is evaluated by reconstructing the postselected, quantum states. The experimental data is in full agreement with theory, but it features for half of the preparations small deviations from the postselected quantum states. These disagreements result from experimental errors which influence directly the argument acquisitions. Nonetheless, all acquisitions reproduce correctly the discontinuous jumps of the quantum phase. A part of these theoretical and experimental results led to a first publication [39] in 2016. In a recent work, the protocol of controlled quantum evolutions is used to study technical or experimental difficulties that arise during the implementation of non-linear two-qubit gates [113]. Moreover, the concept to determine weak values for strong measurement strengths is used in the letter [114] published in 2017 (which is criticizable though [115]). The authors report an interferometric measurement scheme that characterizes the weak value of a spin-1/2 operator via direct measurements, using both strong and weak interactions.

In the second part, pre- and postselected weak and modular values of discrete quantum systems are described by a purely geometric approach. For this reason, the Majorana representation is applied on N -level quantum systems, which assigns a correspondence between the states of these systems and symmetric states of $N - 1$ qubits. This representation opens the way to express weak and modular values of N dimensional systems by $N - 1$ independent quantities which possess all a representation on the Bloch sphere. The modulus is determined by a product of $N - 1$ square roots of probability ratios and the argument by a sum of $N - 1$ spherical polygons. Furthermore, the argument of weak and modular values is associated to the geometric Pancharatnam phase that has a non-controversial physical meaning with no classical counterpart. All these theoretical results led to a submitted publication [38] in 2017. On the basis of the geometric description of modular values of two-level quantum systems in the first publication [39], the geometric origin of the argument of modular values is studied in reference [116] published in 2016. The authors show that the argument of the modular value of an arbitrary operator can be represented by a geometric Pancharatnam phase and by an intrinsic phase with a dynamical contribution.

The interest of this geometric approach to the physical analysis of weak and modular values is shown using direct applications in three fields of weak measurement theory. In a first application, this approach identifies the purely geometric origin of discontinuous phase effects around arbitrary large weak values. Well-reported for the qubit case, the studies point out that this phase discontinuity of higher-level quantum systems are caused by a jump of 2π of at least one solid angle on the Bloch sphere. Similar effects are observed for weak values of qubits during the controlled evolution experiments illustrated in chapter 2. Then, in a second theoretical application, the controlled evolution procedure revealing this time modular values of pre- and postselected high-level quantum systems is reproduced by manipulating the simpler multi-qubit systems. The equivalence between these systems of different algebraic structures is demonstrated and requires the preparation of entangled multi-qubit states. While the experimental realization of these multi-qubit protocols is mostly limited by current technologies, this multi-qubit manipulation can be helpful in particular and simple cases. To do this, a pre- and postselected ensemble of a three-level quantum system is selected that induces a constant modular value. Thus, the measurement protocol simply applies (via a nonlocal transformation) two local operators on the two-qubit probe state. In a third application, the geometric framework is used to rewrite the quantum three-box paradox in terms of entangled two-qubit states. In this way, the quantum paradox is extended to a larger class of quantum phenomena: quantum entanglement. The geometric description of this quantum paradox shows that the origin of the negative sign occurring in one the weak values – which has been sometimes interpreted has a -1 pseudo-probability in the literature – is directly related to a geometric quantum phase defined on the Bloch sphere.

In summary, this thesis provides an interferometric measurement protocol to determine the polar components of weak and modular values. Using polarization-entangled photons, the experimental feasibility of this measurement protocol is pointed out for weak and even for strong measurement strengths. Thereby, the protocol does not suffer the limitations of the standard weak measurement technique for large weak and modular values. Additionally, a geometric representation of weak and modular values is introduced for discrete quantum systems. This geometric approach is used to the physical analysis of discontinuous jumps of the quantum phase, or in the field of quantum paradoxes. This theoretical framework allows to recast pre- and postselected experiments manipulating high-level quantum systems in form of entangled multi-qubit states by

applying local and nonlocal transformations. In a next step, more general forms of weak and modular values of three and high-level quantum systems could be studied. It should be realised, however, that higher-level quantum systems give rise to more complexer multi-qubit protocols implementing nontrivial, multi-qubit transformations. Thus, most of the theoretical protocols are limited by current technologies.

Another perspective is the realization of the three-box experiment by manipulating pre- and postselected qubit states. The Hong–Ou–Mandel interferometer with variable transmission and reflection indices seems to be promising to implement strong and weak measurements of entangled two-qubit states. On the one hand, strong measurements with equal transmission and reflection indices lead to the contextual ABL-formula, and on the other hand, weak measurements with a small reflection index provide the weak probabilities. To simplify to a maximum the experimental set-up, the maximally entangled Bell states (with a von Neumann entropy of 1 rather than an entropy of 0.81) are examined in between the pre- and postselection process. Thus, the separable qubit states chosen during the pre- and postselection process in chapter 6 must slightly be modified. In this way, our version of the three-box experiment can be realized by using only one nonlocal transformation, here the Hong–Ou–Mandel interferometer, in between the pre- and postselection.

The application of the geometric description on other quantum paradoxes is under consideration. For example, the quantum Cheshire cat experiment seems to be suitable for the geometric formalism [30]. The surprising effect in this interferometric experiment based on pre- and postselection is the ability to “separate” the location of a particle from its spin-1/2 component: the particle is located in one path of the Mach–Zehnder interferometer, and its spin property in the other one. Similarly to the three-box paradox, this paradoxical behavior of the pre- and postselected system is investigated with weak measurements [51]. Recently, spin-1 operators were proposed to realize the quantum Cheshire cat experiment [26]. In fact, the observation in between pre- and postselection bases on the application of projection operators to identify the location of the particle, and on the application of the spin-1/2 operator $\hat{\sigma}_r$. The measurement of the spin-1/2 component in the second path takes place by implementing the operator $\hat{\Pi}_2 \hat{\sigma}_r$ with the eigenvalues $+1$ or -1 if the spin component is present, and the eigenvalue 0 if the spin component is not there. Thus, the geometric framework should be used this time to transform symmetric two-qubit states into three-level quantum states.

Bibliography

- [1] Y. Aharonov, D. Z. Albert, and L. Vaidman, “How the result of a measurement of a component of the spin of a spin-1/2 particle can turn out to be 100,” *Physical Review Letters*, vol. 60, no. 14, pp. 1351–1354, 1988.
- [2] Y. Kedem and L. Vaidman, “Modular values and weak values of quantum observables,” *Physical Review Letters*, vol. 105, no. 23, p. 230401, 2010.
- [3] Y. Aharonov and L. Vaidman, “The two-state vector formalism: An updated review,” in *Time in Quantum Mechanics* (J. G. Muga, R. S. Mayato, and L. Eguisquiza, eds.), no. 734 in Lecture Notes in Physics, pp. 399–447, Springer Berlin Heidelberg, 2008.
- [4] C. Ferrie and J. Combes, “How the result of a single coin toss can turn out to be 100 heads,” *Physical Review Letters*, vol. 113, no. 12, p. 120404, 2014.
- [5] A. Brodutch, “Comment on “how the result of a single coin toss can turn out to be 100 heads”,” *Physical Review Letters*, vol. 114, no. 11, p. 118901, 2015.
- [6] L. Vaidman, “Comment on “how the result of a single coin toss can turn out to be 100 heads”,” *arXiv:1409.5386*, 2014.
- [7] J. Dressel, “Weak values as interference phenomena,” *Physical Review A*, vol. 91, no. 3, p. 032116, 2015.
- [8] L. Qin, W. Feng, and X.-Q. Li, “Simple understanding of quantum weak values,” *Scientific Reports*, vol. 6, p. 20286, 2016.

- [9] O. Hosten and P. Kwiat, “Observation of the spin hall effect of light via weak measurements,” *Science*, vol. 319, no. 5864, pp. 787–790, 2008.
- [10] P. B. Dixon, D. J. Starling, A. N. Jordan, and J. C. Howell, “Ultrasensitive beam deflection measurement via interferometric weak value amplification,” *Physical Review Letters*, vol. 102, no. 17, p. 173601, 2009.
- [11] D. J. Starling, P. B. Dixon, A. N. Jordan, and J. C. Howell, “Optimizing the signal-to-noise ratio of a beam-deflection measurement with interferometric weak values,” *Physical Review A*, vol. 80, no. 4, p. 041803, 2009.
- [12] Y. Tang and A. E. Cohen, “Optical chirality and its interaction with matter,” *Physical Review Letters*, vol. 104, no. 16, p. 163901, 2010.
- [13] H. Rhee, Y.-G. June, J.-S. Lee, K.-K. Lee, J.-H. Ha, Z. H. Kim, S.-J. Jeon, and M. Cho, “Femtosecond characterization of vibrational optical activity of chiral molecules,” *Nature*, vol. 458, no. 7236, pp. 310–313, 2009.
- [14] J. S. Lundeen, B. Sutherland, A. Patel, C. Stewart, and C. Bamber, “Direct measurement of the quantum wavefunction,” *Nature*, vol. 474, no. 7350, pp. 188–191, 2011.
- [15] J. Z. Salvail, M. Agnew, A. S. Johnson, E. Bolduc, J. Leach, and R. W. Boyd, “Full characterization of polarization states of light via direct measurement,” *Nature Photonics*, vol. 7, no. 4, pp. 316–321, 2013.
- [16] J. S. Lundeen and C. Bamber, “Procedure for direct measurement of general quantum states using weak measurement,” *Physical Review Letters*, vol. 108, no. 7, p. 070402, 2012.
- [17] S. Kocsis, B. Braverman, S. Ravets, M. J. Stevens, R. P. Mirin, L. K. Shalm, and A. M. Steinberg, “Observing the average trajectories of single photons in a two-slit interferometer,” *Science*, vol. 332, no. 6034, pp. 1170–1173, 2011.
- [18] R. Flack and B. J. Hiley, “Weak measurement and its experimental realisation,” *Journal of Physics: Conference Series*, vol. 504, no. 1, p. 012016, 2014.
- [19] A. Matzkin, “Weak measurements of trajectories in quantum systems: classical, Bohmian and sum over paths,” *Journal of Physics A: Mathematical and Theoretical*, vol. 48, no. 30, p. 305301, 2015.

- [20] K. J. Resch, J. S. Lundeen, and A. M. Steinberg, “Experimental realization of the quantum box problem,” *Physics Letters A*, vol. 324, no. 2–3, pp. 125–131, 2004.
- [21] J. S. Lundeen and A. M. Steinberg, “Experimental joint weak measurement on a photon pair as a probe of Hardy’s paradox,” *Physical Review Letters*, vol. 102, no. 2, p. 020404, 2009.
- [22] Y. Aharonov and L. Vaidman, “Complete description of a quantum system at a given time,” *Journal of Physics A: Mathematical and General*, vol. 24, no. 10, p. 2315, 1991.
- [23] T. Ravon and L. Vaidman, “The three-box paradox revisited,” *Journal of Physics A: Mathematical and Theoretical*, vol. 40, no. 11, p. 2873, 2007.
- [24] J. Dressel and A. N. Jordan, “Weak values are universal in von Neumann measurements,” *Physical Review Letters*, vol. 109, no. 23, p. 230402, 2012.
- [25] J. Dressel and A. N. Jordan, “Significance of the imaginary part of the weak value,” *Physical Review A*, vol. 85, no. 1, p. 012107, 2012.
- [26] A. Di Lorenzo, “Measurement of a spin-1 system,” *Physics Letters A*, vol. 379, no. 30–31, pp. 1681–1688, 2015.
- [27] X. Xiao and Y.-L. Li, “Protecting qutrit-qutrit entanglement by weak measurement and reversal,” *The European Physical Journal D*, vol. 67, no. 10, p. 204, 2013.
- [28] X. Xiao, “Protecting qubit-qutrit entanglement from amplitude damping decoherence via weak measurement and reversal,” *Physica Scripta*, vol. 89, no. 6, p. 065102, 2014.
- [29] M. Jerger, Y. Reshitnyk, M. Oppliger, A. Potočnik, M. Mondal, A. Wallraff, K. Goodenough, S. Wehner, K. Juliusson, N. K. Langford, and A. Fedorov, “Contextuality without nonlocality in a superconducting quantum system,” *Nature Communications*, vol. 7, p. 12930, 2016.
- [30] Y. Aharonov, S. Popescu, D. Rohrlich, and P. Skrzypczyk, “Quantum Cheshire cats,” *New Journal of Physics*, vol. 15, no. 11, p. 113015, 2013.

- [31] S. Pancharatnam, “Generalized theory of interference, and its applications,” *Proceedings of the Indian Academy of Sciences - Section A*, vol. 44, no. 5, pp. 247–262, 1956.
- [32] H. Kobayashi, S. Tamate, T. Nakanishi, K. Sugiyama, and M. Kitano, “Observation of geometric phases in quantum erasers,” *Journal of the Physical Society of Japan*, vol. 80, no. 3, p. 034401, 2011.
- [33] S. Tamate, H. Kobayashi, T. Nakanishi, K. Sugiyama, and M. Kitano, “Geometrical aspects of weak measurements and quantum erasers,” *New Journal of Physics*, vol. 11, no. 9, p. 093025, 2009.
- [34] R. M. Camacho, P. B. Dixon, R. T. Glasser, A. N. Jordan, and J. C. Howell, “Realization of an all-optical zero to π cross-phase modulation jump,” *Physical Review Letters*, vol. 102, no. 1, p. 013902, 2009.
- [35] D. R. Solli, C. F. McCormick, R. Y. Chiao, S. Popescu, and J. M. Hickmann, “Fast light, slow light, and phase singularities: A connection to generalized weak values,” *Physical Review Letters*, vol. 92, no. 4, p. 043601, 2004.
- [36] Arvind, K. S. Mallesh, and N. Mukunda, “A generalized Pancharatnam geometric phase formula for three-level quantum systems,” *Journal of Physics A: Mathematical and General*, vol. 30, no. 7, p. 2417, 1997.
- [37] S. Tamate, K. Ogawa, and M. Kitano, “Bloch-sphere representation of three-vertex geometric phases,” *Physical Review A*, vol. 84, no. 5, p. 052114, 2011.
- [38] M. Cormann and Y. Caudano, “Geometric description of modular and weak values in discrete quantum systems using the Majorana representation,” *Journal of Physics A: Mathematical and Theoretical*, 2017 (accepted paper).
- [39] M. Cormann, M. Remy, B. Kolaric, and Y. Caudano, “Revealing geometric phases in modular and weak values with a quantum eraser,” *Physical Review A*, vol. 93, no. 4, p. 042124, 2016.
- [40] J. Preskill, “Lecture notes for physics 229: Quantum information and computation,” *California Institute of Technology*, vol. 12, 1998.
- [41] J. v. Neumann, *Mathematical Foundations of Quantum Mechanics*. Princeton N.J.: Princeton University Press, 1st ed., 1955.

- [42] A. G. Kofman, S. Ashhab, and F. Nori, “Nonperturbative theory of weak pre- and post-selected measurements,” *Physics Reports*, vol. 520, no. 2, pp. 43–133, 2012.
- [43] Y. Aharonov, P. G. Bergmann, and J. L. Lebowitz, “Time symmetry in the quantum process of measurement,” *Physical Review*, vol. 134, no. 6, pp. 1410–1416, 1964.
- [44] Y. Aharonov and D. Rohrlich, “The quantum world,” in *Quantum Paradoxes*, pp. 265–286, Wiley-VCH Verlag GmbH, 2005.
- [45] Y. Aharonov, S. Popescu, and J. Tollaksen, “A time-symmetric formulation of quantum mechanics,” *Physics Today*, vol. 63, no. 11, pp. 27–32, 2010.
- [46] I. M. Duck, P. M. Stevenson, and E. C. G. Sudarshan, “The sense in which a “weak measurement” of a spin-1/2 particle’s spin component yields a value 100,” *Physical Review D*, vol. 40, no. 6, pp. 2112–2117, 1989.
- [47] R. Jozsa, “Complex weak values in quantum measurement,” *Physical Review A*, vol. 76, no. 4, p. 044103, 2007.
- [48] L. M. Johansen, “Weak measurements with arbitrary probe states,” *Physical Review Letters*, vol. 93, no. 12, p. 120402, 2004.
- [49] S. Sponar, T. Denkmayr, H. Geppert, H. Lemmel, A. Matzkin, J. Tollaksen, and Y. Hasegawa, “Weak values obtained in matter-wave interferometry,” *Physical Review A*, vol. 92, no. 6, p. 062121, 2015.
- [50] J. Tollaksen, Y. Aharonov, A. Casher, T. Kaufherr, and S. Nussinov, “Quantum interference experiments, modular variables and weak measurements,” *New Journal of Physics*, vol. 12, no. 1, p. 013023, 2010.
- [51] T. Denkmayr, H. Geppert, S. Sponar, H. Lemmel, A. Matzkin, J. Tollaksen, and Y. Hasegawa, “Observation of a quantum Cheshire cat in a matter-wave interferometer experiment,” *Nature Communications*, vol. 5, 2014.
- [52] A. M. Brańczyk, P. E. M. F. Mendonça, A. Gilchrist, A. C. Doherty, and S. D. Bartlett, “Quantum control of a single qubit,” *Physical Review A*, vol. 75, no. 1, p. 012329, 2007.

- [53] R. Vijay, C. Macklin, D. H. Slichter, S. J. Weber, K. W. Murch, R. Naik, A. N. Korotkov, and I. Siddiqi, “Stabilizing Rabi oscillations in a superconducting qubit using quantum feedback,” *Nature*, vol. 490, no. 7418, pp. 77–80, 2012.
- [54] G. J. Pryde, J. L. O’Brien, A. G. White, T. C. Ralph, and H. M. Wiseman, “Measurement of quantum weak values of photon polarization,” *Physical Review Letters*, vol. 94, no. 22, p. 220405, 2005.
- [55] T. A. Brun, L. Diósi, and W. T. Strunz, “Test of weak measurement on a two- or three-qubit computer,” *Physical Review A*, vol. 77, no. 3, p. 032101, 2008.
- [56] H. F. Hofmann, “Sequential measurements of non-commuting observables with quantum controlled interactions,” *New Journal of Physics*, vol. 16, no. 6, p. 063056, 2014.
- [57] S. Wu and K. Mølmer, “Weak measurements with a qubit meter,” *Physics Letters A*, vol. 374, no. 1, pp. 34–39, 2009.
- [58] Y. Shikano and S. Tanaka, “Estimation of spin-spin interaction by weak measurement scheme,” *Europhysics Letters*, vol. 96, no. 4, p. 40002, 2011.
- [59] J. P. Groen, D. Ristè, L. Tornberg, J. Cramer, P. C. de Groot, T. Picot, G. Johansson, and L. DiCarlo, “Partial-measurement backaction and nonclassical weak values in a superconducting circuit,” *Physical Review Letters*, vol. 111, no. 9, p. 090506, 2013.
- [60] M. S. Blok, C. Bonato, M. L. Markham, D. J. Twitchen, V. V. Dobrovitski, and R. Hanson, “Manipulating a qubit through the backaction of sequential partial measurements and real-time feedback,” *Nature Physics*, vol. 10, no. 3, pp. 189–193, 2014.
- [61] H. F. Hofmann and C. Ren, “Direct observation of temporal coherence by weak projective measurements of photon arrival time,” *Physical Review A*, vol. 87, no. 6, p. 062109, 2013.
- [62] L. M. Johansen, “Quantum theory of successive projective measurements,” *Physical Review A*, vol. 76, no. 1, p. 012119, 2007.
- [63] L. M. Johansen, “Reconstructing weak values without weak measurements,” *Physics Letters A*, vol. 366, no. 4–5, pp. 374–376, 2007.

- [64] Y. Suzuki, M. Iinuma, and H. F. Hofmann, “Violation of Leggett–Garg inequalities in quantum measurements with variable resolution and back-action,” *New Journal of Physics*, vol. 14, no. 10, p. 103022, 2012.
- [65] A. M. Steinberg, “How much time does a tunneling particle spend in the barrier region?,” *Physical Review Letters*, vol. 74, no. 13, pp. 2405–2409, 1995.
- [66] J. G. Kirkwood, “Quantum statistics of almost classical assemblies,” *Physical Review*, vol. 44, no. 1, pp. 31–37, 1933.
- [67] P. A. M. Dirac, “On the analogy between classical and quantum mechanics,” *Reviews of Modern Physics*, vol. 17, no. 2-3, pp. 195–199, 1945.
- [68] V. Bargmann, “Note on Wigner’s theorem on symmetry operations,” *Journal of Mathematical Physics*, vol. 5, no. 7, pp. 862–868, 1964.
- [69] M. Iinuma, Y. Suzuki, G. Taguchi, Y. Kadoya, and H. F. Hofmann, “Weak measurement of photon polarization by back-action-induced path interference,” *New Journal of Physics*, vol. 13, no. 3, p. 033041, 2011.
- [70] L. B. Ho and N. Imoto, “Full characterization of modular values for finite-dimensional systems,” *Physics Letters A*, vol. 380, no. 25–26, pp. 2129–2135, 2016.
- [71] L. B. Ho and N. Imoto, “The two different aspects of the modular value,” *arXiv:1602.01594*, 2016.
- [72] N. W. M. Ritchie, J. G. Story, and R. G. Hulet, “Realization of a measurement of a “weak value”,” *Physical Review Letters*, vol. 66, no. 9, pp. 1107–1110, 1991.
- [73] J. M. Knight and L. Vaidman, “Weak measurement of photon polarization,” *Physics Letters A*, vol. 143, no. 8, pp. 357–361, 1990.
- [74] D. J. Starling, P. B. Dixon, A. N. Jordan, and J. C. Howell, “Precision frequency measurements with interferometric weak values,” *Physical Review A*, vol. 82, no. 6, p. 063822, 2010.
- [75] Y.-W. Cho, H.-T. Lim, Y.-S. Ra, and Y.-H. Kim, “Weak value measurement with an incoherent measuring device,” *New Journal of Physics*, vol. 12, no. 2, p. 023036, 2010.

- [76] M. D. Turner, C. A. Hagedorn, S. Schlamminger, and J. H. Gundlach, “Picoradian deflection measurement with an interferometric quasi-autocollimator using weak value amplification,” *Optics Letters*, vol. 36, no. 8, p. 1479, 2011.
- [77] N. Brunner, V. Scarani, M. Wegmüller, M. Legré, and N. Gisin, “Direct measurement of superluminal group velocity and signal velocity in an optical fiber,” *Physical Review Letters*, vol. 93, no. 20, p. 203902, 2004.
- [78] Q. Wang, F.-W. Sun, Y.-S. Zhang, Jian-Li, Y.-F. Huang, and G.-C. Guo, “Experimental demonstration of a method to realize weak measurement of the arrival time of a single photon,” *Physical Review A*, vol. 73, no. 2, p. 023814, 2006.
- [79] Y. Aharonov and D. Bohm, “Significance of electromagnetic potentials in the quantum theory,” *Physical Review*, vol. 115, no. 3, pp. 485–491, 1959.
- [80] P. G. Kwiat, E. Waks, A. G. White, I. Appelbaum, and P. H. Eberhard, “Ultrabright source of polarization-entangled photons,” *Physical Review A*, vol. 60, no. 2, pp. 773–776, 1999.
- [81] J. A. Carlson, M. D. Olmstead, and M. Beck, “Quantum mysteries tested: An experiment implementing Hardy’s test of local realism,” *American Journal of Physics*, vol. 74, pp. 180–186, 2006.
- [82] J. Altepeter, E. Jeffrey, and P. Kwiat, *Advances In Atomic, Molecular, and Optical Physics*, vol. 52. Elsevier, 2005.
- [83] S. S. Shapiro and M. B. Wilk, “An analysis of variance test for normality (complete samples),” *Biometrika*, vol. 52, no. 3-4, pp. 591–611, 1965.
- [84] S. S. Shapiro, M. B. Wilk, and H. J. Chen, “A comparative study of various tests for normality,” *Journal of the American Statistical Association*, vol. 63, no. 324, pp. 1343–1372, 1968.
- [85] G. A. F. Seber and C. J. Wild, *Nonlinear regression*. Hoboken, NJ: Wiley-Interscience, 2003.
- [86] J. H. Dane and C. G. Topp, eds., *Methods of Soil Analysis: Part 4 Physical Methods*. No. 5.4 in SSSA Book Series, Madison, WI: Soil Science Society of America, 2002.

- [87] C. K. Hong, Z. Y. Ou, and L. Mandel, “Measurement of subpicosecond time intervals between two photons by interference,” *Physical Review Letters*, vol. 59, no. 18, pp. 2044–2046, 1987.
- [88] X. Yan, *Linear Regression Analysis: Theory and Computing*. World Scientific, 2009.
- [89] D. F. V. James, P. G. Kwiat, W. J. Munro, and A. G. White, “Measurement of qubits,” *Physical Review A*, vol. 64, no. 5, p. 052312, 2001.
- [90] E. Majorana, “Atomi orientati in campo magnetico variabile,” *Il Nuovo Cimento (1924-1942)*, vol. 9, no. 2, pp. 43–50, 1932.
- [91] F. Eriksson, “On the measure of solid angles,” *Mathematics Magazine*, vol. 63, no. 3, pp. 184–187, 1990.
- [92] N. Mukunda and R. Simon, “Quantum kinematic approach to the geometric phase. I. General formalism,” *Annals of Physics*, vol. 228, no. 2, pp. 205–268, 1993.
- [93] M. V. Berry, “Quantal phase factors accompanying adiabatic changes,” *Proceedings of the Royal Society of London A: Mathematical, Physical and Engineering Sciences*, vol. 392, no. 1802, pp. 45–57, 1984.
- [94] A. Tomita and R. Y. Chiao, “Observation of Berry’s topological phase by use of an optical fiber,” *Physical Review Letters*, vol. 57, no. 8, pp. 937–940, 1986.
- [95] Y. Aharonov and J. Anandan, “Phase change during a cyclic quantum evolution,” *Physical Review Letters*, vol. 58, no. 16, pp. 1593–1596, 1987.
- [96] J. Samuel and R. Bhandari, “General setting for Berry’s phase,” *Physical Review Letters*, vol. 60, no. 23, pp. 2339–2342, 1988.
- [97] J. L. Martínez-Fuentes, J. Albero, and I. Moreno, “Analysis of optical polarization modulation systems through the Pancharatnam connection,” *Optics Communications*, vol. 285, no. 4, pp. 393–401, 2012.
- [98] W. Ganczarek, M. Kuś, and K. Życzkowski, “Barycentric measure of quantum entanglement,” *Physical Review A*, vol. 85, no. 3, p. 032314, 2012.

- [99] F. Bloch and I. I. Rabi, “Atoms in variable magnetic fields,” *Reviews of Modern Physics*, vol. 17, pp. 237–244, Apr. 1945.
- [100] A. R. U. Devi, Sudha, and A. K. Rajagopal, “Majorana representation of symmetric multiqubit states,” *Quantum Information Processing*, vol. 11, no. 3, pp. 685–710, 2012.
- [101] S. K. Goyal, B. N. Simon, R. Singh, and S. Simon, “Geometry of the generalized Bloch sphere for qutrits,” *Journal of Physics A: Mathematical and Theoretical*, vol. 49, no. 16, p. 165203, 2016.
- [102] T. L. Curtright and C. K. Zachos, “Elementary results for the fundamental representation of $SU(3)$,” *Reports on Mathematical Physics*, vol. 76, no. 3, pp. 401–404, 2015.
- [103] A. G. White, D. F. V. James, P. H. Eberhard, and P. G. Kwiat, “Nonmaximally entangled states: Production, characterization, and utilization,” *Physical Review Letters*, vol. 83, no. 16, pp. 3103–3107, 1999.
- [104] K. G. H. Vollbrecht and R. F. Werner, “Why two qubits are special,” *Journal of Mathematical Physics*, vol. 41, no. 10, pp. 6772–6782, 2000.
- [105] R. E. George, L. M. Robledo, O. J. E. Maroney, M. S. Blok, H. Bernien, M. L. Markham, D. J. Twitchen, J. J. L. Morton, G. A. D. Briggs, and R. Hanson, “Opening up three quantum boxes causes classically undetectable wavefunction collapse,” *Proceedings of the National Academy of Sciences*, vol. 110, no. 10, pp. 3777–3781, 2013.
- [106] J. Bub and H. Brown, “Curious properties of quantum ensembles which have been both preselected and post-selected,” *Physical Review Letters*, vol. 56, no. 22, pp. 2337–2340, 1986.
- [107] R. E. Kastner, “The three-box “paradox” and other reasons to reject the counterfactual usage of the ABL rule,” *Foundations of Physics*, vol. 29, no. 6, pp. 851–863, 1999.
- [108] K. A. Kirkpatrick, “Classical three-box “paradox”,” *Journal of Physics A: Mathematical and General*, vol. 36, no. 17, p. 4891, 2003.

- [109] J. Finkelstein, “What is paradoxical about the “three-box paradox”?” *arXiv:quant-ph/0606218*, 2006.
- [110] M. Aulbach, D. Markham, and M. Mura0, “The maximally entangled symmetric state in terms of the geometric measure,” *New Journal of Physics*, vol. 12, no. 7, p. 073025, 2010.
- [111] M. Aulbach, D. Markham, and M. Mura0, “Geometric entanglement of symmetric states and the majorana representation,” in *Theory of Quantum Computation, Communication, and Cryptography* (W. v. Dam, V. M. Kendon, and S. Severini, eds.), Lecture Notes in Computer Science, pp. 141–158, Springer Berlin Heidelberg, 2010.
- [112] J. Martin, O. Giraud, P. A. Braun, D. Braun, and T. Bastin, “Multiqubit symmetric states with high geometric entanglement,” *Physical Review A*, vol. 81, no. 6, p. 062347, 2010.
- [113] J. Martínez-Rincón, “Overcoming experimental limitations in a nonlinear two-qubit gate through postselection,” *Quantum Information Processing*, vol. 16, no. 2, p. 45, 2017.
- [114] T. Denkmayr, H. Geppert, H. Lemmel, M. Waegell, J. Dressel, Y. Hasegawa, and S. Sponar, “Experimental demonstration of direct path state characterization by strongly measuring weak values in a matter-wave interferometer,” *Physical Review Letters*, vol. 118, no. 1, p. 010402, 2017.
- [115] L. Vaidman, “Comment on “Experimental demonstration of direct path state characterization by strongly measuring weak values in a matter-wave interferometer”,” *arXiv:1703.01616*, 2017.
- [116] L. B. Ho and N. Imoto, “An interpretation and understanding of complex modular values,” *arXiv:1602.01594*, 2016.
- [117] V. G. Dmitriev, G. G. Gurzadyan, and D. N. Nikogosyan, *Handbook of Nonlinear Optical Crystals*. Berlin ; New York: Springer, 3rd edition ed., 1999.

Appendices



Gaussian meter in von Neumann measurement protocol

In chapter 2, we argue that the weak probability $P_{k,w}$ is the counterpart for weak measurements of the conditional probability defined by the ABL formula (2.11). To demonstrate this point of view, we consider the evolution operator:

$$\hat{U}(t) = \hat{\Pi}_{\perp-k} \otimes \hat{I} + \hat{\Pi}_k \otimes \exp\left[-i\frac{g}{\hbar}\hat{P}\right], \quad (\text{A.1})$$

where the projector $\hat{\Pi}_{\perp-k} = \hat{I} - \hat{\Pi}_k$. The initial meter system $|\psi_m\rangle$ is described by a real Gaussian function with an expectation value of zero and a variance of σ^2 :

$$\psi_m(x) = \langle x|\psi_m\rangle = \frac{1}{\sqrt{\sigma\sqrt{2\pi}}} \exp\left[-\frac{x^2}{4\sigma^2}\right]. \quad (\text{A.2})$$

By considering the preselected probe state $\hat{\rho}_i$ which is finally postselected by $\hat{\Pi}_f$, and the interaction Hamiltonian $\hat{H}_{int} = g(t) \hat{\Pi}_k \otimes \hat{P}$ applied on both systems, the probability to find the probe at the position x after this interaction is:

$$\begin{aligned} P_{if}(x) &= \text{Tr}\left[\hat{\Pi}_f \hat{\Pi}_{\perp-k} \hat{\rho}_i \hat{\Pi}_{\perp-k}\right] |\psi_m(x)|^2 \\ &+ \text{Tr}\left[\hat{\Pi}_f \hat{\Pi}_k \hat{\rho}_i \hat{\Pi}_k\right] |\psi_m(x-g)|^2 \\ &+ 2 \Re\left\{\text{Tr}\left[\hat{\Pi}_f \hat{\Pi}_{\perp-k} \hat{\rho}_i \hat{\Pi}_k\right]\right\} \psi_m(x-g) \psi_m(x). \end{aligned} \quad (\text{A.3})$$

This probability distribution $P_{if}(x)$ is used to establish a relation for the meter mean displacement with respect to the pre- and postselected probe:

$$\bar{x}_{if} = \frac{\int_{-\infty}^{+\infty} x P_{if}(x) dx}{\int_{-\infty}^{+\infty} P_{if}(x) dx}. \quad (\text{A.4})$$

Firstly, the integrals of the three terms appearing in the numerator are calculated:

$$\frac{1}{\sigma\sqrt{2\pi}} \int_{-\infty}^{+\infty} x \exp\left[-\frac{x^2}{2\sigma^2}\right] dx = 0, \quad (\text{A.5})$$

$$\frac{1}{\sigma\sqrt{2\pi}} \int_{-\infty}^{+\infty} x \exp\left[-\frac{(x-g)^2}{2\sigma^2}\right] dx = g, \quad (\text{A.6})$$

$$\frac{1}{\sigma\sqrt{2\pi}} \exp\left[-\frac{g^2}{4\sigma^2}\right] \int_{-\infty}^{+\infty} x \exp\left[-\frac{1}{2\sigma^2}x^2 + \frac{g}{2\sigma^2}x\right] dx = \frac{1}{2}g \exp\left[-\frac{g^2}{8\sigma^2}\right]. \quad (\text{A.7})$$

For the last equality, we used the relation:

$$\int_{-\infty}^{+\infty} x \exp(-ax^2 + bx) dx = \frac{b}{2a} \sqrt{\frac{\pi}{a}} \exp\left(\frac{b^2}{4a}\right). \quad (\text{A.8})$$

Thus, the numerator can be written as following:

$$\int_{-\infty}^{+\infty} x P(x) dx = g \operatorname{Tr} \left[\hat{\Pi}_f \hat{\Pi}_k \hat{\rho}_i \hat{\Pi}_k \right] + g \exp\left[-\frac{g^2}{8\sigma^2}\right] \Re e \left\{ \operatorname{Tr} \left[\hat{\Pi}_f \hat{\Pi}_{1-k} \hat{\rho}_i \hat{\Pi}_k \right] \right\}. \quad (\text{A.9})$$

Then, the three integrals in the denominator are determined:

$$\frac{1}{\sigma\sqrt{2\pi}} \int_{-\infty}^{+\infty} \exp\left[-\frac{x^2}{2\sigma^2}\right] dx = \frac{1}{\sigma\sqrt{2\pi}} \int_{-\infty}^{+\infty} \exp\left[-\frac{(x-g)^2}{2\sigma^2}\right] dx = 1, \quad (\text{A.10})$$

$$\frac{1}{\sigma\sqrt{2\pi}} \exp\left[-\frac{g^2}{4\sigma^2}\right] \int_{-\infty}^{+\infty} \exp\left[-\frac{1}{2\sigma^2}x^2 + \frac{g}{2\sigma^2}x\right] dx = \exp\left[-\frac{g^2}{8\sigma^2}\right]. \quad (\text{A.11})$$

The last equality results from the formula:

$$\int_{-\infty}^{+\infty} \exp[-(ax^2 + 2bx + c)] dx = \sqrt{\frac{\pi}{a}} \exp\left(\frac{b^2}{a} - c\right). \quad (\text{A.12})$$

Finally, the meter displacement for pre- and postselected ensemble is given by:

$$\begin{aligned} \bar{x}_{if} &= g \frac{\operatorname{Tr} \left[\hat{\Pi}_f \hat{\Pi}_k \hat{\rho}_i \hat{\Pi}_k \right] + \exp\left[-\frac{g^2}{8\sigma^2}\right] \Re e \left\{ \operatorname{Tr} \left[\hat{\Pi}_f \hat{\Pi}_{1-k} \hat{\rho}_i \hat{\Pi}_k \right] \right\}}{\operatorname{Tr} \left[\hat{\Pi}_f \hat{\Pi}_k \hat{\rho}_i \hat{\Pi}_k \right] + \operatorname{Tr} \left[\hat{\Pi}_f \hat{\Pi}_{1-k} \hat{\rho}_i \hat{\Pi}_{1-k} \right] + 2 \exp\left[-\frac{g^2}{8\sigma^2}\right] \Re e \left\{ \operatorname{Tr} \left[\hat{\Pi}_f \hat{\Pi}_{1-k} \hat{\rho}_i \hat{\Pi}_k \right] \right\}}, \\ &= C_1(g) \frac{\operatorname{Tr} \left[\hat{\Pi}_f \hat{\Pi}_k \hat{\rho}_i \hat{\Pi}_k \right]}{\operatorname{Tr} \left[\hat{\Pi}_f \hat{\Pi}_k \hat{\rho}_i \hat{\Pi}_k \right] + \operatorname{Tr} \left[\hat{\Pi}_f \hat{\Pi}_{1-k} \hat{\rho}_i \hat{\Pi}_{1-k} \right]} + C_2(g) \Re e \frac{\operatorname{Tr} \left[\hat{\Pi}_f \hat{\Pi}_k \hat{\rho}_i \right]}{\operatorname{Tr} \left[\hat{\Pi}_f \hat{\rho}_i \right]}, \end{aligned} \quad (\text{A.13})$$

where,

$$C_1(g) = \frac{g \left(1 - \exp \left[-\frac{g^2}{8\sigma^2} \right] \right)}{1 + 2 \exp \left[-\frac{g^2}{8\sigma^2} \right] \frac{\Re \left\{ \text{Tr} \left[\hat{\Pi}_f \hat{\Pi}_{1-k} \hat{\rho}_i \hat{\Pi}_k \right] \right\}}{\text{Tr} \left[\hat{\Pi}_f \hat{\Pi}_k \hat{\rho}_i \hat{\Pi}_k \right] + \text{Tr} \left[\hat{\Pi}_f \hat{\Pi}_{1-k} \hat{\rho}_i \hat{\Pi}_{1-k} \right]}}, \quad (\text{A.14})$$

and,

$$C_2(g) = \frac{g \exp \left[-\frac{g^2}{8\sigma^2} \right]}{1 + 2 \left(1 - \exp \left[-\frac{g^2}{8\sigma^2} \right] \right) \frac{\text{Tr} \left[\hat{\Pi}_f \hat{\Pi}_k \hat{\rho}_i \hat{\Pi}_k \right] - \Re \left\{ \text{Tr} \left[\hat{\Pi}_f \hat{\Pi}_k \hat{\rho}_i \right] \right\}}{\text{Tr} \left[\hat{\Pi}_f \hat{\rho}_i \right]}}. \quad (\text{A.15})$$

Both coefficients $C_1(g)$ and $C_2(g)$ are deduced by using the following relationships:

$$\begin{aligned} \Re \left\{ \text{Tr} \left[\hat{\Pi}_f \hat{\Pi}_{1-k} \hat{\rho}_i \hat{\Pi}_k \right] \right\} &= \Re \left\{ \text{Tr} \left[\hat{\Pi}_f \hat{\Pi}_k \hat{\rho}_i \right] \right\} - \text{Tr} \left[\hat{\Pi}_f \hat{\Pi}_k \hat{\rho}_i \hat{\Pi}_k \right], \\ \text{Tr} \left[\hat{\Pi}_f \hat{\Pi}_{1-k} \hat{\rho}_i \hat{\Pi}_{1-k} \right] &= \text{Tr} \left[\hat{\Pi}_f \hat{\rho}_i \right] + \text{Tr} \left[\hat{\Pi}_f \hat{\Pi}_k \hat{\rho}_i \hat{\Pi}_k \right] - 2 \Re \left\{ \text{Tr} \left[\hat{\Pi}_f \hat{\Pi}_k \hat{\rho}_i \right] \right\}. \end{aligned}$$

By applying strong interaction strengths with $\frac{g}{2\sqrt{2}\sigma} \gg 1$, the terms with the factor $\exp \left[-\frac{g^2}{8\sigma^2} \right] \approx 0$ becomes negligible compared to the rest. Thus, the approximations $C_1(g) \approx g$ and $C_2(g) \approx 0$ are generally valid. In contrast, weak interaction strengths with $\frac{g}{2\sqrt{2}\sigma} \ll 1$ induce that $\exp \left[-\frac{g^2}{8\sigma^2} \right] \approx 1 - o(g^2)$. Ignoring all terms higher than the first order (the linear-response regime), the approximation of the coefficients $C_1(g) \approx 0$ and $C_2(g) \approx g$ are applicable for non-diverging values of the weak probability.

We derive a relation for the displacement of the momentum by similar developments as in the position case. First, we calculate the Fourier transform of the Gaussian position distribution $\psi_m(x)$:

$$\begin{aligned} \psi_m(p) &= \frac{1}{\sqrt{2\pi\hbar}} \int_{-\infty}^{+\infty} \psi_m(x) e^{-\frac{ipx}{\hbar}} dx \\ &= \frac{1}{\sqrt{2\pi\hbar}} \frac{1}{\sqrt{\sigma\sqrt{2\pi}}} \int_{-\infty}^{+\infty} e^{-\frac{x^2}{4\sigma^2}} e^{-\frac{ipx}{\hbar}} dx \\ &= \frac{1}{\sqrt{2\pi\hbar}} \frac{1}{\sqrt{\sigma\sqrt{2\pi}}} \sqrt{4\pi\sigma^2} e^{-\frac{p^2\sigma^2}{\hbar^2}} \\ &= \left(\frac{2\sigma^2}{\hbar^2\pi} \right)^{\frac{1}{4}} e^{-\frac{p^2\sigma^2}{\hbar^2}}. \end{aligned} \quad (\text{A.16})$$

Then, we determine the displacement of the momentum by applying the eigenvalue equation $\hat{P}|p\rangle = p|p\rangle$ on the joint probability distribution $P_{if}(p)$ to find the postselect

probe with the momentum p :

$$\begin{aligned}
P_{if}(p) &= \text{Tr} \left[\hat{\Pi}_f \hat{\Pi}_{\perp-k} \hat{\rho}_i \hat{\Pi}_{\perp-k} \right] \langle p | \psi_m \rangle \langle \psi_m | p \rangle \\
&+ \text{Tr} \left[\hat{\Pi}_f \hat{\Pi}_k \hat{\rho}_i \hat{\Pi}_k \right] \langle p | \exp \left(-i \frac{g}{\hbar} \hat{P} \right) | \psi_m \rangle \langle \psi_m | \exp \left(i \frac{g}{\hbar} \hat{P} \right) | p \rangle \\
&+ 2 \Re \left\{ \text{Tr} \left[\hat{\Pi}_f \hat{\Pi}_k \hat{\rho}_i \hat{\Pi}_{\perp-k} \right] \right\} \Re \left\{ \langle p | \exp \left(-i \frac{g}{\hbar} \hat{P} \right) | \psi_m \rangle \langle \psi_m | p \rangle \right\} \\
&- 2 \Im \left\{ \text{Tr} \left[\hat{\Pi}_f \hat{\Pi}_k \hat{\rho}_i \hat{\Pi}_{\perp-k} \right] \right\} \Im \left\{ \langle p | \exp \left(-i \frac{g}{\hbar} \hat{P} \right) | \psi_m \rangle \langle \psi_m | p \rangle \right\} \quad (\text{A.17})
\end{aligned}$$

Thus,

$$\begin{aligned}
P_{if}(p) &= \text{Tr} \left[\hat{\Pi}_f \hat{\Pi}_{\perp-k} \hat{\rho}_i \hat{\Pi}_{\perp-k} \right] |\psi_m(p)|^2 \\
&+ \text{Tr} \left[\hat{\Pi}_f \hat{\Pi}_k \hat{\rho}_i \hat{\Pi}_k \right] |\psi_m(p)|^2 \\
&+ 2 \Re \left\{ \text{Tr} \left[\hat{\Pi}_f \hat{\Pi}_k \hat{\rho}_i \hat{\Pi}_{\perp-k} \right] \right\} \Re \left\{ \exp \left(-i \frac{g}{\hbar} p \right) |\psi_m(p)|^2 \right\} \\
&- 2 \Im \left\{ \text{Tr} \left[\hat{\Pi}_f \hat{\Pi}_k \hat{\rho}_i \hat{\Pi}_{\perp-k} \right] \right\} \Im \left\{ \exp \left(-i \frac{g}{\hbar} p \right) |\psi_m(p)|^2 \right\}. \quad (\text{A.18})
\end{aligned}$$

This joint probability is used to calculate the mean displacement in the momentum space. The first and the second integrals appearing in the numerator are both zero. In addition, we can show that only the last integral contributes on the mean impulsion, since the real part is an even function of p while the imaginary part is an odd function of p :

$$\begin{aligned}
\int_{-\infty}^{+\infty} p \exp \left(-i \frac{g}{\hbar} p \right) |\psi_m(p)|^2 dp &= \left(\frac{2\sigma^2}{\hbar^2 \pi} \right)^{\frac{1}{2}} \int_{-\infty}^{+\infty} p \exp \left(-i \frac{g}{\hbar} p \right) \exp \left(-\frac{2p^2 \sigma^2}{\hbar^2} \right) dp \\
&= -i \left(\frac{2\sigma^2}{\hbar^2 \pi} \right)^{\frac{1}{2}} \frac{\hbar^2 g}{4\sigma^2 \hbar} \int_{-\infty}^{+\infty} \exp \left(-i \frac{g}{\hbar} p \right) \exp \left(-\frac{2p^2 \sigma^2}{\hbar^2} \right) dp \\
&= -i \frac{1}{\sqrt{2\pi}} \frac{g}{2\sigma} \sqrt{\frac{\pi \hbar^2}{2\sigma^2}} \exp \left[-\frac{g^2}{8\sigma^2} \right] \\
&= -i g \frac{\hbar}{4\sigma^2} \exp \left[-\frac{g^2}{8\sigma^2} \right]. \quad (\text{A.19})
\end{aligned}$$

The postselection probability in the momentum representation is the same as in the position representation. Consequently, we can use the result determined in the last

section for the denominator. Finally the mean momentum displacement is:

$$\begin{aligned}
 \bar{p}_{if} &= \frac{\frac{g\hbar}{2\sigma^2} \exp\left[-\frac{g^2}{8\sigma^2}\right] \Im m \left\{ \text{Tr} \left[\hat{\Pi}_f \hat{\Pi}_k \hat{\rho}_i \hat{\Pi}_{1-k} \right] \right\}}{\text{Tr} \left[\hat{\Pi}_f \hat{\Pi}_k \hat{\rho}_i \hat{\Pi}_k \right] + \text{Tr} \left[\hat{\Pi}_f \hat{\Pi}_{1-k} \hat{\rho}_i \hat{\Pi}_{1-k} \right] + 2 \exp\left[-\frac{g^2}{8\sigma^2}\right] \Re e \left\{ \text{Tr} \left[\hat{\Pi}_f \hat{\Pi}_{1-k} \hat{\rho}_i \hat{\Pi}_k \right] \right\}}, \\
 &= \frac{\hbar}{2\sigma^2} C_2(g) \Im m \frac{\text{Tr} \left[\hat{\Pi}_f \hat{\Pi}_k \hat{\rho}_i \right]}{\text{Tr} \left[\hat{\Pi}_f \hat{\rho}_i \right]}, \tag{A.20}
 \end{aligned}$$

where $C_2(g)$ is defined by relation (A.15).

B

Derivation of the meter average

B.1 Relation to the real and the imaginary parts of the modular value

During the quantum controlled evolution the preselected probe state $\hat{\rho}_i = |\psi_i\rangle\langle\psi_i|$ interacts with the qubit meter $\hat{\rho}_m = \frac{1}{2} \left(\hat{I} + P_m \vec{m} \cdot \vec{\sigma} \right)$ via the quantum gate:

$$\hat{U}_{GATE} = \hat{I} \otimes \hat{\Pi}_r + \hat{U}_A \otimes \hat{\Pi}_{-r}, \quad (\text{B.1})$$

with the meter projectors $\hat{\Pi}_{\pm r} = \frac{1}{2} \left(\hat{I} \pm \vec{r} \cdot \vec{\sigma} \right)$. The vectors \vec{m} and \vec{r} are normalized three-dimensional vectors pointing on the Bloch sphere. P_m is the purity of the initial meter state. After the gate interaction, the whole system (meter and probe) state is:

$$\begin{aligned} \hat{\rho} = & \hat{\rho}_i \otimes \hat{\Pi}_r \hat{\rho}_m \hat{\Pi}_r^\dagger + \hat{U}_A \hat{\rho}_i \hat{U}_A^\dagger \otimes \hat{\Pi}_{-r} \hat{\rho}_m \hat{\Pi}_{-r}^\dagger \\ & + \hat{U}_A \hat{\rho}_i \otimes \hat{\Pi}_{-r} \hat{\rho}_m \hat{\Pi}_{-r}^\dagger + \hat{\rho}_i \hat{U}_A^\dagger \otimes \hat{\Pi}_r \hat{\rho}_m \hat{\Pi}_r^\dagger. \end{aligned} \quad (\text{B.2})$$

If we express the initial meter state, as well as the projectors, using their associated vectors on the Bloch sphere, the density operator $\hat{\rho}$ can be transformed to:

$$\begin{aligned} \hat{\rho} = & \frac{1}{4} [(1 + P_m \vec{r} \cdot \vec{m}) \hat{\rho}_i \otimes \left(\hat{I} + \vec{r} \cdot \vec{\sigma} \right) \\ & + (1 - P_m \vec{r} \cdot \vec{m}) \hat{U}_A \hat{\rho}_i \hat{U}_A^\dagger \otimes \left(\hat{I} - \vec{r} \cdot \vec{\sigma} \right) \\ & + P_m \hat{U}_A \hat{\rho}_i \otimes (\vec{m} \cdot \vec{\sigma} - (\vec{r} \cdot \vec{m}) (\vec{r} \cdot \vec{\sigma}) - i (\vec{r} \times \vec{m}) \cdot \vec{\sigma}) \\ & + P_m \hat{\rho}_i \hat{U}_A^\dagger \otimes (\vec{m} \cdot \vec{\sigma} - (\vec{r} \cdot \vec{m}) (\vec{r} \cdot \vec{\sigma}) + i (\vec{r} \times \vec{m}) \cdot \vec{\sigma})]. \end{aligned} \quad (\text{B.3})$$

According to our quantum measurement scheme, the spin observable $\hat{\sigma}_q$ of the meter is then measured and the probe is postselected by the state $|\psi_f\rangle$. Since the spin operator $\hat{\sigma}_q$ verifies $\hat{\sigma}_q = \hat{\Pi}_{+q} - \hat{\Pi}_{-q}$, we first have to calculate the joint probabilities P_{joint}^{+q} and

P_{joint}^{-q} of postselecting the probe state $|\psi_f\rangle$ while measuring the meter observable $\hat{\Pi}_{+q}$ or measuring the meter observable $\hat{\Pi}_{-q}$, respectively: $P_{joint}^{\pm q} = \text{Tr} \left[\left(|\psi_f\rangle\langle\psi_f| \otimes \hat{\Pi}_{\pm q} \right) \hat{\rho} \right]$, where $\hat{\Pi}_{\pm q} = \frac{1}{2} \left(\hat{I} \pm \vec{q} \cdot \vec{\sigma} \right)$. We find then:

$$\begin{aligned}
 P_{joint}^{\pm q} &= \frac{1}{4} [(1 + P_m \vec{r} \cdot \vec{m}) (1 \pm \vec{r} \cdot \vec{q}) |\langle\psi_f|\psi_i\rangle|^2 \\
 &+ (1 - P_m \vec{r} \cdot \vec{m}) (1 \mp \vec{r} \cdot \vec{q}) \left| \langle\psi_f|\hat{U}_A|\psi_i\rangle \right|^2 \\
 &\pm 2P_m (\vec{m} \cdot \vec{q} - (\vec{r} \cdot \vec{m})(\vec{r} \cdot \vec{q})) \Re \langle\psi_f|\hat{U}_A|\psi_i\rangle \langle\psi_i|\psi_f\rangle \\
 &\pm 2P_m ((\vec{r} \times \vec{m}) \cdot \vec{q}) \Im \langle\psi_f|\hat{U}_A|\psi_i\rangle \langle\psi_i|\psi_f\rangle].
 \end{aligned} \tag{B.4}$$

By applying the quantum eraser condition $\vec{r} \cdot \vec{q} = 0$, and by considering:

$$\bar{\sigma}_q^m = \frac{P_{joint}^{+q} - P_{joint}^{-q}}{P_{joint}^{+q} + P_{joint}^{-q}}, \tag{B.5}$$

it can be finally shown that:

$$\bar{\sigma}_q^m = 2P_m \frac{(\vec{m} \cdot \vec{q}) \Re A_m + [(\vec{r} \times \vec{m}) \cdot \vec{q}] \Im A_m}{(1 + P_m \vec{r} \cdot \vec{m}) + (1 - P_m \vec{r} \cdot \vec{m}) |A_m|^2}. \tag{B.6}$$

B.2 Relation to the modulus and the argument of the modular value

The measurement of the modulus $|A_m|$ and the argument $\varphi = \arg A_m$ of the modular value necessitates the introduction of an additional meter transformation \hat{R}_ξ after the nonlocal quantum gate in (B.1) :

$$\hat{R}_\xi = \hat{\Pi}_r + e^{-i\xi} \hat{\Pi}_{-r}. \tag{B.7}$$

This unitary evolution creates a relative phase shift ξ between the orthogonal states $|r\rangle$ and $|-r\rangle$ that is effectively equivalent to a rotation of the modular value in the complex plane. Then, we have to calculate the joint probability P_{joint} of postselecting the probe state $|\psi_f\rangle$ while measuring the meter observable $\hat{\Pi}_q$:

$$\begin{aligned}
 P_{joint} &= \frac{1}{4} [(1 + P_m \vec{r} \cdot \vec{m}) (1 + \vec{r} \cdot \vec{q}) |\langle\psi_f|\psi_i\rangle|^2 \\
 &+ (1 - P_m \vec{r} \cdot \vec{m}) (1 - \vec{r} \cdot \vec{q}) |\langle\psi_f|\psi_i\rangle|^2 |A_m|^2 \\
 &+ 2P_m (\vec{m} \cdot \vec{q} - (\vec{r} \cdot \vec{m})(\vec{r} \cdot \vec{q})) |\langle\psi_f|\psi_i\rangle|^2 |A_m| \cos(\varphi - \xi) \\
 &+ 2P_m ((\vec{r} \times \vec{m}) \cdot \vec{q}) |\langle\psi_f|\psi_i\rangle|^2 |A_m| \sin(\varphi - \xi)],
 \end{aligned} \tag{B.8}$$

with $\varphi = \arg A_m$. By applying the quantum eraser condition with $\vec{r} \cdot \vec{q} = 0$, and by considering three coplanar vectors \vec{m} , \vec{r} , \vec{q} verifying $(\vec{r} \times \vec{m}) \cdot \vec{q} = 0$, it can be finally shown that the joint probability is proportional to:

$$\begin{aligned} P_{joint} &\propto 1 + \frac{2P_m (\vec{m} \cdot \vec{q}) |A_m|}{(1 + P_m \vec{r} \cdot \vec{m}) + (1 - P_m \vec{r} \cdot \vec{m}) |A_m|^2} \cos(\varphi - \xi), \\ &\propto 1 + V \cos(\varphi - \xi) \end{aligned} \quad (\text{B.9})$$

with the factor of proportionality:

$$\frac{1}{4} |\langle \psi_f | \psi_i \rangle|^2 [(1 + P_m \vec{r} \cdot \vec{m}) + (1 - P_m \vec{r} \cdot \vec{m}) |A_m|^2]. \quad (\text{B.10})$$

If we express the vectorial relations $\vec{r} \cdot \vec{m} = \cos(\theta)$ and $\vec{m} \cdot \vec{q} = \sin(\theta)$ by the measurement strength θ , the visibility V can be finally written as:

$$V = \frac{2P_m \tan\left(\frac{\theta}{2}\right)}{C_{\theta+\pi} + C_\theta \tan^2\left(\frac{\theta}{2}\right) |A_m|^2} |A_m|, \quad (\text{B.11})$$

with the coefficients C_ϵ defined by:

$$C_\epsilon = \frac{1 + P_m}{2} + \frac{1 - P_m}{2} \cot^2 \frac{\epsilon}{2}. \quad (\text{B.12})$$

B.3 Relation to the probability ratio x_s

The value of x_s is deduced from a meter configuration that corresponds to non-interfering pathways (no quantum superpositions are created by the gate). To do this, the final meter vectors, noted as $\pm \vec{q}_C$, are chosen parallel to \vec{r} revealing completely the probe state after the quantum gate interaction. The joint probabilities $P_{joint}^{+q_C}$ and $P_{joint}^{-q_C}$ of postselecting the probe state $|\psi_f\rangle$ while measuring the meter observables $\hat{\Pi}_{\pm q_C}$ are respectively:

$$P_{joint}^{+q_C} = \frac{1}{4} (1 + P_m \vec{r} \cdot \vec{m}) |\langle \psi_f | \psi_i \rangle|^2, \quad (\text{B.13})$$

and

$$P_{joint}^{-q_C} = \frac{1}{4} (1 - P_m \vec{r} \cdot \vec{m}) |\langle \psi_f | \psi_i \rangle|^2 |A_m|^2. \quad (\text{B.14})$$

If we apply the vectorial relation $\vec{r} \cdot \vec{m} = \cos(\theta)$, the probability ratio $P_{joint}^{-q_C}/P_{joint}^{+q_C}$ can be finally written as:

$$\frac{P_{joint}^{-q_C}}{P_{joint}^{+q_C}} = \tan^2\left(\frac{\theta}{2}\right) \frac{C_\theta}{C_{\theta+\pi}} |A_m|^2 = x_s, \quad (\text{B.15})$$

with the coefficients C_ϵ defined in relation (B.12).

C

Phase-matching of the nonlinear down-conversion process

Type-I phase matching occurs for an incident pump polarization parallel to the principal plane of the BBO crystal (see figure D.1.a). The generated two daughter photons, the signal and the idler, are perpendicularly polarized to this plane and aligned with the ordinary axis n_o of the BBO. The down-conversion process emit pairs of photons into a cone of half-opening angle α . In the following, we will show that this value is theoretically 2.23° . Mathematically, the phase-matching condition reflecting this down-conversion process can be written as:

$$\vec{k}_p = \vec{k}_i + \vec{k}_s \Leftrightarrow \begin{cases} k_p = k_s \cos \alpha + k_i \cos \alpha \\ 0 = k_s \sin \alpha - k_i \sin \alpha, \end{cases} \quad (\text{C.1})$$

where the pump, signal and idler modes are indexed by the wave vector $\vec{k}_{p,s,i}$. Moreover, the scalar moduli $k_{s,i}$, fixed by the energy conservation, are written as a function of their wavelengths:

$$k_s = \frac{2\pi n_o(\lambda_s)}{\lambda_s}, \quad (\text{C.2})$$

$$k_i = \frac{2\pi n_o(\lambda_i)}{\lambda_i}, \quad (\text{C.3})$$

with refractive indices depending on the wavelength. The relationship between the refractive index and the wavelength for transparent mediums is usually determined by the empirical Sellmeier equation. For the ordinary and extraordinary axes of the BBO

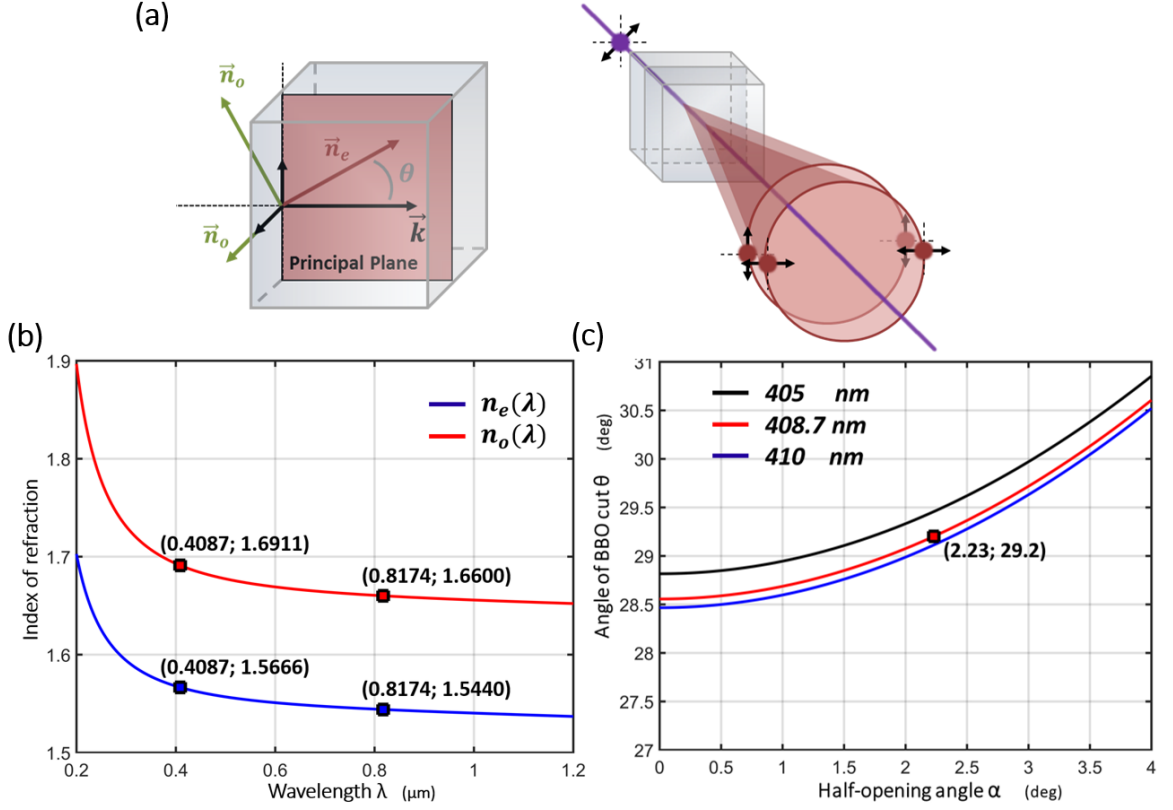


Figure C.1: Phase-matching condition generating the nonlinear down-conversion process inside a type-I BBO. (a) Schematic illustration of a type-I BBO crystal cut at $\theta = 29.2^\circ$ and of the polarization-entangled photon source in the “sandwich configuration”. (b) Calculation of the refractive index of the ordinary n_o (red) and extraordinary axes n_e (blue) of the BBO crystal using the empirical Sellmeier equations with respect to the wavelength λ . (c) The half-opening angle α as a function of the crystal cut θ given for several wavelengths.

crystal, these relations are given by [117]:

$$\begin{aligned}
 n_o &= \left[2.7359 + \frac{0.01878}{\lambda^2 - 0.01822} - 0.01354\lambda^2 \right]^{1/2}, \\
 n_e &= \left[2.3753 + \frac{0.01224}{\lambda^2 - 0.01667} - 0.01516\lambda^2 \right]^{1/2},
 \end{aligned} \tag{C.4}$$

where the wavelengths are expressed in micrometers. Figure D.1.b shows the refractive indices n_o and n_e as a function of the wavelength. The points marked at 408.7 nm and at 817.4 nm correspond to the wavelengths of the pump and of the generated signal

photons, respectively. Because the pump polarization is parallel to the principal plane, the resulting refractive index $n(\theta, \lambda)$ is a function of both the ordinary and extraordinary indices [117]:

$$n(\theta, \lambda) = n_o(\lambda) \sqrt{\frac{1 + \tan^2 \theta}{1 + \left(\frac{n_o(\lambda)}{n_e(\lambda)}\right)^2 \tan^2 \theta}}. \quad (\text{C.5})$$

Alternatively, the angle θ between the propagation direction of the pump beam and the extraordinary axis can be written as a function of the refractive indices:

$$\theta = \arctan \left(\frac{n_e(\lambda_p)}{n_o(\lambda_p)} \sqrt{\frac{n_o^2(\lambda_p) - n^2(\theta, \lambda_p)}{n^2(\theta, \lambda_p) - n_e^2(\lambda_p)}} \right). \quad (\text{C.6})$$

By considering the first scalar relation in (C.1) and by introducing the degenerated frequency condition, with $\lambda_{s,i} = 2\lambda_p = \lambda$, the pump refractive index $n(\theta, \lambda_p)$ must be

$$n(\theta, \lambda_p) = n_o(\lambda) \cos \alpha \quad (\text{C.7})$$

to verify the phase-matching condition. Finally, we obtain the relation between the cut angle θ and the half-opening angle α :

$$\theta = \arctan \left(\frac{n_e(\lambda_p)}{n_o(\lambda_p)} \sqrt{\frac{n_o^2(\lambda_p) - n_o^2(\lambda) \cos^2 \alpha}{n_o^2(\lambda) \cos^2 \alpha - n_e^2(\lambda_p)}} \right). \quad (\text{C.8})$$

By using the Sellmeier equation, we determine a half-opening angle $\alpha = 2.23^\circ$ for a BBO crystal cut at $\theta = 29.2^\circ$ and for a pump wavelength at 408.7 nm (see figure D.1.c).

D

Relative phase induced by a z-cut quartz plate

The z-cut quartz plate is an uniaxial birefringent crystal with the extraordinary axis perpendicular to its flat surfaces. For normal incident light beams, the horizontally and vertically polarized components follow the same path through the crystal and maintain the polarization of the beam. When the incident beam forms an angle ϵ with the normal, as shown in figure D.1.a, the vertical polarization propagates with the same index of refraction $n_o(\lambda)$, but, the horizontal polarization is subjected to the refractive index $n(\epsilon, \lambda)$ [117]:

$$n(\epsilon, \lambda) = n_o(\lambda) \sqrt{\frac{1 + \tan^2 \epsilon}{1 + \left(\frac{n_o(\lambda)}{n_e(\lambda)}\right)^2 \tan^2 \epsilon}}, \quad (\text{D.1})$$

where $n_e(\lambda)$ is the refractive index of the extraordinary axis. The parameter λ indicates that all refractive indices depend on the wavelength of the beam passing through the quartz plate. Because the quartz is a positive uniaxial crystal, with $n_e(\lambda) > n_o(\lambda)$, the extraordinary axis is the slow axis. For the horizontally polarized component of the beam, the optical path length is consequently longer than for the vertically polarized one. The introduced phase change ξ between the orthogonal polarizations is determined by:

$$\xi = \frac{2\pi d}{\lambda} \left(\frac{n(\epsilon, \lambda)}{\cos r_{e,o}} - \frac{n_o(\lambda)}{\cos r_o} \right), \quad (\text{D.2})$$

with the plate thickness d , the refraction angles $r_{e,o}$ for the extraordinary ray (horizontally polarized) and r_o for the ordinary ray (vertically polarized). By applying Snell–Descartes’ law with the refractive index $n_1 = 1$ for the initial medium, it can be shown that:

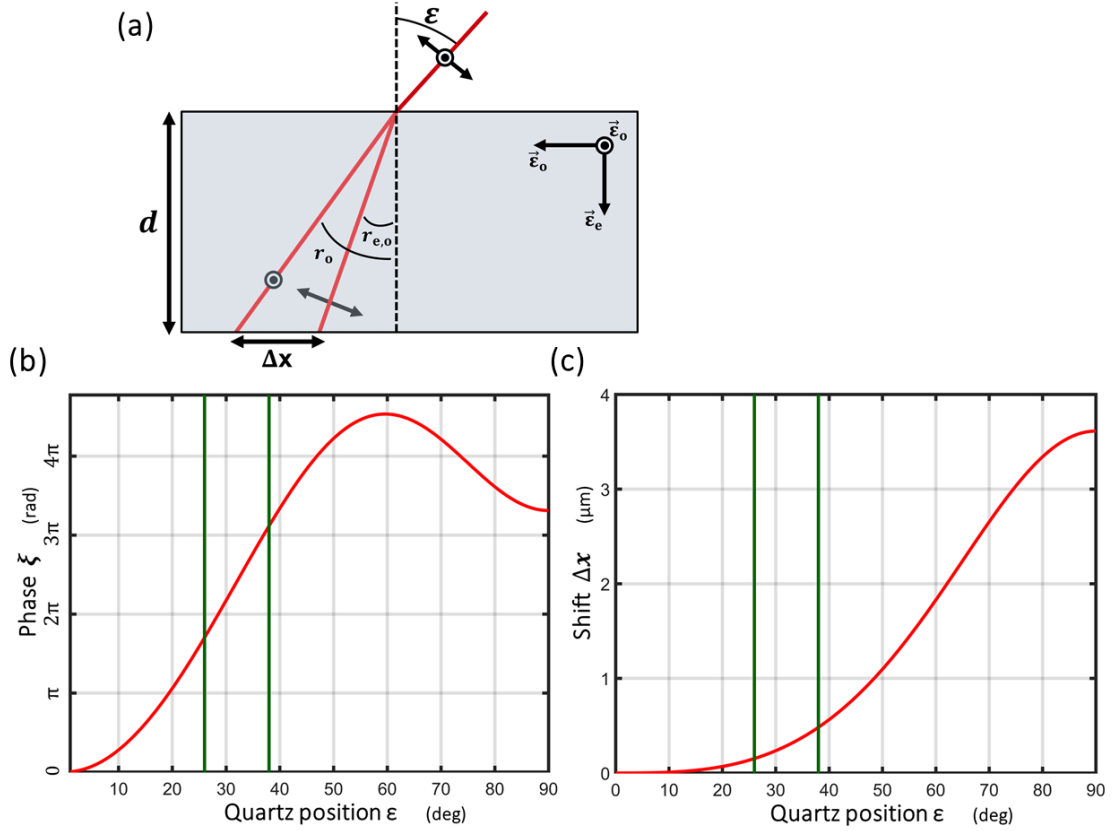


Figure D.1: Phase and position change induced by a z-cut quartz plate. (a) Schematic illustration of the motorized z-cut quartz plate with respect to the incident light beam. (b) Phase change ξ between the horizontal and vertical polarizations with respect to the quartz position ϵ . (c) Spatial shift Δx between the horizontally and vertically polarized raies with respect to the quartz position ϵ . The interval delimited by the green vertical lines illustrates the position range of the motorized quartz plate.

$$r_o = \arcsin\left(\frac{\sin \epsilon}{n_o}\right), \quad (\text{D.3})$$

$$r_{e,o} = \arctan\left(\frac{\sin \epsilon}{n_o \sqrt{1 - \frac{\sin^2 \epsilon}{n_e^2}}}\right). \quad (\text{D.4})$$

By considering a thickness of 1 mm for the quartz plate with the indices of refraction $n_o = 1.538$ and $n_e = 1.547$ at $\lambda = 817.4$ nm, the relative phase ξ between the horizontal and vertical polarizations is represented in figure D.1.b as a function of the quartz rotation angle ϵ . For rotations of the quartz plate from 26° to 38° the induced relative phase varies linearly. Hence, a calibration of the motorized quartz stage by determining

only two coefficients is theoretically possible. As shown in figure D.1.c, the spatial shift Δx between the horizontally and vertically polarized rays at the second interface of the quartz plate is deduced by using:

$$\Delta x = d (\tan r_o - \tan r_{e,o}) . \quad (\text{D.5})$$

Thereby, it is important that this shift is small compared to the diameter, or the waist, of the incident beam. In our case, the diameter of the light cone is experimentally around 0.5 mm. Figure D.1.c reveals clearly that the relative distance Δx is smaller than 0.5 μm for rotations of a quartz plate (with a thickness of 1 mm) from 26° to 38° . This effect is three orders of magnitude smaller than the cone diameter, and is therefore negligible.

E

Quantum tomography table

	Coincidence Counts				Detector Counts			
	N_{13}	N_{14}	N_{23}	N_{24}	N_1	N_3	N_2	N_4
$ H\rangle H\rangle$	283 784	15 427	18 774	290 961	5 878 661	9 313 800	6 888 864	10 591 361
$ H\rangle V\rangle$	17 737	282 986	290 033	16 849	5 871 485	11 118 986	6 853 128	8 914 078
$ H\rangle D\rangle$	154 985	149 504	147 175	154 269	5 879 557	10 019 712	6 855 567	9 729 798
$ H\rangle A\rangle$	147 689	148 196	161 195	153 262	5 887 789	10 451 978	6 865 495	10 013 297
$ H\rangle R\rangle$	155 549	154 920	144 492	154 547	5 846 923	10 105 894	6 830 831	10 100 326
$ H\rangle L\rangle$	143 796	143 115	168 603	148 651	5 874 084	10 176 463	6 839 824	9 387 503
$ V\rangle H\rangle$	14 708	283 576	296 044	14 421	6 611 902	9 315 121	6 120 321	10 593 898
$ V\rangle V\rangle$	287 564	14 401	15 432	296 220	6 607 267	11 137 852	6 119 461	8 929 359
$ V\rangle D\rangle$	149 757	149 847	155 895	157 564	6 624 583	10 018 643	6 129 598	9 773 617
$ V\rangle A\rangle$	151 204	149 114	156 017	152 871	6 616 859	10 474 614	6 126 713	10 028 537
$ V\rangle R\rangle$	157 966	134 479	149 138	169 568	6 590 974	10 117 668	6 070 891	10 119 530
$ V\rangle L\rangle$	146 937	161 499	158 912	142 308	6 617 007	10 205 175	6 071 572	9 410 425
$ D\rangle H\rangle$	159 156	136 824	149 100	165 895	6 059 181	9 312 937	6 695 106	10 607 876
$ D\rangle V\rangle$	137 634	159 095	167 897	145 884	6 034 902	11 111 713	6 648 128	8 911 377
$ D\rangle D\rangle$	268 468	35 289	33 771	277 293	6 092 655	10 053 303	6 699 244	9 765 808
$ D\rangle A\rangle$	28 635	263 321	283 779	32 043	6 044 440	10 440 187	6 660 011	10 000 406
$ D\rangle R\rangle$	147 847	122 402	160 459	179 326	6 019 038	10 089 972	6 612 669	10 093 214
$ D\rangle L\rangle$	155 035	177 828	160 615	129 790	5 789 731	9 622 748	6 321 374	8 697 354
$ A\rangle H\rangle$	140 239	163 287	166 744	140 197	6 422 689	9 324 821	6 334 005	10 611 803
$ A\rangle V\rangle$	168 467	138 099	138 424	166 932	6 396 684	11 133 399	6 290 462	8 887 294
$ A\rangle D\rangle$	40 149	264 514	268 660	36 662	6 432 543	10 048 993	6 303 928	9 740 381
$ A\rangle A\rangle$	269 014	34 085	34 948	273 704	6 414 798	10 463 607	6 313 313	9 989 103
$ A\rangle R\rangle$	171 770	162 110	125 923	148 934	6 403 532	10 090 898	6 284 008	10 101 898
$ A\rangle L\rangle$	135 438	136 605	176 231	161 123	6 418 594	10 188 347	6 291 421	9 413 211
$ R\rangle H\rangle$	144 123	166 105	160 123	142 426	6 077 295	9 273 615	6 470 912	10 566 521
$ R\rangle V\rangle$	160 817	132 233	148 116	172 133	6 070 509	11 114 605	6 457 463	8 857 104
$ R\rangle D\rangle$	130 392	139 950	174 526	170 842	6 083 120	10 011 756	6 464 047	9 717 427
$ R\rangle A\rangle$	176 967	155 567	130 109	147 081	6 074 686	10 440 022	6 460 577	9 958 317
$ R\rangle R\rangle$	39 179	260 207	268 879	41 086	6 068 141	10 101 385	6 442 712	10 106 359
$ R\rangle L\rangle$	261 593	40 621	44 086	263 695	6 068 304	10 159 228	6 450 534	9 438 886
$ L\rangle H\rangle$	146 361	141 921	160 881	156 279	6 212 900	9 267 181	6 317 553	10 542 853
$ L\rangle V\rangle$	154 554	158 396	151 390	146 121	6 214 540	11 118 918	6 308 935	8 873 799
$ L\rangle D\rangle$	152 641	177 890	150 700	125 354	6 204 301	9 991 582	6 303 948	9 713 996
$ L\rangle A\rangle$	147 871	123 518	164 453	175 086	6 222 419	10 446 049	6 329 874	9 965 261
$ L\rangle R\rangle$	260 751	40 446	43 706	263 642	6 071 561	10 183 970	6 448 186	9 406 104
$ L\rangle L\rangle$	39 512	251 483	272 634	37 801	6 200 274	10 153 993	6 292 675	9 395 460

Table E.1: Coincidence counts and total counts to reconstruct the experimental produced two-photon state $\hat{\rho}_{exp}^{(1)}$ given in (3.35).

F

Quantum tomography density matrix

In chapter 3, we use four preparations to determine real weak values. The meter purity P_m and the measurement strength θ resulting from the prepared two-qubit state ρ_{exp} are analysed by the quantum tomography method. Since the strength θ decreases from the first to the fourth preparation, the real part of the element (1,1) in the density matrices increases (and the real part of the element (4,4) decreases). As a result, the non-classical elements (red bars) are small for weak measurement strengths.

Set-up 2.

$$\hat{\rho}_{exp}^{(2)} = \begin{pmatrix} 0.734 & 0.008 - 0.017i & 0.009 + 0.006i & 0.330 - 0.004i \\ 0.008 + 0.017i & 0.013 & 0.000 - 0.008i & 0.003 - 0.001i \\ 0.009 - 0.006i & 0.000 + 0.008i & 0.009 & 0.005 + 0.012i \\ 0.330 + 0.004i & 0.003 + 0.001i & 0.005 - 0.012i & 0.244 \end{pmatrix} \quad (\text{F.1})$$

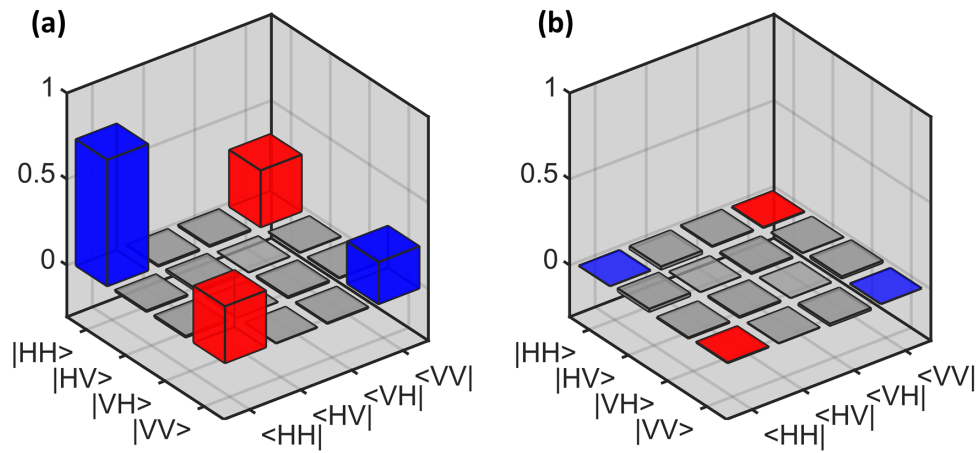


Figure F.1: Schematical representation of the (a) real and (b) imaginary parts of the density matrix $\hat{\rho}_{exp}^{(2)}$.

Set-up 3.

$$\hat{\rho}_{exp}^{(3)} = \begin{pmatrix} 0.955 & 0.008 + 0.009i & 0.007 - 0.005i & 0.138 + 0.004i \\ 0.008 - 0.009i & 0.010 & -0.001 + 0.004i & 0.000 - 0.002i \\ 0.007 + 0.005i & -0.001 - 0.004i & 0.006 & 0.002 - 0.002i \\ 0.138 - 0.004i & 0.000 + 0.002i & 0.002 + 0.002i & 0.029 \end{pmatrix} \quad (\text{F.2})$$

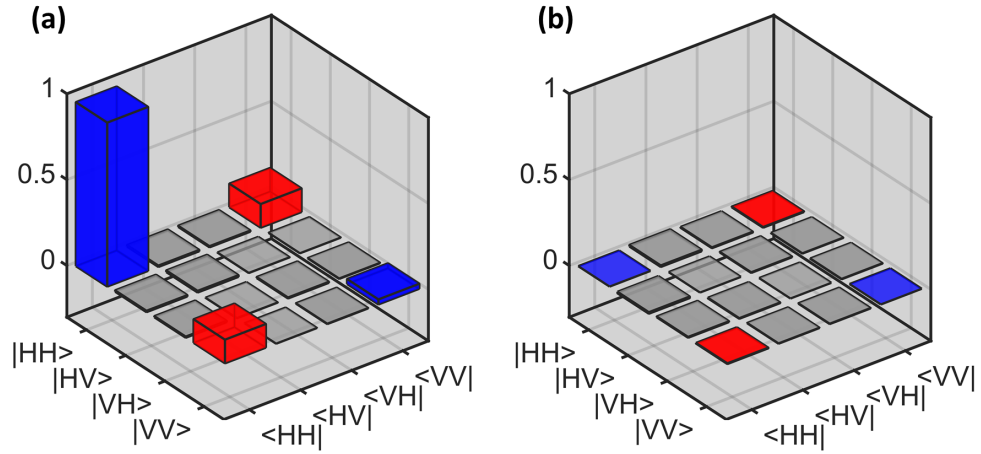


Figure F.2: Schematical representation of the (a) real and (b) imaginary parts of the density matrix $\hat{\rho}_{exp}^{(3)}$.

Set-up 4.

$$\hat{\rho}_{exp}^{(4)} = \begin{pmatrix} 0.984 & -0.000 + 0.005i & -0.001 - 0.003i & 0.039 + 0.008i \\ -0.000 - 0.005i & 0.009 & -0.002 + 0.001i & 0.000 - 0.001i \\ -0.001 + 0.003i & -0.002 - 0.001i & 0.005 & 0.000 - 0.000i \\ 0.039 - 0.008i & 0.000 + 0.001i & 0.000 + 0.000i & 0.002 \end{pmatrix} \quad (\text{F.3})$$

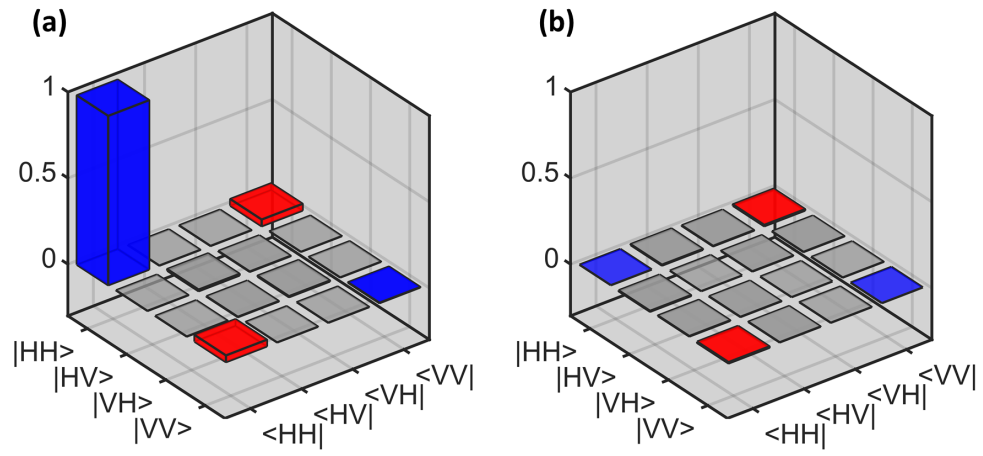


Figure F.3: Schematical representation of the (a) real and (b) imaginary parts of the density matrix $\hat{\rho}_{exp}^{(4)}$.

G

Modulus of complex weak value

In chapter 3, we use four preparations to determine complex weak values. Because we put the focus on the readouts of the weak values argument in this section, the experimental results for the modulus of set-up 2 and 3 are given now in the Appendix.

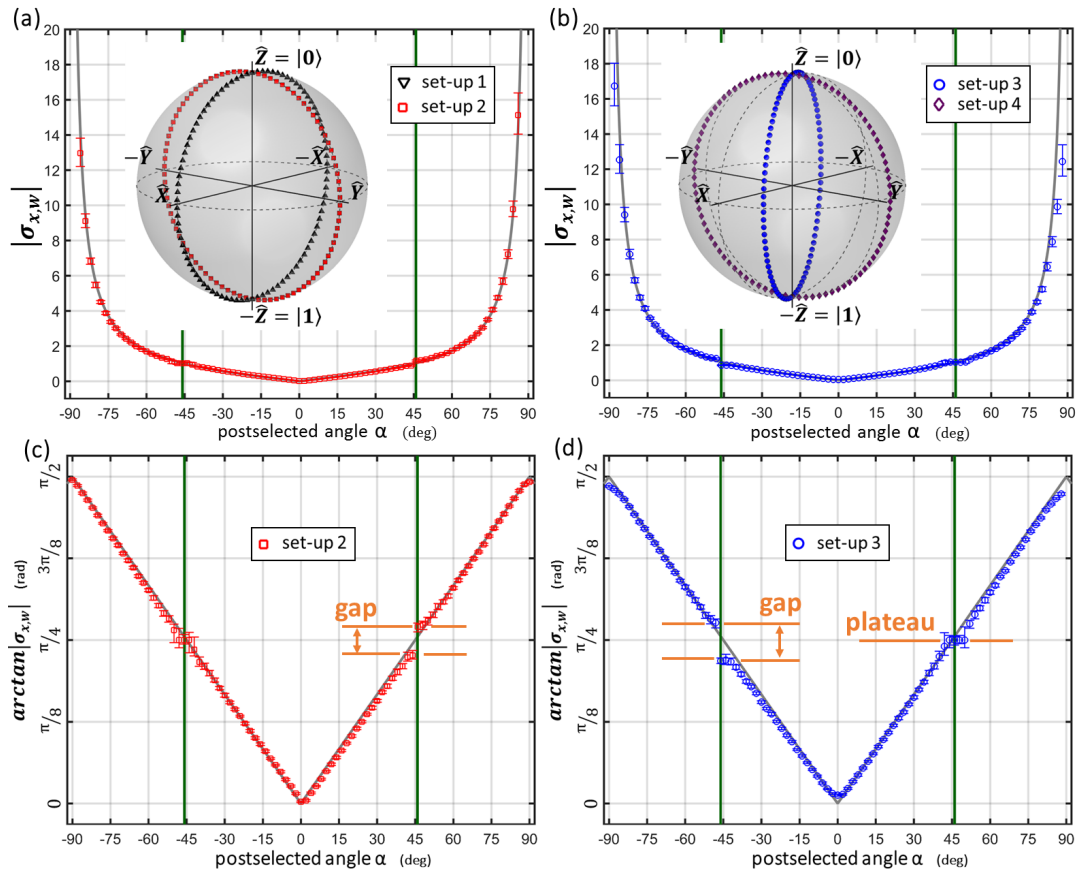


Figure G.1: Modulus of complex weak values: (a-b) the unbounded modulus $|\sigma_{x,w}(\alpha, \phi)|$ and (c-d) the corresponding bounded values of $\arctan|\sigma_{x,w}(\alpha, \phi)|$ are represented for the relative phases $\phi_2 = \pi/2$ and $\phi_3 = \pi/7$.

H

Weak and modular values of qubit observables expressed using Bloch vectors

H.1 Projection probability and modulus expression

The projection probability between two arbitrary qubit states $|\langle\phi_v|\phi_u\rangle|^2$ is given by the trace $\text{Tr} [\hat{\Pi}_v \hat{\rho}_u]$ where the projector is $\hat{\Pi}_v = \frac{1}{2}(\hat{I} + \vec{v} \cdot \vec{\sigma})$ and the density operator is equivalently expressed by $\hat{\rho}_u = \frac{1}{2}(\hat{I} + \vec{u} \cdot \vec{\sigma})$. Products between Pauli matrices verify the well-known property [42]

$$(\vec{v} \cdot \vec{\sigma})(\vec{u} \cdot \vec{\sigma}) = (\vec{v} \cdot \vec{u}) \hat{I} + j (\vec{v} \times \vec{u}) \cdot \vec{\sigma} \quad (\text{H.1})$$

due to their commutation rules, where j is the unit imaginary number. The operator to be traced is thus given by

$$\hat{\Pi}_v \hat{\rho}_u = \frac{1}{4} (1 + \vec{v} \cdot \vec{u}) \hat{I} + \frac{1}{4} [\vec{u} + \vec{v} + j (\vec{v} \times \vec{u})] \cdot \vec{\sigma}. \quad (\text{H.2})$$

When taking the trace, only the first term survives because Pauli matrices are traceless. Thus, the projection probability is equal to

$$|\langle\phi_v|\phi_u\rangle|^2 = \text{Tr} [\hat{\Pi}_v \hat{\rho}_u] = \frac{1}{2} (1 + \vec{v} \cdot \vec{u}). \quad (\text{H.3})$$

Since weak and modular values are given by products and ratios of state overlaps through expressions (4.2) and (4.7), their modulus take the form of products and ratios of square roots of the form $|\langle\phi_v|\phi_u\rangle| = \sqrt{\frac{1}{2}(1 + \vec{v} \cdot \vec{u})}$.

H.2 Qubit projection Operator

The weak value of a qubit projector is by definition [42]

$$\hat{\Pi}_{r,w} = \frac{\langle \phi_f | \hat{\Pi}_r | \phi_i \rangle}{\langle \phi_f | \phi_i \rangle} = \frac{\text{Tr} \left[\hat{\Pi}_f \hat{\Pi}_r \hat{\rho}_i \right]}{\text{Tr} \left[\hat{\Pi}_f \hat{\rho}_i \right]}. \quad (\text{H.4})$$

The denominator is given by expression (H.3) with the appropriate substitutions $\vec{u} = \vec{i}$ and $\vec{v} = \vec{f}$. To find the numerator, we start from result (H.2) but with the substitutions $\vec{u} = \vec{i}$ and $\vec{v} = \vec{r}$, so that

$$\begin{aligned} \hat{\Pi}_f \hat{\Pi}_r \hat{\rho}_i &= \frac{1}{4} \left(1 + \vec{r} \cdot \vec{i} \right) \hat{\Pi}_f + \frac{1}{4} \hat{\Pi}_f \left[\vec{i} + \vec{r} + j \left(\vec{r} \times \vec{i} \right) \right] \cdot \vec{\sigma} \\ &= \frac{1}{8} \left(1 + \vec{r} \cdot \vec{i} \right) \left(\hat{I} + \vec{f} \cdot \vec{\sigma} \right) + \frac{1}{8} \left(\hat{I} + \vec{f} \cdot \vec{\sigma} \right) \left[\vec{i} + \vec{r} + j \left(\vec{r} \times \vec{i} \right) \right] \cdot \vec{\sigma}, \end{aligned} \quad (\text{H.5})$$

where we replaced the projector $\hat{\Pi}_f = \frac{1}{2}(\hat{I} + \vec{f} \cdot \vec{\sigma})$ by its expression. Using property (H.1) to resolve the product between the Pauli matrices, this expression expands to

$$\begin{aligned} \hat{\Pi}_f \hat{\Pi}_r \hat{\rho}_i &= \frac{1}{8} \left(1 + \vec{r} \cdot \vec{i} \right) \left(\hat{I} + \vec{f} \cdot \vec{\sigma} \right) + \frac{1}{8} \left[\vec{i} + \vec{r} + j \left(\vec{r} \times \vec{i} \right) \right] \cdot \vec{\sigma} \\ &+ \frac{1}{8} \vec{f} \cdot \left[\vec{i} + \vec{r} + j \left(\vec{r} \times \vec{i} \right) \right] \hat{I} + \frac{1}{8} j \left\{ \vec{f} \times \left[\vec{i} + \vec{r} + j \left(\vec{r} \times \vec{i} \right) \right] \right\} \cdot \vec{\sigma}. \end{aligned} \quad (\text{H.6})$$

Taking the trace of this expression suppresses all the terms involving Pauli matrices, so that the weak value of the projector $\hat{\Pi}_r$ is finally given by:

$$\Pi_{r,w} = \frac{\text{Tr} \left[\hat{\Pi}_f \hat{\Pi}_r \hat{\rho}_i \right]}{\text{Tr} \left[\hat{\Pi}_f \hat{\rho}_i \right]} = \frac{1}{2} \frac{1 + \vec{f} \cdot \vec{r} + \vec{r} \cdot \vec{i} + \vec{f} \cdot \vec{i} + j \left[\vec{f} \cdot \left(\vec{r} \times \vec{i} \right) \right]}{1 + \vec{f} \cdot \vec{i}}. \quad (\text{H.7})$$

The argument of the weak value given by (4.5) is deduced immediately from this expression by considering the real and the imaginary part of the numerator (proper care should be given to the sign of the numerator and denominator in the arctangent function to determine the correct quadrant of the angle).

H.3 Qubit unitary operator

The modular value $\sigma_{r,m}^{\alpha,\beta}$ of the qubit unitary operator $\hat{U}_{\sigma_r}^{\alpha,\beta} = e^{j\frac{\beta}{2}} e^{-j\frac{\alpha}{2}\hat{\sigma}_r}$ is defined by

$$\sigma_{r,m}^{\alpha,\beta} = e^{j\frac{\beta}{2}} \frac{\langle \phi_f | e^{-j\frac{\alpha}{2}\hat{\sigma}_r} | \phi_i \rangle}{\langle \phi_f | \phi_i \rangle} = e^{j\frac{\beta}{2}} \frac{\text{Tr} \left[\hat{\Pi}_f e^{-j\frac{\alpha}{2}\hat{\sigma}_r} \hat{\rho}_i \right]}{\text{Tr} \left[\hat{\Pi}_f \hat{\rho}_i \right]}. \quad (\text{H.8})$$

The denominator is given by expression (H.3) with the appropriate substitutions $\vec{u} = \vec{i}$ and $\vec{v} = \vec{f}$. Considering that the Pauli operator can be expressed as the difference between two orthogonal projectors $\hat{\sigma}_r = \hat{\Pi}_r - \hat{\Pi}_{-r}$, we can write the numerator as:

$$\text{Tr} \left[\hat{\Pi}_f e^{-j\frac{\alpha}{2}\hat{\sigma}_r} \hat{\rho}_i \right] = e^{-j\frac{\alpha}{2}} \text{Tr} \left[\hat{\Pi}_f \hat{\Pi}_r \hat{\rho}_i \right] + e^{j\frac{\alpha}{2}} \text{Tr} \left[\hat{\Pi}_f \hat{\Pi}_{-r} \hat{\rho}_i \right]. \quad (\text{H.9})$$

The calculation of the first trace was already performed in expressions (H.6–H.7), while the second trace can be obtained from this previous result by replacing the vector \vec{r} by $-\vec{r}$. Therefore, we find that the numerator (H.9) becomes

$$\begin{aligned} & \frac{e^{-j\frac{\alpha}{2}}}{4} \left(1 + \vec{f} \cdot \vec{r} + \vec{r} \cdot \vec{i} + \vec{f} \cdot \vec{i} + jV \right) + \frac{e^{j\frac{\alpha}{2}}}{4} \left(1 - \vec{f} \cdot \vec{r} - \vec{r} \cdot \vec{i} + \vec{f} \cdot \vec{i} - jV \right) \\ &= \frac{1}{2} \left\{ \cos \frac{\alpha}{2} \left(1 + \vec{f} \cdot \vec{i} \right) + \sin \frac{\alpha}{2} \left[V - j \left(\vec{f} \cdot \vec{r} + \vec{r} \cdot \vec{i} \right) \right] \right\}. \end{aligned} \quad (\text{H.10})$$

where we wrote the signed volume of the parallelepiped defined by the vector triad by $V = \vec{f} \cdot (\vec{r} \times \vec{i})$. In the end, we obtain the following expression for the modular value as a function of Bloch vectors:

$$\sigma_{r,m}^{\alpha,\beta} = e^{j\frac{\beta}{2}} \frac{\cos \frac{\alpha}{2} \left(1 + \vec{f} \cdot \vec{i} \right) + \sin \frac{\alpha}{2} \left[V - j \left(\vec{f} \cdot \vec{r} + \vec{r} \cdot \vec{i} \right) \right]}{1 + \vec{f} \cdot \vec{i}}.$$

The total argument of the modular value can be readily deduced from the expression above. It contains a dynamical contribution $(\beta - \alpha)/2$ and a geometrical contribution defined by $\Omega = -\Omega_{irsf}/2$. We now evaluate the geometrical contribution Ω in terms of Bloch vectors:

$$\Omega = \arg \left\{ \left\{ \cos \frac{\alpha}{2} \left(1 + \vec{f} \cdot \vec{i} \right) + \sin \frac{\alpha}{2} \left[V - j \left(\vec{f} \cdot \vec{r} + \vec{r} \cdot \vec{i} \right) \right] \right\} e^{j\frac{\alpha}{2}} \right\}, \quad (\text{H.11})$$

where the phase factor at the end is required to remove the appropriate dynamical contribution. By expanding this expression, we find the value of the geometric phase

as a function of Bloch vectors:

$$\Omega = \arg \left\{ \begin{aligned} & \left[1 + \vec{f} \cdot \vec{i} + V \tan \frac{\alpha}{2} + (\vec{f} \cdot \vec{r} + \vec{r} \cdot \vec{i}) \tan^2 \frac{\alpha}{2} \right] \\ & + j \left[1 + \vec{f} \cdot \vec{i} + V \tan \frac{\alpha}{2} - (\vec{f} \cdot \vec{r} + \vec{r} \cdot \vec{i}) \right] \tan \frac{\alpha}{2} \end{aligned} \right\}. \quad (\text{H.12})$$

This solid angle can be expressed as the sum of two contributions $\Omega = \Omega_1 + \Omega_2$, where

$$\Omega_1 = \arg \left\{ \begin{aligned} & \left[1 + \vec{f} \cdot \vec{i} + V \tan \frac{\alpha}{2} + (\vec{f} \cdot \vec{r} + \vec{r} \cdot \vec{i}) \tan^2 \frac{\alpha}{2} (\vec{r} \cdot \vec{i}) \right] \\ & + j \left[(\vec{f} \cdot \vec{i}) (\vec{r} \cdot \vec{i}) + V \tan \frac{\alpha}{2} (\vec{r} \cdot \vec{i}) - \vec{f} \cdot \vec{r} \right] \tan \frac{\alpha}{2} \end{aligned} \right\}, \quad (\text{H.13})$$

$$\Omega_2 = \arg \left\{ \left[1 + \vec{r} \cdot \vec{i} \tan^2 \frac{\alpha}{2} \right] + j \left[\tan \frac{\alpha}{2} (1 - \vec{r} \cdot \vec{i}) \right] \right\}. \quad (\text{H.14})$$

Using a symbolic computation package, it is straightforward to show that $\tan \Omega = \tan(\Omega_1 + \Omega_2) = (\tan \Omega_1 + \tan \Omega_2) / (1 - \tan \Omega_1 \tan \Omega_2)$ and that the angles are defined in the proper quadrants. The values given above for Ω_1 and Ω_2 result directly from the definitions of

$$\Omega_1 = \arg \left[1 + \vec{f} \cdot \vec{s} + \vec{s} \cdot \vec{i} + \vec{f} \cdot \vec{i} + j \vec{f} \cdot (\vec{s} \times \vec{i}) \right] = -\frac{1}{2} \Omega_{isf}, \quad (\text{H.15})$$

$$\Omega_2 = \arg \left[1 + \vec{s} \cdot \vec{r} + \vec{r} \cdot \vec{i} + \vec{s} \cdot \vec{i} + j \vec{s} \cdot (\vec{r} \times \vec{i}) \right] = -\frac{1}{2} \Omega_{irs}, \quad (\text{H.16})$$

where the vector \vec{s} was expressed by Rodrigue's rotation formula (4.8). As a result, the geometrical phase is related to the solid angle by $\Omega = -\frac{1}{2}(\Omega_{isf} + \Omega_{irf}) = -\frac{1}{2}\Omega_{irsf}$.

I

Algebraic structure of qutrits

We introduce the density matrix of the qutrit $\hat{\rho}_n$ in terms of the 8-dimensional real vector \vec{n} :

$$\hat{\rho}_n = \frac{1}{3} \left(\hat{I} + \sqrt{3} \vec{n} \cdot \vec{\lambda} \right), \quad (\text{I.1})$$

with $\vec{\lambda}$ the vector containing the eight Gell-Mann λ -matrices. For pure states the vector \vec{n} verifies the pair of constraints [101]:

$$\vec{n} \cdot \vec{n} = 1, \quad \vec{n} * \vec{n} = \vec{n}, \quad (\text{I.2})$$

where the second product defines the star-product $\mathbb{R}^8 \rightarrow \mathbb{R}^8$ on vector \vec{n} . The star product results directly from the algebraic structure of the λ -matrices, which is verified [101]:

$$\lambda_j \lambda_k = \frac{2}{3} \delta_{jk} + \sum_l d_{jkl} \lambda_l + i \sum_l f_{jkl} \lambda_l, \quad (\text{I.3})$$

so that it is defined by $(\vec{n} * \vec{n})_l = \sqrt{3} \sum_{j,k} d_{jkl} n_j n_k$. The structure constants of the Lie algebra of $SU(3)$ d_{jkl} and f_{jkl} are totally symmetric and antisymmetric in their indices, respectively. All independent nonvanishing components are:

$$\begin{aligned} d_{118} = d_{228} = d_{338} = -d_{888} &= \frac{1}{\sqrt{3}}, \\ d_{146} = d_{157} = -d_{247} = d_{256} &= \frac{1}{2}, \\ d_{344} = d_{355} = -d_{366} = -d_{377} &= \frac{1}{2}, \\ d_{448} = d_{558} = -d_{668} = -d_{778} &= -\frac{1}{2\sqrt{3}}, \\ f_{123} = 1, \quad f_{458} = f_{688} &= \frac{\sqrt{3}}{2}, \\ f_{147} = f_{246} = f_{257} = f_{345} &= f_{516} = f_{637} = \frac{1}{2}. \end{aligned} \quad (\text{I.4})$$

Similarly to the qubit case, any unitary evolution operator applied on qutrits can be written in the form of:

$$\hat{U}_{\lambda_r}^{\alpha,\beta} = e^{i\beta} e^{-i\alpha\hat{\lambda}_r}, \quad (\text{I.5})$$

with $\hat{\lambda}_r = \vec{r} \cdot \vec{\hat{\lambda}}$ and the normalized vector $\vec{r} \in \mathbb{R}^8$. The characteristic polynomial of the traceless Hermitian operator $\hat{\lambda}_r$ is:

$$\hat{\lambda}_r^3 = \det(\hat{\lambda}_r) \hat{I} + \frac{1}{2} \text{tr} [\hat{\lambda}_r^2] \hat{\lambda}_r, \quad (\text{I.6})$$

with $\text{tr} [\hat{\lambda}_r^2] = 2$ because $\hat{\lambda}_r^2 = \frac{2}{3} \hat{I} + \frac{1}{\sqrt{3}} (\vec{r} * \vec{r}) \cdot \vec{\hat{\lambda}}$.

J

Majorana representation for an arbitrary state

After application of the unitary operators, an arbitrary initial state can be written as $|\psi_i''\rangle = (e^{j\chi_1} \cos \epsilon \sin \theta, e^{j\chi_2} \sin \epsilon \sin \theta, \cos \theta)^T$. Its Majorana polynomial is given by

$$z^2 - \sqrt{2} \sin \epsilon \tan \theta e^{j\chi_2} z + \cos \epsilon \tan \theta e^{j\chi_1} = 0, \quad (\text{J.1})$$

where the roots $z_{1,2} = \tan(\frac{\beta_{1,2}}{2}) e^{j\alpha_{1,2}}$ provide the coefficients of the qubits states $|\phi_i^{(1,2)}\rangle = e^{-j\frac{\alpha_{1,2}}{2}} \cos \frac{\beta_{1,2}}{2} |0\rangle + e^{j\frac{\alpha_{1,2}}{2}} \sin \frac{\beta_{1,2}}{2} |1\rangle$. The solutions are given by

$$\alpha_{1,2} = \frac{\chi_1}{2} \pm (-1)^k \arccos \left(\frac{\sqrt{2} \sin \epsilon \tan \theta}{S} \cos \tilde{\chi} \right),$$

$$\beta_{1,2} = 2 \arctan \left(\frac{S \pm \sqrt{S^2 - 4 \cos \epsilon \tan \theta}}{2} \right), \quad (\text{J.2})$$

where we defined $\tilde{\chi} = \frac{2\chi_2 - \chi_1}{2}$ and $S = \sqrt{2 \cos \epsilon \tan \theta + \sin^2 \epsilon \tan^2 \theta + \sqrt{\rho}}$ with $\rho = 4 \cos^2 \epsilon \tan^2 \theta + \sin^4 \epsilon \tan^4 \theta - 4 \cos \epsilon \sin^2 \epsilon \tan^3 \theta \cos(2\tilde{\chi})$. The parameter k in the relation of $\alpha_{1,2}$ is zero if the condition $0 \leq \tilde{\chi} < \pi$ is satisfied, and equals one if $\pi \leq \tilde{\chi} < 2\pi$.

K

Orthogonal-state decomposition

To prove that the symmetric state $|\Psi\rangle = K (|\phi^{(1)}\rangle|\phi^{(2)}\rangle + |\phi^{(2)}\rangle|\phi^{(1)}\rangle)$ is equivalent to the superposition of two orthogonal states $|\Psi\rangle = c_+|+\rangle - c_-|-\rangle$, we start the demonstration with the final result and derive the symmetric state. By considering the real parameters c_{\pm} and the state vectors $|\pm\rangle$, which are given by:

$$\begin{aligned} c_{\pm} &= K (1 \pm |\langle\phi^{(2)}|\phi^{(1)}\rangle|) , \\ |\pm\rangle &= \frac{1}{\sqrt{2}} \left(\sqrt{1 \pm |\langle\phi^{(2)}|\phi^{(1)}\rangle|} |\epsilon_0\rangle \pm e^{-i\phi_{12}} \sqrt{1 \mp |\langle\phi^{(2)}|\phi^{(1)}\rangle|} |\epsilon_1\rangle \right) , \end{aligned} \quad (\text{K.1})$$

with $\phi_{12} = \arg\langle\phi^{(1)}|\phi^{(2)}\rangle$ and the states:

$$|\epsilon_0\rangle = |\phi^{(1)}\rangle , \quad (\text{K.2})$$

$$|\epsilon_1\rangle = (1 - |\langle\phi^{(2)}|\phi^{(1)}\rangle|^2)^{-\frac{1}{2}} (|\phi^{(2)}\rangle - \langle\phi^{(1)}|\phi^{(2)}\rangle |\phi^{(1)}\rangle) , \quad (\text{K.3})$$

we deduce that $|\pm\rangle$ is:

$$\begin{aligned} &= \frac{1}{\sqrt{2}} \left(\sqrt{1 \pm |\langle\phi^{(2)}|\phi^{(1)}\rangle|} |\phi^{(1)}\rangle \pm e^{-i\phi_{12}} \sqrt{\frac{1 \mp |\langle\phi^{(2)}|\phi^{(1)}\rangle|}{1 - |\langle\phi^{(2)}|\phi^{(1)}\rangle|^2}} (|\phi^{(2)}\rangle - \langle\phi^{(1)}|\phi^{(2)}\rangle |\phi^{(1)}\rangle) \right) , \\ &= \frac{1}{\sqrt{2}} \left(\frac{1 \pm |\langle\phi^{(2)}|\phi^{(1)}\rangle|}{\sqrt{1 \pm |\langle\phi^{(2)}|\phi^{(1)}\rangle|}} |\phi^{(1)}\rangle \pm \frac{1}{\sqrt{1 \pm |\langle\phi^{(2)}|\phi^{(1)}\rangle|}} (e^{-i\phi_{12}} |\phi^{(2)}\rangle - |\langle\phi^{(2)}|\phi^{(1)}\rangle| |\phi^{(1)}\rangle) \right) , \\ &= \frac{1}{\sqrt{2}} \frac{1}{\sqrt{1 \pm |\langle\phi^{(2)}|\phi^{(1)}\rangle|}} (|\phi^{(1)}\rangle \pm e^{-i\phi_{12}} |\phi^{(2)}\rangle) . \end{aligned} \quad (\text{K.4})$$

This allows to re-write:

$$c_{\pm} |\pm\rangle = \frac{K}{2} (|\phi^{(1)}\rangle|\phi^{(1)}\rangle \pm e^{-i\phi_{12}} (|\phi^{(1)}\rangle|\phi^{(2)}\rangle + |\phi^{(2)}\rangle|\phi^{(1)}\rangle) + e^{-i2\phi_{12}} |\phi^{(2)}\rangle|\phi^{(2)}\rangle) . \quad (\text{K.5})$$

Finally, the state $|\Psi\rangle = c_+|+\rangle - c_-|-\rangle = e^{-i\phi_{12}} K (|\phi^{(1)}\rangle|\phi^{(2)}\rangle + |\phi^{(2)}\rangle|\phi^{(1)}\rangle)$ with the additional global phase $e^{-i\phi_{12}}$. Because weak values are invariant under gauge transformations, the global phase has no importance.

L

Orthogonal-state decomposition of the three-box states

The two vectors $|\Psi''_1\rangle$ and $|\Psi''_3\rangle$ are in the subspace spanned by $|\phi_r\rangle|\phi_r\rangle$ and $|\phi_{-r}\rangle|\phi_{-r}\rangle$. The qubit states are

$$|\phi_m^{(1,2)}\rangle = \left(\frac{1 \mp \sqrt{2\sqrt{3}-3}}{\sqrt{3}} \right)^{\frac{1}{2}} |0\rangle \pm \left(1 - \frac{1 \pm \sqrt{2\sqrt{3}-3}}{\sqrt{3}} \right)^{\frac{1}{2}} |1\rangle, \quad (\text{L.1})$$

$$|\phi_n^{(1,2)}\rangle = \sqrt{\frac{3-\sqrt{3}}{3}} |0\rangle + 3^{-\frac{1}{4}} e^{\mp i\phi_n} |1\rangle, \quad (\text{L.2})$$

with $\phi_n = \arctan \sqrt{9+6\sqrt{3}}$. To find the expressions (6.12) and (6.14) associated with boxes one and three, the procedure is to construct the symmetrized states according to formula (4.35), but after making a basis change from $\{|0\rangle, |1\rangle\}$ to $\{|\phi_r\rangle, |\phi_{-r}\rangle\}$. This gives the qutrit states $(\frac{\sqrt{3}}{2}, 0, \frac{1}{2})^T$ and $(-\frac{1}{2}, 0, \frac{\sqrt{3}}{2})^T$, which as expected have a nul projection on the state $\frac{1}{\sqrt{2}}(|\phi_r\rangle|\phi_{-r}\rangle + |\phi_{-r}\rangle|\phi_r\rangle)$.